Quantum Degenerate Fermi-Bose Mixtures of ^{40}K and ^{87}Rb in 3D Optical Lattices

Dissertation
zur Erlangung des Doktorgrades
des Departments Physik
der Universität Hamburg

vorgelegt von
Silke Ospelkaus-Schwarzer

aus Boppard

Hamburg
2006

Gutachter der Dissertation:	Prof. Dr. Klaus Sengstock Prof. Dr. Werner Neuhauser Prof. Dr. Tilman Pfau
Gutachter der Disputation:	Prof. Dr. Klaus Sengstock Prof. Dr. Günter Huber
Datum der Disputation:	21.12.2006
Vorsitzender des Prüfungsausschusses:	Dr. Klaus Petermann
Vorsitzender des Promotionsausschusses:	Prof. Dr. Günter Huber
Dekan der Fakultät für Mathematik, Informatik und Naturwissenschaften:	Prof. Dr. Arno Frühwald

Abstract

Recent years have seen spectacular progress towards the realization of novel strongly correlated systems with homonuclear ultracold quantum gases. The strongly correlated regime has been demonstrated to be accessible both by means of strong, periodic confinement as demonstrated in experiments with optical lattices and through strong resonant interactions which can be produced by means of Feshbach resonances.

Given the impressive development seen in homonuclear systems, heteronuclear systems composed of particles with different quantum-statistical behavior (Fermi-Bose mixtures) offer an even wider spectrum of possibilities for quantum simulation and strongly correlated phases, in particular when loaded into an optical lattice and combined with the possibility of almost arbitrary interactions through Feshbach resonances.

In this thesis, experiments with Fermi-Bose mixtures in 3-dimensional optical lattices and under the influence of tunable heteronuclear interactions are presented. An experiment allowing for the creation of large mixtures of quantum degenerate fermionic ^{40}K and bosonic ^{87}Rb gases has been set up together with C. Ospelkaus. The onset of degeneracy in both components is demonstrated, and effects of the heteronuclear attractive background interaction are studied.

Heteronuclear Feshbach resonances have been used for the first time in order to change the interaction properties of the mixture in a controlled fashion. This has allowed the study of the complete phase diagram of harmonically trapped mixtures, ranging from stable attractively interacting mixtures over a Feshbach-driven controlled mean field collapse of the system for strong attractive interactions, the onset of phase separation for strong repulsive interactions to stable, repulsively interacting mixtures. The studies of Feshbach resonances have also led to the identification of the first p-wave heteronuclear resonance.

The periodic potential of an optical lattice is an ideal environment for simulation of quantum many-body Hamiltonians and systems of reduced dimensionality. Theoretical results for fermionic and bosonic atoms in optical lattices are presented, both in a single particle picture, highlighting the role of the external trapping potential, as well as in the interacting many-particle limit.

This thesis documents the first realization of a Fermi-Bose quantum many-body system in a 3D optical lattice. In these experiments, the effect of a small fermionic fraction on the coherence properties of the bosonic sample is investigated. Already a small fermionic "impurity" fraction strongly affects the coherence properties of the bosonic cloud. The quantitative analysis shows that in the presence of the fermionic component, decoherence of the bosonic ensemble occurs at much lower lattice depths than for a pure bosonic sample. The surprisingly large effect has triggered an intense discussion on possible explanations in terms of thermodynamic properties, mean field models and disorder-related localization scenarios.

Combining tunable interactions with 3-dimensional optical lattices, formation of heteronuclear Feshbach molecules in single wells of the lattice is demonstrated for the first time, along with a determination of the molecular binding energy and lifetime. By subsequent two-color photoassociation schemes, these (externally) ground state molecules may be transferred into their internal ground state where they exhibit a permanent electric dipole moment. This may result in the realization of novel quantum gases with anisotropic interactions.

This thesis has partly been published in the following research publications:

- C. Ospelkaus *et al.*, Phys. Rev. Lett. **97**, 120402 (2006) [1].
- S. Ospelkaus *et al.*, Phys. Rev. Lett. **97**, 120403 (2006) [2].
- S. Ospelkaus *et al.*, Phys. Rev. Lett. **96**, 180403 (2006) [3].
- C. Ospelkaus *et al.*, Phys. Rev. Lett. **96**, 020401 (2006) [4].
- S. Ospelkaus, *et al.*, Journal of Modern Optics, advanced online publication (2006) [5].

Zusammenfassung

Das Feld ultrakalter homonuklearer Quantengase wurde in den letzten Jahren durch fundamentale Fortschritte in der Realisierung stark korrelierter Systeme geprägt. Das Regime starker Korrelation wurde sowohl durch starke äußere Einschlusspotentiale in optischen Gittern als auch durch starke resonante Wechselwirkung an einer Feshbach-Resonanz erreicht.

Heteronukleare Systeme gemischter Quantenstatistik (Fermi-Bose Mischungen), kombiniert mit dreidimensionalen optischen Gittern und einstellbarer Wechselwirkung, eröffnen die Perspektive, fundamental neue Quantenphasen stark korrelierter Systeme zu realisieren und in einer extrem reinen und kontrollierbaren Umgebung zu studieren.

In dieser Arbeit wurde zusammen mit C. Ospelkaus ein Experiment zum Studium ultrakalter Fermi-Bose Mischungen aus ^{40}K und ^{87}Rb in dreidimensionalen optischen Gittern mit einstellbarer Wechselwirkung aufgebaut. Ausgehend von quantentarteten Mischungen großer Teilchenzahl wurden Effekte der attraktiven Hintergrundwechselwirkung zwischen den Konstituenten untersucht.

Die Durchstimmbarkeit der Wechselwirkung an einer heteronuklearen Feshbach-Resonanz wurde erstmalig demonstriert und die grundlegenden Phasen harmonisch gefangener Fermi-Bose Mischungen untersucht. Dies reicht von einem wechselwirkungsinduzierten Kollaps im Falle attraktiver Wechselwirkung über stabile Mischungen attraktiver und repulsiver Wechselwirkung bis hin zur Phasenseparation im Falle starker repulsiver Wechselwirkung.

Periodische optische Potentiale bieten eine ideale Umgebung zur Simulation von Vielteilchen-Hamiltonoperatoren und niederdimensionalen Systemen. Grundlegende theoretische Ergebnisse für fermionische und bosonische Systeme in optischen Gittern werden sowohl aus der Perspektive eines Einteilchenbildes als auch eines Vielteilchenbildes mit und ohne Wechselwirkung vorgestellt.

Im Rahmen dieser Arbeit wurde erstmalig ein Vielteilchensystem gemischter Statistik in einem dreidimensionalen optischen Gitter realisiert. In ersten Experimenten wurden die Kohärenzeigenschaften der bosonischen Komponente unter dem Einfluss der fermionischen Atome untersucht. Bereits eine kleine Beimischung fermionischer Atome beeinflusst die Kohärenzeigenschaften der Bosonen signifikant und induziert einen Kohärenzverlust in der bosonischen Wolke bei wesentlich flacheren Gittern als im rein bosonischen System. Die Ursache dieses erstaunlich großen Effektes wird derzeitig kontrovers diskutiert. Als mögliche Ursachen werden thermodynamische Eigenschaften des Ladeprozesses der Mischung in das Gitter, eine Verschiebung des Übergangs einer superfluiden in eine Mott-isolierende Phase unter dem Einfluss der heteronuklearen Wechselwirkung sowie unordnungsinduzierte Lokalisierungsphänomene diskutiert.

Schließlich wird die erstmalige Erzeugung langlebiger heteronuklearer Feshbach-Moleküle in einem optischen Gitter vorgestellt. In diesen Experimenten wird die Durchstimmbarkeit der Wechselwirkung an einer Feshbach Resonanz mit dreidimensionalen optischen Gittern kombiniert. Die Effizienz des Assoziationsprozesses wird charakterisiert und die Bindungsenergie und Lebensdauer der Moleküle gemessen. Für heteronukleare Moleküle aus ^{40}K und ^{87}Rb wird ein permanentes elektrisches Dipolmoment in ihrem absoluten Grundzustand vorhergesagt. Diese heteronuklearen Moleküle bieten daher weitreichende Perspektiven zum Studium von Quantengasen anisotroper dipolarer Wechselwirkung.

Teile dieser Arbeit wurden in nachfolgenden Publikationen veröffentlicht:

- C. Ospelkaus *et al.*, Phys. Rev. Lett. **97**, 120402 (2006) [1].
- S. Ospelkaus *et al.*, Phys. Rev. Lett. **97**, 120403 (2006) [2].
- S. Ospelkaus *et al.*, Phys. Rev. Lett. **96**, 180403 (2006) [3].
- C. Ospelkaus *et al.*, Phys. Rev. Lett. **96**, 020401 (2006) [4].
- S. Ospelkaus, *et al.*, Journal of Modern Optics, advanced online publication (2006) [5].

Contents

Chapter 1

Introduction

Nature distinguishes between two fundamental types of particles: fermions and bosons, depending on the spin of the particle. Particles with half-integer spin are called fermions and obey Fermi-Dirac statistics. As a result of Fermi-Dirac statistics, in a system of indistinguishable particles, at most one particle can occupy a given quantum state. Particles with integer spin are called bosons and obey Bose-Einstein statistics. Any single-particle eigenstate of a physical system can be occupied by an arbitrary number of bosons.

While all of the basic building blocks of an atom are fermions, an atom as a whole has bosonic or fermionic character depending on its total angular momentum. For a gas of atoms confined in an external potential, the quantum statistical properties of the atoms become important at ultralow temperatures where the thermal deBroglie wavelength of the constituents is on the order of the interparticle separation. For bosonic atoms, this leads to the onset of Bose-Einstein condensation as observed for the first time in 1995 in a gas of ^{87}Rb in the group of Eric Cornell and Carl Wieman [6], in ^{23}Na in the group of Wolfgang Ketterle [7] and for ^{7}Li in the group of Randy Hulet [8] in the special case of attractive interactions. For fermionic atoms, the onset of degeneracy is less spectacular due to the absence of a phase transition. In an ultracold spin-polarized fermionic gas, the appearance of a macroscopic Fermi sea has first been demonstrated in the group of D. S. Jin in 1999 [9].

While the pioneering work on quantum degenerate gases revealed important quantum phenomena such as interference, superfluidity and nonlinear atom optics, recent years have seen spectacular progress in the realization of novel strongly correlated systems with ultracold quantum matter. Strong correlations are observed either when the interactions between the constituents become very strong (e. g. at Feshbach resonances) or when strong confinement imposes stringent boundary conditions (e. g. in the periodic potential of an optical lattice).

Atomic systems offer a high degree of control of both the external confinement and the interactions between the constituents. The latter has become possible with the advent of Feshbach resonances [10, 11] which allow control of s-wave and even higher order scattering between atoms through external fields. Feshbach resonances have been the key to a series of ground breaking experiments. For two-component fermionic gases, they have allowed the exploration of the BCS-BEC crossover and demonstrated that fermions and bosons are not as far from one another as it may seem: A Bose-Einstein condensate of diatomic

molecules made from two fermionic atoms can be continuously transformed into a BCS state of atomic cooper pairs [12, 13, 14, 15, 16, 17].

The "confinement-induced" approach to strongly correlated phases was first proposed for a gas of repulsively interacting bosons in 1998 by D. Jaksch and coworkers [18]. In particular, it was demonstrated that bosonic atoms loaded into an optical lattice are an ideal model system for the simulation of the Bose Hubbard Hamiltonian known from condensed matter physics, and it was predicted that the phase transition from a superfluid to a Mott-insulating state can be induced by merely increasing the lattice depth. The theoretical prediction, together with the experimental demonstration of [19], highlighted the potential of ultracold atoms in optical lattices for simulations of quantum many-body systems and for the realization of strongly-correlated systems. Optical lattices have since been the key to the observation of intriguing phenomena such as a Tonks-Girardeau gas of atoms in a one-dimensional geometry [20, 21] or a Kosterlitz-Thouless transition in a 1D lattice (2D geometry) [22]. Two-body bound states (molecules) in homonuclear systems have been engineered [23, 24] and most recently, evidence for fermionic superfluidity has been reported in a cloud of ^{6}Li loaded into a 3D optical lattice [25].

As a completely new area in the field of ultracold quantum gases, multicomponent quantum gases in 3D optical lattices have recently attracted a lot of attention. In the case of mixtures of fermionic and bosonic atoms, the different quantum-statistical behavior of the components gives rise to fundamentally novel quantum many-body phases. In the extreme case of pairing of fermions with one or more bosons, a whole zoo of new quantum phases of these "composite fermions" has been predicted [26]. Fermi-Bose mixtures in 3D optical lattices may exhibit fermionic pairing which is mediated by the presence of bosonic atoms in full analogy to solid state superconductivity, and there are interesting connections to high-T_C superconductivity. [27, 28, 29]. Even before such "atom pairs" form, Fermi-Bose correlations are predicted to become manifest in polaron-related physics of fermions dressed by a bosonic cloud [30] and quantum percolation [31]. These phenomena are connected to disorder induced localization scenarios. In reduced dimensionality, phenomena such as charge-density waves [30, 29] and supersolids [32] are predicted to occur.

From the experimental point of view, there has been an impressive series of experiments on homonuclear systems which I have partly mentioned above, but experiments on heteronuclear systems in lattices, which Fermi-Bose mixtures are a special case of, have been scarce. By the end of 2005, the only experiment with Fermi-Bose mixtures in optical lattices has been reported by Ott and coworkers at LENS [33]. In these experiments, the "insulating" behavior of a trapped ideal Fermi gas in a 1D lattice has been compared to collisionally induced transport of fermionic atoms in the presence of a bosonic cloud.

This thesis demonstrates several milestones towards the realization of a fundamentally novel quantum many-body system with mixed statistics and tunable interactions in 3D optical lattices. Apart from the first demonstration of tuning of heteronuclear interactions in the vicinity of a Feshbach resonance (see chapter 4), it presents the first realization of a Fermi-Bose many-body system in a 3D optical lattice (chapter 6). Tunability of interactions and 3D optical lattices have finally been combined for engineering of heteronuclear molecules (chapter 7) with important prospects for quantum computation, the realization of novel quantum gases with dipolar interactions and fundamental physics such as the search for a permanent electric dipole moment of the electron [34].

This thesis is organized as follows:

In **chapter 2**, I will describe the experimental apparatus for the preparation of quantum degenerate Fermi-Bose mixtures of ^{40}K and ^{87}Rb which has been set up from scratch within this thesis together with C. Ospelkaus. As an ideal basis for all subsequent experiments, this setup has produced the so far largest particle numbers in quantum degenerate ^{40}K–^{87}Rb mixtures. The ^{40}K–^{87}Rb system is characterized by a large attractive background interaction between fermions and bosons. This attractive interaction can give rise to a simultaneous collapse of the system beyond critical conditions, and I will describe symptoms of the collapse as observed in the experiment. The findings in this regime of large particle numbers have been published in C. Ospelkaus *et al.*, Phys. Rev. Lett. **96**, 020401 (2006) and are described in detail in the thesis of Christian Ospelkaus [35].

An important step towards the realization of tunable interactions is dipole trapping of the mixture. Using an optical dipole trap, the magnetic field degree of freedom is no longer necessary for trapping, but can be used to control the interactions via a homogeneous magnetic field at Feshbach resonances. In the case of heteronuclear mixtures, where the constituents have different mass, both species will exhibit a different gravitational sag in a dipole trap; in particular for shallow traps, this may result in a significantly reduced overlap of the mixture and inhibits any experiments relying on interacting mixtures. **Chapter 3** presents a crossed dipole trap at a special "magic" wavelength developed within this thesis which compensates for the differential gravitational sag and ensures an optimal overlap of the constituents for subsequent experiments with tunable interactions.

Chapter 4 presents experiments on harmonically trapped mixtures in the vicinity of a heteronuclear Feshbach resonance. While heteronuclear Feshbach resonances have previously been identified through increased inelastic collisional losses at MIT [36] and JILA [37], no tuning of elastic heteronuclear collisions had been reported before in the literature. I will first describe how we precisely determine the resonance positions and identify one of the resonances as p-wave. Tuning of heteronuclear interactions over a wide range is then demonstrated at an s-wave resonance located at 547 G. The effect of heteronuclear interactions is studied based on the mean field energy of the condensate both for attractive and repulsive interactions. The tunable interaction is also found to significantly affect the time of flight expansion of the mixture. As a function of the heteronuclear interaction, we observe both attractively and repulsively interacting stable mixtures and the occurrence of instabilities for strong resonant interactions. In the case of strong attractive interactions, this gives rise to an induced mean field collapse of the mixture, and for strong repulsive interactions, phase separation is observed. Due to the available and experimentally studied Fermi-Bose mixtures, repulsively interacting mixtures are completely unexplored, and accessing this part of the phase diagram of the harmonically trapped mixture has only become possible as a result of tunable interactions. Parts of this chapter have been published in S. Ospelkaus *et al.*, Phys. Rev. Lett. **97**, 120403 (2006).

The optical lattice part of this thesis starts with **chapter 5**. I will first review the theory of optical lattices and the description of non-interacting particles confined in a periodic potential. I will discuss the resulting band structure in a homogeneous system and highlight important differences for the case of an underlying harmonic trap. Leaving the limit of the non-interacting system, I will review how interacting many-body systems are treated in the Hubbard model. I will discuss the optical lattice setup for Fermi-Bose mixtures which has been realized in this thesis and present measurements with pure

bosonic and fermionic ensembles in the optical lattice.

In chapter **6**, I will present the first realization of a Fermi-Bose mixed many-body system in a 3D optical lattice. In particular, we have studied how the coherence properties of the bosonic component are affected by the presence of a fermionic "impurity" admixture. We find that already a very small impurity admixture causes a significant loss of coherence in the bosonic component. This phenomenon is studied as a function of the fermionic atom number in the system. The observations have generated a lot of interest, and several approaches are currently being pursued in order to understand the observed phenomena from a theoretical point of view. Possible scenarios include reversible thermodynamic processes, mean field Fermi-Bose interaction physics and disorder-related localization phenomena. Parts of this chapter have been published in S. Ospelkaus *et al.*, Phys. Rev. Lett. **97**, 180403 (2006).

In chapter **7**, tunable heteronuclear interactions and 3D optical lattices are combined for the first time. This has resulted in the controlled association of heteronuclear Feshbach molecules. These molecules are of particular interest, since they may later be transferred into their internal ground state where they exhibit long-range anisotropic interactions making them potential building blocks of future quantum computation schemes [38], novel dipolar quantum gases and the additional perspective of measurements of P- and T-violating effects [34]. This chapter closely follows C. Ospelkaus *et al.*, Phys. Rev. Lett. **97**, 180402 (2006); details can be found in the PhD thesis of Christian Ospelkaus [35].

Chapter 2

Large particle number Fermi-Bose mixtures in a magnetic trap

Within this thesis, an experimental apparatus for the preparation and study of quantum degenerate Fermi-Bose mixtures of ^{40}K and ^{87}Rb in 3D optical lattices has been designed and built up from scratch together with Christian Ospelkaus. In this chapter, an overview on the experimental apparatus and different techniques for the study of quantum degenerate mixtures will be given. The main emphasis will be on the techniques specific for the preparation of mixtures. Additional and complementary details on the apparatus can be found in the thesis of Christian Ospelkaus [35].

The setup realized within this thesis has produced the so far largest particle numbers in quantum degenerate ^{40}K–^{87}Rb mixtures. As the ^{40}K–^{87}Rb system is characterized by a large attractive background interaction between fermions and bosons ($a_{\mathrm{FB}} = -215(10)a_0$), the system is unstable with respect to mean-field collapse when reaching critical densities. I will briefly discuss the symptoms of the collapse as observed in the experiment during the final stage of evaporative cooling. The findings in this regime of large particle numbers have been published in C. Ospelkaus *et al.*, Phys. Rev. Lett. **96**, 020401 (2006) and are described in detail in the thesis of Christian Ospelkaus [35].

2.1 Vacuum apparatus

Experiments with quantum degenerate gases require both excellent ultrahigh vacuum conditions for long lifetimes of the atomic ensembles on the order of several 10 s and excellent optical access for cooling, trapping and manipulation of the atomic clouds by various sophisticated laser beam configurations. Both requirements impose stringent conditions on the design of the vacuum chamber. Fig. 2.1 shows a sketch of the vacuum system that has been designed for the preparation of quantum degenerate mixtures in 3D optical lattices within this thesis. The vacuum apparatus (which is based on the setup successfully used in the BEC experiment in our group [39, 40]) consists of two glass cells as the most relevant vacuum chamber elements, the upper vapor cell and the lower UHV-cell attached to the central vacuum chamber. The two chamber design reflects the different cooling stages on the way to quantum degenerate mixtures requiring different vacuum conditions. In the upper part of the vacuum apparatus (the preparation chamber), high background vapor

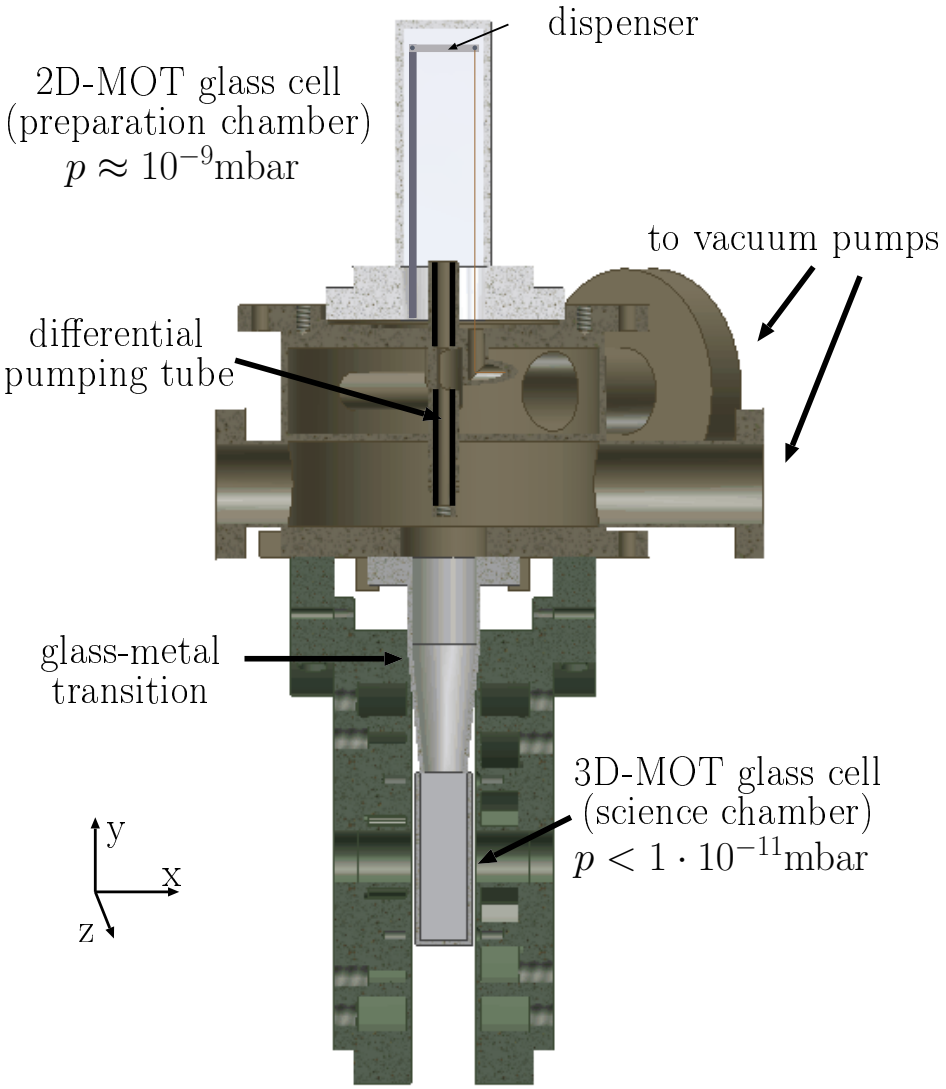

Figure 2.1: Sketch of the vacuum chamber design. The apparatus consists of two vacuum chambers, the preparation chamber in the upper part of the apparatus and the science chamber in the lower part of the apparatus which are connected by a differential pumping tube. The differential pumping tube is designed to maintain a vapor pressure gradient of 2 to 3 orders of magnitude.

pressure has to be maintained to provide a reservoir of atoms. At a vapor pressure of typically 10^{-9} mbar, atoms from the background vapor are caught and precooled by dissipative light fields in combination with magnetic fields in a 2D magneto-optical trap [41]. The continuous intense collimated atomic beam of ^{87}Rb and ^{40}K is transferred through a differential pumping tube to the lower part of the vacuum apparatus where the precooled atoms are recaptured in a 3D magneto-optical trap [42], evaporatively cooled to quantum degeneracy and further manipulated. The connecting differential pumping tube between the two chambers is designed to maintain a vapor pressure gradient of 2 1/2 orders of magnitude ensuring excellent ultrahigh vacuum conditions of typically $< 1 \cdot 10^{-11}$mbar in the lower part of the apparatus (the science chamber). The UHV conditions allow us to trap cold thermal atom clouds with lifetimes of several minutes (cf. Fig. 2.10). The differential pumping tube has a length of 100 mm and is 4 mm in diameter, resulting in a conductance of 0.23 ls^{-1}. The effect of differential pumping is further enhanced through graphite tubes preventing especially alkali atoms from creeping down the differential pumping tube. Both chambers are pumped by 55 ls^{-1} ion getter pumps[1] in addition to a titanium sublimation pump on the science chamber side of the apparatus.

Excellent optical access to both chambers is achieved by use of optical quality quartz glass cells. To ensure a high atom flux from the 2D magneto-optical trap in the preparation chamber and to avoid losses due to transverse velocity spread of the 2D-MOT atomic beam, care has been taken to keep the distance between the two vacuum chambers as short as possible. To this end, the upper glass cell is sealed by a Helicoflex spring seal directly to the stainless steal sealing surface of the central connection chamber whereas the glass-metal transition of the lower glass cell is kept as short as possible (8 cm), resulting in a total distance between the central trapping volumes of the two chambers of 28 cm.

2.2 Atom sources

The necessary background vapor pressure for the preparation of cold atomic beams of ^{87}Rb and ^{40}K is provided by dispensers which are mounted directly in the 2D-MOT glass cell in the upper part of the vacuum apparatus (see Fig 2.1). The necessary current for the operation of the dispensers is provided through two current feedthroughs in the upper part of the vacuum apparatus.

Whereas commercial ^{87}Rb dispensers[2] are available, the low abundance of ^{40}K in natural potassium of only 0.012% limits the usefulness of commercially available potassium dispensers. With commercial potassium dispensers made of natural potassium, the number of potassium atoms collected in the vapor cell would be severely limited. However, potassium enriched to $\approx 6\%$ ^{40}K is available in form of a salt, KCl[3]. Following the procedure outlined in [43], a very efficient potassium source can be constructed by mixing the enriched salt with Ca as reducing agent. Similar to the design developed at JILA, our sources[4] contain 5 mg of KCl in addition to ca. 15 mg pure calcium and rely on the well-known reduction reaction $2\mathrm{KCl} + \mathrm{Ca} \longrightarrow 2\mathrm{K} + \mathrm{CaCl_2}$. By heating the mixture of

[1] Star Cell 55, Varian Inc. (Italy)

[2] In our experiments, we use dispensers from SEAS Getters (Rb/NF/7/17/FT10-10).

[3] The salt KCl enriched in ^{40}K is available from Trace Sciences international Corporation

[4] The sources have been constructed in cooperation with Dr. Kathrin Hofmann and Prof. Dr. Barbara Albert from the chemistry department.

KCl and Ca, K is released into the vacuum whereas Cl is recaptured by the Ca atoms, forming the salt $CaCl_2$. To avoid contamination of the vacuum, both KCl and Ca have to be very pure. The calcium was therefore baked out for one week at 350°C to drive out any impurities. As KCl is very hygroscopic, the salt was heated for several days to ≈ 100°C to drive out any residual water. KCl and Ca are subsequently finely ground, sieved and mixed. The mixture is then filled into a small boat made of nichrome foil[5] which has been annealed under vacuum conditions for several days prior to use. Every preparation step is done under pure argon atmosphere to avoid any contact of the ingredients with water or oxygen. In daily operation, heating of the mixture to a few hundred degrees centigrade is done by running a current through the nichrome boat and thereby enabling the chemical reduction reaction.

A major concern in the preparation of these sources is the lifetime. Commercially available alkali metal dispensers, although containing only 2-5 mg of alkali metal, usually serve as reliable atom sources in a typical BEC apparatus for more than one year. To get an estimate on the lifetime of our self-made sources, we have compared the lifetime of our sources to commercially available potassium dispensers containing natural potassium. The characterization measurement was done in a small test apparatus where both commercially available dispensers containing natural potassium and self-made potassium dispensers where operated for several weeks at a current much higher than the usual operation current in a typical BEC experiment. The amount of potassium released from these sources was estimated based on the fluorescence of ^{39}K excited on the D_2-line at 766.7nm (see Fig. 2.2 a)). Fig. 2.2 b) shows the time evolution of the fluorescence signal of potassium atoms released from a commercial potassium dispenser compared to the fluorescence signal of a self-made dispenser. Numerically integrating the fluorescence signal over time demonstrates that the self-made dispenser is comparable to the commercial one within a factor of two.

2.3 Laser systems

During the different stages of the experiment, different laser frequencies for cooling, trapping, repumping and detection of the two atomic species are necessary and have to be generated. An overview of the necessary laser frequencies for both isotopes is given in table 2.1.

Compared to a single-species experiment, a two-species experiment requires twice as many laser frequencies to be integrated into the apparatus. In the following, the two different laser systems for ^{40}K and ^{87}Rb will be described. Whereas the ^{87}Rb laser system is based on the techniques developed in our group at the neighboring BEC experiment [39, 40], no previous experience for the design of a laser system for ^{40}K had been available in our group. The laser systems are designed to deliver largely sufficient trapping and repumping power for both atomic species allowing the operation of large-volume magneto-optical traps with large atom numbers. Additional details on the characterization of the ^{87}Rb laser system can be found in the diploma thesis of Jürgen Fuchs [44].

[5] Nichrome foil from Goodfellow

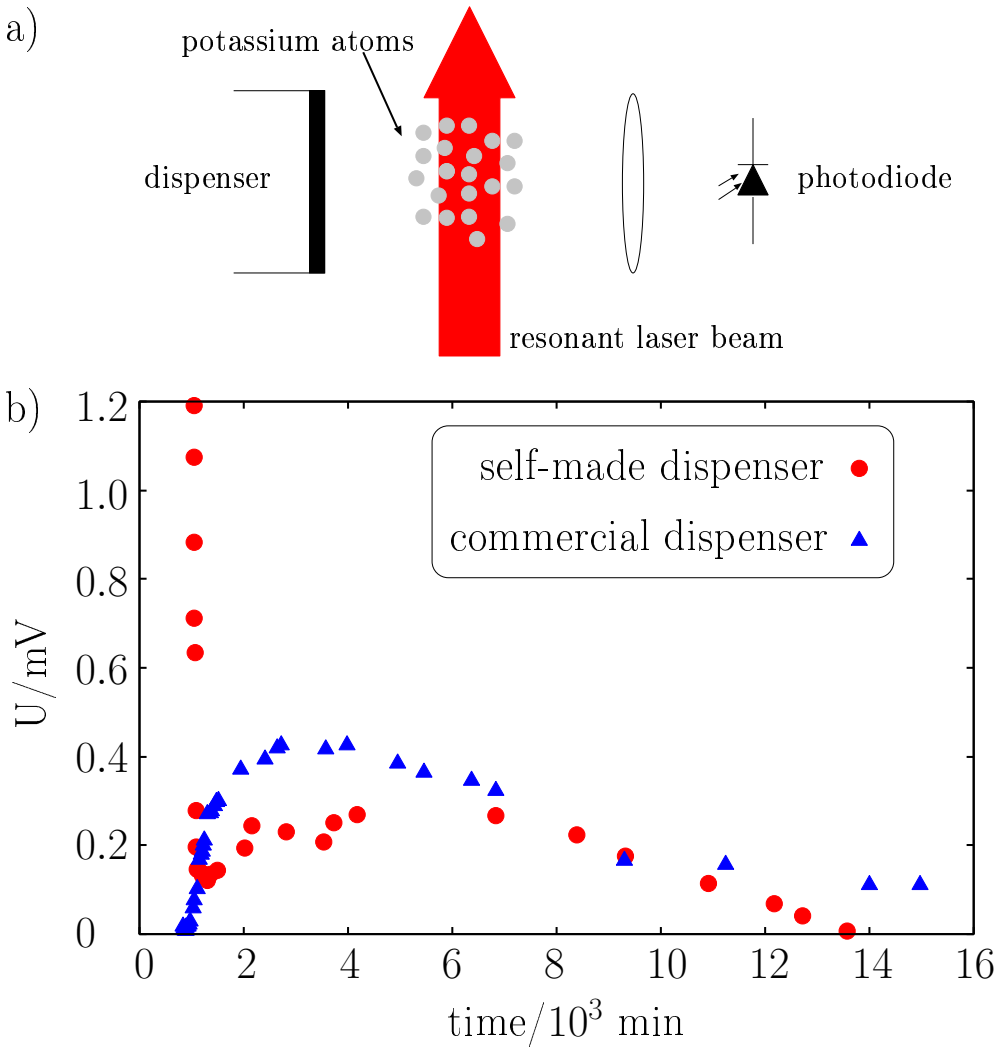

Figure 2.2: a) Sketch of the experimental setup for the dispenser characterization: Potassium atoms released from the self-made/commercial dispenser are excited on the D_2-line. The fluorescence is detected on a photodiode. b) Characterization measurement: Fluorescence signal of the potassium atoms released from both the commercial (triangles) and the self-made dispenser (circles) recorded over several weeks. The initial "divergence" in the fluorescence signal of the self-made dispenser is due to a too high current chosen in the initial phase of the experiment.

Element		Transition	Detuning
^{40}K	2D/3D-MOT(cooling)	$4^2S_{1/2}F = 9/2 \rightarrow 4^2P_{3/2}F = 11/2$	red-detuned
^{40}K	repumping	$4^2S_{1/2}F = 7/2 \rightarrow 4^2P_{3/2}F = 9/2$	red-detuned
^{40}K	detection	$4^2S_{1/2}F = 9/2 \rightarrow 4^2P_{3/2}F = 11/2$	resonant
^{40}K	state preparation	$4^2S_{1/2}F = 9/2 \rightarrow 4^2P_{3/2}F = 11/2$	resonant
^{40}K	pushing beam	$4^2S_{1/2}F = 9/2 \rightarrow 4^2P_{3/2}F = 11/2$	blue-detuned
^{87}Rb	2D/3D-MOT(cooling)	$5^2S_{1/2}F = 2 \rightarrow 5^2P_{3/2}F = 3$	red-detuned
^{87}Rb	repumping	$5^2S_{1/2}F = 1 \rightarrow 5^2P_{3/2}F = 2$	resonant
^{87}Rb	detection	$5^2S_{1/2}F = 2 \rightarrow 5^2P_{3/2}F = 3$	resonant
^{87}Rb	state preparation	$5^2S_{1/2}F = 2 \rightarrow 5^2P_{3/2}F = 3$	resonant
^{87}Rb	pushing beam	$5^2S_{1/2}F = 2 \rightarrow 5^2P_{3/2}F = 3$	blue-detuned

Table 2.1: Overview of the necessary laser frequencies for cooling and trapping of ^{40}K and ^{87}Rb.

2.3.1 Rb laser system

The ^{87}Rb laser system is based entirely on semiconductor laser diodes. Two grating stabilized external cavity diode lasers are stabilized to the saturated absorption crossover resonances ^{87}Rb $F = 2 \leftrightarrow F' = 2, 3$ and ^{87}Rb $F = 1 \leftrightarrow F' = 1, 2$ of the D_2-line ($5^2S_{1/2} \rightarrow 5^2P_{3/2}$) at $\lambda \approx 780$ nm using FM-spectroscopy. These two laser frequencies serve as a starting point for the generation of light in the vicinity of the cooling transition ^{87}Rb $F = 2 \leftrightarrow F' = 3$ and the repumping line ^{87}Rb $F = 1 \leftrightarrow F' = 2$ (c.f. Fig. 2.3). Using acousto-optic modulators, laser frequencies for different purposes such as cooling and trapping in 2D and 3D magneto-optical traps, optical pumping for spin-polarization prior to loading of the magnetic trap, detection and repumping are produced. The different laser frequencies are subsequently amplified by additional slave lasers (injection locked diode lasers).

Both for the operation of an efficient 2D and a large-volume 3D magneto-optical trap, cooling light with a total power of at least 100 mW is required at the experimental apparatus. To match these power requirements, the cooling light is amplified at the final stage by two separate tapered amplifier setups prior to guiding the light via single-mode optical fibers to the experiment. The amplifying medium has a gain of approximately 10 dB and a maximum output power of 500 mW, requiring approximately 50 mW of seeding power to achieve the 500 mW of maximum output specified. The tapered amplifier is therefore seeded by an additional "slave" laser which is itself injection locked by a few hundred μW of light from the grating stabilized diode laser operated in the vicinity of the cooling transition. The slave laser as well as the amplifying medium are protected from retroreflections by optical diodes with a typical isolation performance of 30 dB. For beam shaping of the amplified laser light which has a strongly anisotropic divergence, collimation of the amplified laser light is performed in two steps. In the first step, the laser light is collimated in the vertical direction by a spherical collimator; in the second step, additional beam shaping is performed by a cylindrical lens providing collimation in the horizontal direction. To ensure fast and effective switching of the cooling light, an electro-optical modulator is used in a final stage before fiber coupling of the laser light. Note that despite

careful beam shaping, typical coupling efficiencies into a single-mode optical fiber are on the order of 40%, allowing for a typical cooling power of >150 mW at the experimental apparatus while operating the tapered amplifier at a moderate output power of 400 mW.

The laser light is generated on a separate laser table and any light is transported to the experiment by single-mode optical fibers for mode-cleaning. A detailed description of the full Rb laser system and the locking scheme is given in Appendix A.

2.3.2 K laser system

The laser light for manipulation of ^{40}K atoms on the D_2-transition ($4^2S_{1/2} \rightarrow 4^2P_{3/2}$) at $\lambda \approx 767$nm is delivered by two independent sources: a 1.6W Ti:Sa laser providing the necessary frequencies for cooling, trapping, manipulation and detection of ^{40}K on the $F = 9/2 \rightarrow F' = 11/2$ transition and a commercial MOPA-system from Toptica Photonics with a power of up to 400 mW to allow for sufficient repump power for both the 2D and the 3D magneto-optical trap on the ^{40}K $F = 7/2 \rightarrow F' = 9/2$ transition. As our ^{40}K 3D magneto-optical trap is operated in a dark-SPOT [45] configuration (see section 2.4.2.1), light for an additional "dark-spot" repumper is required. Due to the small hyperfine splitting in the excited state $4P_{3/2}$ manifold, a relatively strong repumping laser is required which operates almost as a second cooling laser. Details on the locking scheme for the Ti:Sa laser and the MOPA laser can be found in Appendix B. Due to the low abundance of ^{40}K in natural potassium, both lasers have been locked to saturated absorption spectra of ^{39}K having a natural abundance of 93.26%. The necessary frequencies for cooling, trapping, detection, state preparation and repumping are then generated by several acousto-optic modulators which at the same time assure rapid switching of the respective laser frequencies. As in the case of the Rb laser system, any light necessary for the manipulation of ^{40}K is generated on a separate laser table and transported to the experiment via single-mode optical fibers. A detailed description of the laser system can be found in Appendix B.

2.3.3 Combining the two laser systems

A major concern in the design of the whole apparatus was to ensure optimum optical access to the main experimental chamber despite the enormous amount of laser frequencies and laser beams necessary for precooling and detection of both ^{87}Rb and ^{40}K. Whenever possible, the laser light for ^{40}K and ^{87}Rb has therefore been overlapped prior to fiber coupling. The overlapping of laser beams for potassium and rubidium has been done using special dichroic mirrors HR-coated at 780 nm and AR-coated at 767 nm. The laser beams for pushing, state preparation and detection for potassium are overlapped with the respective laser beams for the rubidium isotope before being transported to the experiment proper by three optical fibers. The 2D- and 3D-MOT laser beams, however, are overlapped with the respective repumping beams separately for the two isotopes and then transported to the experiment.

2.4 A two-species 2D/3D magneto-optical trap combination

The first precooling step on the way to quantum degeneracy in alkali gases is trapping and cooling by magneto-optical traps [42]. In magneto-optical traps, the combination of

trapping light fields and quadrupolar magnetic fields provides the necessary confining and dissipative forces for the accumulation and cooling of atoms. In a typical magneto-optical trap, the phase space density of a room temperature gas at 300 K is enhanced by a factor of 10^6 achieving final phase space densities of typically 10^{-6}. In our experiment, we use a combination of two different magneto-optical traps for trapping and cooling of atoms: In the upper part of the apparatus, a two-species 2-dimensional magneto-optical trap is used to prepare an intense collimated atomic beam of both ^{40}K and ^{87}Rb. These transversally cold but longitudinally hot atoms are subsequently recaptured in a 3D magneto-optical trap in the UHV part of the apparatus (see Figure 2.1). In the following section, the setup of the 2D/3D two-species magneto-optical trap combination will be described and the performance of the magneto-optical traps for ^{40}K and ^{87}Rb will be discussed. Finally, we study the mutual influence of the ^{40}K and ^{87}Rb magneto-optical traps on each other for simultaneous operation.

2.4.1 Two-species 2D magneto-optical trap

The principle of a two-dimensional magneto-optical trap has first been used for compression and transverse cooling of atomic beams [46, 47, 48]. However, two-dimensional cooling can also be used for the generation of a transversally cold and slow atomic beam suitable for efficient loading of 3D-magneto-optical traps. Such a high-flux atomic beam (10^{10}atoms/s) prepared from a two-dimensional magneto-optical trap has first been demonstrated by Diekmann and coworkers in ^{87}Rb [41]. Two-dimensional magneto-optical traps have been investigated by several groups worldwide [49, 50, 51]. However, apart from our work on ^{40}K [5] and a very recent work on the bosonic potassium isotopes ^{39}K and ^{41}K [52], no work has been done on potassium.

2.4.1.1 Operation principle and setup of the 2D-MOT

In the upper glass cell of our vacuum apparatus (see Fig. 2.1), a background vapor of both ^{87}Rb and ^{40}K is generated. The glass cell which is separated from the UHV-chamber by a differential pumping tube is surrounded by four rectangular coils which generate a two-dimensional magnetic quadrupole field. The zero line of the magnetic field is along the axis of the pumping tube. Four laser beams with an almost rectangular beam shape (1.4 cm x 7 cm beam diameter) propagate perpendicular to the zero line of the magnetic field and enclose a large cooling volume inside the vacuum chamber. The laser beams are circularly polarized in the usual MOT configuration. The laser beams have been adjusted such as to extend the cooling volume almost down to the beginning of the differential pumping tube. Thermal atoms that enter the cooling volume are slowed down due to dissipative light forces in the radial direction and compressed on the zero line of the magnetic field. The atoms form a transversally cold but longitudinally hot atomic beam. Nevertheless, the longitudinal velocity distribution does not correspond to the velocity distribution of a thermal atomic beam. The reason is that atoms with initially high longitudinal velocity will only stay inside the cooling volume for a very short time - too short to be effectively cooled down radially. An additional pushing beam along the line of zero magnetic field enhances the flux of atoms in the direction towards the UHV chamber.

In the experiment, we operate the 2D-MOT with a 2D magnetic quadrupole field

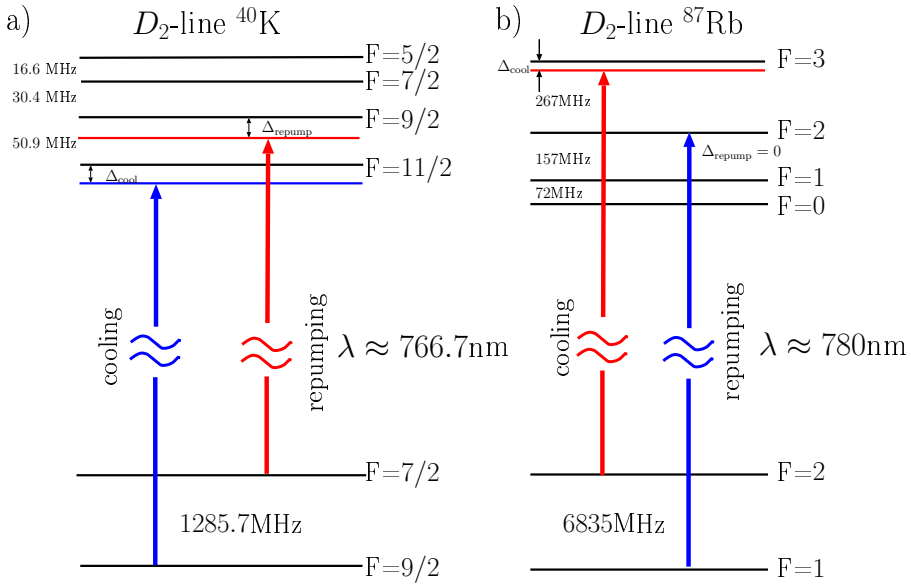

Figure 2.3: Hyperfine structure of the D_2-line of ^{40}K and ^{87}Rb respectively. a) Cooling and repumping occur on different hyperfine transitions of the ^{40}K D_2-line. Both cooling and repumping light is slightly red-detuned to the corresponding hyperfine transition. b) In the case of ^{87}Rb, only the cooling laser is red-detuned.

of 18 G/cm in the intersecting regions of the laser beams. The 2D-MOT beams are realized by two retroreflected laser beams which are collimated and shaped by cylindrical lenses. The retroreflection is realized in a lens mirror cat's eye configuration with an additional quarter wave plate for reversal of the circular polarization. Both orthogonal beams contain light on the cooling and repumping transitions of ^{40}K at 767 nm and ^{87}Rb at 780 nm (see Fig. 2.3) for simultaneous two-species operation. The beams are overlapped using dichroic mirrors immediately after fiber-outcoupling and beam collimation. The overlapped beams are then split into two separate laser beams using polarizing beam splitter cubes, then enlarged to a beam diameter of 14 mm and finally shaped by the cylindrical lenses. Achromatic waveplates are used to polarize the overlapped laser beams for both isotopes simultaneously.

2.4.1.2 2D MOT optimization

The 2D magneto-optical trap has been characterized for both species. The main optimization criterion is the loading rate of the 3D magneto-optical trap reflecting the trappable flux created by the 2D MOT. As we have found no mutual influence of one species on the other in the 2D-MOT, we optimized the two 2D-MOTs for ^{40}K and ^{87}Rb separately.

^{87}Rb 2D-MOT 2D-MOT operation for ^{87}Rb has been reported and characterized in previous experiments [41, 51, 39]. Similar to these experiments, we use the $F = 2 \rightarrow F' = 3$ cycling transition for trapping and cooling and the $F = 1 \rightarrow F' = 2$ transition for repumping (see Fig. 2.3). Optimizing the ^{87}Rb 2D-MOT, we find comparable characteristics to

previous experiments. In brief, we typically use a total cooling laser power of > 100 mW combined with a repumping power of 3 mW. Optimal operation is found for a cooling light detuning of $-3\ \Gamma$ relative to the $F = 2 \rightarrow F' = 3$ cycling transition. However, the optimal detuning is slightly dependent on the chosen 3D-MOT detuning due to matching of velocity classes in the beam with the 3D-MOT capture range. As in [39], the use of an additional pushing beam enhances the flux of atoms of the 2D-MOT by almost a factor of 10 as compared to a factor of 2 in [41]. The effect of the pushing beam is two-fold. First, it reverses the direction of propagation of low-velocity atoms which move away from the 3D-MOT and add them to the trappable atom flux. Second, for an optimized detuning, the pushing beam accelerates the lowest velocity atoms to a few 10 m/s just in the capture range of the 3D-MOT. It thereby significantly reduces the divergence of the atomic beam emerging from the 2D-MOT, minimizing losses by atoms hitting the walls of the differential pumping tube. In Fig. 2.4, the influence of the detuning and the power of the pushing

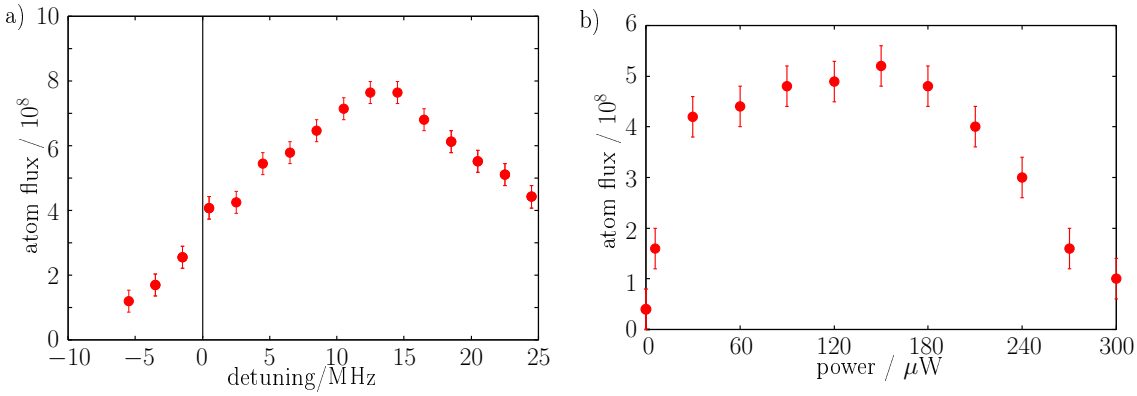

Figure 2.4: Influence of detuning and power of the pushing beam on the loading rate of a ^{87}Rb 2D-MOT. a) Loading rate as a function of detuning. b) Loading rate when varying the power of the pushing beam. The Gaussian beam diameter of the pushing beam is approximately 2.6 mm.

beam on the loading rate of a ^{87}Rb 3D-MOT is shown. Whereas the loading rate of the 3D-MOT rapidly decreases with increasing red-detuning, optimal loading is observed for a blue-detuning of $+2\ \Gamma$. With increasing red-detuning, the pushing beam interacts more and more with high-velocity atoms moving away from the differential pumping tube and slows them down, but does not reverse their velocity distribution. Only very few atoms are therefore added to the trappable atom flux. However, a moderately blue-detuned laser beam mainly interacts with the low-velocity tail of atoms moving towards the pumping tube and accelerates them significantly minimizing losses (see above). Note that the characterization measurements of Fig. 2.4 have been done at a moderate background vapor pressure in the upper glass cell. The atomic flux can be significantly enhanced by choosing a large ^{87}Rb vapor pressure. Atomic beams with typically $> 2 \cdot 10^9$/s and up to $1 \cdot 10^{10}$/s have been prepared in the experiment, allowing the accumulation of $\approx 10^{10}$ atoms in the 3D-MOT within less than 10 s.

^{40}K 2D-MOT To prepare a cold atomic beam of ^{40}K atoms, we use the $F = 9/2 \rightarrow F' = 11/2$ transition for cooling and trapping and the $F = 7/2 \rightarrow F' = 9/2$ transition for repumping (see Fig. 2.3a)). Due to the small hyperfine splitting of potassium in the excited state manifold, "losses" of potassium via non-resonant excitation to the $4^2P_{3/2}F' = 9/2$ state and subsequent decay into the $F = 7/2$ ground state are very likely. Sufficient repumping power is therefore required to transfer the atoms back into the cooling cycle on the $F = 9/2 \rightarrow F' = 11/2$ transition. Typically, the ^{40}K 2D-MOT has been operated with a total cooling power of 100 mW and a repumping power of 30 mW. Optimal operation of the 2D-MOT has been observed for red-detuned cooling and red-detuned repumping light. The detunings optimizing the atomic flux are on the order of $-3\ \Gamma$ for both cooling and repumping light[6]. Adding a pushing beam along the line of zero magnetic field increases the atomic flux by a factor of 2. Again, best performance of the pushing beam is observed with blue-detuned light. The smaller enhancement of the atomic flux in the case of ^{40}K as compared to the ^{87}Rb case is probably due to the tight and inverted hyperfine structure of the $4^2P_{3/2}$ state. With increasing blue-detuning, the probability of inducing $F = 9/2 \rightarrow F' = 9/2$ transitions grows. The $F = 9/2$ ground state is, however, subject to a fast depletion to the $F = 7/2$ ground state which is dark for subsequent pushing cycles. Further enhancement of the atomic flux should therefore be possible upon addition of a blue-detuned repumper. We typically operate the ^{40}K 2D-MOT with atom fluxes of $5{\cdot}10^6$/s which is mainly limited by the relatively low vapor pressure of ^{40}K as compared to ^{87}Rb, but largely sufficient for our experiments. Higher atomic fluxes have been observed when increasing the current through our self-made dispensers, thereby increasing the background vapor pressure of ^{40}K in the upper glass-cell.

2.4.2 Two-species 3D-MOT

The two-species 3D-MOT is loaded from the 2D-MOT and is operated in the UHV-part of the apparatus at a background gas pressure of $1 \cdot 10^{-11}$ mbar. The 3D-MOT region is located between two planar coil arrangements which provide the 3D magnetic quadrupole field for magneto-optical trapping as well as a Ioffe-Pritchard type field for magnetic trapping (see Fig. 2.1). The cooling and repumping light for both ^{40}K and ^{87}Rb is transported to the experiment separately for each species by a single optical fiber. The six individual laser beams for the 3D-MOT are then prepared as follows: First the light for each species is split up into three beams. The laser light for the two different species is overlapped using dichroic mirrors. The three beams for the three MOT axes are enlarged to a beam diameter of 24 mm and finally, each beam is again split up into two to provide counter-propagating beams for each axis. For more details, see the thesis of Christian Ospelkaus [35]. The careful design of the two-species 3D-MOT optics has allowed the integration of a 3D optical lattice and four detection systems into the setup (cf. section 5.4).

2.4.2.1 Two-species 3D-MOT optimization

Magneto-optical trapping of ^{87}Rb is a standard technique established in many laboratories worldwide and has proven to be relatively insensitive to specific optimization parameters.

[6]Note that the detuning of the repumping laser can only be adjusted simultaneously for both the 2D and the 3D-MOT.

We have therefore only roughly optimized the ^{87}Rb MOT parameters and concentrated on the optimization of the ^{40}K-MOT system and the simultaneous operation of the ^{40}K and ^{87}Rb-MOT.

^{87}Rb 3D-MOT Optimal operation for the ^{87}Rb MOT is found for a cooling light detuning of $-3.5\ \Gamma$ relative to the $F = 2 \rightarrow F' = 3$ cycling transition and an on-resonant repumper on the $F = 1 \rightarrow F' = 2$ transition. We operate our ^{87}Rb 3D-MOT with a total cooling power of 160 mW and a total repumping power of 20 mW at a magnetic field gradient of 10 G/cm. With these parameters, we are able to trap up to 10^{10} ^{87}Rb atoms within less than 10 s loading time. The atom number is determined from a fluorescence signal measured on a photodiode.

^{40}K 3D-MOT As compared to ^{87}Rb, 3D magneto-optical trapping of ^{40}K has some peculiarities: As already discussed in the context of the 2D-MOT, due to the relatively small hyperfine splitting in the excited state manifold, magneto-optical trapping of ^{40}K requires relatively high repumping power and it is beneficial to operate the repumper red-detuned relative to the repumping transition [53, 54]. This is even more important in the case of the bosonic isotopes of potassium where the hyperfine splitting in the excited state is even one order of magnitude smaller than the hyperfine splitting of ^{40}K [55, 56, 53, 57]. In addition, the ^{40}K 3D-MOT shows strong intensity dependent and density dependent losses in a standard bright 3D-MOT configuration. This is illustrated in Fig. 2.5, where we have analyzed the achievable atom numbers in the 3D-MOT as a function of the cooling light intensity and the lifetime of the 3D-MOT as a function of the magnetic field gradient (enhancing the density of the ensemble). Best operation of the ^{40}K 3D magneto-optical trap is observed at very low intensities of 1 mW/cm^2 corresponding to a total cooling power of 27 mW (!). With increasing laser light intensity, the achievable atom number in the 3D-MOT decreases exponentially, indicating strong light assisted collisional losses. The lifetime of the 3D-MOT decreases with increasing magnetic field gradient, reducing the lifetime of the ^{40}K MOT to < 5 s at a magnetic field gradient of 10 G/cm (which is a magnetic field gradient at the lower edge of what is reasonable for the operation of a ^{87}Rb MOT in our experiment).

Both signatures indicate strong light-assisted inelastic collisional losses which can be reduced significantly by applying the dark SPOT technique. The "Dark **S**pontaneous-**F**orce **O**ptical **T**rap" has been demonstrated by Wolfgang Ketterle and coworkers in 1993 with sodium [45]. The dark SPOT is a magneto-optical trap which confines most of the atoms in the hyperfine ground state which does not interact with the cooling light, the so-called "dark" hyperfine ground state. Atoms in this "dark" hyperfine ground state are most naturally produced in every magneto-optical trap operated with alkali atoms: The cooling transition is never fully closed, and off-resonant excitation produces atoms in hyperfine states in the excited state manifold which decay into the "dark" ground state within a few nanoseconds. In a dark SPOT, these atoms in the "dark" hyperfine ground state are accumulated in the center of the magneto-optical trap by strongly reducing or even blocking the repumping light intensity in a certain spatial region. In this region, atoms leaving the cooling cycle due to non-resonant excitation will not be transferred back and will therefore spend most of their time in this dark hyperfine ground state.

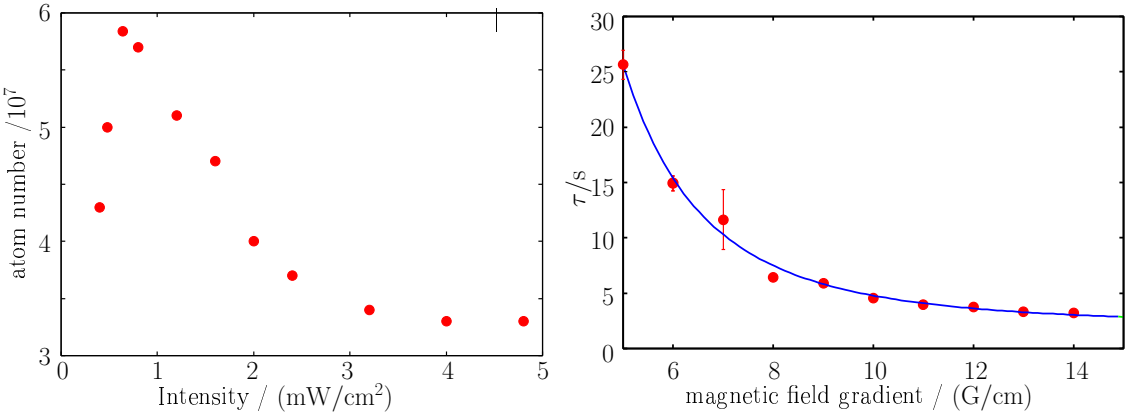

Figure 2.5: Intensity and density dependent losses in the ^{40}K 3D-MOT a) Achievable atom number in the ^{40}K MOT as a function of the cooling light intensity. b) Lifetime of the ^{40}K 3D-MOT as a function of the magnetic field gradient.

Only when leaving the dark region of the magneto-optical trap, the atoms interact with the repumper and become visible for the trapping light which will transfer them back to the center of the trap. The effect of the dark SPOT is thus twofold: First, it significantly reduces losses due to inelastic collisions between ground- and excited state atoms. Second, the dark SPOT leads to higher atomic densities as the fluorescence light of the MOT is diminished, thereby reducing the outward radiation pressure.

In our experiment, we have realized a dark SPOT for potassium by integrating a second repumping path into the experiment where the central 5 mm of repumping light are blocked. This is done by passing the repumping beam through a glass plate with a small black dot and imaging the black dot onto the atomic ensemble. The repumping light in this dark region is thereby reduced by a factor of 30. A sketch of the setup can be found in the diploma thesis of Marlon Nakat [58]. Note that the bright repumper is still necessary for final repumping of the "dark" $F = 7/2$ atoms into the "bright" $F = 9/2$ state prior to detection or loading of the atoms into the magnetic trap.

Fig. 2.6 shows a comparison of the loading curve and lifetime of a dark SPOT in comparison to an ordinary bright ^{40}K MOT. As can be seen from the figure, atom numbers in the bright ^{40}K MOT saturate at approximately $2.5 \cdot 10^7$ atoms, whereas in the dark SPOT, atom numbers of $> 1.5 \cdot 10^8$ have easily been achieved, thereby increasing ^{40}K atom numbers by more than a factor of 5. In addition, the lifetime of the ^{40}K dark SPOT is almost a factor of 20 larger than the lifetime of a corresponding bright MOT (see Fig. 2.6b).

Combining the two magneto-optical traps When combining the two-species MOT for the first time, the two MOTs have been operated at the same laser detunings and magnetic-field gradient used to optimize the single-species MOTs. The most important observation is a significant decrease in the ^{40}K atom numbers when the two MOTs for the two species are operated simultaneously. Atom numbers in the ^{87}Rb cloud are, however, not affected at all. The strong performance reduction of a ^{40}K MOT due to an overlapping

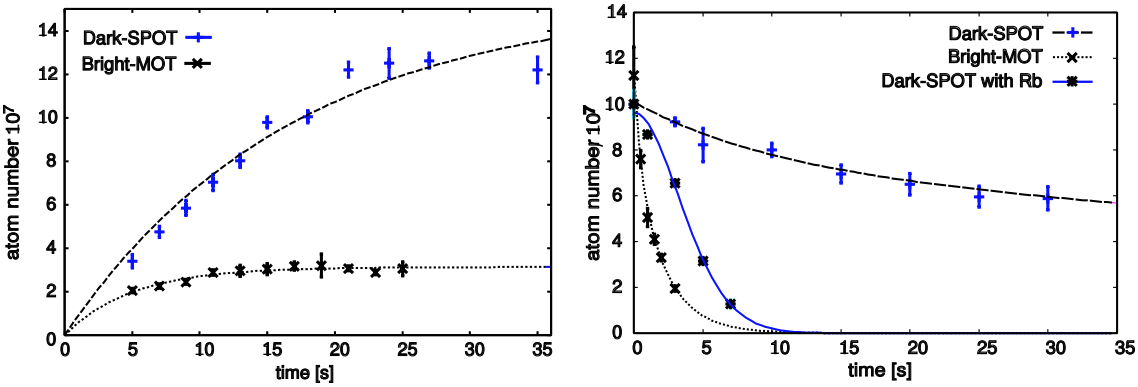

Figure 2.6: Comparison of the loading and lifetime of a ^{40}K dark SPOT and bright MOT. a) Comparison of the loading characteristics: The dark SPOT loading saturates at much larger particle number than the bright MOT. b) Comparison of the lifetime of the dark SPOT and the bright MOT: The lifetime of the dark SPOT is almost a factor of twenty larger than the lifetime of a comparable bright MOT. An overlapping ^{87}Rb MOT induces enhanced losses in the dark SPOT. However, the lifetime of the dark SPOT overlapped with a ^{87}Rb MOT is still larger than the lifetime of a pure bright ^{40}K MOT (cf. section 2.4.2.1)

^{87}Rb MOT has first been reported by J. M. Goldwin and coworkers [59] and suggested light-assisted heteronuclear collisions to be responsible for ^{40}K losses in the two-species MOT. Fig. 2.7 shows the final atom numbers in the ^{40}K dark SPOT after 20 s of loading time while varying the loading time $t_{\mathrm{Rb_{load}}} = 0$ of ^{87}Rb between 0 and 20 s. Whereas we achieve more than 10^8 ^{40}K atoms in a single species ^{40}K MOT ($t_{\mathrm{Rb_{load}}} = 0$), atom numbers in the ^{40}K dark SPOT decrease by a factor of almost 4 when simultaneously loading ^{40}K and ^{87}Rb. In addition, the lifetime of the ^{40}K dark SPOT is significantly decreased by the presence of the ^{87}Rb MOT (see Fig. 2.6 (right)). However, the lifetime of the combined ^{40}K dark SPOT and ^{87}Rb MOT is still above the one of a pure bright ^{40}K MOT, but the rubidium-induced losses dominate the lifetime of the ^{40}K ensemble and constrain the maximum achievable ^{40}K atom numbers. For a further optimization of the ^{40}K atom numbers, we take advantage of the relatively fast ^{87}Rb-MOT loading leading to a saturation of the ^{87}Rb MOT within 3-10 s. The strategy is therefore to keep the loading time for the potassium MOT fixed at the dark SPOT saturation time of 20 s and to load the rubidium atoms during the last seconds of this time. This two-step loading in combination with a dark SPOT for ^{40}K has provided maximum particle numbers in our experiment.

In addition, we have investigated the laser parameter dependence of a pure ^{40}K dark SPOT in comparison to a combined ^{40}K dark SPOT / ^{87}Rb MOT. The result of these investigations is shown in Fig. 2.8. These graphs have been obtained for a loading time of 20 s and a magnetic field gradient of 10 G/cm along the coil axis. However, whereas the optimum laser parameters for the ^{40}K dark SPOT change only slightly due to the presence of the ^{87}Rb MOT, the figure impressively demonstrates the dominating ^{87}Rb induced losses in the ^{40}K cloud. Table 2.2 summarizes the optimum parameters and achieved particle

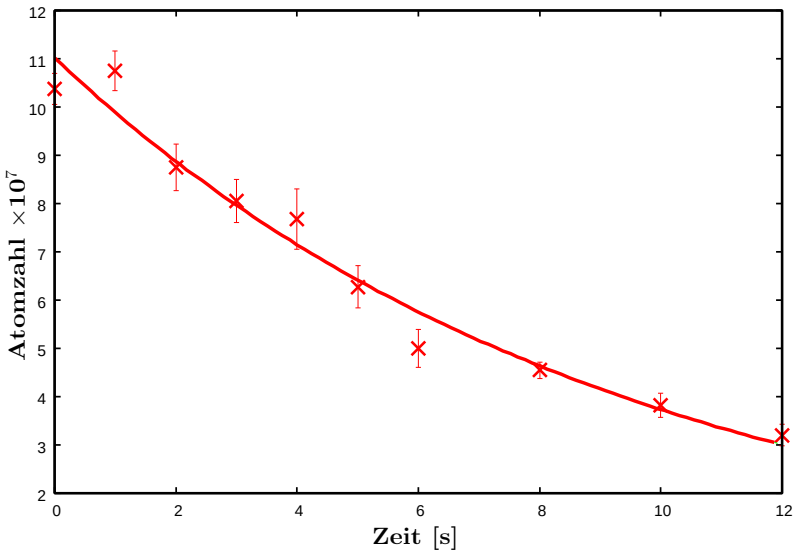

Figure 2.7: Final atom numbers in the ^{40}K dark SPOT after 20 s of loading time while varying the loading time t_{load} of ^{87}Rb between 0 and 20s. Whereas we achieve more than 10^8 ^{40}K atoms in a single species ^{40}K MOT ($t_{\mathrm{Rb_{load}}} = 0$), atom numbers in the ^{40}K dark SPOT decrease by a factor of almost 4 when simultaneously loading ^{40}K and ^{87}Rb.

numbers for a single ^{40}K dark SPOT and the combined system.

parameter	^{40}K-MOT	combined MOT ^{40}K / ^{87}Rb
loading time for data below	20 s	20 s / 10 s
power - pushing-beam	30 μW	30 μW / 100 μW
magnetic field gradient	10 G/cm	10 G/cm
intensity per beam - cooling laser	8 mW/cm^2	9 mW/cm^2 / 9 mW/cm^2
detuning - cooling laser	-26 MHz	-22 MHz / -20 MHz
intensity per beam - repumper	2 mW/cm^2	2 mW/cm^2 / $<$ 1 mW/cm^2
detuning - repumper	-33 MHz	-23 MHz / 0 MHz
lifetime	$>$ 90 s	$\approx$ 5 s / $>$ 90 s
atom number	3×10^8	5×10^7 / 5×10^9

Table 2.2: Optimum parameters for cooling and trapping of ^{40}K and mixtures of ^{40}K and ^{87}Rb.

2.5 Optical molasses and state preparation

Typical MOT temperatures are on the order of a few hundred μK. A further reduction in temperature can be achieved by polarization gradient cooling [60, 61] in optical molasses. After loading of the two MOTs, the magnetic field gradient is quickly switched off and the detuning of the cooling lasers is ramped to a detuning appropriate for sub-Doppler cooling ($\Delta \approx -5\Gamma$). We then perform a 10 ms polarization gradient cooling phase with the counter-propagating σ^+ and σ^- circularly polarized MOT beams. Although we have

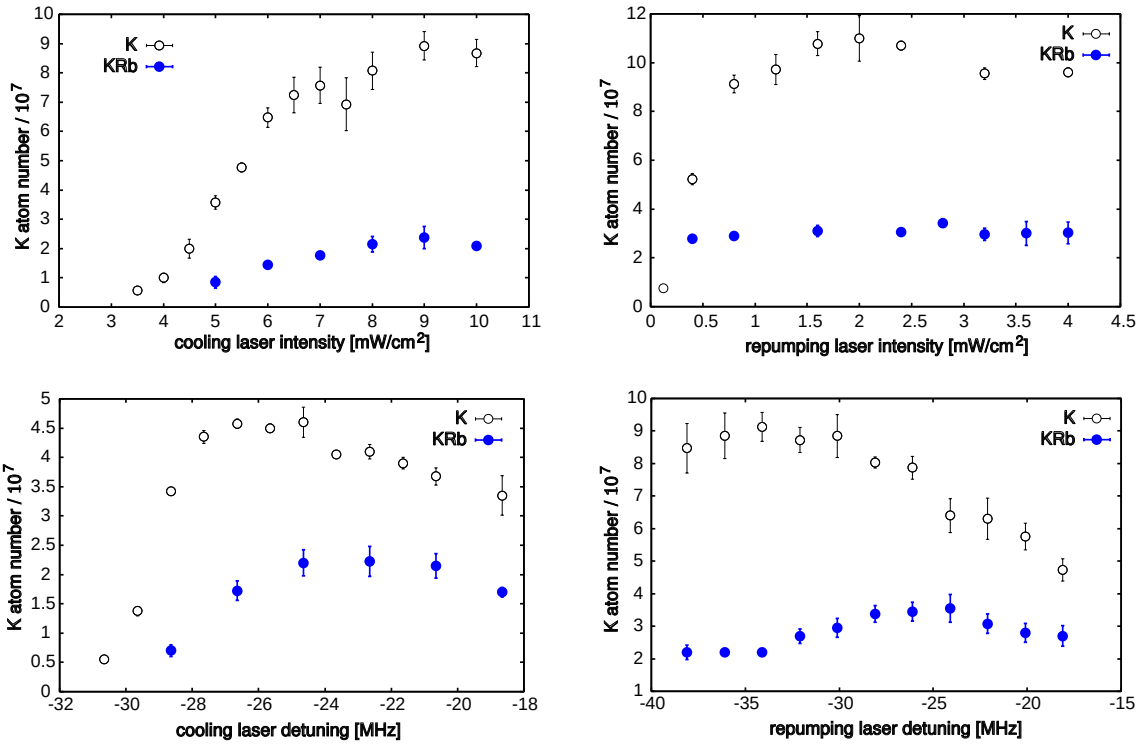

Figure 2.8: Optimization of the laser parameters for a ^{40}K dark SPOT in comparison to a combined ^{87}Rb MOT and ^{40}K dark SPOT. The non-varied parameters for an individual graph have been chosen close to the optimum. The slight differences in maximum atom number were due to different dispenser currents and do not significantly affect the optimization result.

not systematically studied the effect of optical molasses cooling, the additional reduction in temperature compared to a MOT is clearly visible in the extension of the ^{87}Rb cloud in the magnetic trap prior to evaporative cooling.

Due to the smaller mass of ^{40}K, conditions for sub-Doppler cooling, which is limited to a few atomic recoil energies, are not as favorable for ^{40}K as for ^{87}Rb. However, there is some controversy about that in recent literature [62, 9]. In our experiment, we have passed on without a systematic study of the temperature of the ^{40}K dark SPOT in comparison to temperature after the molasses stage. Instead, we have just optimized the laser detuning of the ^{40}K molasses to produce the largest number of cold ^{40}K after sympathetic cooling with ^{87}Rb.

The polarization gradient cooling phase is followed by a short state preparation light pulse of typically 100 μs where atoms released from the molasses are spin polarized on the $F = 9/2 \rightarrow F' = 11/2$ and $F = 2 \rightarrow F' = 3$ cycling transition for ^{40}K and ^{87}Rb thereby optically pumping them into the Zeeman states $|F = 9/2, m_F = 9/2 >$ and $|F = 2, m_F = 2 >$ which can be trapped magnetically. For optical pumping we use a magnetic guiding field of 1 G.

2.6 Magnetic trapping

Optical cooling methods relying on spontaneous light scattering have shown to be limited by the cooling mechanism itself. Spontaneous scattering not only limits achievable temperatures to the temperature of a photon recoil, but also severely limits densities by radiation pressure forces. For observation of quantum degeneracy in a gas of atoms, it is therefore necessary to confine the atoms in a different kind of trap and to provide cooling methods that do not rely on spontaneous scattering. The most common technique in cold atom experiments is the confinement of atoms in a magnetic trap [63, 64] combined with evaporative cooling of the atoms [65, 66, 67].

2.6.1 Magnetic trapping of ^{40}K and ^{87}Rb

Magnetic trapping relies on the interaction of a permanent magnetic dipole moment of neutral atoms with an inhomogeneous magnetic field. The trapping potential of an atom with magnetic moment $\vec{\mu}$ in a magnetic field $\vec{B}(\vec{r})$ is given by

$$V(\vec{r}) = -\vec{\mu} \cdot \vec{B}(\vec{r}) = -g_F m_F \mu_B |\vec{B}| \tag{2.1}$$

where μ_B is the Bohr magneton, m_F the magnetic quantum number and g_F is the Lande g-factor. The above equation only makes sense under the assumption that the magnetic moments of the atoms when moving through the magnetic field adiabatically follow the magnetic field. This is the case as long as the precession of the magnetic moment of the atom around the B-field is fast compared to the motion of the atom along the field lines:

$$\hbar\omega_{\text{Lamor}} = m_F g_F \mu_B |\vec{B}| \gg \frac{|\dot{\vec{B}}|}{|\vec{B}|} \tag{2.2}$$

In this case, atoms in states with $g_F m_F < 0$ ("weak-field seeking states") tend to stay at a local minimum of the magnetic field whereas atoms with $g_F m_F > 0$ ("high-field seeking

states") are trapped at a local maximum of the magnetic field. Maxwell's equations, however, prohibit a local maximum of the magnetic field. Hence, magnetic trapping is limited to the weak-field seeking states [68].

In the case of ^{87}Rb, atoms in the $|F = 2, m_F = 2, 1\rangle$ and $|F = 1, m_F = -1\rangle$ can be trapped magnetically, whereas in ^{40}K, a whole bunch of spin states ($|F = 9/2, m_F = 9/2\rangle$, $|9/2, 7/2\rangle$, ...$|9/2, 1/2\rangle$ and $|F = 7/2, m_F = -7/2\rangle$, $|7/2, -5/2\rangle$, ..., $|7/2, -1/2\rangle$) are low-field seeking states. Simultaneous trapping of ^{40}K and ^{87}Rb in a single magnetic trap is however limited to combinations of spin states which are stable against spin changing collisions. In our experiment, we have chosen the polarized ^{40}K $|F = 9/2, m_F = 9/2\rangle$ ^{87}Rb $|F = 2, m_F = 2\rangle$ configuration for simultaneous magnetic trapping and sympathetic cooling (see below).

2.6.2 Magnetic trap design

This section only reviews basic common techniques and peculiarities of magnetic trapping. A very detailed discussion of our magnetic trap design can be found in Christian's PhD thesis [35] and the diploma thesis of Ralf Dinter [69]. The most simple coil configuration appropriate for magnetic trapping of atoms is given by two coils in anti-Helmholtz configuration giving rise to a magnetic quadrupole field. The magnetic field is thus zero in the center of the trap and linearly increases in all three directions. However, this magnetic trap has one decisive disadvantage: At $|\vec{B}| = 0$, the adiabatic following condition of equation 2.2 is no longer fulfilled. In this case, spinflips of the atoms can occur, so-called Majorana transitions, and eventually transfer atoms from the low-field seeking to high-field seeking states. The Majorana losses become the more important the colder the atoms get and effectively prevent the achievement of quantum degeneracy in these traps without further precautions [7, 70].

In our experiment, we have followed a very common approach: The use of a magnetic field configuration with non-zero magnetic field in the center and a quadratic increase of the magnetic field away from the center. Such a magnetic field configuration is realized by the Ioffe-Pritchard trap [71] and its numerous variants. The original trap is made up of four horizontal Ioffe bars providing the radial confinement and two axial coils closing the trap in the axial direction. The magnetic field of such a trap at the trap center is given by:

$$\vec{B} = B_0 \begin{pmatrix} 0 \\ 0 \\ 1 \end{pmatrix} + B' \begin{pmatrix} x \\ -y \\ 0 \end{pmatrix} + \frac{B''}{2} \begin{pmatrix} -xz \\ -yz \\ z^2 - 1/2(x^2 + y^2) \end{pmatrix}$$

where B_0 is the bias field, B' the radial gradient and B'' the axial curvature. The resulting trapping potential is cigar-shaped with strong radial and weak axial confinement. In the axial direction, the potential is harmonic with a trapping frequency

$$\omega_{ax} = \sqrt{\frac{g_F m_F \mu_B}{m} B''}.$$

In the radial direction, the potential has a harmonic minimum near the origin with a radial trapping frequency of

$$\omega_{rad} = \sqrt{\frac{g_F m_F \mu_B}{m} \tilde{B}''}$$

where $\tilde{B}'' = \frac{B'^2}{B_0} - \frac{B''}{2}$ is the radial curvature. Far away from the trap center, the potential increases linearly in the radial direction. The radial curvature and thus the radial

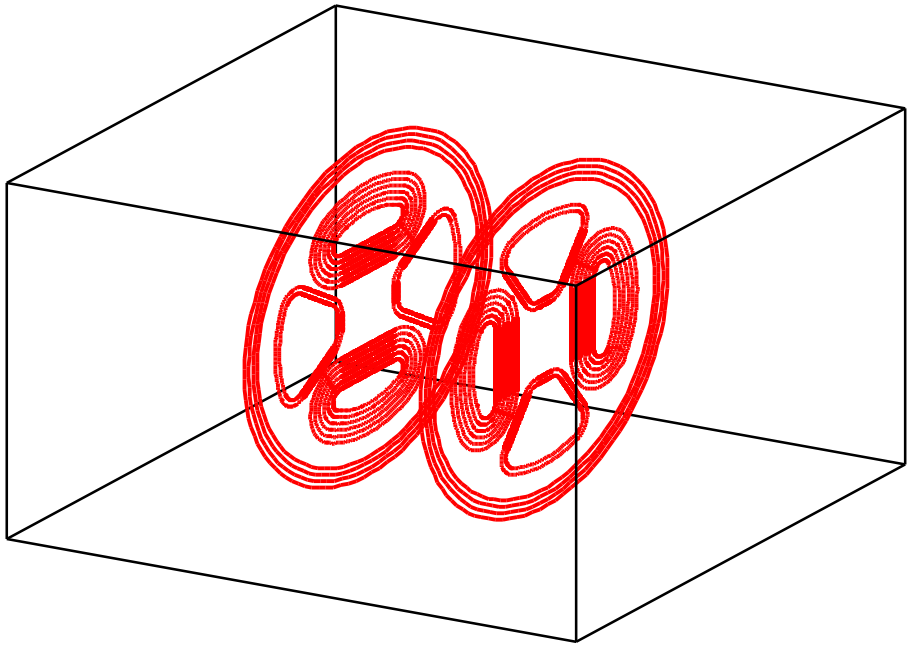

Figure 2.9: Coil configuration for the magnetic trap. Our magnetic trap is a hybrid between the original cloverleaf and the 4Dee-trap. Compared to the 4Dee-trap, the additional cloverleaves (with less windings than the Dees) provide additional radial gradient at the cost of axial curvature, while still offering the excellent 2π optical access in the radial direction characteristic for the cloverleaf trap. Calculated axial and radial trapping frequencies are $2\pi \cdot 11.2\,\mathrm{Hz}$ and $2\pi \cdot 214\,\mathrm{Hz}$, respectively (for ^{87}Rb) at an operating current of 110 A and a total power consumption of 2.5 kW.

confinement is strongly dependent on the offset field B_0. With increasing offset field, the radial confinement decreases and for $B_0 = (2B'^2)/(3B'')$, a weak isotropic magnetic trap is realized with $\omega_{ax} = \omega_{rad}$. Whereas the weak isotropic trap is convenient for loading of the trap from the MOT, the compressed trap is favorable for evaporative cooling where fast rethermalization and thus a large elastic scattering rate is required.

The magnetic trap in our experiment is based on the Ioffe Pritchard geometry although a different coil configuration compared to the original design is used (see Fig. 2.9). The design has been based on the design of the magnetic trap in the BEC experiment of our group [39, 40] and is described in detail in [35]. We have realized a hybrid setup based on the cloverleaf coil configuration [72] and on the 4 Dee trap [73]. Compared to the original Ioffe configuration with 4 Ioffe bars and pinch coils, the cloverleaf setup is characterized by excellent full 2π optical access in the radial direction. However, it requires a total of 12 coils (8 cloverleaves, also called quadrupole coils, 2 pinch coils and 2 anti-bias coils in Helmholtz configuration). The 4-Dee trap, on the other hand, drops 4 of the cloverleaves and needs no pinch coils, but the radial confinement cannot be made as strong as in the original cloverleaf trap. Our concept achieves the excellent optical access and the strong

radial confinement of the cloverleaf trap without the pinch coils. The axial curvature is provided by reducing the number of windings on four of the eight quadrupole coils (we refer to these coils as "cloverleaves", whereas the other four (strong) coils are called "Dees"). Additionally, this scheme only requires a pair of Helmholtz coils to provide an additional offset field which can make the radial confinement weaker ("uncompressed trap"). Note that the Helmholtz coils play exactly the opposite role as in the original cloverleaf geometry, where the pinch coils produce a large offset field in addition to the axial curvature, and the Helmholtz coils are activated to lower the offset field and make the radial confinement stronger.

The magnetic trap is operated with a current of 110 A. The decompressed magnetic trap is almost spherically symmetric with a trapping frequency of $\omega^{^{87}\mathrm{Rb}} = 2\pi \cdot 11.2$ Hz. During compression, the axial trapping frequency remains at the value of $2\pi \cdot 11.2$ Hz while the radial trapping frequency is $\omega_{\mathrm{rad}}^{^{87}\mathrm{Rb}} = 2\pi \cdot (200 - 300)$ Hz, depending on the value of the offset field.

Operation of a magnetic trap requires sophisticated electronics for fast switching of the involved high currents. Using high speed IGBTs, we are able to ramp down the currents in the magnetic trap within 40 μs. The voltage across the IGBTs is limited to 800 V by varistors to avoid damage to the semiconductors, which implies that the current is ramped down linearly at constant voltage in contrast to the more familiar exponential decay.

2.6.3 Loading of the magnetic trap

After accumulation of atoms in the MOT and subsequent polarization gradient cooling, the atoms are prepared in a spin state appropriate for magnetic trapping. In our experiment, we use a mixture of ^{40}K in the $|F = 9/2, m_F = 9/2\rangle$ state and ^{87}Rb in the $|F = 2, m_F = 2\rangle$ state. Atoms in these states are prepared using σ^+ light on the corresponding cycling transitions starting from ensembles in the $F = 9/2$ and $F = 2$ state respectively. We then switch on the decompressed magnetic trap with trapping frequencies of $\omega_x^{\mathrm{Rb}} = \omega_y^{\mathrm{Rb}} = \omega_z^{\mathrm{Rb}} = 2\pi \cdot 11$ Hz to allow for almost mode-matched and efficient loading of the magnetic trap. The magnetic trap is then compressed adiabatically in the radial direction during 1.5 s. We typically prepare $3 \cdot 10^{9}$ ^{87}Rb atoms and $2 \cdot 10^{7}$ ^{40}K atoms in the magnetic trap.

2.6.4 Lifetime of thermal atoms in the magnetic trap

For the achievement of quantum degeneracy in a gas of cold atoms, an evaporative cooling stage of up to 30 s is required. It is therefore essential to realize a long lifetime of the atoms in the magnetic trap. The lifetime of thermal atoms in the magnetic trap is limited by collisions with hot background gas atoms. To characterize the lifetime of our magnetic trap, a pure ^{87}Rb cloud of 10^9 atoms in the $|F = 2, m_F = 2\rangle$ state has been prepared in the compressed magnetic trap. The atom number has then been measured as a function of hold time in the magnetic trap. Fig. 2.10 shows the corresponding characteristic decay. We observe an almost purely exponential decay with a $1/e$ lifetime of (260 ± 50) s which is largely sufficient for evaporative cooling to quantum degeneracy.

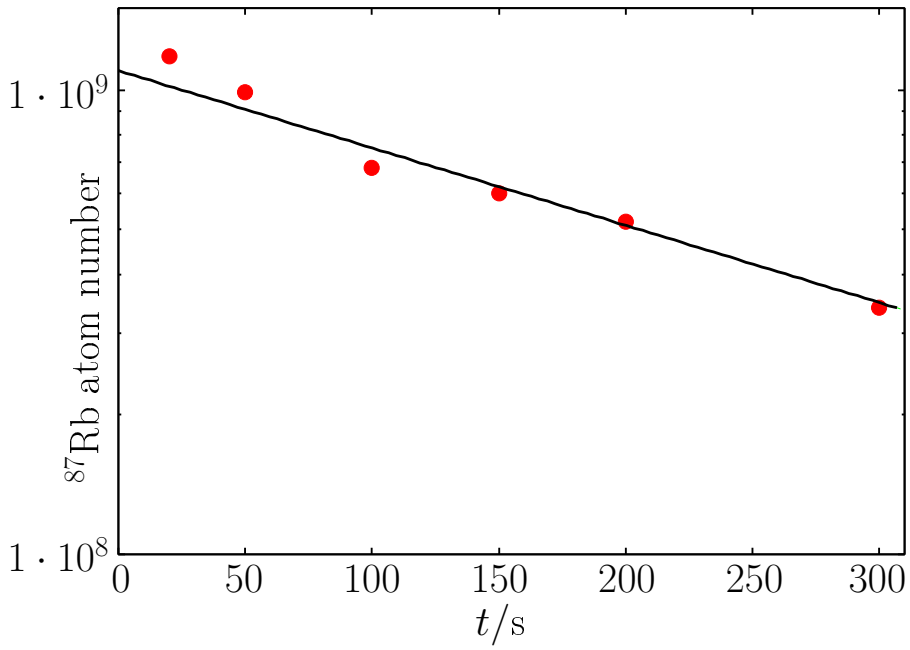

Figure 2.10: Decay of a pure thermal ^{87}Rb ensemble of initially 10^9 atoms in the magnetic trap. The decay is purely exponential with a $1/e$-lifetime of (260 ± 50) s

2.7 Absorption imaging of atomic clouds

The standard technique to gain information about dilute atomic gases is absorption imaging. The atoms are illuminated by low-intensity < 50 μs pulses of resonant laser light. For absorption imaging, we use the $|F = 9/2\rangle \rightarrow |F = 11/2\rangle$ and $|F = 2\rangle \rightarrow |F = 3\rangle$ transitions for detection of ^{40}K and ^{87}Rb, respectively. The atoms absorb the photons and scatter them into 4π. The shadow of the atomic ensemble can be imaged onto a CCD camera. A quantitative description of this shadow is given by Lambert-Beer's law. The intensity of a near-resonant laser beam propagating in z-direction transmitted through an atomic ensemble with the density distribution $n(x, y, z)$ is given by

$$I(x, y) = I_0(x, y) \exp\left(-\frac{1}{2}\sigma_0 \int dz n(x, y, z)\right) \tag{2.3}$$

where σ is the cross section of the atoms for photon scattering. Based on the measured intensity distribution of the transmitted light, conclusions about the observed atom number in a certain spatial area defined by the coordinates $x, x + \Delta$ and $y, y + \Delta$ and thus the density distribution of the atoms after (!) time of flight can be drawn. The atom number within this area, e.g. imaged onto a single pixel of a CCD camera, is given by

$$N(x, x + \Delta, y, y + \Delta) = -\frac{\Delta^2}{\sigma} \ln \frac{I(x, y)}{I_0(x, y)} \tag{2.4}$$

During a typical resonant imaging pulse, an atom scatters up to 300 photons, making the absorption imaging technique destructive. In typical measurement series, each data point

requires a new ensemble to be prepared. The preparation of atomic clouds has therefore to be as reproducible as possible.

The actual imaging process does not rely on a single picture of the atoms' shadow. Imperfections in the profile of the imaging beam and interference effects make the actual absorption image very noisy. In addition, disturbing background signals arise even in the absence of imaging light due to residual background light falling onto the CCD chip. To reduce both sources of imperfections as much as possible during a typical absorption process, three images are taken: The first image takes an absorption image of the atomic cloud. The second image, the so-called reference image, is taken under the same experimental conditions (exposure time, intensity of detection light) but without atoms. These two images are divided by each other, thereby reducing noise due to imperfections in the beam profile of the imaging beam as long as they are stationary between both exposures. A third image is then taken in a last step, under the same experimental conditions as the two previous images but without the detection flash. This dark image is subtracted from the absorption and the reference image. The integrated column density is then obtained from

$$OCD(x,y) = \ln \frac{I_{\mathrm{noatoms}}(x,y) - I_{\mathrm{dark}}(x,y)}{I_{\mathrm{atoms}}(x,y) - I_{\mathrm{dark}}(x,y)} \tag{2.5}$$

which is directly related to the atom number in a certain spatial area via

$$N(x, x+\Delta, y, y+\Delta) = -\frac{\Delta^2}{\sigma} OCD(x,y) \tag{2.6}$$

2.7.1 Optical setup

We have integrated four detection systems in our experiment. Two of them allow simultaneous detection of the two atomic species in a single run (see below). Three of the imaging systems are overlapped with the MOT and lattice axes. These detection systems allow accurate alignment of the lattice laser beams (see 5.4.2). Two of these "lattice" imaging systems are operated with resonantly tuned MOT light whereas the third is operated with a separate detection beam. Another optical lattice axis (our main detection axis) is realized along the z-axis of our apparatus (see Fig. 2.1). Most of the absorption images in this thesis are taken along this axis of our apparatus. A typical setup of an imaging system is shown in Fig. 2.11. The resonant laser light is outcoupled from the fiber, carefully collimated by a large NA achromatic lens and then sent onto the atomic cloud. The detection lens system consists of two achromatic high-quality lenses with typical focal lengths of $f_1 = 120$ mm and $f_2 = 250$ mm realizing a 1:2 magnification. To minimize imperfections of the image due to lens errors, we have put them as near as possible to each other. In this configuration, the second lens compensates to a maximum degree for the lens errors from the first lens. The finite numerical aperture of the first lens limits the resolution of the imaging system to a diffraction limited resolution of 4 μm. In the experiment, we observe a resolution of 6 μm. This is probably due to imperfections in the lens alignment which are not perfectly parallel with respect to each other and the 2 mm thick glass interfaces of the vacuum cell.

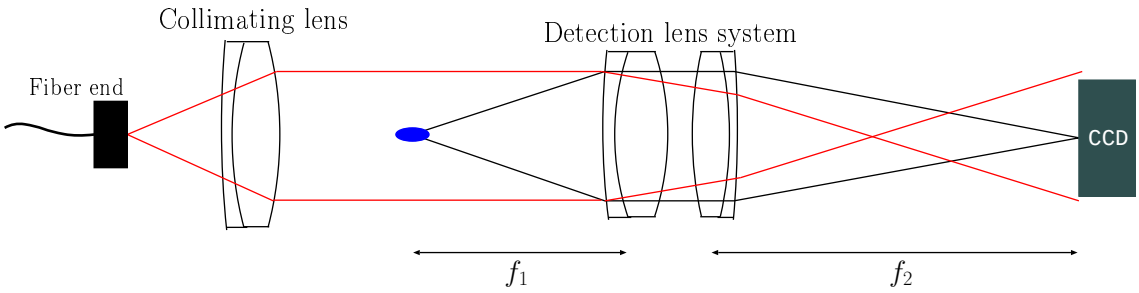

Figure 2.11: Optical Setup of a detection system.

2.7.2 Time-of-flight imaging

Dilute atomic gases are typically imaged in time-of-flight absorption imaging. Any confining atom traps are suddenly switched off and the atoms are allowed to expand for $3-25$ ms. The reason for absorption imaging after time-of-flight instead of in-trap imaging is twofold.

1. The spatial extensions of typical ultracold atomic gases in a confining trap are on the order of a few 10μm while the imaging resolution is on the same order of magnitude.

2. The in-trap optical density of typical atomic clouds is so dense that the laser beam is completely dark after passing through the atomic cloud. The absorption imaging picture is then of limited use, as no information on the density distribution can be extracted from these images.

After time of flight of $3-25$ ms, however, the atomic clouds are typically a few hundred μm in size and the densities of the atomic clouds are significantly reduced.

2.7.3 Two-species imaging

In a single experimental run, we simultaneously image both ^{40}K and ^{87}Rb cloud on a single detection axis. This is done by taking advantage of the extremely short interframing time of interline CCD camera chips (ca. 200 μs). A typical imaging sequence then consists of three double frames. The first double frame consists of two absorption images, one of the ^{40}K cloud and one of the ^{87}Rb cloud. The ^{40}K cloud is typically imaged after $3-5$ ms time of flight, whereas we allow for $20-25$ ms time of flight for the ^{87}Rb cloud. We then have to allow for >100 ms read-out time for the two images. The second double frame then consists of the two reference images for the two clouds, followed by the last double frame with the dark images. For more details on the different imaging schemes, see [35]).

2.8 Cooling to quantum degeneracy - Evaporative cooling

2.8.1 Evaporative cooling of ^{87}Rb to quantum degeneracy

Evaporative cooling [65, 66, 67] has proved to be a reliable way to bridge the gap in phase space density between laser cooling and quantum degeneracy in dilute atomic gases [6, 8, 7]. It increases the phase space density of atomic gases by more than 6 orders of magnitude. The main idea is the following: Atoms with velocities in the high kinetic energy tail of the Maxwell-Boltzmann distribution are removed from the trap. The remaining atoms rethermalize by elastic collisions resulting in a lower temperature. Apart from a decrease in temperature, evaporative cooling has proved to effectively increase the density of an atomic ensemble.

In a magnetic trap, this cooling mechanism can be realized efficiently by rf-induced forced evaporation. The applied rf defines the trap height of the magnetic trapping potential via the resonance condition $\hbar\omega_{\mathrm{rf}} = \mu_B g_F |\vec{B}(\vec{r})|$. The trap depth is then given by $E_{\mathrm{depth}} = \hbar\left(\omega_{\mathrm{rf}} - \omega_0\right)$ where $\omega_0 = \mu_B g_F B_0/\hbar$ and B_0 is the magnetic field at the magnetic field minimum of the trap. Any atoms with kinetic energy above E_{depth} are removed from the trap by a sequence of induced spin flips from a low-field seeking to a high-field seeking state. Decreasing the radio-frequency results in a continuous decrease of the trap height, thereby efficiently decreasing the temperature of the gas.

Evaporative cooling of ^{87}Rb is performed starting from a thermal ensemble of ^{87}Rb atoms in the compressed magnetic trap of up to $3 \cdot 10^9$ atoms in the $|F = 2, m_F = 2\rangle$ state with typical trapping frequencies of 11 Hz in the axial and $210 - 250$ Hz in the radial direction. The radial trap frequencies are achieved by lowering the offset field of the magnetic trap to values of $\propto 0.5$ G. The forced evaporative cooling process is controlled by a radio-frequency field generated by an arbitrary sweep function generator which allows predefined phase continuous radio-frequency sweeps between 0....150 MHz [35]. In our experiment, the evaporation ramp starts at 35 MHz with a linear ramp of 6 seconds down to 5 MHz, a second ramp within 3 s down to 2 MHz and a final ramp with a ramp speed of $0.25 - 0.5$ MHz/s preparing pure Bose-Einstein condensates of up to $\propto 4 \cdot 10^6$ atoms. During the evaporation ramp the phase space density of the ensemble is increased by almost 6 orders of magnitude with a factor of 10^3 loss in atoms.

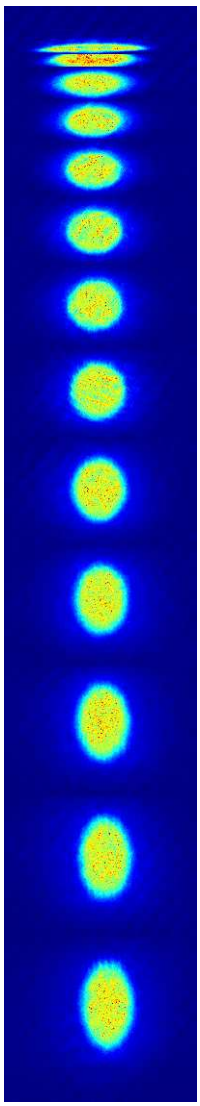

Figure 2.12: BEC in time of flight. $\Delta t = 1, 3, ...25$ ms

Fig. 2.12 shows the expansion series of a Bose-Einstein condensate with $> 1 \cdot 10^6$ atoms prepared in our magnetic trap. The time-of-flight images show the reversion of aspect ratio typical for Bose-Einstein condensates with intrinsic repulsive interactions in a cigar-shape trap.

2.8.2 Sympathetic cooling of fermionic potassium to quantum degeneracy

Due to the Pauli principle, elastic collisions in ultracold fermionic quantum gases are suppressed in a one-component spin-polarized Fermi gas. Whereas $s-$wave collisions are forbidden due to the Pauli exclusions principle, the cross-section of allowed higher-order p-wave scattering decreases quadratically with decreasing temperature: $\sigma_p \propto T^2$ [74]. Evaporative cooling (which relies on efficient rethermalization via elastic scattering [65]) is thus highly inefficient in a one-component Fermi gas. Direct evaporative cooling of fermionic atoms is only possible in two-component Fermi gases as successfully demonstrated at JILA in a $|F = 9/2, m_F = 9/2\rangle \otimes |F = 9/2, m_F = 7/2\rangle$ mixture. These pioneering experiments led to the first observation of quantum degeneracy in fermionic gases [9].

In our experiments, we have decided to follow another approach by sympathetically cooling the fermionic ^{40}K atoms in the $|F = 9/2,\ m_F = 9/2\rangle$ state in a bath of bosonic ^{87}Rb in the $|F = 2,\ m_F = 2\rangle$ state in a magnetic trap [75]. The idea of sympathetic cooling is not a new one. Originally proposed in the context of plasmas, sympathetic cooling of neutral atoms has first been demonstrated in a bath of cryogenically cooled helium [76]. Later on, two overlapping BECs have been produced by sympathetic cooling in a two-component ^{87}Rb spin mixture [77]. Fermionic ^{6}Li atoms cooled in a bath of bosonic ^{7}Li atoms [78] have led to the first observation of simultaneous quantum degeneracy in a mixture of dilute atomic bosonic and fermionic quantum gases [79]. Efficient sympathetic cooling to quantum degeneracy in a mixture of fermionic ^{40}K in a bath of bosonic ^{87}Rb has first been demonstrated at LENS [75]. The efficiency of the cooling relies on the large and negative scattering length between ^{40}K and ^{87}Rb in the above spin states (for the most recent value $a_{FB} = (-215 \pm 10)a_0$, see [80]). While the large value ensures efficient rethermalization, the attractive interaction arranges for a good spatial overlap.

Production of our first BEC as a benchmark and demonstration of magneto-optical trapping of ^{40}K showed that no principal obstacles to sympathetic cooling of the mixture remained. We obtained first evidence of sympathetic cooling only two weeks after the production of the first BEC. For simultaneous magnetic trapping, both species are prepared via optical pumping in their doubly polarized spin state ($|F = 9/2,\ m_F = 9/2\rangle$ for ^{40}K and $|F = 2,\ m_F = 2\rangle$ for ^{87}Rb). In these states, both atomic species experience the same trapping potential while the trapping frequencies of the two species in the trapping potential differ by a factor of $\omega_{\mathrm{K}}/\omega_{\mathrm{Rb}} = \sqrt{m_{\mathrm{Rb}}/m_{\mathrm{K}}}$.

Sympathetic cooling of ^{40}K to quantum degeneracy is performed by selectively evaporating ^{87}Rb while ^{40}K is cooled in the bath of ^{87}Rb atoms. The selectivity of the evaporation process relies on the fact that the gyromagnetic factors of the resonance frequency in the magnetic trap for ^{87}Rb is about twice the resonance frequency for ^{40}K. Both ^{40}K in the $|F = 9/2,\ m_F = 9/2\rangle$ state and ^{87}Rb in the $|F = 2,\ m_F = 2\rangle$ state have the same magnetic moment but different numbers of magnetic sublevels in the respective hyperfine manifold. Thus, they experience the same trapping potential but with an rf-cutoff differing by a factor of 2.25. In terms of temperature, a 1 MHz change in rf corresponds to a change of the potential height of 96 μK for ^{87}Rb and 216 μK for ^{40}K. Given an offset field of 0.7 G, the radio-frequency reaching the trap bottom for ^{87}Rb still corresponds to a trap depth of 59 μK for ^{40}K. It is thus possible to restrict the evaporation losses to the rubidium atoms and sympathetically cool the potassium ensemble, which quickly

thermalizes with the cold ^{87}Rb cloud due to the large interspecies collisional elastic cross section.

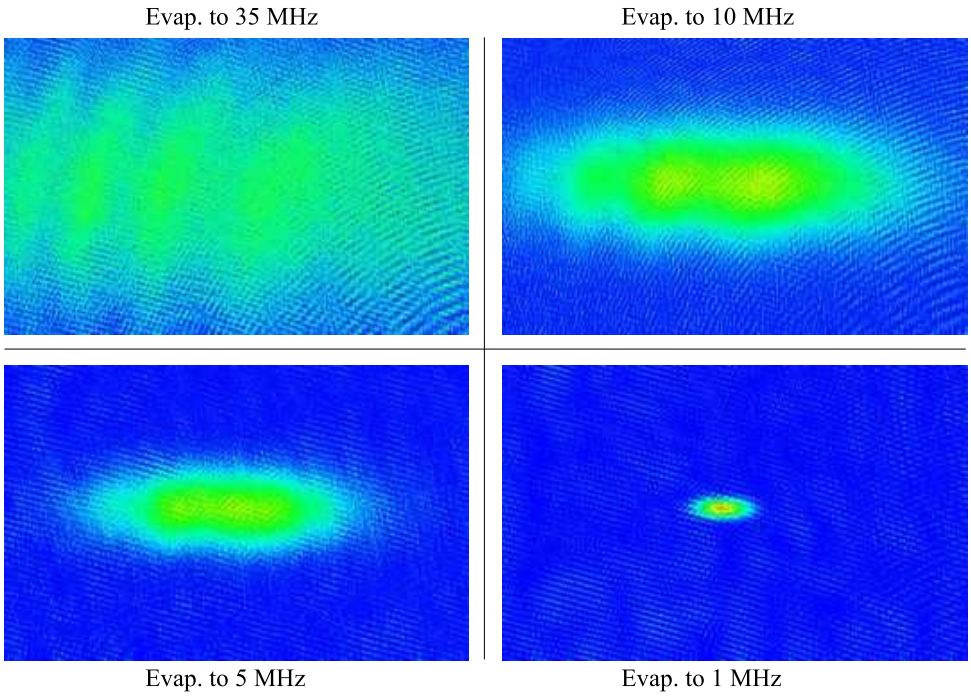

Figure 2.13: Observation of sympathetic cooling. Shown are absorption images of potassium atoms which are taken after different end frequencies of the rubidium evaporation ramp. The density increase and temperature decrease over several orders of magnitude are clearly visible.

The efficiency of the cooling process of the ^{40}K cloud is nicely illustrated in figure 2.13. The figure shows images of the potassium cloud at different end frequencies of the radio frequency ramp while rubidium is being evaporated. While absolute particle numbers are hard to extract when the gas is still relatively dilute, we estimate that particle loss of potassium during the evaporation is relatively small. While the fermion particle number seems to remain stable, a considerable density increase and temperature decrease over several orders of magnitude is clearly visible from these images. The last image in figure 2.13 is taken at a frequency of 1 MHz, when the potassium cloud is not yet in the quantum degenerate regime.

In the experiment, we have optimized the evaporative cooling process by splitting the rf-ramp into two or three linear sweeps with fixed end frequencies and sequentially maximizing the particle number at the end of each sweep with the sweep rate as optimization parameter. The resulting rf sweep differs from an optimized pure ^{87}Rb sequence only during the last (low frequency) sweep, when the ^{87}Rb particle number becomes similar to the ^{40}K particle number. Typical atom numbers in the two clouds throughout the evaporation process are given in Fig. 2.14. Whereas we observe very little atom losses in the ^{40}K cloud, atom numbers in the ^{87}Rb cloud are reduced by 2 orders of magnitude due

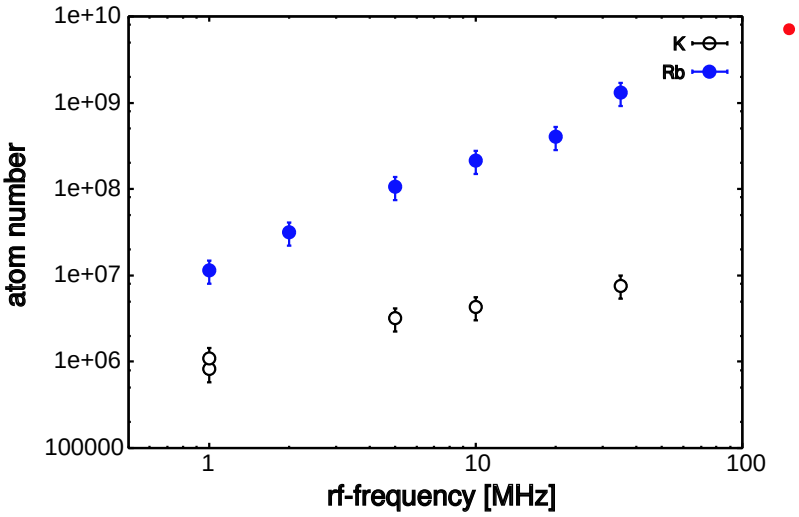

Figure 2.14: Atom numbers in the ^{40}K and ^{87}Rb cloud throughout the sympathetic cooling process. Whereas we observe very little losses in the ^{40}K cloud, the atom numbers in the ^{87}Rb cloud are decreased by 3 orders of magnitude due to forced evaporation

to forced evaporation. The moderate losses of ^{40}K during the evaporation ramp are likely due to the small fraction of atoms with an energy larger than the ^{40}K trap depth. At low temperatures near the end of the evaporation ramp the ^{40}K losses slightly increase. This indicates the onset of a new loss mechanism, dominating at high densities, which we identify as 3-body K-Rb-Rb collisions. This loss process is characterized by the rate equation

$$\frac{\dot{N}_F(t)}{N_F(t)} = -K_3 \cdot \int \mathrm{d}^3 r \, n_B^2(r,t) \, \frac{n_F(r,t)}{N_F(t)}$$

where n_B and n_F are the boson and fermion densities. Analyzing a set of decay series both in the degenerate and non-degenerate regime, we measure the three-body loss rate coefficient to be $K_3 = (2.8 \pm 1.1) \cdot 10^{-28}\,\mathrm{cm}^6/\mathrm{s}$ for our experimental parameters [5]. Note the value extracted from our measurements is a factor of 10 smaller than a previously reported value (cf. [81]). However, this is good news as a low three-body decay rate is essential for the realization of long-lived mixtures and a variety of experiments relying on a long lifetime of the atomic clouds.

Starting from 40 MHz, we optimize the evaporative cooling process by splitting the rf-ramp in two or three[7] linear sweeps with fixed end frequencies and sequentially maximizing the particle number at the end of each sweep with the sweep rate as optimization parameter. The resulting rf sweep sequence differs from an optimized "pure rubidium" sequence essentially only during the last (low frequency) sweep, when the ^{87}Rb particle number becomes similar to the ^{40}K particle number. The onset of mixed species three-particle losses in this low temperature and high density regime favors fast cooling with relatively high evaporation losses over efficient but slow evaporation. For our parameters, we found an optimum mixed species sweep rate on the order of 0.5 MHz/s as compared

[7]For maximum particle numbers we use two sweeps, for minimum collective excitations of the mixture the last of these two sweeps has to be split, such that degeneracy can be approached more slowly.

to an optimum sweep rate of $\approx 250\,\mathrm{kHz/s}$ for single species ^{87}Rb ensembles. If all of the ^{87}Rb atoms are removed during the evaporation sequence, we obtain Fermi gases of up to $3 \cdot 10^6$ ^{40}K atoms at $T/T_F = 0.2$ or $9 \cdot 10^5$ at $T/T_F = 0.1$. Maximizing the particle numbers for both ^{40}K and ^{87}Rb in a quantum degenerate Fermi-Bose mixture we obtain up to $> 1 \cdot 10^6$ atoms in the condensate coexisting with $7.5 \cdot 10^5$ ^{40}K atoms, limited by the attractive ^{87}Rb-^{40}K interactions, which cause a (possibly excitation induced) collapse of the mixture as discussed in the next section.

2.9 Detection of quantum degeneracy in fermionic gases

Whereas the onset of Bose-Einstein condensation is immediately visible due to the striking bimodal distribution of the time-of-flight images and the inversion of the BEC's aspect ratio during time of flight, the onset of Fermi degeneracy deserves a more careful analysis of the time-of-flight absorption images. Figure 2.15 shows an absorption image of about $7 \cdot 10^5$ fermionic ^{40}K atoms at $T/T_F \approx 0.25$. No striking feature indicates the onset of quantum degeneracy. Instead, a continuous crossover from non-degenerate to degenerate gases happens which can only be detected through careful temperature and atom number analysis of the time of flight images. This is performed by fitting 2D Fermi-Dirac profiles to the experimental data, thereby determining the temperature of the gas. Combined with information about the atom number in the system, we obtain the degeneracy parameter T/T_F.

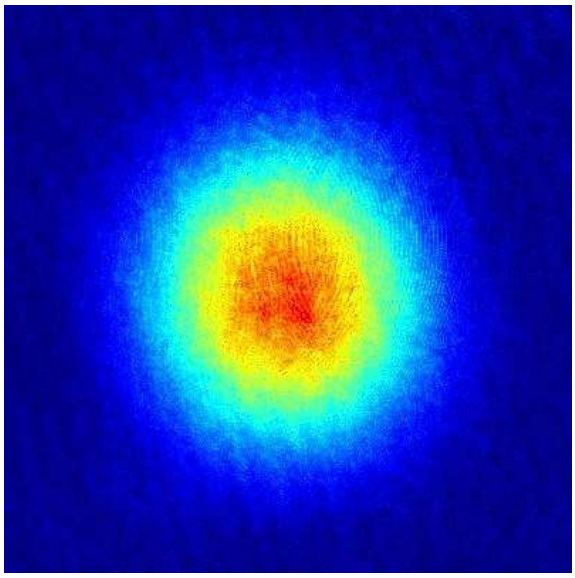

Figure 2.15: Quantum degenerate Fermi gas of $7 \cdot 10^5$ fermionic ^{40}K atoms at $T/T_F = 0.25$

Figure 2.16 shows 1D profiles of Fermi gases both deeply in the degenerate regime and at moderate T/T_F. In both cases, we have fitted a 2D Fermi-Dirac profile. As can be seen from these figures, the onset of quantum degeneracy is most striking when the Fermi-Dirac 1D expansion profile is compared to a hypothetical Maxwell-Boltzmann gas with the same particle number and temperature as obtained from the Fermi-Dirac fit. For

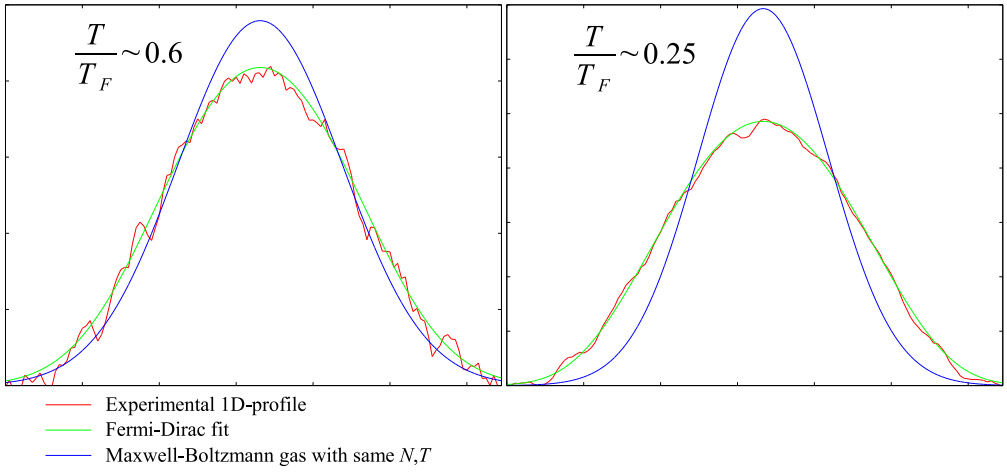

Figure 2.16: Thermometry for a degenerate Fermi gas.

a detailed discussion of the techniques to extract temperature and degeneracy information from time-of-flight images of fermionic and bosonic gases see Christian's thesis [35].

2.10 Interaction effects during evaporation

In our experiment, we have been able to produce the to our knowledge so far highest particle numbers in the ^{40}K / ^{87}Rb system with $> 7 \cdot 10^5$ ^{40}K atoms coexisting with a Bose-Einstein condensate of $> 1 \cdot 10^6$ atoms. The observation of stable large-particle number mixtures has been of particular importance. At that time, scattering properties of ^{40}K and ^{87}Rb were still controversially discussed. The only thing about the heteronuclear scattering of ^{40}K and ^{87}Rb that was known for sure was the attractive character of heteronuclear interactions which gives rise to a mean-field collapse (see [82], section 4.3) above certain critical particle numbers. In 2002, critical particle numbers for the occurrence of the mean-field collapse [82] of the mixture of $N_{\mathrm{K}} \approx 2 \cdot 10^4$ and $N_{\mathrm{Rb}} \approx 10^5$ [81]) had been reported. Although this observation suggested an excitingly large value for the attractive interspecies interaction, characterized by an s-wave scattering length of $-395a_0$, the observation appeared to impose severe constraints on maximally achievable particle numbers. Nowadays, the current best value for the scattering length is derived from precise spectroscopy of Feshbach resonances to be $(-215 \pm 10)a_0$ [80].

In our experiment we have been able to access various regimes of mixtures, ranging from dense thermal ^{87}Rb clouds of 10^7 atoms right at the phase transition point, coexisting with a moderately degenerate Fermi gas of $2 \cdot 10^6$ ^{40}K atoms, to deeply degenerate mixtures with almost pure condensates of $> 7 \cdot 10^5$ ^{40}K and $> 1 \cdot 10^6$ ^{87}Rb atoms only limited by the observation of a (possibly excitation enhanced) mean-field collapse of the mixture. Fig. 2.17 shows the simultaneously achieved particle numbers in the ^{40}K cloud as a function of condensed ^{87}Rb atoms, as observed in our experiments (blue data points). Data points in red indicate instable mixtures where instability has been detected either through a decay dynamics of the mixture incompatible with three-body decay [4] or through a sudden

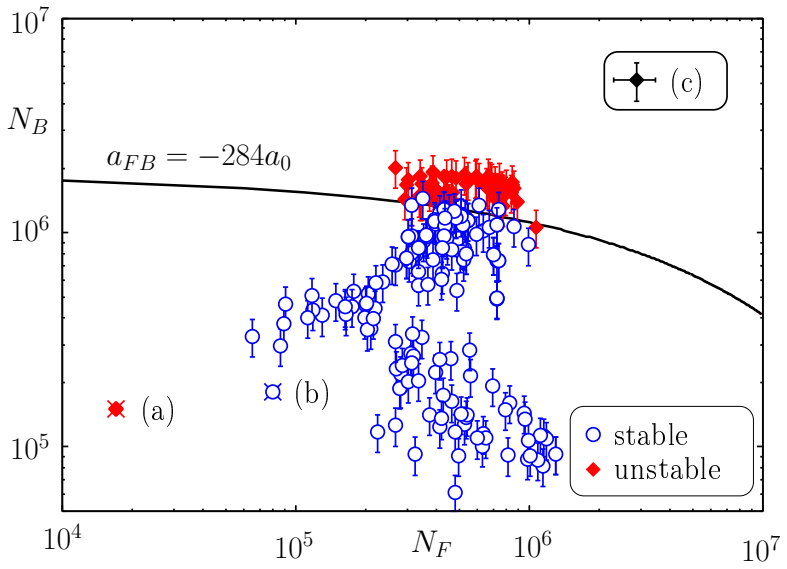

Figure 2.17: Stability diagram for the ^{40}K / ^{87}Rb mixture. The uncertainty in $N_{\mathrm{Rb}}/N_{\mathrm{K}}$ is assumed to be 20%/30%. The error on N_F is not critical and is given exemplarily in (c). The solid black line is based on the theory of ref. [83] and $a_{FB} = -284\,a_0$. (a) is the critical particle number reported in ref. [84] (here the trap had a different aspect ratio, but a similar mean trapping frequency $\bar{\nu}_K = 134\,\mathrm{Hz}$, as compared to our experiment with $\bar{\nu}_K = 133\,\mathrm{Hz}$). (b) is a stable particle number reported in [85] (for a mean trapping frequency $\bar{\nu}_K = 127\,\mathrm{Hz}$).

step-like loss of particles in the fermionic component (see below). The black line is the instability limit due to a mean-field collapse of the mixture as derived from an *equilibrium* mean-field model and based on a scattering length of $-284a_0$ (thereby providing an upper limit on the scattering length).

The derived *upper limit* on the scattering length is larger than the most recent value of the scattering length suggested by Feshbach spectroscopy of $(-215 \pm 10)a_0$ (see [80] and section 4.2.4). In order to achieve the regime of very high particle numbers, the optimum method was to use a relatively fast evaporation ramp in the last stage of evaporative cooling, inducing strong shape oscillations [35, 5] in the mixture. These significantly enhance the density of the mixture compared to an *equilibrium* situation.

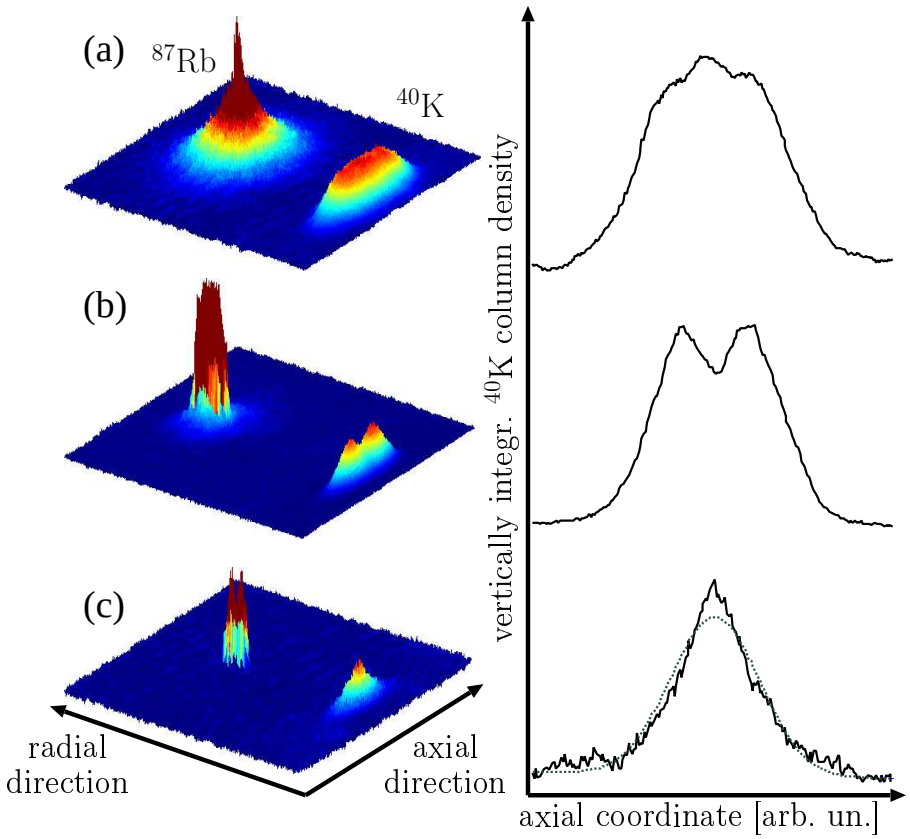

Figure 2.18: Typical evolution of an overcritical mixture after an evaporation ramp (rate -1 MHz/s) stopped and held fixed for 15 ms at 80 kHz (a), 50 kHz (b) and 20 kHz (c) above the ^{87}Rb trap bottom of 490 kHz. Left-hand side: 3D representation of absorption images with false-color coding of the optical density. ^{87}Rb and ^{40}K images are taken in the same run, although at different TOF: 20 ms (^{87}Rb) and $3-5$ ms (^{40}K). Right-hand side: corresponding ^{40}K axial line profiles integrated along the vertical direction.

During the last stage of evaporative cooling, we observe strong interaction induced effects. These effects become clearly visible in the axial ^{40}K density distribution. Due to the relatively short time of flight (TOF), this should closely reflect the in trap distribution. The fast ramp speed (1 MHz/s) in this experiment means that we are potentially dealing

with strongly out of equilibrium samples. Already at the phase transition point (a) of the bosonic cloud, we observe strong distortions of the axial ^{40}K density profile. The profile looks like a chopped off Fermi profile with a peak in the center of the flat top which we ascribe to the interaction with the bosonic component (peak density $\approx 4 \cdot 10^{14}\,\mathrm{cm}^{-3}$). For a large BEC (b) the ^{40}K profile exhibits a pronounced hole in the trap center which we ascribe to a strong localized loss process due to the interaction with the BEC. These losses are too fast for transport in the slow axial direction to be able to continuously maintain the undisturbed density profile by refilling the center of the trap from the outer regions. As we shall see, this fast loss (e. g. from Fig. 2.19 $\leq 10\,\mathrm{ms}$) is a signature of the mean field collapse of the mixture. After the collapse, we observe that ^{40}K distributions sharply peaked in the center remain stable for relatively long timescales exceeding 100 ms (c). A Fermi-Dirac fit to the data is shown as a dotted line for comparison. We attribute this peaked distribution to the Fermi-Bose attraction creating an additional trapping potential for the fermions ("mean field dimple" in the magnetic trap potential).

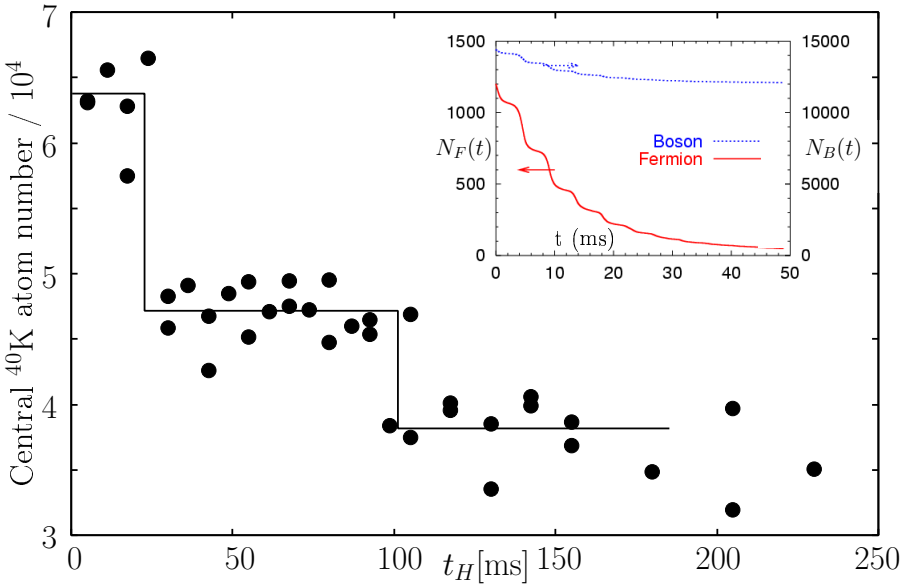

Figure 2.19: Decay of the fermionic component in a slightly overcritical mixture. The first sudden drop is the initial collapse; the second drop is one "revival" of the collapse. The line is to guide the eye. For comparison, the inset shows results from dynamical modelling of the collapse (taken from [86]).

The strong depletion of the Fermi cloud in the center is accompanied by rapid particle loss of approximately two thirds of the fermionic particle number. We ascribe this loss to the mean field collapse of the mixture. Beyond critical particle numbers, the mean field potential is no longer balanced by the repulsive interaction in the ^{87}Rb BEC and the outward bound Fermi pressure, so that the part of the mixture overlapping with the BEC contracts rapidly to such large densities that enormous 3-body losses reduce the overall particle number in this region to an undercritical value. It is therefore natural that we observe the collapse in the vicinity of strong contracting mean field effects of the Bose gas on the fermionic distribution (see Fig. 2.18a) and c); cf. [87]). Although the ensemble is

out of equilibrium and shows very complex dynamics *after* this rapid loss [86], one can intuitively imagine that the Fermi distribution depleted in the center of the cloud is refilled from the outside parts of the sample on a timescale related to the axial trap frequency, possibly leading to repeated local collapses, until the mixture will become undercritical and reestablish an equilibrium situation. In order to observe this phenomenon, we have prepared a mixture where the bosonic part ($\approx 10^7$ atoms) has only started condensing and observed the evolution of the ensemble at constant evaporation frequency. As the condensate grows due to the mild remaining evaporative cooling, it reaches the critical particle number of $N_B = 1.2 \cdot 10^6$. Due to the near-equilibrium situation before, the collapse now only leads to a relatively small loss in total particle number but is still clearly visible in the ^{40}K atom number integrated over the central part of the TOF image as shown in Fig. 2.19. After the first collapse, this number remains constant for some time and then drops abruptly again[8]. Such "revivals" of the collapse have been predicted in a recent numerical analysis of the collapse dynamics ([86], see inset in Fig. 2.19), although in a spherically symmetric configuration with $\nu_{\mathrm{Rb}} = 100\,\mathrm{Hz}$.

[8]The refilling is not visible for the chosen TOF of 3 ms and integration area of $83\,\mu\mathrm{m} \times 62\,\mu\mathrm{m}$.

Chapter 3

A "magic" optical dipole trap

Although most experiments on quantum degenerate atomic gases rely in some way on magnetic trapping for evaporative cooling, optical dipole traps offer a couple of important advantages: First, the geometry of an optical dipole trap can be varied easily, allowing for rapid switching between 1D-like geometries and spherically symmetric traps. Second, far off-resonance optical dipole traps confine atoms (almost) irrespective of their spin state and allow the use of an external magnetic field as a completely independent parameter. The latter enables a large variety of experiments including the use of Feshbach resonances for the control of interactions in ^{40}K and ^{87}Rb mixtures (see chapter 4) and molecule formation (see chapter 7).

Apart from these very general considerations, the shallow optical dipole trap described in the following chapter has allowed us to overcome one of the main limitations in experiments dealing with two different atomic species with different mass m. In general, different atomic species simultaneously confined in the same magnetic or optical trap will experience different gravitational sags. Depending on the chosen trapping frequencies in the direction of gravity, the differential gravitational sag can easily adopt values on the order of 100 μm to 1 mm. The reduced overlap of the two simultaneously confined clouds impedes any experiment relying on interacting mixtures. The issue of a different gravitational sag becomes especially important when working with weakly confined low-density mixtures which are required when preparing atomic clouds with the ultimate goal of loading them into optical lattices. Many experiments on atoms in optical lattices rely on lattice site occupation numbers on the order of 1 and hence require the preparation of atomic clouds with densities on the order of the lattice site density which is given by $n_{\mathrm{Lattice}} = (2/\lambda)^3$ and is on the order of $10^{13}/\mathrm{cm}^3$ in our experiment.

To overcome the above-mentioned limitations, a shallow optical dipole trap for the simultaneous trapping of quantum degenerate Fermi-Bose mixtures of ^{40}K and ^{87}Rb has been realized in our experiment. The optical dipole trap is designed to compensate for the differential gravitational sag between ^{40}K and ^{87}Rb. It relies on a careful choice of the dipole laser wavelength responsible for the confinement in the direction of gravity. This "magic"[1] optical dipole trap assures optimal overlap of the two different atomic species

[1] We call the wavelength necessary for compensation of the differential gravitational sag between ^{40}K and ^{87}Rb "magic" wavelength. Note that the term "magic" wavelength is used differently depending on context.

even in cases where low densities and low trapping frequencies are required.

In the following chapter, I will start with a short review on optical dipole traps followed by a brief reminder on the role of the gravitational sag for atoms confined in harmonic potentials. After some design considerations for the "magic" optical dipole trap for ^{40}K and ^{87}Rb, the "magic" wavelength will be derived theoretically and compared to a measurement in our experiment. The chapter will conclude with characterization measurements of the "magic" dipole trap.

3.1 The optical dipole force

Atoms placed in an inhomogeneous light field experience a force which, depending on the detuning of the field relative to the atomic transitions, points in or against the direction of the light field gradient. In the late sixties, it has been pointed out that this force can be used to design traps for atoms [88, 89]. The first optical dipole trap for neutral atoms has been demonstrated by Steve Chu and coworkers in 1986 [90]. Twelve years later, Stamper-Kurn and coworkers realized the first optically trapped quantum degenerate gas [91]. Today, these Far Off Resonance Traps (FORTs) are a standard tool in ultracold atom laboratories worldwide (for a review see [92]).

The simplest FORT operates with red-detuned light and consists of one polarized laser beam focused to a waist of typically a few ten to hundred microns. In this case, atoms are attracted into regions of high intensity. In a semiclassical simplified picture this can be understood as follows: In a two-level atom with resonance frequency ω_0, the inhomogeneous light field with frequency (ω_{Laser}) will induce an oscillating dipole moment. Due to the red detuning of the light field relative to the atomic transition ($\omega_{\mathrm{laser}} < \omega_0$), the oscillating dipole moment will oscillate in phase and atoms are attracted to the regions of high intensity. However, in case of a blue detuned light field $\omega_{\mathrm{laser}} > \omega_0$ the induced dipole moment will oscillate out-of-phase and atoms are repelled from regions with high intensity.

In a dressed-state picture of the atom-field interaction, one obtains the following expression for the potential $V(\vec{r})$ felt by a two-level atom [93]

$$V(\vec{r}) = -\frac{3\pi c^2}{2\omega_0^2}\left(\frac{\Gamma}{\omega_0 - \omega_{\mathrm{L}}} - \frac{\Gamma}{\omega_0 + \omega_{\mathrm{L}}}\right) \cdot I(\vec{r}), \tag{3.1}$$

where Γ is the linewidth of the transition and $I(\vec{r})$ is the intensity of the confining laser light.

As $V(\vec{r}) \propto I(\vec{r})$, the geometry of the realized trap is determined by the intensity distribution of the confining laser light. The most common and well-established technique is to confine atoms in the focus of a red-detuned Gaussian laser beam. In the case of a laser beam with power P propagating in the z direction, the intensity distribution is given by

$$I(r,z) = \frac{2P}{\pi w(z)^2} \exp\left(-2\frac{r^2}{w(z)^2}\right) \tag{3.2}$$

with the z-dependent focus $w(z) = w_0\sqrt{1 + (z/z_R)^2}$, where the Rayleigh range z_R is the characteristic length scale in the direction of propagation and w_0 the waist at $z = 0$. In

the case of ultracold atomic clouds, the radial and axial extension of the cloud is typically much smaller than the characteristic length scales of the potential w_0 and z_R. The intensity distribution can therefore be expanded in a Taylor series to

$$I(r,z) \approx \frac{2P}{\pi w(z)^2}\left(1 - 2\left(\frac{r}{w_0}\right)^2 - \left(\frac{z}{z_R}\right)^2\right). \tag{3.3}$$

Combining equations 3.1 and 3.3, a cylindrically symmetric harmonic potential is obtained, characterized by the (usually steep) radial and (weak) axial trap frequencies:

$$\omega_r = \tfrac{2}{w_0}\sqrt{-\tfrac{V(0)}{m}} \quad \text{and} \quad \omega_r = \tfrac{1}{z_R}\sqrt{-\tfrac{2V(0)}{m}}. \tag{3.4}$$

The dipole potential of a Gaussian laser beam both for the case of red-detuned and blue-detuned light in the $z = 0$ plane is illustrated in Fig. 3.1. Whereas the potential has a minimum in the case of red-detuned light, it has a maximum for blue-detuned light and is therefore repulsive in the latter case.

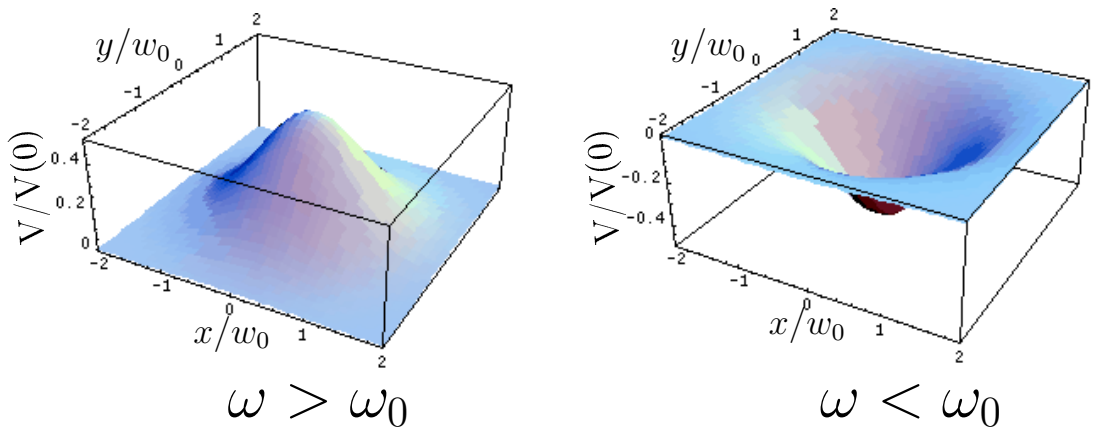

Figure 3.1: Dipole potential of a Gaussian laser beam for both, red-detuned and blue-detuned laser light for $z = 0$.

Based on equation 3.1, there are two knobs for increasing the potential, either through increasing the intensity or by decreasing the detuning. At first sight, it could seem favorable to choose a very small detuning in order to minimize the necessary laser intensity at a fixed potential depth. However, photons scattering off atoms induce heating and loss processes for the atoms confined in optical dipole traps. The scattering rate Γ is given by

$$\Gamma_{\text{scatt}} = \frac{3\pi c^2}{2\hbar\omega_0^3}\left(\frac{\omega_{\text{Laser}}}{\omega_0}\right)^3\left(\frac{\Gamma}{\omega_0 - \omega_{\text{Laser}}} + \frac{\Gamma}{\omega_0 + \omega_{\text{Laser}}}\right)^2 I(\vec{r}). \tag{3.5}$$

and decreases with $1/(\omega_{\text{Laser}} - \omega_0)^2$ as compared to the potential depth which decreases only linearly with the detuning (cf. equation 3.1). It is therefore favorable to choose the detuning of the dipole trap frequency ω_{Laser} relative to the atomic transition ω_0 as large as practically feasible to suppress inelastic loss processes as much as possible.

Multilevel atoms The above simplified picture for the case of a two-level atom can easily be extended to the multilevel case [93]. In the case of a multilevel atom prepared in a specific ground state $|g\rangle$, coupling of the laser light to any transition to an excited state $|e\rangle$ has to be taken into account. The different contributions will then simply sum up to a dipole potential bearing in mind the coupling strength of the different transitions. In the case of alkali atoms, the most important contributions to the dipole potential of a red-detuned dipole trap are given by the D_1 and the D_2 line, i.e. the transitions $n^2S_{1/2} \rightarrow n^2P_{1/2}$ and $n^2S_{1/2} \rightarrow n^2P_{3/2}$ respectively. In the case of ^{87}Rb, these two transitions occur at 795 nm and 780 nm, respectively, whereas the corresponding transitions in ^{40}K have a slightly higher energy with wavelengths of 769 nm and 766.7 nm, respectively.

3.2 Gravitational sag

The trapping potential formed by external magnetic or optical fields is modified due to the presence of the gravitational potential. In general, gravity does not change the shape of the trapping potential, however, the center of the confining trap, either optical or magnetic, is shifted away from the center of the unperturbed trapping potential. This has important consequences for the overlap of two simultaneously confined species. Assuming harmonic trapping for the atoms and including the effect of gravity, the trapping potential for the atoms is given by

$$V(\vec{r}) = \frac{1}{2}m\omega^2 y^2 + mgy. \tag{3.6}$$

Searching for the minimum of the external potential, one immediately obtains the gravitational sag y_{sag} to be given by

$$y_{\mathrm{sag}} = -g/\omega^2 \tag{3.7}$$

At first glance, the gravitational sag seems to be independent of the mass of the confined atoms and therefore independent of the atomic species; however, in optical traps, the harmonic trapping frequency ω is proportional to $\sqrt{-V(0)/m}$ (cf. equation 3.4) where $V(0)$ is the depth of the external potential and m the mass of the confined species. The decisive parameter is therefore given by the ratio of the depth of the trapping potential and the atomic mass.

Fig. 3.2 (solid red line) shows the gravitational sag of an atom confined in a harmonic potential for typical values of the trapping frequency of the external confinement. As can be seen from the figure, depending on the chosen trapping frequency, the gravitational sag can easily reach values on the order of $10 - 1000$ μm.

Let us now consider the case relevant for our experiments: Simultaneous confinement of both ^{40}K and ^{87}Rb in a far-off resonance dipole trap. Typical optical dipole traps for alkali atoms operate at a wavelength of round about 1 μm. The detuning of the laser light relative to the D_1 and D_2-line of both species is in this case comparable and hence, the trap depth for both species in a good approximation equal. In this case, the differential gravitational sag between the two species is determined solely by the mass ratio of the two species. Fig. 3.2 (blue dashed-dotted line) shows a plot of the differential gravitational sag between ^{40}K and ^{87}Rb as a function of the ^{87}Rb trapping frequency in the specific case described above. From the figure, it is obvious that the differential gravitational sag

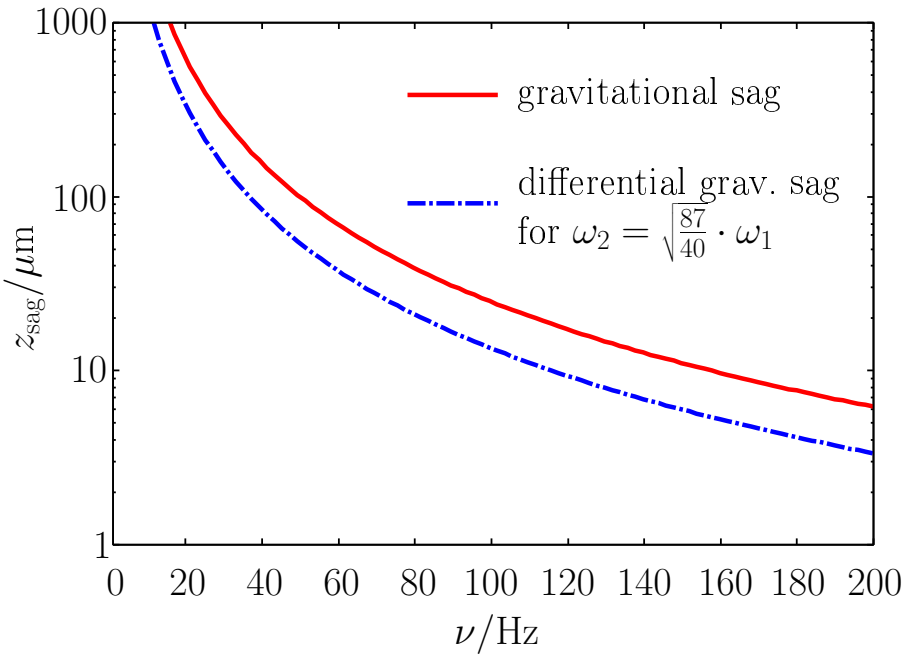

Figure 3.2: Gravitational sag as a function of the trapping frequency of the external harmonic confinement (solid line) and differential gravitational sag between two species with $m_1 = \frac{87}{40} \cdot m_2$ experiencing the same trapping potential $V_0^{m_1} = V_0^{m_2}$ (dashed-dotted line).

significantly reduces the overlap between the two simultaneously confined species. At a still moderate confinement of about $\omega = 2\pi \cdot 50\mathrm{Hz}$, the differential gravitational sag is approximately 50μm which is a factor of 5 larger than the Thomas-Fermi-Radius of a Bose-Einstein condensate of 10^5 atoms and comparable to the spatial extension of a Fermi gas of the same atom number at $T = 0$.

3.3 Dealing with the gravitational sag

To avoid issues with poor overlap in mixtures of ^{40}K and ^{87}Rb, an optical dipole trap has to be designed which minimizes the differential gravitational sag between the two components and hence allows weak (mean) harmonic confinement and the realization of low-density clouds. Based on the above considerations two routes seem possible:

1. The first option is to realize a strongly asymmetric trapping potential with large trapping frequency ω_{grav} and tight confinement in the direction of gravity and trapping frequencies $\omega_\perp$ as weak as possible in the two directions perpendicular to the gravitational force while at the same time keeping the mean harmonic trapping frequency $\omega = \left(\omega_{\mathrm{grav}}\omega_\perp^2\right)^{1/3}$ on the order of a few ten Hz. Such a geometry can be achieved using cylindrical lenses. However, due to the strong confinement in the direction of gravity, the aspect ratio of the trap will be necessarily very high which is unfavorable for the efficient loading of optical lattices.

2. Another option is to allow for a possibly *large* but *equal* gravitational sag of both components, eliminating the *differential* gravitational sag completely irrespective of the chosen trapping frequencies in the direction of the gravitational force. Following section 3.2, this can be achieved by realizing the same *trapping frequencies* for both species (cf. equation 3.7) which one obtains through a suitable choice of the dipole laser wavelength (cf. section 3.4). A decisive advantage of this second approach is that it does not rely on a specific trap geometry and even spherically symmetric clouds can be realized.

We have decided to follow the second route. The idea of the "magic" dipole trap is the following: The trap is operated as a crossed dipole trap with two independent laser beams propagating in z and x direction, respectively (both perpendicular to gravity, see Fig. 2.1). One of the beams (the so-called "magic" beam, x-direction) is operated at the "magic" wavelength of $\approx$ 807nm, where the trapping frequencies for ^{40}K and ^{87}Rb are equal, thus the gravitational sag is the same for the two components (cf. section 3.4 for a theoretical prediction and section 3.7 for a measurement of the "magic" wavelength). This beam is held at a fixed intensity and barely compensates for gravity. In addition, this beam ensures confinement in the z direction.[2] A second beam of the crossed trap is derived from our lattice laser and operates at a wavelength of $\lambda = 1.03$ μm. It is adjusted such that the center of the beam coincides with the equilibrium position of the atoms in the "magic" beam. This beam ensures confinement in the two remaining directions: the x direction and the direction of gravity (y-direction).

3.4 Theoretical calculation of the "magic" wavelength

Following the discussion of section 3.2, the "magic" wavelength of an optical dipole trap in which the gravitational sag of both ^{40}K and ^{87}Rb is equal is determined by the condition that the radial trap frequencies for both components are equal:

$$\frac{\omega_{\mathrm{K}}}{\omega_{\mathrm{Rb}}} \equiv 1. \tag{3.8}$$

This condition is of course only adequate in case that the assumption of harmonic trapping and thus, the reasoning of section 3.2 is justified. For clouds of ultracold atoms confined in optical dipole traps, harmonic trapping can be assumed as long as the thermal energy of the ensemble is much smaller than the depth of the confining potential. Combining condition 3.8 with the expression for the radial harmonic trapping frequency of equation 3.4, the condition for equal gravitational sag between ^{40}K and ^{87}Rb reads as follows:

$$V_{\mathrm{K}}(0)/V_{\mathrm{Rb}}(0) \equiv m_{\mathrm{Rb}}/m_{\mathrm{K}} \tag{3.9}$$

which means that the ratio of depths of the optical dipole potential has to be inversely proportional to the ratio of masses.

Adapting equation 3.1 to the multiplet structure of real atoms, one can calculate the depth of the optical dipole potential and the associated trap frequencies (see equation 3.4)

[2] Due to the large Rayleigh range of the magic beam, contributions of the magic beam to the trap frequency in x-direction are negligible. Contributions in the direction of gravity are also negligible due to the vanishing curvature of the magic beam at the position of maximum gradient $r = w_0/2$.

as a function of the dipole laser wavelength. As already mentioned in section 3.1, the most important contributions to the dipole potential of a red-detuned dipole trap in alkali atoms are given by the D_1 and the D_2 line. As the considered range of detuning of the dipole trap from the relevant atomic transitions of both ^{40}K and ^{87}Rb is on the order of > 5 nm and therefore large compared to the hyperfine splitting of both the ground state $^2S_{1/2}$ and the involved excited states $^2P_{1/2}$ and $^2P_{3/2}$, one can neglect the hyperfine splitting. To obtain the correct dipole potentials, one has to account only for the fine structure of the atoms. We therefore sum up the contributions of both the D_1 and D_2 lines.

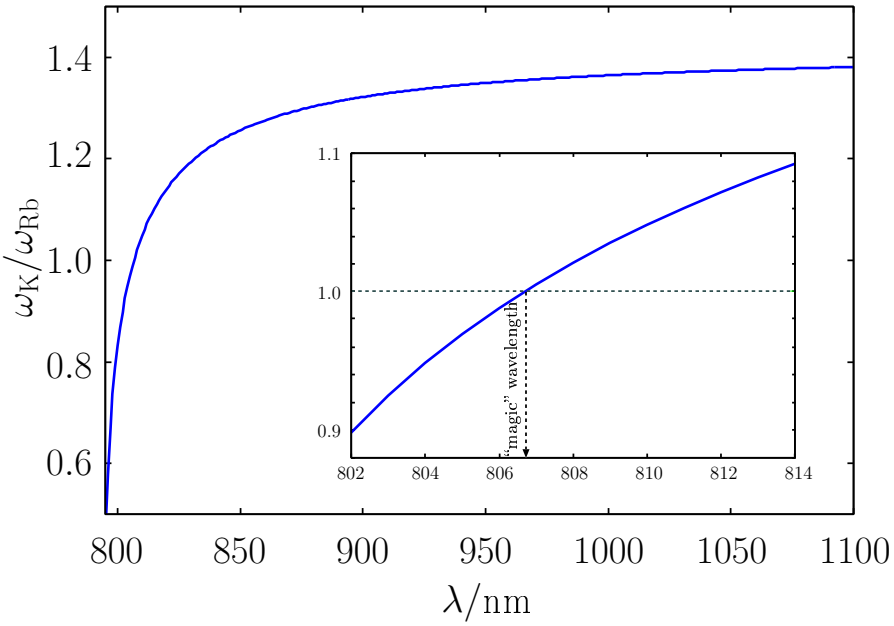

Figure 3.3: Ratio of trapping frequencies for ^{40}K and ^{87}Rb ω_K/ω_{Rb} as a function of the dipole laser wavelength. Note that the condition $\omega_K/\omega_{Rb} \equiv 1$ defines the "magic" wavelength where the differential gravitational sag is zero.

Fig 3.4 shows the calculated ratio of the radial trap frequency of ^{40}K and ^{87}Rb as a function of the dipole laser wavelength. Equal harmonic trapping frequencies (see condition 3.8) are obtained at a wavelength of 806.7 nm. This is the wavelength where the differential gravitational sag of ^{40}K and ^{87}Rb in a red-detuned optical dipole trap of Gaussian focus is zero. Below the "magic" wavelength, the ratio of trapping frequencies drops below 1, corresponding to a tighter confinement of ^{87}Rb than for ^{40}K, whereas the opposite is true above the "magic" wavelength. For large red-detunings, corresponding to wavelengths on the order of 1 μm, the ratio of trap frequencies asymptotically assumes the value of $\sqrt{87/40}$ which is determined by the mass ratio of the two species. In this case, the potential depths for both species are equal. In Fig. 3.4, the differential gravitational sag is plotted as a function of the dipole laser wavelength for a couple of fixed trapping frequencies. Note that the trapping frequency has been fixed for the ^{87}Rb component to various values whereas the trapping frequency of ^{40}K varies according to Fig. 3.4 as a function of wavelength. For any assumed trapping frequency, the differential gravitational sag shows a zero crossing at the "magic" wavelength whereas below and above the "magic"

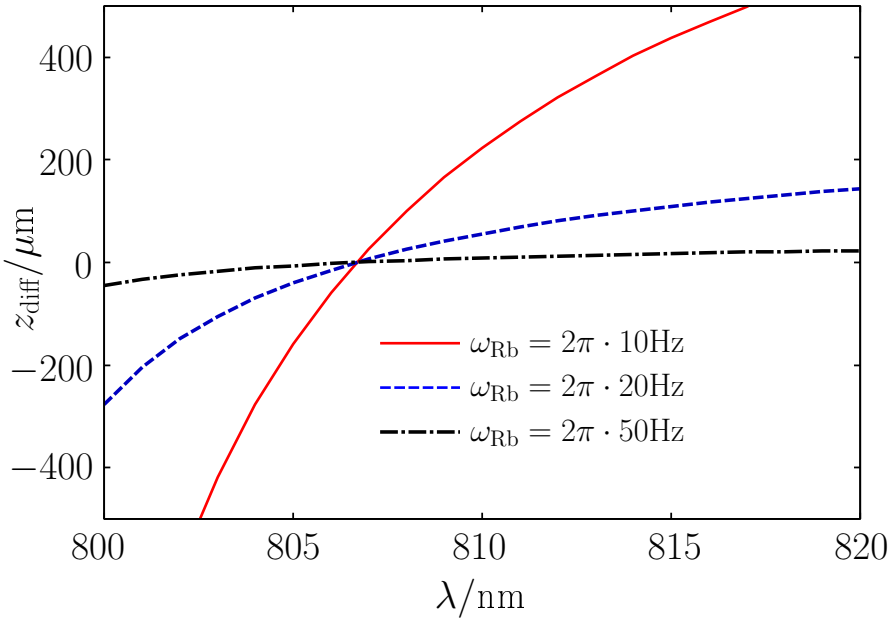

Figure 3.4: Differential gravitational sag as a function of the dipole laser wavelength for various fixed trapping frequencies for ^{87}Rb. Independent of the trapping assumed trapping frequency, the differential gravitational sag shows a zero crossing at the "magic" wavelength of 806.7 nm. Positive differential gravitational sag above the magic wavelength describes cases where the Rubidium component has a larger gravitational sag than the Potassium component. Negative differential gravitational sag describe the opposite case which is true for wavelengths below the magic wavelength.

wavelength the differential gravitational sag is dependent on the trapping frequency of the external harmonic confinement. Note that a positive differential gravitational sag describes cases where the ^{40}K component is above the ^{87}Rb component in the trap whereas negative differential gravitational sag accounts for the opposite case.

The existence of the "magic" wavelength for ^{40}K and ^{87}Rb in a red-detuned optical dipole trap is only due to the fact that the D_1 and D_2 transitions of rubidium at 795 nm and 780 nm respectively are red-detuned relative to the corresponding transitions in potassium which occur at 769.9 nm and 766.7 nm. Red-detuned dipole traps therefore have a larger detuning from the potassium transitions than the corresponding rubidium transitions and are correspondingly deeper for the rubidium component than for the potassium component. This allows the compensation of the twice as large gravitational potential for rubidium.

3.5 Spin and polarization dependence

So far, the theoretical analysis of the magic wavelength has been done under the assumption that we operate the dipole trap with linearly polarized (π^0) light. Only in this case, the spin dependence of the dipole potential can be neglected. However, in the current geometry of our experiment, it has been most practical to shine in the magic beam along

the quantization axis (x-axis, see Fig. 2.1). Since true π^0 light is impossible in this geometry, the one remaining possibility to provide spin-independent trapping is to use linearly polarized light. For any deviation from linearly polarized light, the dipole force is thus spin dependent. For large detuning of the dipole laser light relative to the hyperfine splitting, the dipole potential is given by [92]

$$V_{pot}(\vec{r})\,[F, m_F] = \frac{\pi c^2 \gamma}{2\omega_0^3}\left(\frac{1-\mathcal{P}g_F m_F}{\omega_L - \omega_{0,D_1}} + \frac{2+\mathcal{P}g_F m_F}{\omega_L - \omega_{0,D_2}}\right) I(\vec{r}) \tag{3.10}$$

where $\mathcal{P}$ denotes the laser polarization ($\mathcal{P} = \pm 1, 0$ for $\sigma^{\pm}$ and π^0 polarization) and g_F is the Lande-factor. For convenience, the counter-rotating terms have not been written down although, they have been considered in the calculations. In the case of linear polarization, equation 3.10 reduces to the equation 3.4, and the dipole force is independent of the chosen spin state, yielding a theoretical "magic" wavelength of 806.7nm.

This picture changes when operating the dipole trap with elliptically Polaris ed laser light characterized by the ellipticity ϵ. In this case, the coupling strength of the dipole laser light is different for the different spin states and depends strongly on the chosen polarization. This is illustrated in figure 3.5 which shows the "magic" wavelength for ^{40}K and ^{87}Rb as a function of $\xi = \tan^{-1}\epsilon$ of the laser light for various spin mixtures of ^{40}K and ^{87}Rb. Apart from the spin mixture used for sympathetic cooling in the magnetic trap and used for the measurement of the magic wavelength of section 3.7 (^{87}Rb in the $|F = 2, m_F = 2\rangle$ state and ^{40}K in the $|F = 9/2, m_F = 9/2\rangle$ state), any stable mixture with ^{87}Rb being in the $|F = 1, m_F = 1\rangle$ absolute ground state and ^{40}K in an arbitrary Zeeman substate of the $|F = 9/2, m_F\rangle$ ground state manifold has been considered. Note that the combinations $|F = 9/2, m_F = -9/2\rangle \otimes |F = 1, m_F = 1\rangle$ and $|F = 9/2, m_F = -7/2\rangle \otimes |1, 1\rangle$ have been used for the molecule and Feshbach resonance experiments of chapter 7 and 4.

3.6 The choice of experimental parameters

As outlined in section 3.3, the magic trap is operated as a crossed dipole trap with the intensity of the "magic" beam held fixed merely compensating for gravity and the second beam at $\lambda = 1.03$ μm adjusted to coincide with the equilibrium position of the atoms in the magic beam and providing confinement in the direction of gravity and perpendicular to the direction of propagation of the "magic" beam. The magic beam is derived from a Ti:Sa laser which allows tuning of its wavelength over several ten nanometers around the predicted "magic" wavelength of 806.7 nm.[3] The second beam has been derived from our lattice laser. Fig. 3.6 shows the overlapping scheme for the crossed dipole trap. Both laser beams propagate horizontally but orthogonal one to another. We prepare linear polarization for both laser beams, realizing π^0 polarization for the 1030nm beam relative to the quantization axis and a superposition of $\sigma^{\pm}$ light for the magic beam. The first laser beam (at 1030 nm) is overlapped with the main detection axis of our experiment (see Fig. 2.1, z-axis) using a dichroic mirror. The "magic" beam (along the x-axis) is overlapped with the horizontal MOT axis and one of the lattice laser beams using an

[3]The Ti:Sa has been provided by our colleagues from the Spinor BEC experiment. Light from the Ti:Sa has been guided with a 25m fiber from the neighboring room to our lab. Thank you!

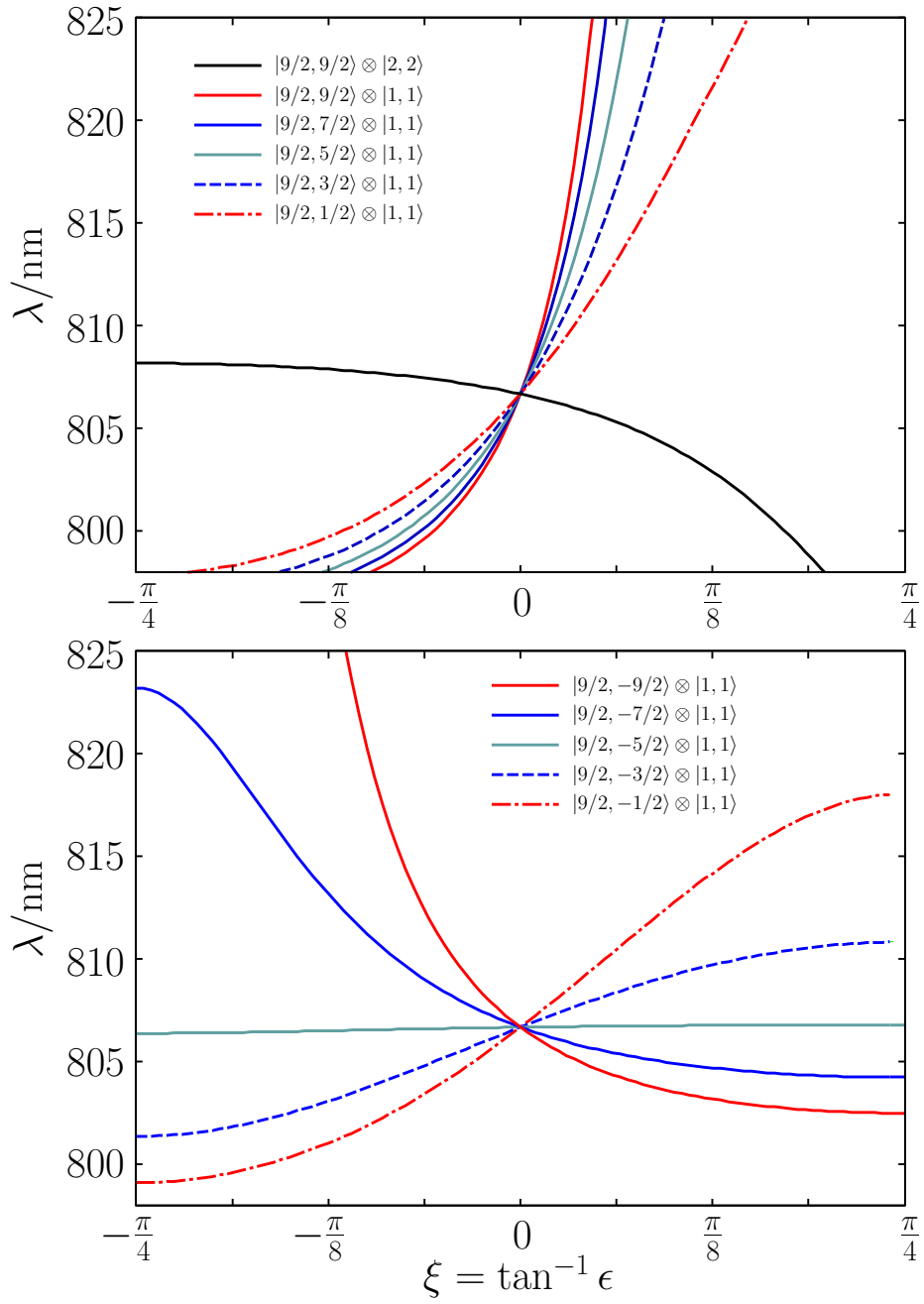

Figure 3.5: Spin and polarization dependence of the magic wavelength. The magic wavelength for the spin combinations $|F = 2, m_F = 2 > \otimes |F = 9/2, m_F = 9/2 >$ and $|F = 1, m_F = 1 > \otimes |F = 9/2, m_F >$ have been calculated as a function of ellipticity of the laser light.

additional dichroic mirror AR coated for 767 nm and 780 nm and HR coated for 830nm. The mirror is operated at $> 45°$ to shift the HR-edge of the mirror to somewhat lower

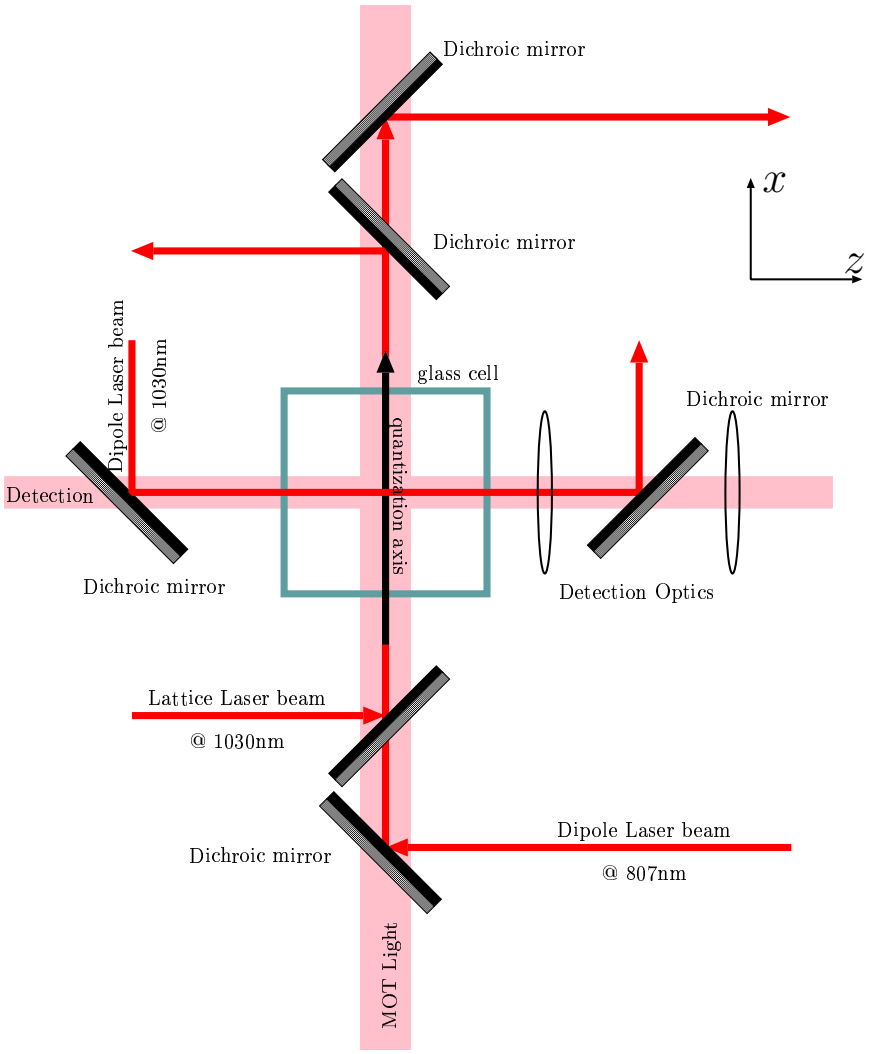

Figure 3.6: Overlapping scheme for the magic dipole trap.The magic beam is overlapped with one lattice axis and the MOT axis whereas the second beam at 1030nm is overlapped with the detection axis.

wavelength needed for the reflection of the magic beam.[4]

The magic beam focus has been chosen to allow for trapping frequencies below 100 Hz even under the influence of the gravitational potential. Neglecting the effect of gravity the above requirement is trivial to fulfil since the intensity of the dipole laser beam can be chosen arbitrarily weak realizing trapping frequencies even below 1 Hz independent of the chosen focus. However, when gravity is taken into account, the combination of laser focus and intensity (determining the trapping frequency) has to be chosen to provide at least the force necessary for the compensation of the gravitational force. The gradient of the dipole

[4]The mirror was produced by Laseroptik Garbsen for the neighboring BEC experiment where HR for 830 nm and AR for 780 nm is needed. We have used the mirror somewhat beyond specifications. However, choosing an angle slightly larger than the 45°, the reflection at 805 nm was still larger than 90%.

trapping potential is largest at $r = w_0/2$ (cf. Fig. 3.8). In order to hold the atoms against gravity, the gradient of the dipole trapping potential at this position has to be at least as large as the gravitational force which is given by mg. Fig. 3.7 shows the required power

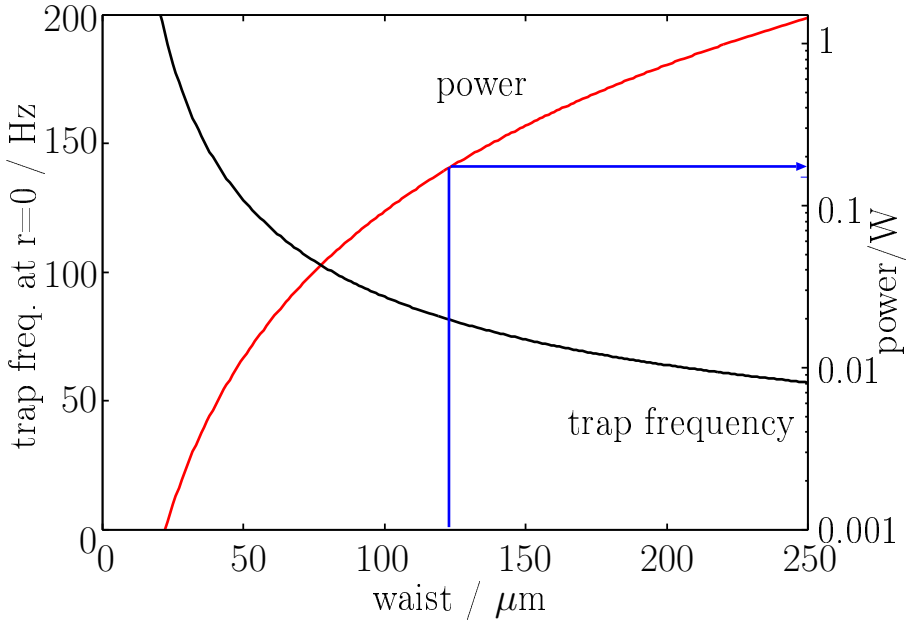

Figure 3.7: Required power as a function of the chosen dipole trap waist for compensation of the gravitational force at $z = 0, r = w_0/2$, assuming the magic wavelength of 806.7nm. In the same diagram, the hypothetical harmonic trapping frequency for these dipole trap parameters is shown. In our experiment, we have chosen $w_0 \approx 120$ μm allowing for trapping frequencies of ≈ 80 Hz.

as a function of the chosen dipole trap waist for compensation of the gravitational force at $z = 0, r = w_0/2$, assuming the magic wavelength of 806.7nm. In the same diagram, we have plotted the hypothetical radial harmonic trapping frequency for these dipole trap parameters, this time evaluated at $r = z = 0$. As can be seen from the figure, for a dipole trapping frequency in the direction of gravity below 100 Hz, a waist of 100 μm is required along with a power of > 100 mW. Estimating the maximal available power for the dipole trap after beam preparation and fiber coupling below 200 mW , we have chosen a beam waist of ≈ 120 μm corresponding to a radial trap frequency of ≈ 80 Hz at $z = r = 0$ when the dipole trap power is exactly chosen to compensate for gravity. Note that the actual trap frequency at $z = 0, r \neq 0$ certainly differs somewhat from the $z = r = 0$ value due to the decreasing curvature of the Gaussian beam dipole potential with increasing r (see Fig. 3.8) and it is therefore hard to predict the actual trap frequency.

3.7 Measurement of the magic wavelength

Based on the criterion of equation 3.9, the magic wavelength of ^{40}K and ^{87}Rb has been determined experimentally by a measurement of the ratio of the radial trapping frequen-

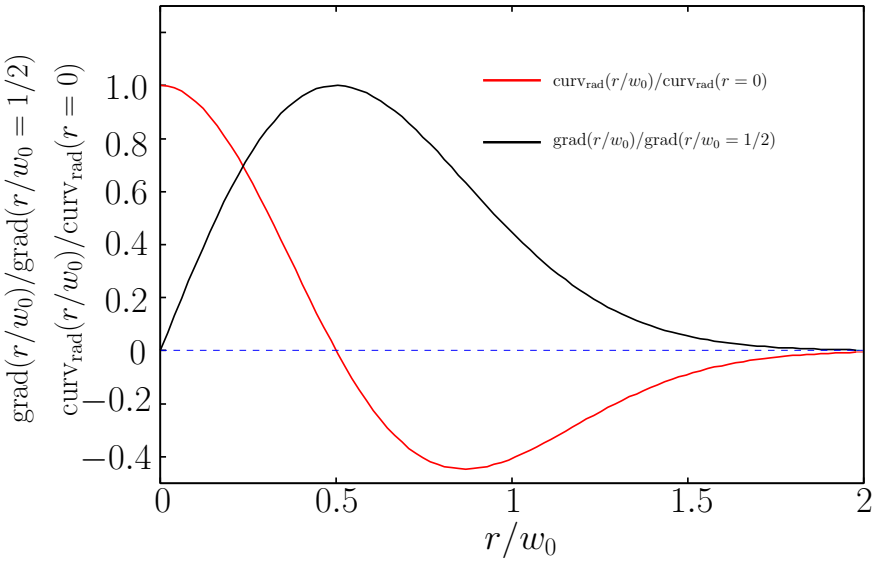

Figure 3.8: Potential gradient (acceleration) $\mathrm{grad}_{\mathrm{rad}}(r)$ of a typical Gaussian beam profile dipole potential and the curvature $\mathrm{curv}_{\mathrm{rad}}(r)$ as a function of the radial coordinate r. Note that the potential gradient and the curvature have been normalized differently: The potential gradient has been normalized to its maximum value at $r = w_0/2$ whereas the curvature has been normalized to its value at $r = 0$.

cies of the simultaneously confined species as a function of the dipole laser wavelength. In order to measure the trap frequency of either ^{40}K or ^{87}Rb in the optical dipole trap formed solely by the Gaussian intensity profile of the magic beam, ultracold mixtures of potassium and rubidium have been prepared in our magnetic trap in a spin mixture of $|F = 9/2, m_F = 9/2\rangle$ and $|F = 2, m_F = 2\rangle$, respectively. Shortly before reaching quantum degeneracy, the magic beam of the crossed optical dipole trap has been ramped up and the ensemble has subsequently been transferred into this dipole trap. At this point either the rubidium or the potassium component has been removed from the trap to avoid interactions between ^{40}K and ^{87}Rb to distort the measurement. The remaining cloud has then been excited to a center of mass oscillation in the direction of gravity by a short switch off of the confining trap and a subsequent recapture. The center of mass oscillation of the ensemble in the focussed beam trap has then been recorded over approximately four to five oscillation periods and the oscillation frequency extracted from the measurement. The measurement of the radial oscillation frequency of rubidium and potassium has been repeated at four different wavelengths between 800 nm and 820 nm.

Fig. 3.9 shows the measured ratio of trapping frequencies as a function of the dipole laser wavelength along with the theoretical prediction. The measured "magic" wavelength of 807.9 nm differs from the theoretical prediction of 806.7nm by ≈ 1.2 nm. In addition, we experimentally observe a linear dependence of the ratio of trap frequencies as a function of the dipole laser wavelength, whereas theory predicts a square-root like behavior. For the calculation of the magic wavelength, both the rotating and counter-rotating terms of the D_1 and D_2-lines have been taken into account, whereas the influence of higher energy levels has been neglected. While the consideration of higher energy levels could somehow

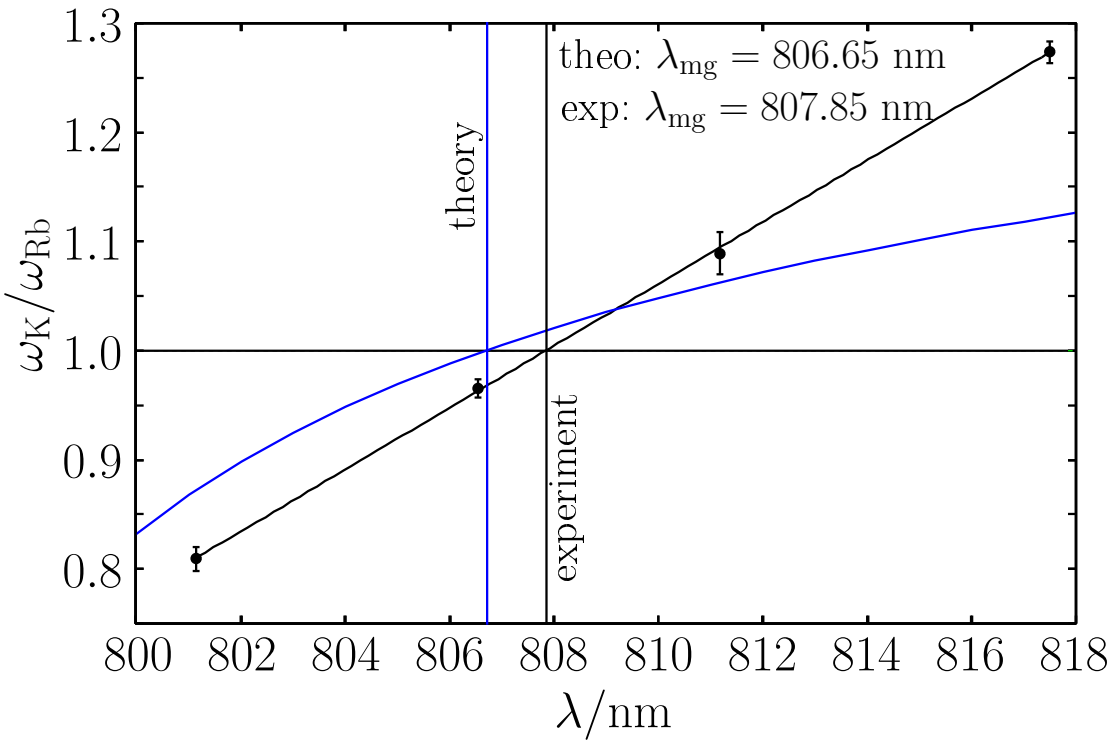

Figure 3.9: Comparison of the measured "magic" wavelength to the theoretical prediction. Whereas theory predicts a wavelength of 806.65nm, the measurement yields 807.85nm.

shift the calculated magic wavelength in either direction, it is not expected to significantly transform the general square-root behavior into the experimentally observed linear one. This linear behavior is possibly due to a systematic effect.

One possible source of systematic error is the gravitational sag itself. Let us consider the case $\lambda < \lambda_{mag}$: In this case, the gravitational sag for ^{40}K atoms is larger than the gravitational sag for ^{87}Rb atoms ($r_K > r_{Rb}$). Due to the decreasing curvature with increasing r, the ratio of trapping frequencies between potassium and rubidium ω_K/ω_{Rb} is then smaller than the theoretical value at $r = 0$. For $\lambda > \lambda_{mag}$, ^{87}Rb atoms experience a larger gravitational sag than ^{40}K atoms and the theoretical value for ω_K/ω_{Rb} is smaller than the experimental one. However, this effect cannot account for a systematic shift of the "magic wavelength", only for the square-root vs. linear behavior.

A second source of systematics is the polarization that we have prepared for the "magic" beam (see section 3.6) along with the dichroic mirror operated at $> 45°$ somewhat beyond specifications. We have tried to prepare mainly $s-$polarized light relative to the dichroic mirror axis, but a residual fraction of $p-$polarization up to $\approx 10 - 20\%$ is likely. The dichroic mirror introduces a wavelength dependent phase shift $\psi(\lambda)$ between the $s-$ and $p-$polarization. This phase shift varies between $> \pi/2$ at 820 nm and $< \pi/4$ at 800 nm, thereby introducing an imbalance between σ^+ and σ^- polarized light after reflection.[5] Starting with an intensity of s-polarized and p-polarized light $I_s = (1 - f)I_0$

[5]The values for the relative phase shift have been provided by calculations of Christian Petter (Laserop-

and $I_p = fI_0$ with $0 < f < 1$, assuming a phase shift of ψ between the two polarizations, the intensity of σ^+ and σ^- light after reflection at the mirror is given by

$$I_{\sigma^\pm} = \frac{I_0}{2}\left(1 \pm f \sin\psi(\lambda)\right) \tag{3.11}$$

which yields a wavelength dependent imbalance given by $\Delta I/I_0 = (I_{\sigma^+} - I_{\sigma^-})/I_0 = f \sin\psi(\lambda)$. The intensity imbalance at 807 nm is then approximately 17%, leading to a shift of the magic wavelength due to polarization issues of ≈ 1 nm, which is on the order of the observed shift with respect to the π calculation. The wavelength dependent phase shift might also be at the heart of the significantly different dependence of the theoretical trap frequency ratio compared to the measured dependence (square-root vs. linear).

3.8 Degenerate mixtures in the magic trap

Quantum degenerate mixtures in the magic trap are prepared starting from an evaporatively cooled purely magnetically trapped Fermi-Bose mixture of ^{40}K and ^{87}Rb in the $|9/2, 9/2> \otimes |2, 2>$ state. The evaporation ramp is stopped right at the phase transition point of the bosonic thermal cloud to a Bose Einstein condensate. At this point, the crossed dipole trap is ramped up using a linear ramp of 500 ms. Quantum degeneracy is achieved in the combined magnetic and optical potential in a final step of forced rf-induced evaporative cooling. In the next step, we realize purely optical trapping of the quantum degenerate mixture by carefully ramping down the confining inhomogeneous magnetic field within $50-100$ ms while at the same time increasing the bias field to ≈ 20 G to assure spin conservation throughout the ramp down process of the magnetic trapping potential. The ramp down process is usually accompanied by mild heating of the atomic clouds which is compensated for in a final step of purely optical evaporation. This last step of cooling is induced by decreasing the intensity of the 1030 nm beam by $20 - 40\%$ within a few hundred milliseconds. However, the magic beam is held at fixed intensity. Achieved particle numbers in the deeply degenerate regime are a few times 10^5 ^{87}Rb atoms in a condensate with no discernible thermal cloud and up to $1 \cdot 10^5$ fermionic atoms.

As mentioned above, the intensity of the magic beam is chosen to barely compensate for gravity. The trapping frequency of the magic beam for the ^{87}Rb component in z-direction is measured to be $\omega_z = 2\pi \cdot 50$ Hz. The intensity of the crossed beam is chosen to realize the same trapping frequencies for the ^{87}Rb component in y- and x-direction thereby realizing a shallow almost spherically symmetric trapping potential without facing issues with differences in the gravitational sag of the two components.

The realization of the magic trap has been an essential prerequisite both for the observation of tuning of interactions in the vicinity of heteronuclear Feshbach resonances (see chapter 4) and the engineering of heteronuclear molecules (see chapter 7).

tik Garbsen).

Chapter 4

Tuning of heteronuclear interactions

In the early days of ultracold quantum gases, a lot of interest in a particular atomic species was motivated by its static scattering properties; in the case of ^{87}Rb e. g., the moderately large background scattering length, combined with favorable collisional losses (and technical considerations such as cooling laser sources), is the main reason for the fact that the overwhelming majority of BEC experiments relies on ^{87}Rb these days. This picture changed dramatically with the advent of Feshbach resonances.

A Feshbach resonance is a phenomenon originally introduced in the context of nuclear physics [94]. In cold atomic gases, these resonance phenomena have been discussed since 1992, especially for Cs [95, 96] which at the time seemed to be the most promising candidate for the observation of BEC in a dilute atomic gas. A Feshbach resonance allows tuning of the interaction properties of an atomic gas from repulsive to attractive and vice versa. It occurs when the energy of the colliding atoms in an open channel resonantly couples to a quasibound molecular state in a closed channel. Such resonances have been suggested to be inducible via static electric fields [97], rf radiation [98], via far-resonant or near-resonant laser fields [99, 100] or via homogeneous magnetic fields [95, 96, 101, 102]. Nowadays, magnetically induced Feshbach resonances are a very versatile and common tool in cold atom laboratories. They occur when the magnetic moment of the bound state in the closed channel is different from the magnetic moment of the open channel and the energy of the bound state can thus be continuously tuned through the open channel dissociation limit.

The first observation of Feshbach resonances in cold atom scattering has been reported almost simultaneously by P. Courteille and coworkers in ^{85}Rb [10] and by S. Inouye and coworkers in a BEC of ^{23}Na [11]. Tuning of interactions was demonstrated by Inouye and coworkers in the vicinity of the resonance by a static homogeneous magnetic field. Magnetically induced Feshbach resonances have later been reported in almost any alkali atom: ^{6}Li [103] and ^{7}Li [104, 105], ^{23}Na [11], ^{40}K [106], ^{85}Rb [10, 107], ^{87}Rb [108] and ^{133}Cs [109]. Recently, optically induced Feshbach resonances have been reported in [110, 111].

The availability of an additional knob to tune the scattering length has had important consequences for the development of the field. On the one hand, the fact that interaction

parameters no longer have to be taken for granted has enabled new species to be condensed which would otherwise have been very difficult to nearly impossible, such as ^{85}Rb [112] or ^{133}Cs [113]. Tuning of interactions is needed in order to achieve efficient rethermalization in this case. On the other hand, a large class of experiments exploring degenerate gases had been studying the properties of the system in terms of atom numbers or trap frequencies, whereas in many situations the parameter which is physically interesting is the interaction, and Feshbach resonances allow this knob to be turned just by changing the magnetic field. ^{7}Li, for example, is a system with a strong attractive background interaction, allowing the production of BECs of only a few thousand atoms before the onset of collapse [8]. Phenomena like the collapse have first been observed by varying the atom number in the sample [114], thereby only indirectly affecting interactions through the density. Feshbach resonances allow these phenomena to be directly observed as a function of interactions.

Feshbach resonances have allowed to enter the regime of strongly correlated systems and have made a whole class of experiments possible which have no analogon in neighboring fields such as solid state physics. To name only one example, let us look at the BCS-BEC crossover in two-component Fermi gases interacting at a Feshbach resonance [12, 13, 14, 15, 16]. When the interaction in the sample is strong and repulsive, diatomic molecules can be formed and further cooled through evaporative cooling [115, 116]. These molecules can even form a Bose-Einstein condensate [117, 118], and when the interaction is subsequently varied from repulsive to strongly attractive, fermions pair up in momentum space and realize a BCS-like state of Cooper pairs. In fact, due to the Feshbach resonance, a continuous crossover from a molecular BEC to a fermionic superfluid can be realized. Apart from the BCS-BEC crossover, Feshbach resonances have been the key to success in ground breaking experiments such as solitons [105, 104], collapse [119], molecule formation [120, 121, 122, 123, 124, 125, 126, 127, 118, 24].

In any case, the impressively large variety of experiments relying on Feshbach resonances have exclusively made use of *homonuclear* Feshbach resonances, that is Feshbach resonances arising between spin states of a *single* atomic species. However, the study of *heteronuclear* Feshbach resonances in collisions between certain spin states of two *different* atomic species (either bosonic or fermionic) is still in its infancy. Heteronuclear Feshbach resonances have been identified for the first time in Fermi-Bose mixtures of ^{6}Li - ^{23}Na at MIT [36] and in ^{40}K-^{87}Rb at JILA [37]. The identification has been reported through increased inelastic collisions and atom loss at the resonance, but no tuning of interactions has been reported.

The control of heteronuclear interactions offers fascinating perspectives in Fermi-Bose mixed systems and Fermi-Fermi systems of different mass: In Fermi-Fermi systems, heteronuclear Feshbach resonances would open the way to the exploration of the BCS-BEC crossover in a two-species fermion mixture with unequal mass [128, 129]. In Fermi-Bose systems, a different and complementary approach to fermionic superfluidity has been suggested in which the interaction between fermionic atoms is provided by bosonic atoms taking over the role of phonons in the solid state superconductor [130, 131, 132, 28]. When loaded into three-dimensional optical lattices, a wealth of different phases with no equivalent in condensed matter systems have been predicted to exist [28, 26, 133, 134]. In addition, heteronuclear Feshbach molecules which have been produced for the first time within this thesis (see chapter 7) could be used as a starting point for the creation of polar molecules with novel anisotropic interactions. These polar molecules have bright perspec-

tives as sensitive probes for physics beyond the standard model, such as a measurement of the permanent electric dipole moment of the electron [34].

In this chapter, the first demonstration of the tunability of heteronuclear interactions in the vicinity of a Feshbach resonance arising between ^{40}K and ^{87}Rb will be presented. To provide evidence for tuning of interactions and thus a variation of the scattering length around these heteronuclear resonances, the interaction energy of the Bose-Einstein condensate coexisting with a quantum degenerate Fermi gas is measured in the vicinity of a heteronuclear Feshbach resonance. Additional and complementary information is gained from a measurement of interaction effects of the Fermi gas on an expanding Bose-Einstein condensate and vice versa. As a first application of heteronuclear Feshbach resonances, the phase diagram for harmonically trapped Fermi-Bose mixtures ranging from collapse for large attractive interactions to phase separation in the case of strong repulsive interactions [82] has been studied within this thesis. Tuning of interactions has subsequently been used for the first formation of ultracold heteronuclear molecules (see chapter 7).

The following chapter will start with a short review on the known properties and open questions concerning background scattering properties and Feshbach resonances in a Fermi-Bose mixture of ^{40}K and ^{87}Rb. I will then present loss measurements for the identification of the resonances and the first observation of a p-wave resonance in heteronuclear scattering. I will then discuss theoretically the influence of heteronuclear interactions, either attractive or repulsive, on the density distributions of harmonically trapped Fermi-Bose mixtures and discuss the instabilities occurring in the limit of strong interactions. Finally, I will present our measurements demonstrating tunability of heteronuclear interactions in the vicinity of a Feshbach resonance: Starting from the measurement of heteronuclear interaction effects in stable Fermi-Bose mixtures, I will show how we access the various phases (ranging from collapse to phase separation) of the harmonically trapped mixture. Parts of this chapter have been published in [2].

4.1 Feshbach resonances and background scattering properties

Historically, Fermi-Bose mixtures share a lot with the above development for homonuclear systems, and this thesis describes important steps from studies based on the background interaction to tunable interactions and heteronuclear molecule creation at Feshbach resonances. Below, I will give a "historical" perspective on our understanding of the background interactions in the case of ^{40}K and ^{87}Rb; this is intimately related to the identification of Feshbach resonances and their assignment to specific features in a collisional model, as we shall see.

The achievement of quantum degeneracy in a mixture of ^{40}K and ^{87}Rb by sympathetic cooling was first reported in 2002 by G. Roati and coworkers at LENS [75]. In these experiments, efficient rethermalization in the mixture of ^{40}K and ^{87}Rb has been reported, suggesting a large triplet scattering length $|a_{FB}| = 330^{+160}_{-100} a_0$ from the experimental data. In these measurements, the attractive character of the interaction as predicted by [135] has been confirmed by studies on the effect of the Fermi gas on the condensate's aspect ratio after time-of-flight [87]. Additional evidence for the attractive character of the interspecies interaction was given by the observation of a bimodal distribution of the fermionic cloud

after time-of-flight held together during expansion by the Bose-Einstein condensate [87]. From report on a mean-field collapse of the mixture by the LENS group at rather low particle numbers of $2 \cdot 10^4$ ^{40}K atoms and $1 \cdot 10^5$ ^{87}Rb atoms [81], the interaction between ^{40}K and ^{87}Rb was determined to be even stronger $a_{\mathrm{FB}} = -(395 \pm 15)a_0$ as a result of quantitative comparison of the experimental findings on the critical particle numbers for collapse with mean-field theory [84].

The observation of stable particle numbers above the reported critical particle numbers by the JILA group [85] and the preparation of stable mixtures of up to $1.2 \cdot 10^6$ ^{87}Rb atoms in the condensate and $7.5 \cdot 10^5$ ^{40}K atoms in this thesis along with the observation of a possibly excitation enhanced mean-field collapse of the mixture above these stable particle numbers suggested an upper limit on the scattering length of $-284a_0$ (see [35, 4] and chapter 2.9). This was confirmed by the first observation of heteronuclear Feshbach resonances along with a collisional model suggesting a triplet scattering length of $(-281 \pm 15)a_0$ [37]. The following extensive study of the magnetic-field locations of 13 interspecies resonances resulted in significantly different scattering background parameters for the interspecies s-triplet scattering length of $(-215 \pm 5)a_0$ between ^{40}K and ^{87}Rb [136, 137] and some differences in the assignment of $p-$ or $s-$wave character to the individual resonances (see table 4.1).

^{40}K$\otimes^{87}$Rb	Resonance position	$\Delta B_{\mathrm{exp}}{}^{1}$	l
$\|9/2, -9/2\rangle \otimes \|1, 1\rangle$	494.0 G (from [136])	-0.5 G	s [136]/p [37]
$\|9/2, -9/2\rangle \otimes \|1, 1\rangle$	514.2 G (from [136])	-0.5 G	p [136]/s [37]
$\|9/2, -9/2\rangle \otimes \|1, 1\rangle$	545.4 G (from [136])	-1.2 G	s [37, 136]

Table 4.1: Overview on the resonances that have been investigated within this thesis. Two of them have previously been predicted to exhibit either s- or p-wave character, depending on the collisional model. Experimental evidence for the p-wave character of the 515 G resonance has been reported in the measurements performed in this thesis.

In this thesis, we have concentrated our measurements on three resonances in the vicinity of 500 G (see table 4.1). When we started working on Feshbach resonances, there was no experimental evidence concerning the $s-$ or $p-$wave character of the individual features, and there were different assignments of the resonances. We have precisely determined the position of these resonances and have detected a systematic small shift compared to the previously observed resonance positions with consequences for the interaction parameters (see section 4.2.4.2) and have for the first time observed a p-wave resonance in heteronuclear scattering, thereby confirming the theoretical assignment of [136] (see section 4.2.4.1). We have then used the broadest of the available resonances to observe tuning of the scattering parameters.

4.2 Identification of Feshbach resonances

The enhancement of the scattering length in the vicinity of a Feshbach resonance is usually accompanied by enhanced inelastic losses. Loss spectroscopy is therefore a common technique for the identification of Feshbach resonance positions.

4.2.1 Experimental techniques

4.2.1.1 Preparation of "Feshbach-resonant" mixtures

For the preparation of "Feshbach-resonant" mixtures, we start with a magnetically trapped thermal ensemble of ^{40}K $\otimes$ ^{87}Rb in the low-field seeking but non-resonant $|9/2, 9/2\rangle \otimes |2, 2\rangle$ states. Slightly before reaching the critical temperature for condensation T_c of the bosonic ^{87}Rb ensemble, we ramp up the optical dipole potential of our "magic" trap (see chapter 3) within 500 ms. In the combined optical and magnetic potential, a last step of rf-induced evaporation is performed within 1 s and a quantum degenerate mixtures prepared. While ramping down the magnetic trapping potential care has to be taken not to induce spin flips in either potassium or rubidium affecting the polarization of the atomic ensemble. To this end, an offset field of a few ten Gauss is applied throughout the ramp-down process. Residual heating of the cloud during the ramp down is subsequently compensated for by a last step of purely optical evaporation in the crossed dipole trap. We typically end up with a quantum degenerate mixture of $5 \cdot 10^4$ ^{40}K and up to $2 \cdot 10^5$ ^{87}Rb atoms and no discernible bosonic thermal fraction.

The mixture of $|F = 9/2, m_F = 9/2\rangle \otimes |F = 2, m_F = 2\rangle$ states is favorable for evaporative cooling in a magnetic trap because of the large magnetic moment of both states and the stability of the polarized mixture against spin changing collisions. However, the corresponding molecular potentials involved in the appearance of a Feshbach resonance have the same magnetic moment and the relative energy of open and bound channels are thus not tunable one against the other as a function of magnetic field [138]. As a consequence, no Feshbach resonances have been predicted or measured in a mixture of these states. Most of the heteronuclear Feshbach resonances between ^{40}K and ^{87}Rb occur in a mixture with ^{87}Rb in the $|1, 1\rangle$ state and potassium in some Zeeman substate of the lower hyperfine level $|9/2, X\rangle$. As the broadest of the resonances has been predicted to occur in the $|9/2, -9/2\rangle \otimes |1, 1\rangle$ absolute ground state, we concentrated on resonances in these states in the magnetic field range of 500 G.

Feshbach resonant mixtures in the above states are prepared using the following procedure: After achieving quantum degeneracy in the optical trap in a $|F = 9/2, m_F = 9/2\rangle \otimes |F = 2, m_F = 2\rangle$ mixture, the offset field assuring spin conservation is ramped up to a value of 20 G. The desired spin mixture is then produced using a sequence of Landau Zener transfers [139, 140]. First, we transfer ^{87}Rb atoms from $|2, 2\rangle$ to $|1, 1\rangle$ by a 100 kHz microwave sweep at $\approx$ 6.8 GHz and remove any residual atoms in the $F = 2$ hyperfine manifold by a resonant light pulse. Second, we transfer ^{40}K atoms into the $|9/2, -7/2\rangle$ state by performing an rf sweep of 100 kHz across 8 spin spates at the same magnetic field within 40 ms, achieving close to 100% efficiency. We subsequently ramp up the magnetic field to a value near the resonance.[2]. Note that at this stage, the prepared mixture in the $|9/2, -7/2\rangle \otimes |1, 1\rangle$ states is non-resonant, allowing for an equilibration time of the magnetic field on the order of a few hundred ms. Depending on the experiment to be performed, the resonant mixture in the $|9/2, -9/2\rangle \otimes |1, 1\rangle$ states is then prepared either by a π-pulse on the ^{40}K $|9/2, -7/2\rangle \rightarrow |9/2, -9/2\rangle$ transition or by a short Landau-Zener transfer of 3 ms and 50 kHz width on the same transition.

[2]For a detailed description of the microwave and rf manipulation setup, see the diploma thesis of Manuel Succo [141].

4.2.1.2 Magnetic field control

Loss measurements on the ^{40}K-^{87}Rb mixture performed at JILA [37] and LENS [136] suggested the availability of heteronuclear resonances possibly suitable for tuning of interactions in the magnetic field range round about 500 G. The predicted and partially measured widths of the different resonances vary between a few ten mG and a few hundred mG, the broadest having a predicted width of approximately 3G. For precise control of interactions via Feshbach resonances even on relatively narrow resonances, we aimed at having the magnetic field in the 500 G range reproducible down to the 10 mG level which corresponds to a magnetic field accuracy of approximately 10^{-5}. To this end, the external current programming input of the Helmholtz coil DELTA power supply soon proved to be unsuitable even in initial experiments. One of the limiting elements was the isolation amplifier used to guarantee galvanic separation between the analog output of our DSP system and the analog input of the power supply.

The envisioned magnetic field stability and reproducibility below the 10^{-5} level has only been achieved by means of an external current regulator (for details, see the PhD thesis of Christian Ospelkaus [35] and the diploma thesis of Leif Humbert [142]). The DELTA power supply has been operated in constant voltage mode and the current through the Helmholtz coils was controlled by the external controller relying on a precision DANFYSIK ULTRASTAB 867-200I current transducer. The current was controlled around a fixed value of approximately 70 A necessary for the generation of magnetic fields of approximately 547 G. An additional modulation input provides the necessary variations around the set value of $\pm$2A, corresponding to a magnetic field variation of $\pm$14 G. The restriction to a moderate "tuning" range of the magnetic field, however large compared to the width of the studied resonances, avoids the performance of the regulator to be limited by the "noisy" isolation amplifiers. One drawback of this restriction is of course the necessary change of the fixed "central" current when switching between different resonances.

Note that the achieved magnetic field stability and reproducibility below the 10 mG level has been the key for the identification of one of the resonances as p-wave (see subsection 4.2.3 below) and the precise measurement of the binding energy of heteronuclear molecules in a 3D lattice (see chapter 7), allowing the resolution of collisional shifts of a few kHz on the ^{40}K $|9/2,-7/2\rangle$ to $|9/2,-9/2\rangle$ transition.

4.2.1.3 Magnetic field calibration - Rf Spectroscopy

A precise magnetic field calibration has been performed using rf spectroscopy on the ^{40}K $|9/2,-7/2\rangle \rightarrow |9/2,-9/2\rangle$ transition and cross-checked by spectroscopy on the ^{87}Rb $|1,1\rangle \rightarrow |1,0\rangle$ transition. At 500 G, these transitions have a magnetic field sensitivity of 67 kHz/G and 594 kHz/G, respectively, and occur at $\approx$ 80 MHz and $\approx$ 350 MHz. The much lower magnetic field sensitivity of the ^{40}K transition compared to the ^{87}Rb transition is mainly due to the relatively small hyperfine coupling of the ^{40}K $^2S_{1/2}$ ground state. The Paschen-Back regime is therefore already reached at magnetic field values of approximately 200 G. To perform rf spectroscopy on the above-mentioned transitions, a quantum degenerate mixture of ^{40}K and ^{87}Rb is prepared in the $|9/2,-7/2\rangle \otimes |1,1\rangle$ states at 20 G. After removal of one of the components by a resonant light pulse, the magnetic field is ramped up to a certain fixed value. Rf pulses are then irradiated in the vicinity

of the atomic Zeeman transition frequency. The pulse frequency is varied around the resonance frequency. The magnetic field is subsequently switched off quickly and state sensitive detection is performed using the well-known Stern-Gerlach technique. Prior to using pulses, the search interval for the resonance frequency has been narrowed down to 10 kHz by appropriate rf Landau Zener transfers. Starting with rf pulses of extremely low intensity but fixed length, the power of the rf pulse is adjusted to realize π-pulses on resonance. From the measured resonance center, the magnetic field values can then be deduced based on the well-known Breit-Rabi formula. The above procedure has been repeated at 5 magnetic field values for ^{40}K and ^{87}Rb.

Our first rf spectra have been limited by magnetic field drifts in the laboratory and AC magnetic noise. After removing sources of AC noise from the experiment with the help of a fluxgate probe, reproducible rf spectra for both ^{40}K and ^{87}Rb atoms have been observed. We have observed a Fourier limited linewidth with rf pulses of 0.8 ms on the $|9/2, -7/2\rangle \rightarrow |9/2, -9/2\rangle$ at about 500 G, indicating that AC fluctuations are smaller than 20 mG. Synchronization of the experimental cycle with the 50 Hz mains frequency even improved the performance. The magnetic field calibration is found to have an overall drift of smaller than 10 mG over several weeks.

4.2.2 Identification of the resonances

4.2.2.1 The 547 G resonance

In a first experiment, we tried to reproduce the position of the previously identified broad resonance at 545.4 G [37, 136]. Starting from a quantum degenerate $|9/2, -7/2\rangle \otimes |1, 1\rangle$ ^{40}K–^{87}Rb ensemble at high magnetic fields in the vicinity of the expected resonance position, we transfer the $|9/2, -7/2\rangle$ state to the "Feshbach-resonant" $|9/2, -9/2\rangle$ state by a Landau Zener rf ramp of 100 kHz within 3 ms. The transfer efficiency throughout the probed magnetic field range is larger than 90%. The "resonant" mixture is then held at a fixed magnetic field value for 300 ms and the left-over ^{40}K and ^{87}Rb is detected after time of flight. Again we perform state sensitive detection based on the Stern-Gerlach technique. This allows us to detect simultaneously eventual incomplete initial state transfer from $|9/2, -7/2\rangle \rightarrow |9/2, -9/2\rangle$, thereby checking our magnetic field calibration online during the sampling process with an uncertainty < 1.5 G. We have checked for loss features ± 7 G around the expected resonance position with a sampling of 0.02 A, corresponding to 0.14 G and could detect a pronounced feature at 547 G in both ^{40}K and ^{87}Rb and an additional loss feature in the ^{87}Rb cloud only at 551.4 G. The corresponding spectrum is shown in Fig. 4.1. In these experiments, the mixture has been held for 300 ms. The relatively long hold time resulted in a complete loss of ^{40}K atoms in a magnetic field range of approximately (547 ± 1) G and is therefore inappropriate for a "precision" determination of the heteronuclear resonance position. Due to the long hold times, we were able to observe a second feature in the ^{87}Rb cloud which stems from a previously identified ^{87}Rb Feshbach resonance with a width of 0.2 mG at 551.47 G [108]. We observed the loss feature at 551.45 G within the experimental uncertainty of 30 mG of reference [108]. Apart from the above-mentioned online-check of our magnetic field calibration due to the 100 kHz Landau Zener transfer, the precision measurement of ^{87}Rb resonance positions of reference [108] provided an independent check of our magnetic field calibration.

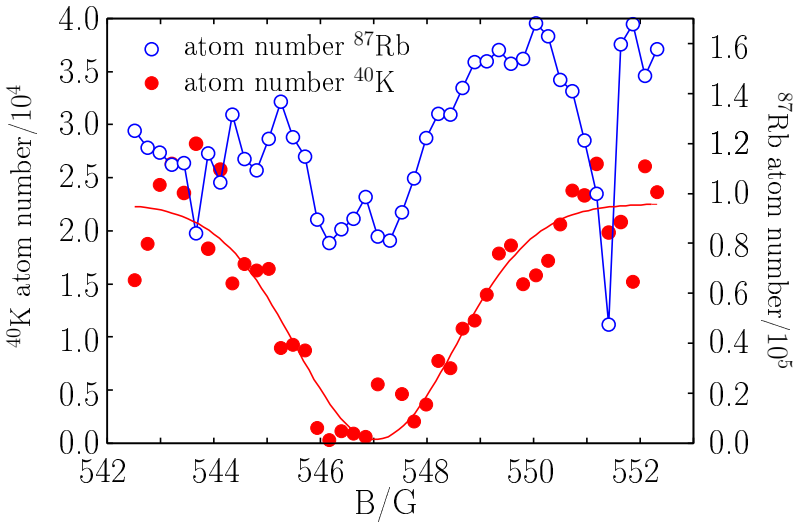

Figure 4.1: Loss spectrum for both the ^{40}K and ^{87}Rb component of a heteronuclear mixture in the vicinity of 547 G. The mixture has been held for 300 ms. A pronounced loss feature in both the ^{40}K and ^{87}Rb component is observed at approximately 547 G. An additional feature only visible in the Rb component is located at 551.45 G. This second feature stems from a known Rb resonance in the $|1,1\rangle$ state at 551.47(3) G with a width of 0.2 mG, providing an independent confirmation of our magnetic field calibration.

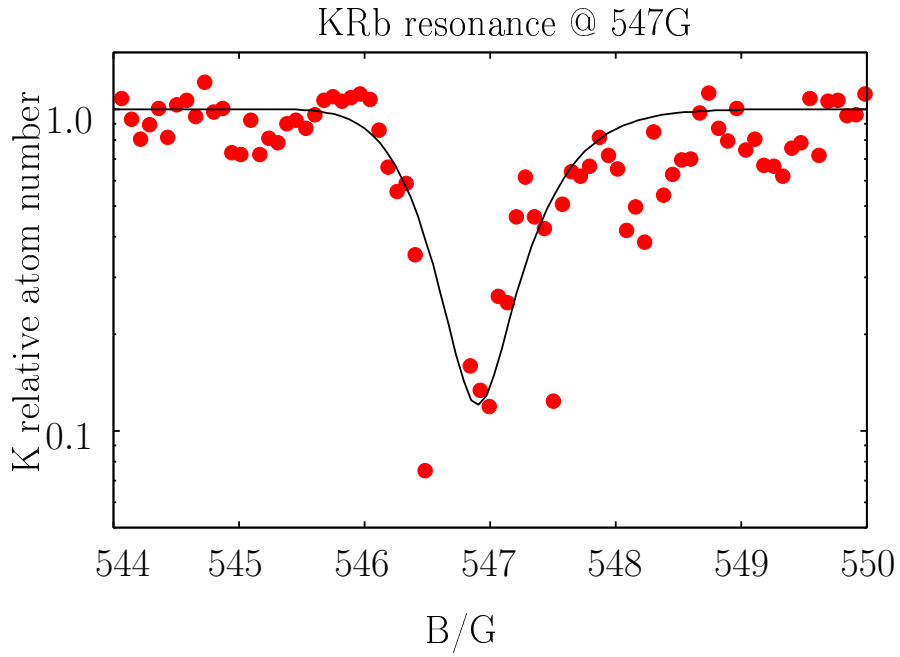

Figure 4.2: Loss spectrum for the ^{40}K component of a heteronuclear mixture in the vicinity of 547 G. The mixture has been held for 40 ms. A pronounced loss feature in the ^{40}K component is observed at (546.9 ± 0.4) G.

For a more precise measurement of the resonance position of the heteronuclear resonance, we thus repeated the measurement in the vicinity of 547 G, this time choosing a hold time of 40 ms and a much finer sampling of 0.07 G. The corresponding loss spectrum of the ^{40}K cloud is shown in Fig. 4.2. Note that the loss spectrum shows the relative losses of ^{40}K atoms during the hold time which have been plotted in a logarithmic plot. From this spectrum, the resonance position can be determined to be at (546.9 ± 0.4)G.[3] Although a precision determination of the resonance position by loss spectra is a bold venture in quantum degenerate Fermi-Bose mixtures due to mean-field instabilities (see section 4.5 below) which might enhance or suppress loss processes, a pronounced shift of the resonance positions by 3.9 G and 1.5 G from the values reported in references [37] and [136] has been observed in both measurements. The validity of the observed shift has been supported by our precise magnetic field calibration performed in the immediate vicinity of the resonance and rechecks by Landau Zener transfers and the observed ^{87}Rb resonance. To get some more insight into the nature of the observed shift, we extended our loss measurements to two additional resonances also occurring in the absolute ground state of the ^{87}Rb-^{40}K mixture $|9/2, -9/2\rangle \otimes |1, 1\rangle$ at 495 G and 515 G.

4.2.2.2 Resonances at 495 G and 515 G

The measurements have been performed similarly to the experiments reported in section 4.2.2.1. We have prepared the system in the $|9/2, -7/2\rangle \otimes |1, 1\rangle$ state at the desired magnetic field and then transferred the fermionic component into the Feshbach-resonant $|9/2, -9/2\rangle$ state by a 100 kHz wide rf sweep after the field has settled. We then waited for a given time. Whereas a distinct loss feature in the ^{40}K cloud was observed after a hold time of 50 ms in case of the 495 G resonance, we had to significantly lengthen the hold time in case of the 515 G resonance. In the latter case, we used a hold time of 350 ms after the final transfer. The ^{40}K loss spectra for the 495 G and the 515 G resonances are shown in Fig. 4.3 and Fig. 4.4. The positions of the resonances are found to be 495.28(5) G and 515.2 G. Again we observe a slight shift of the resonance positions as compared to the measurements at LENS [136] and JILA [37] reporting center positions of 494.0 G / 514.2 G and 492 G / 512 G. The shift of $\propto 1-2$ G on a magnetic field of 500 G seems like a minor correction. However, it has consequences on the Fermi-Bose interaction parameters which can be deduced from the resonance positions (see section 4.2.4). In addition, the 515 G resonance feature shows a pronounced doublet-structure providing strong evidence for the p-wave nature of the resonance (see section 4.2.3).

4.2.3 p-wave resonance in a mixture of ^{40}K and ^{87}Rb

At 515 G, we clearly observe a doublet feature in the resonant atom loss. Such a doublet feature has previously been found in p-wave scattering between fermionic atoms in different internal spin states [143, 144, 145, 146]. Reference [147] predicted a $p-$wave resonance to occur in the ^{40}K-^{87}Rb system at magnetic fields of (540 ± 30)G, with the $|m_l| = 1$ peak located approximately 300 mG above the $|m_l| = 0$ peak. $p-$wave resonances occur when the energy of the incoming particles in a scattering channel is large enough to overcome the

[3] The error bars have been estimated by taking the half width at half maximum of the corresponding loss spectrum.

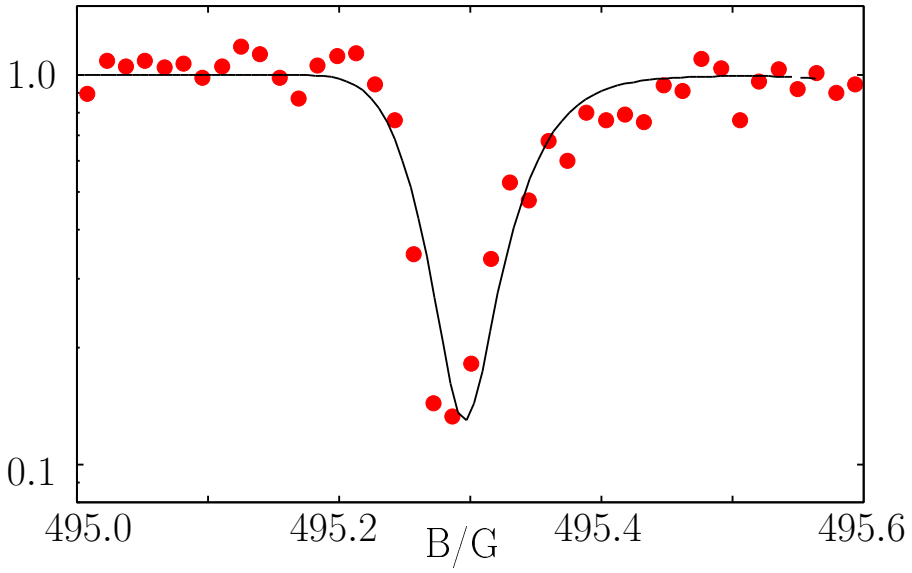

Figure 4.3: ^{40}K loss feature of the 495.28 ± 0.05G resonance after a hold time of 50ms.

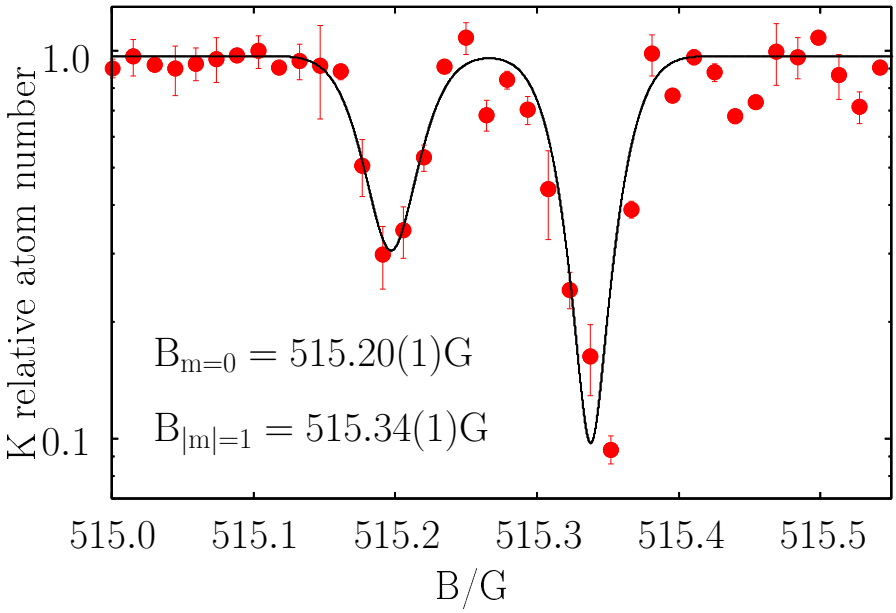

Figure 4.4: Doublet structure observed in ^{40}K atom loss at 515 G, showing the p-wave nature of this heteronuclear resonance.

energy barrier of the centrifugal potential. A characteristic feature of $p-$wave resonances is a doublet structure in the observed loss spectra. The partial-wave projection onto the quantization axis given by the external magnetic field can adopt three different values: $m = 0, \pm 1$. Due to dipole-dipole interaction of the valence electrons of the involved atoms, the degeneracy between the $|m| = 1$ and $|m| = 0$ collisional channels is broken which results in a splitting of the corresponding Feshbach resonance [147]. Note that the splitting of the resonance channels provides access to tuning of the anisotropy of the interaction. Fig. 4.4 shows the observed loss spectrum of the ^{40}K cloud at 515 G. We observe the loss features corresponding to the $|m| = 1$ and $|m| = 0$ collisional channels at 515.2 G and 515.34 G. The fact that we have been able to resolve the characteristic structure although separated only by 140 mG and each feature having a width of 50 mG impressively demonstrates the quality of our magnetic field stability and accuracy.

Note that the measurements reported in this thesis provide evidence for the existence of higher-order partial wave resonances in a Fermi-Bose mixture of ^{40}K and ^{87}Rb for the first time.

4.2.4 Consequences for the interaction parameters

The measurements on three of the Feshbach resonances arising in the absolute ground state of the ^{40}K–^{87}Rb mixture reported in this thesis have profound impact on the interaction parameters between ^{40}K and ^{87}Rb.

4.2.4.1 p-wave nature of the 515 G resonance

Following the pioneering work by S. Inouye and coworkers at JILA [37] on heteronuclear Feshbach resonances, a collisional model has been developed ascribing a $p-$wave character to the 495 G resonance and fixing the interaction parameters between ^{40}K and ^{87}Rb to $(-54 \pm 12)a_0$ and $(-281 \pm 15)a_0$ for singlet and triplet scattering length, respectively. A recent study following the work by Ferlaino and coworkers at LENS [136] provided an almost complete overview of the available Feshbach resonances occurring in different spin states of the ^{40}K–^{87}Rb hyperfine ground state manifold along with a collisional model resulting in significantly different scattering background parameters between ^{40}K and ^{87}Rb [136]. The two collisional models ascribe different character, either s- or p-wave character, to the resonances occurring at 495 G and 515 G. Whereas reference [37] ascribed p-wave character to the 495 G resonance and $s-$wave character to the 515 G resonance, reference [136], however, ascribed $p-$wave character to the 515 G resonance; but no direct evidence for this assignment has been available. The doublet structure of the 515 G resonance, however, as measured in our experiment and shown in Fig. 4.4 demonstrates the $p-$wave nature of the 515 G resonance and provides evidence for this aspect of the most recent assignment of reference [136].

4.2.4.2 Systematic shift of the resonances

Feshbach spectroscopy along with an associated collisional model is a sensitive way for the reliable determination of background scattering parameters. However, the scattering parameters depend critically on the involved molecular potentials which on their part are calculated based on the observed Feshbach resonance positions. Based on Feshbach

States ^{40}K$\otimes^{87}$Rb	Resonance position [136]	Resonance position (this thesis)	l
$\|9/2,-9/2\rangle \otimes \|1,1\rangle$	494.0 G	495.28(1) G	s
$\|9/2,-9/2\rangle \otimes \|1,1\rangle$	514.2 G	515.20(1) / 515.34(1) G	p
$\|9/2,-9/2\rangle \otimes \|1,1\rangle$	545.4 G	546.9(4) G	s

Table 4.2: Comparison of the observed resonance positions for 3 of the heteronuclear Feshbach resonances in ^{40}K and ^{87}Rb. Compared are the values measured within this thesis and a previous resonance observation at LENS [136].

spectroscopy and the collisional model of [136], the background scattering length between ^{40}K and ^{87}Rb has been calculated to be $a_{\text{singlet}} = (-108 \pm 3)a_0$ and $a_{\text{triplet}} = (-205 \pm 5)a_0$. However, a slight systematic shift of the resonance positions towards lower magnetic field values has influenced the background scattering parameters for the ^{40}K–^{87}Rb mixture. Table 4.2 summarizes our findings compared to previous studies by the LENS group [136] which resulted in a correction of the background interaction parameters to $(-111 \pm 5)a_0$ for the singlet scattering length and $(-215 \pm 10)a_0$ for triplet scattering [80].

4.3 Phases of harmonically trapped mixtures

In this section, I will give a a short review on the modelling of harmonically trapped Fermi-Bose mixtures based on a mean-field approach. I will discuss a variety of interaction effects as well as the different phases and instabilities that occur in these mixtures depending on the sign and the strength of the heteronuclear interaction.

4.3.1 Modelling harmonically trapped mixtures

The behavior of harmonically trapped Fermi-Bose mixtures at $T = 0$ under the influence of heteronuclear interactions can be quantitatively described by a mean-field model [82]. Within this formalism, the mutual influence of both components on each other is described by additional mean field potentials. These mean-field potentials generated by one of either species confine/repel the respective other component: The Fermi gas "feels" an additional mean-field potential U^{F}_{MF} generated by the bosonic cloud which is proportional to the interaction strength a_{FB} and the bosonic density n_{B}:

$$U^{\text{F}}_{\text{MF}} = \frac{2\pi\hbar^2}{\mu_{\text{FB}}} a_{\text{FB}} n_{\text{B}}(\vec{r}) \tag{4.1}$$

where μ_{FB} is the reduced mass: $\mu_{\text{FB}} = \frac{m_{\text{F}} \cdot m_{\text{B}}}{m_{\text{F}} + m_{\text{B}}}$. Correspondingly, the Bose Einstein condensate feels an additional potential U^{B}_{MF} induced by the fermionic cloud and which is hence proportional to the fermionic density n_{F}:

$$U^{B}_{\text{MF}} = \frac{2\pi\hbar^2}{\mu_{\text{BF}}} a_{\text{FB}} n_{\text{F}}(\vec{r}). \tag{4.2}$$

The effective trapping potential for the fermionic and bosonic cloud is thus composed of the external trapping potentials $V_{\text{F,ext}}$ and $V_{\text{B,ext}}$ and the additional mean-field potentials and is given by

$$U_{\text{B/F}}(r) = V_{\text{B/F},ext}(r) + U^{\text{B/F}}_{\text{BF}} \tag{4.3}$$

Neglecting the kinetic energy for the condensate, we can use the Thomas-Fermi approximation for the density distribution of both harmonically trapped clouds, and obtain a set of coupled equations where the components influence each other via heteronuclear interactions:

$$\begin{aligned} n_{\mathrm{B}}(\vec{r}) &= \frac{1}{U_{\mathrm{BB}}}\left[\mu_{\mathrm{B}} - \frac{2\pi\hbar^2}{\mu_{\mathrm{FB}}} a_{\mathrm{FB}} \cdot n_{\mathrm{F}}(\vec{r}) - V_{\mathrm{B,ext}}(\vec{r})\right] \\ n_{\mathrm{F}}(\vec{r}) &= \frac{(2m_{\mathrm{F}})^{3/2}}{6\pi^2\hbar^3}\left[E_{\mathrm{F}} - V_{\mathrm{F,ext}}(\vec{r}) - \frac{2\pi\hbar^2}{\mu_{\mathrm{FB}}} a_{\mathrm{FB}} \cdot n_{\mathrm{B}}(\vec{r})\right]^{3/2} \end{aligned} \tag{4.4}$$

In these equations, $V_{\mathrm{B/F,ext}}(\vec{r}) = \frac{1}{2} m_{\mathrm{F/B}}(\omega^2_{\mathrm{B/F}_x} x^2 + \omega^2_{\mathrm{B/F}_y} y^2 + \omega^2_{\mathrm{B/F}_z} z^2$ is the external harmonic trapping potential and $U_{\mathrm{BB}} = 4\pi\hbar^2 a_{\mathrm{BB}}/m_{\mathrm{B}}$ accounts for interactions between bosonic atoms. a_{BB} is the Bose-Bose s-wave scattering length, μ_{B} is the chemical potential of the bosonic cloud and E_{F} the Fermi energy.

The solutions to this system of coupled equations can be obtained by iterative insertion of one density distribution into the other equation starting from equilibrium-density distributions for vanishing heteronuclear interactions. In each step, a numerical search for the chemical potential μ_{B} and the Fermi energy E_{F} under the condition of fixed particle numbers N_{F} and N_{B} is performed (see also [35]).

Due to the much larger density of a Bose-Einstein condensate compared to a Fermi gas of comparable atom numbers ($n_{\mathrm{B}}/n_{\mathrm{F}} \approx 10-100$), the effect of heteronuclear interaction on the fermionic cloud is usually much larger than the reverse effect on the condensate. The following discussion will adopt this approach by starting the discussion with the effects on the fermionic cloud and only then consider the back-action of the affected fermionic cloud on the Bose-Einstein condensate. Note that this iterative reasoning reflects the iterative numerical solution of the system of coupled equations.

4.3.2 Interaction effects and phases of harmonically trapped mixtures

Attractive interactions Let us start our discussion of interaction effects with weak attractive heteronuclear interaction ($a_{\mathrm{FB}} < 0$). In this case, the effective potential for the fermionic cloud is given by the external trapping potential and a steep additional mean-field dimple in the center of the external potential. The deformed effective trapping potential gives rise to a bimodal fermionic density distribution (see Fig. 4.5(right)) with a relatively dilute broad pedestal and a steep and dense core in the center where the density of the fermionic cloud is significantly enhanced due to the presence of the BEC. Depending on the strength of the heteronuclear interaction, the enhanced density of the fermionic cloud has significant effects on the Bose condensate which itself feels an additional mean-field potential which increases the density of the bosonic cloud. In the case of weak attractive interactions, the influence of the fermions on the bosons is relatively weak and the iterative calculation of disturbed density distributions of the fermions and the bosons converges after some iterations, resulting in significantly enhanced but stable coupled density distributions.

However, the picture changes dramatically above a certain critical interaction strength: Now, the additional mean-field potential is so strong that the density distributions in each step are considerably compressed resulting in a strong back-action in the next iterative

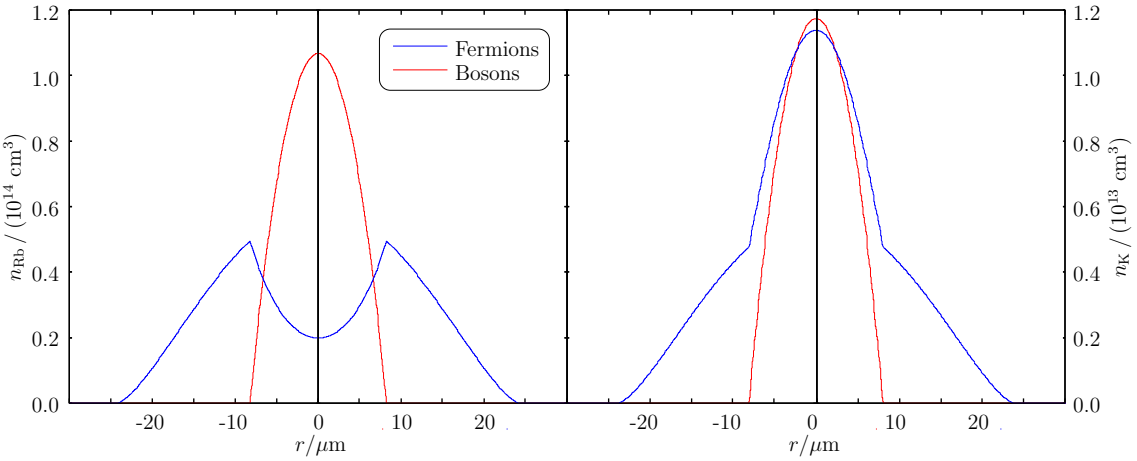

Figure 4.5: Density profiles of interacting mixtures ($N_F = N_B = 10^5$) (left) for repulsive heteronuclear interactions $U_{\mathrm{FB}}/U_{\mathrm{BB}} = 4$ (right) for attractive heteronuclear interactions $U_{\mathrm{FB}}/U_{\mathrm{BB}} = -4$

step. In this case, the iterative process does not converge and a stable coupled solution of the equations 4.4 do not exist. This is a regime of instability for the case of attractive interactions: The mean-field potential of the bosonic cloud overcomes the outward bound Pauli pressure of the Fermi gas and the mixture is unstable with respect to mean-field collapse.

4.3.2.1 Repulsive interactions

For weak repulsive heteronuclear interactions, fermions feel a repulsive mean-field potential in the center of the fermionic trapping potential. Due to the much larger density of the BEC and the smaller spatial extension of the BEC compared to the fermionic cloud, the mean-field potential has the form of an inverted dimple in the center of the trap. The condensate thus acts as a repulsive bump in the center of the fermionic cloud pushing the fermionic cloud out of the center of the trap (see Fig. 4.5(left)). The fermionic density overlapping with the center of the BEC will be reduced whereas the fermionic density in the border areas of the potential increases.

When the repulsive core in the center becomes too strong, the fermionic density distribution in the center of the trap vanishes completely. In this limit, the mixture is unstable with respect to phase separation. A fermionic shell surrounds a dense core of the Bose-Einstein condensate. The shell of fermions significantly compresses the Bose-Einstein condensate.

4.4 Tuning of interactions in stable harmonically trapped Fermi-Bose mixtures

A large variety of experiments relying on tuning of interactions have been made with *homonuclear* systems since the first observation of Feshbach resonances in 1998 [10, 11].

The study of *heteronuclear* Feshbach resonances in collisions of two *different* atomic species (either bosonic or fermionic) is still in its infancy. In this and the following section, I will demonstrate tuning of heteronuclear interactions in the vicinity of a Feshbach resonance in a harmonically trapped Fermi-Bose mixture. These experiments are the first to provide evidence for the tunability of the heteronuclear scattering length.[4] I will start the discussion of experiments on harmonically trapped Fermi-Bose mixtures with tunable scattering length with a discussion of observable interaction effects in *stable* mixtures.

Evidence for tuning of interactions in the heteronuclear ^{40}K–^{87}Rb mixture is provided in two different and complementary ways:

1. In a first experiment, we study tuning of interactions by a measurement of the mean-field energy of the Bose Einstein condensate as a function of magnetic field in the vicinity of a Feshbach resonance. Due to the heteronuclear interaction the Bose-Einstein condensate is confined in the combined potential of the external dipole trap and the heteronuclear mean-field potential. The latter becomes stronger as the heteronuclear interaction increases. Hence, the effective confinement of the Bose-Einstein condensate which determines its mean-field energy, is changed. A measurement of this interaction-dependent mean-field energy is performed by a sudden switch off of all confining potentials including the additional mean-field potential and an observation of the time-of-flight expansion of the condensate. A sudden switch off of the mean-field potential is realized in a good approximation by suddenly switching off the Feshbach field, reducing the heteronuclear scattering length to its background value. A related study has been done in the very first demonstration of tuning of homonuclear interactions in a Bose-Einstein condensate of ^{23}Na [11] in the vicinity of a Feshbach resonance.

2. In a second experiment, we study the influence of the heteronuclear interaction on the time-of-flight expansion of the Bose-Einstein condensate and the Fermi gas. When the heteronuclear interaction is left on during time-of-flight, the expansion of the two clouds is either slowed down due to attractive interaction or influenced by repulsive interactions. The study is performed by a sudden switch off of the external dipole trapping potential while the Feshbach field is left on during time of flight.

For our studies, we have used the broadest of the available s-wave resonances which we observe at B_0=546.8(1) G. The resonance center position has been determined by the transition between strong attractive and repulsive interactions (see below). At the resonance, the scattering length varies dispersively as a function of the external magnetic field [101]

$$a_{\mathrm{FB}} = a_{\mathrm{BG}} \cdot (1 - \Delta B/(B - B_0)). \tag{4.5}$$

In equation 4.5, B_0 is the resonance center, $a_{\mathrm{BG}} = -185a_0$ [148] is the background scattering length between bosons and fermions in the respective spin state and ΔB is the width of the resonance which in our case has been predicted to be -2.9 G [136]. Note that the width of the Feshbach resonance can be negative. In our case, this means that the scattering length will diverge to $a \to +\infty$ below the resonance ($B < B_0$) and $a \to -\infty$ above the resonance ($B > B_0$). A sketch of the expected variation of the scattering length

[4] Tuning of heteronuclear interactions has been reported almost simultaneously at LENS [148].

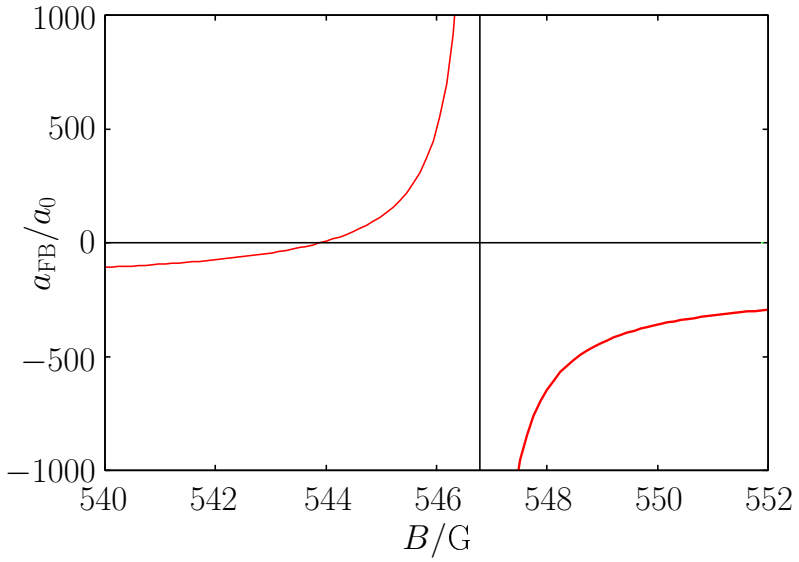

Figure 4.6: Theoretically predicted variation of the Fermi-Bose scattering length a_{FB} across the heteronuclear Feshbach resonance at 546.8(1) G. We assumed a width of $\Delta B = -2.9$ G (see reference [136] and a background scattering length of $a_{\mathrm{bg}} = -185a_0$ (see reference [148]).

as a function of the magnetic field for the ^{40}K–^{87}Rb s-wave resonance at $B = 546.8(1)$ G is given in Fig. 4.6.

4.4.1 Experimental sequence

For the following measurements, a quantum degenerate mixture of ^{40}K and ^{87}Rb in the $|9/2, -7/2\rangle \otimes |1, 1\rangle$ of typically $5 \cdot 10^4$ ^{40}K and $1 \cdot 10^5$ ^{87}Rb atoms has been prepared in the magic optical dipole trap. The transfer $|9/2, -7/2\rangle \rightarrow |9/2, -9/2\rangle$ to the resonant $|9/2, -9/2\rangle$ state in ^{40}K is performed at two fixed magnetic field values by a rf Landau-Zener transfer after the field has settled. For studies above the resonance ($B > B_0$), where the heteronuclear interaction is expected to be attractive ($a_{\mathrm{FB}} < 0$), the final transfer is performed at a magnetic field of 550.5 G. For studies below the resonance center ($B < B_0$), where the heteronuclear interaction is expected to be repulsive ($a_{\mathrm{FB}} > 0$) the transfer is done at $B = 543.8$ G. At these magnetic field values, the heteronuclear scattering length is still moderately attractive in both cases and not too different from the background scattering length between ^{40}K and ^{87}Rb in the $|9/2, -7/2\rangle \otimes |1, 1\rangle$ mixture. This is important in order not to induce oscillations in both clouds due to the sudden change of the scattering length. After the final transfer at these two magnetic field values, the field is ramped to varying values in the immediate vicinity of the resonance either from above or below. The ramp is performed within 50 ms, thereby changing a_{FB} adiabatically with respect to any other time scale in the experiment: $\dot{a}/a \ll \omega_i$ so that the clouds remain

in equilibrium within the field ramp [11, 149].[5] We then probe the expansion of the cloud at different values of the heteronuclear scattering length and under different conditions.

4.4.2 Evidence for tuning I: Mean-field energy of the BEC

While the kinetic energy of a Bose-Einstein condensate in the trap is negligible (Thomas-Fermi limit), the energy of the BEC is dominated by its interaction energy given by

$$E_I/N = \frac{(2\pi)^3\hbar}{m} a_{\mathrm{BB}} \langle n_{\mathrm{B}} \rangle . \tag{4.6}$$

In this equation, a_{BB} denotes the Bose-Bose scattering length, $\langle n_{\mathrm{B}} \rangle$ is the average density of the condensate, N the number of atoms of mass m. This mean-field energy of the condensate can be measured by time-of-flight expansion. During time-of-flight, the stored interaction energy is converted into the kinetic energy of a freely expanding condensate.

At first glance, the interaction energy of the condensate, proportional to the mean density and the bosonic scattering length, seems to be independent of the value of the heteronuclear scattering length. However, the effect of heteronuclear interaction enters through the density of the Bose-Einstein condensate which is affected by the presence of the fermionic cloud. The trapped fermions, along with the heteronuclear interaction, act as an additional heteronuclear mean-field potential forming an effective potential $U_{\mathrm{B}}(\vec{r})$ composed of the dipole trapping potential $V_{\mathrm{B,ext}}$ and the mean-field potential U^{B}_{MF} and determines the density distribution of the bosonic cloud via the Thomas Fermi equation $n_{\mathrm{B}}(\vec{r}) = (\mu_{\mathrm{B}} - U_{\mathrm{B}}(\vec{r}))/U_{\mathrm{BB}}$ where $U_{\mathrm{BB}} \propto a_{\mathrm{BB}}$ (c.f. section 4.3).

In the case of attractive interactions, the density distribution of the fermionic cloud interacting with the BEC is increased compared to the non-interacting case. The effective confinement of the BEC is thus increased with increasing attractive heteronuclear interaction in the vicinity of the resonance, enhancing the density and the mean-field energy according to equation 4.6. Along with the intrinsic repulsion of the Bose-Einstein condensate, characterized by the positive bosonic scattering length $a_{\mathrm{BB}} = 100.4(1)a_0$ [150], the effect is observable through the increasing kinetic energy of the bosonic cloud after time-of-flight.

In the case of repulsive interactions, the condensate acts as a repulsive bump in the center of the fermionic cloud, pushing the fermionic cloud out of the center of the trap. The fermionic density overlapping with the center of the BEC will be reduced, whereas the fermionic density in the border areas of the potential increases. In this case, the additional fermionic curvature acting on the condensate will push the bosons towards the center of the trap, thereby increasing density and mean field energy of the condensate. However, the effect is smaller than the enhancement of density in the attractive case.

4.4.2.1 Some theoretical results

The above intuitive picture can be supported by numerical simulations. The simulations rely on the mean-field model of section 4.3 [82] and provide a self-consistent calculation of the densities of the harmonically trapped fermionic and bosonic cloud, considering the

[5] In the immediate vicinity of the resonance, the adiabaticity condition may break down as $\dot{a}/a$ becomes comparable to ω_i

additional heteronuclear mean-field potentials $U_{\mathrm{MF}}^{\mathrm{F}}$ and $U_{\mathrm{MF}}^{\mathrm{B}}$. For an introduction into the model see section 4.3. Fig. 4.7 shows the theoretically expected variation of the mean-field energy E_I of a condensate of 10^5 bosons in the vicinity of the Feshbach resonance at 546.8(1) G, interacting with a fermionic cloud of $5 \cdot 10^4$ atoms via a varying heteronuclear scattering length $a_{\mathrm{FB}}(B)$. In the figure, I have plotted the interaction energy of the condensate as a function of $B - B_0$, where B_0 is the resonance position. The mean field energy has been calculated according to equation 4.6 and is normalized to the mean field energy of a pure condensate. The behavior of the scattering length in the vicinity of the resonance is determined by equation 4.5 with an assumed width of the resonance of $\Delta B = -2.9$ G. I have plotted the interaction energy only for stable interacting mixtures. In the same diagram, a sketch of the expected heteronuclear scattering length is plotted.

On the repulsive side of the resonance (low-field side), the interaction energy of the condensate increases by 20% compared to the non-interacting case. At the same time, the heteronuclear scattering length varies between 0 at ≈ -3 G and $\approx 400a_0$ before the onset of phase separation. On the high field side of the resonance, where heteronuclear interactions are attractive, the effect of heteronuclear interactions is much more pronounced: the mean-field energy of the condensate increases by almost a factor of 2 while the scattering length is increased by approximately the same factor. The effect of heteronuclear interactions on the mean-field energy of the condensate is thus strongest on the attractive side of the resonance whereas only a slight effect is observed on the repulsive side.

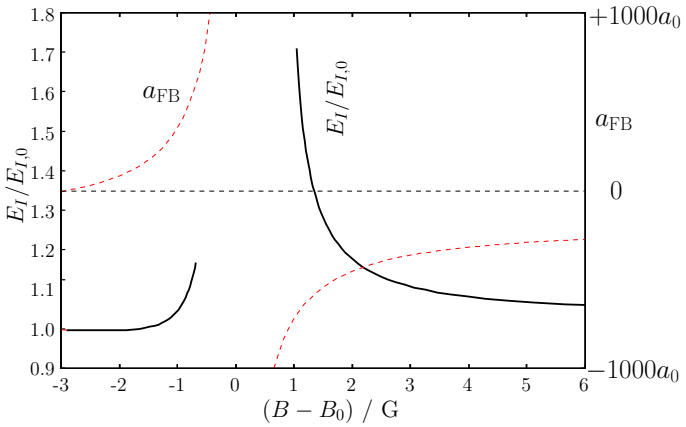

Figure 4.7: Theoretically predicted variation of the mean-field energy of the condensate as a function of $B - B_0$ in the vicinity of the 546.8(1) G Feshbach resonance. The mean-field energy is normalized to the interaction energy of a pure bosonic condensate.

4.4.2.2 Experimental data

In the above sections, we have seen that the mean field energy of a Bose-Einstein condensate in a Fermi-Bose mixture does depend on the value of the heteronuclear scattering length, although the dependence can only be calculated numerically. The interaction energy can be measured in a time-of-flight expansion experiment where all confining potentials are suddenly switched off, thus converting the stored mean-field energy into kinetic energy. The kinetic energy per particle is just given by $E_K/N = \frac{1}{2}mv_{\mathrm{rms}}^2$ where v_{rms} is

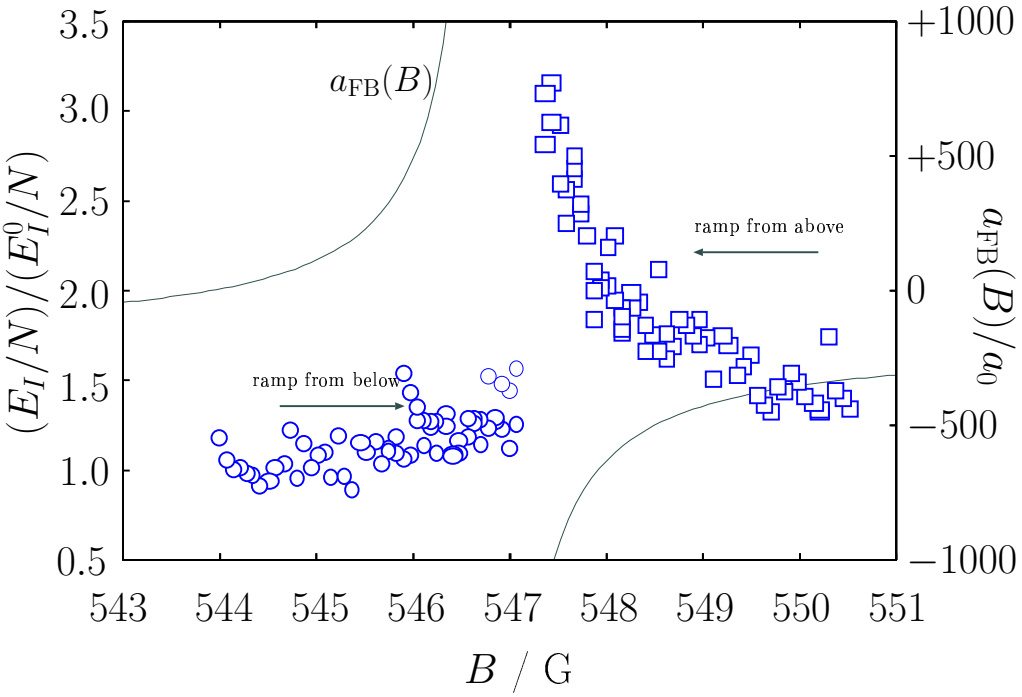

Figure 4.8: Interaction energy of a BEC per particle in the vicinity of a heteronuclear resonance normalized to the interaction energy of a pure condensate. On both sides of the resonance, the interaction energy increases although the effect is much more pronounced on the attractive side of the resonance where both the fermionic and the bosonic density distribution is enhanced. On the repulsive side of the resonance the interaction energy increases only slightly. In the same diagram, I have plotted the expected variation of the heteronuclear scattering length across the resonance according to equation 4.6.

the mean-root-squared velocity. Both the atom number N and the velocity $v_{\rm rms}$ can be extracted from time-of flight images, more precisely $v_{\rm rms}$ from the size of the cloud after time of flight. Fig. 4.8 shows a measure of the condensates mean-field energy per particle as a function of the magnetic field in the vicinity of the 546.8(1) G heteronuclear Feshbach resonance. The experimental procedure for the preparation of resonant mixtures in the vicinity of the resonance is described in section 4.4.1. After the final magnetic field ramp from either above or below the resonance center to final field values near the resonance and a 10 ms hold time, both the Feshbach field and the external optical potential are suddenly switched off and ^{40}K and ^{87}Rb are detected after time-of-flight.

On the low-field side of the resonance, the interaction energy increases only slightly with increasing repulsive heteronuclear interaction. Within the investigated magnetic field range below the resonance, the scattering length is expected to vary from 0 to $+1000a_0$. In the same magnetic field interval, the interaction energy is observed to increase only by 25%. A comparable effect has been predicted by the theoretical calculations of section 4.4.2.1. On the high-field side of the resonance, the effect of heteronuclear interactions is much more pronounced. The heteronuclear scattering length is expected to vary between $-300a_0$

and $-1000a_0$ within the investigated magnetic field range. As can be seen from the data, the mean-field energy per particle stored in the condensate increases in the same interval by a factor of 3 which is quite comparable to theory where an increase in heteronuclear interaction by a factor of 2 resulted in an increase in interaction energy of the condensate by the same factor (see section 4.4.2.1).

For magnetic field values above $B > 551$ G, the heteronuclear scattering length is expected to recover slowly to its background value of $-185a_0$. Consequently, the interaction energy per particle is expected to saturate somewhat above the interaction energy of a pure condensate. On the low magnetic field side, however, the scattering length changes sign from repulsive interaction to attractive at $B \approx 543.9$ G. Below this zero-crossing, the scattering length will become negative and eventually recover the negative background interaction. Hence, the interaction energy per particle is expected to increase again below the zero-crossing converging towards the same interaction energy as far above the resonance.

4.4.3 Evidence for tuning II: Interaction effects during expansion

In a second experiment, we have studied the influence of the heteronuclear interaction on the time-of-flight expansion of the Bose-Einstein condensate and the Fermi gas. When the heteronuclear interaction is left on during time-of-flight, the expansion of the two clouds is either slowed down due to attractive interactions or influenced by repulsive interactions. The study is performed as described in section 4.4.1. The external dipole potential is suddenly switched off, whereas the Feshbach field is left on during time-of-flight expansion.

The effect of attractive interactions on the time-of-flight expansion of the bosonic and fermionic cloud has already been studied in [87] in a Fermi-Bose mixture of ^{40}K and ^{87}Rb. However, in these experiments, the heteronuclear interaction was determined by the background interaction strength and could not be tuned. The observations in [87] are therefore restricted to the observation of an affected time-of-flight expansion of the bosonic and fermionic cloud, respectively, in comparison to the expansion of a pure bosonic or fermionic cloud.

Fig. 4.9 shows the width of the bosonic and fermionic cloud after 7.5 ms and 25.2 ms time-of-flight. To account for enhanced particle loss in the vicinity of the resonance, the observed width data should be normalized by $N^{1/5}$ and $N^{1/6}$ for the bosonic and fermionic cloud, respectively.[6] However, the observed particle number loss is on the order of 20% in the studied magnetic field range and the correction due to particle number variations is therefore below 5%. On the repulsive side of the resonance, where the effect of interaction on the time-of-flight expansion is very weak compared to the attractive case, particle loss is even smaller. In the same diagram, I have plotted the expected variation of the heteronuclear scattering length across the resonance.

On the high-field side of the resonance, where heteronuclear interactions are attractive, we observe the width of both the fermionic and the bosonic cloud to decrease when approaching the resonance. This is a clear signature for increasing heteronuclear attraction. The simultaneous expansion of both clouds is slowed down due to the attractive potential that is present throughout the expansion process. However, the effect of the heteronuclear

[6] The equilibrium width of a non-interacting Fermi gas grows with $N^{1/6}$ whereas the width of a Bose-Einstein condensate increases with $N^{1/5}$

attractive interaction on the expansion of the BEC and the Fermi gas is twofold. On the one hand, the densities of both components are significantly increased inside the trap. This enhancement of density which corresponds to a tighter confinement of either of the clouds, will lead to a faster expansion (as discussed for the bosonic cloud in section 4.4.2). On the other hand, the condensate and degenerate Fermi gas will interact during expansion and most importantly in the early stages of time of flight, thereby reducing significantly the expansion rate. This slow-down mechanics is determined by the relative dynamics between the condensate and the degenerate Fermi gas and dominates the experiments.

On the repulsive side of the resonance, however, the effects of heteronuclear interaction are less pronounced. The width of the condensate after time-of-flight stays almost constant, whereas the width of the Fermi gas after time of-flight increases slightly. In the immediate vicinity of the resonance, this increase exhibits a change of slope. When the fermionic density at the trap center vanishes at even higher repulsion, the potential felt by the Bose cloud will rather be that of the pure external trapping potential with quite a sharp transition to a very steep higher order potential created by the fermionic density in the outer shell, at the edges of the condensate. We identify this region with the regime from 546.4 G to the center of the resonance at 546.8 G where, as seen in Fig. 4.8, the width of the condensate saturates. This may indicate that at complete phase separation, the repulsive interaction leads to a rapid expansion of the Fermi gas suddenly accelerated outside when the external potential is switched off and the repulsive bump of the BEC in the center maintained.

4.5 Observing collapse and phase separation

As we have seen in the previous section, interactions between fermions and bosons can fundamentally affect the properties of the system such as the density of the components and expansion properties. However, when increasing the scattering length above a certain critical interaction strength, two instabilities can occur: collapse for the case of attractive interactions and phase separation for the case of repulsive interactions. In our experiments, we have for the first time been able to access the complete phase diagram of the mixture and observe clear signatures of both collapse and phase separation. The phase diagram has been accessed through tuning of interactions in the vicinity of the Feshbach resonance. Although the mean-field collapse of a harmonically trapped Fermi-Bose mixture has been studied before, in those experiments critical conditions have been achieved by increasing particle numbers in the system, holding the value of the heteronuclear interaction fixed (see [81, 4, 35] and chapter 2.10), whereas in the experiments reported here, the collapse is induced by tuning of the heteronuclear scattering length.

4.5.1 Mean-field collapse

For attractive interactions above a certain critical value, the Fermi-Bose mixture is expected to become unstable with respect to collapse. In the vicinity of the resonance occurring at 546.8 G, attractive interactions are strongest immediately above the resonance center. In Fig. 4.9, the corresponding region has been shaded in grey. This region immediately above the resonance center has been studied in detail in Fig. 4.10. Fig. 4.10 shows the atom numbers of both the fermionic and the bosonic cloud as a function of

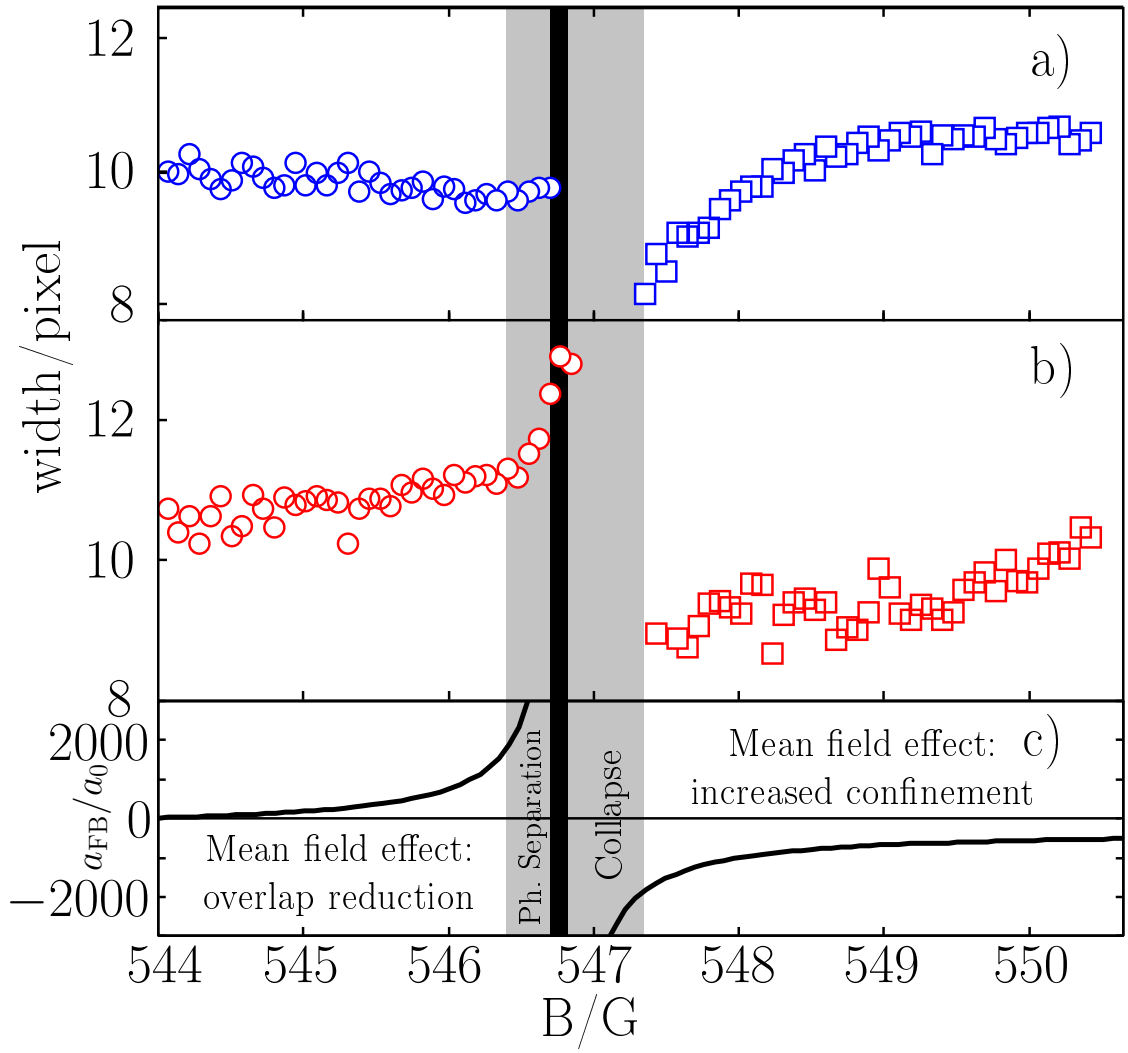

Figure 4.9: Observed width of the components after time-of-flight expansion as a function of magnetic field when the resonant interaction is left on during expansion. (Top) Width of the bosonic cloud. (Middle) Width of the fermionic cloud. (Bottom) Heteronuclear scattering length. The region shaded in grey indicates the magnetic field regions where instability with respect to collapse and phase separation have been observed (see below). The black vertical line marks the observed transition from attractive to repulsive interactions (resonance center). (1 pixel $\hat{=}$ 3.2μm; time of flight 25.2 ms for ^{87}Rb and 7.5 ms for ^{40}K).

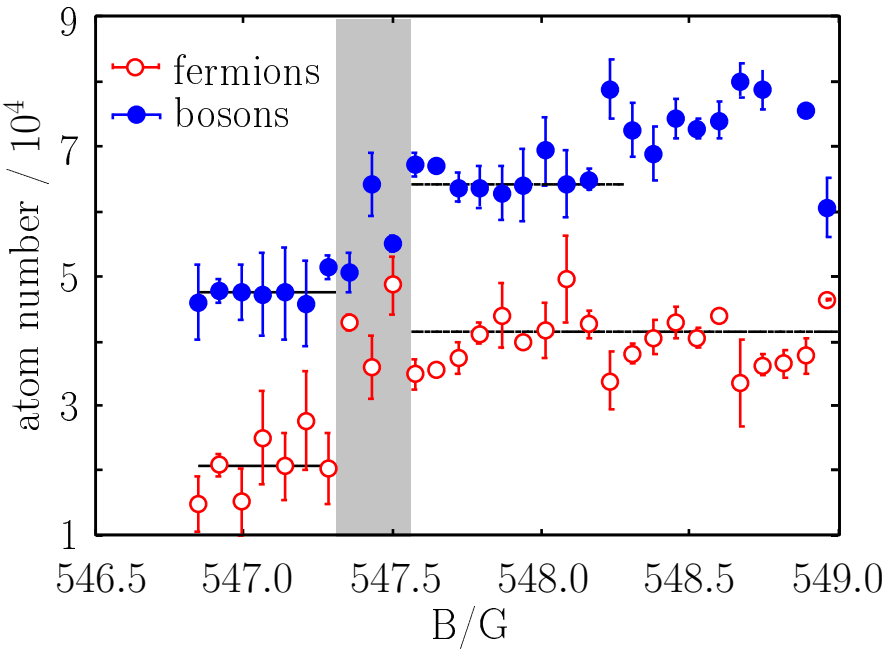

Figure 4.10: Induced mean field collapse of the mixture. Sudden drop of atom numbers for critical heteronuclear interactions.

magnetic field when adiabatically approaching the resonance from above similar to the experiments in section 4.4.1. In the vicinity of 547.4 G (at a detuning of about 0.6 G above the resonance), we observe a sudden drop in both the fermionic and the bosonic atom number. We loose almost 50% of the fermionic atoms and a significant fraction of the bosonic cloud. In contrast to previous work, reporting the onset of instability as a function of atom number (see previous chapter and [81]), the collapse is now due to tuning of interactions above a certain critical interaction strength in an otherwise undercritical mixture. The precise magnetic field value at which the collapse happens is of course dependent on the initially prepared atom number. In the experiments, we observe the onset of the collapse at a magnetic field value corresponding to a theoretically predicted scattering length of $-1000a_0$.

To gain some information about the time scale on which the collapse happens, we have repeated the experiment in a slightly varied version: In this case, we have stopped the magnetic field ramp at the observed critical magnetic field value and then varied the hold time of the mixture, thereby observing the collapse happen as a function of time. This is illustrated in Figure 4.11. We cannot fully exclude some residual variation of the scattering length due to settling of the magnetic field after the nominal stop of the ramp. The onset of the collapse, again visible as a sudden drop in atom number, is retarded by a timescale given roughly by the trap frequency and happens on a timescale <1 ms. The dynamics associated with the collapse can be seen in Fig. 4.11 bottom and Fig. 4.12. Fig. 4.12 shows two time of flight images of the fermionic cloud prior to the collapse and after the collapse has happened (when leaving the Feshbach field on during expansion). Prior to the collapse, the density of the fermionic cloud is strongly enhanced. The fermionic density

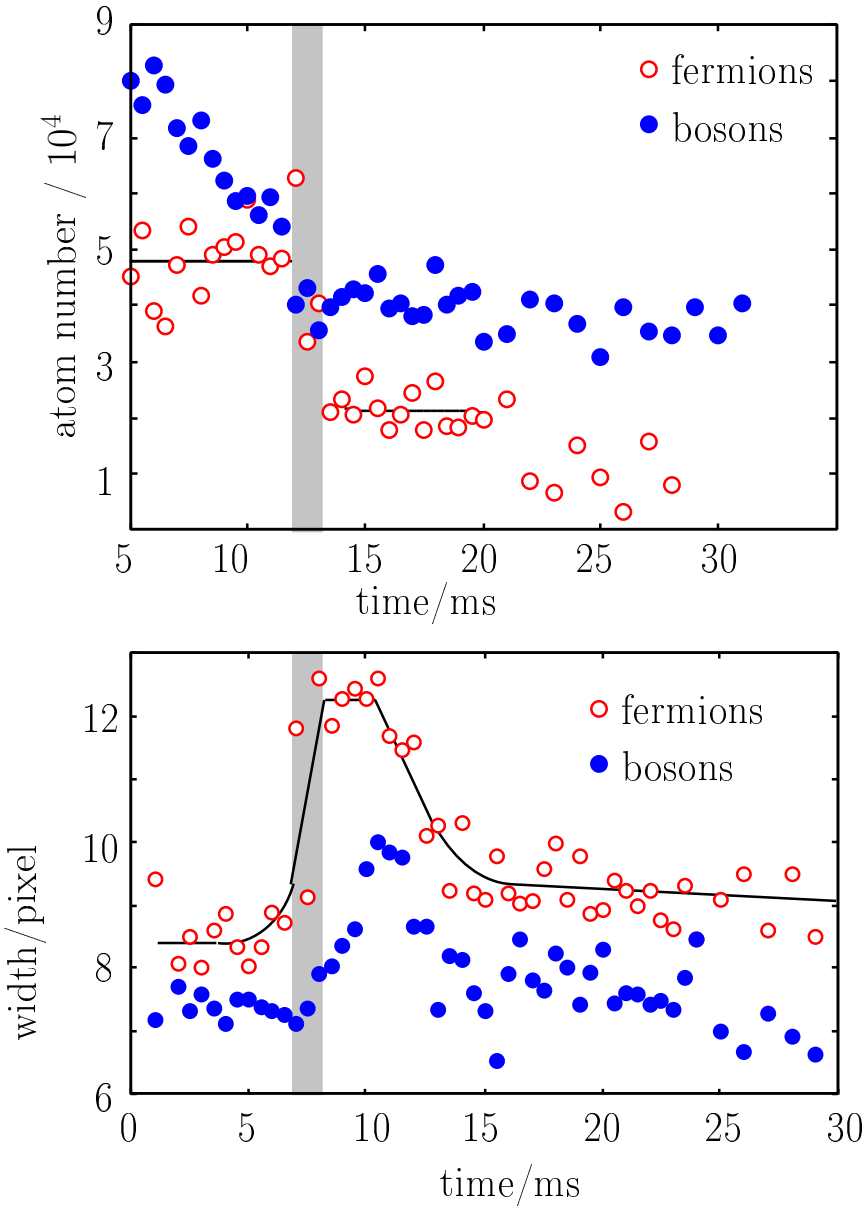

Figure 4.11: Induced mean field collapse of the mixture. The onset of the collapse is retarded by a timescale given by the trap frequency. As the collapse happens, the sample is excited and heated, visible in the width of the fragments. After the collapse, the mixture finds a new equilibrium.

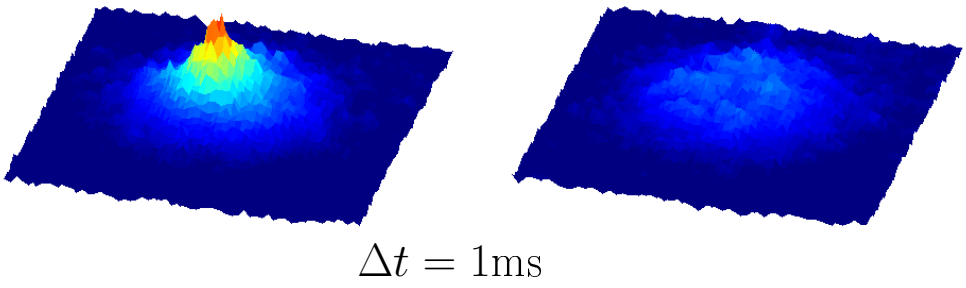

Figure 4.12: Sample time of flight images showing the bimodal distribution in the fermionic component and the sudden collapse of the system.

profile after time of flight shows a bimodal distribution with a broad and dilute bottom and a very dense center. The latter part of the fermionic cloud is trapped inside the mean-field potential of the BEC. When critical conditions for collapse are achieved, this central core suddenly disappears. During the collapse, the overlap region of the fermionic cloud with the BEC is destroyed by a giant three-body implosion, leaving behind only the broad dilute pedestal. The three-body implosion causes significant heating and excitation in the remaining sample, reflected in the evolution of the width of the fermionic cloud as the collapse happens (see Fig. 4.12). After the collapse, the mixture assumes a new equilibrium which is reflected in the decreasing width of the fermionic cloud after the collapse has happened.

4.5.2 Phase separation

Phase separation due to repulsive interactions in a composite system of harmonically trapped fermions and bosons has been discussed in theory [82, 151], but never been explored in experiment. Tuning of heteronuclear interactions has enabled us to enter the regime of repulsive heteronuclear interactions, where phase separation occurs. In the limit of vanishing differential shift due to gravity and for our experimental parameters, phase separation will occur as a shell of Fermions surrounding a dense BEC core (as we have seen above).

Inside a harmonic trap and in the presence of gravity, atoms experience a gravitational sag given by $-g/\omega^2$. For systems with different masses, such as the ^{87}Rb / ^{40}K system, this will in general lead to a differential gravitational sag between the components, as the trap frequencies may be different. A slightly different gravitational sag breaks the symmetry of the system and therefore favors phase separation to occur in the vertical direction. As a consequence, the position of the fermionic component in the time of flight image is shifted upwards as a function of detuning from resonance, with an even stronger

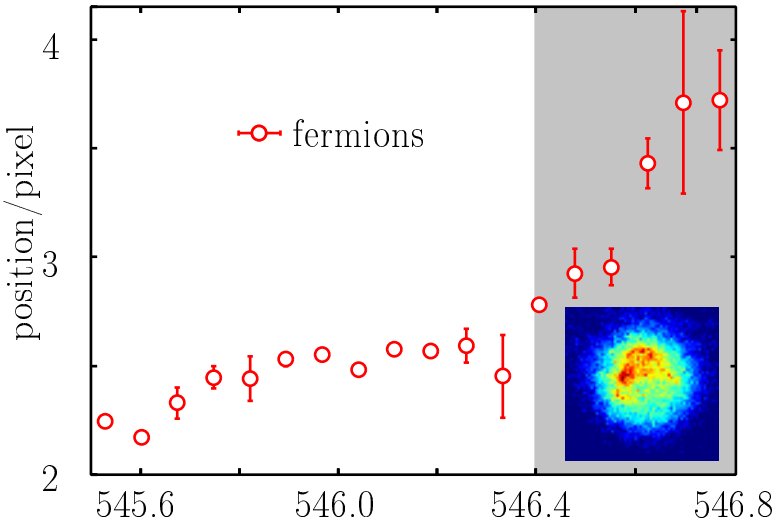

Figure 4.13: Vertical position of the Fermi gas as a function of magnetic field. The grey shaded area indicates the assumed region of full phase separation, where the fermionic density is expected to vanish at the BEC core. Due to gravitational symmetry breaking, the fermions are pushed above the BEC, an effect amplified by time of flight expansion. The inset shows the corresponding fermionic density distribution where most of the density is concentrated in the upper part of the image.

slope in the region of complete phase separation (see Fig. 4.13). An important aspect is that the shift in position between fermions and bosons in the trap is amplified by the repulsive interaction during expansion if we leave on the interaction. Thus, the small initial symmetry-breaking in the direction of gravity is strongly enhanced and clearly visible in absorption images such as in the inset of Fig. 4.13, where the Fermionic density is concentrated in the upper part of the image.

Chapter 5

Quantum degenerate atomic gases in 3D optical lattices

Quantum degenerate gases in optical lattices provide unique opportunities for engineering of many-body Hamiltonians discussed in the context of condensed matter systems and even beyond in a very pure and controllable environment: The periodic potentials realized by optical lattices are almost defect-free. By tuning the depth of the lattice, the strength of the crystal can be controlled, thereby controlling e. g. tunnelling with respect to on-site interaction. Playing with lattices of different geometries and dimensionalities, one, two- and three-dimensional geometries can be realized and continuously transformed from one into another. In addition, the use of Feshbach resonances allows the precise control of interactions between the atoms even allowing for continuous tuning from repulsive interactions to attractive interactions and vice versa [95, 96, 101, 102, 10, 11].

The possibility of realizing strongly correlated systems with ultracold atoms loaded into 3D optical lattices has first been pointed out in a seminal paper by D. Jaksch and coworkers in 1998 who discussed the realization of the Bose Hubbard Hamiltonian with ultracold bosons loaded into 3D optical lattices [18, 152]. The experimental observation of the quantum phase transition from a superfluid to a Mott-Insulator state with repulsively interacting bosons followed in a pioneering experiment by M. Greiner and coworkers in 2002 [19]. Following experiments with either bosonic or fermionic atoms in optical lattices demonstrated the enormous degree of control inherent in these intriguing physical systems [19, 153, 154, 20, 21, 155, 156, 157, 24, 25, 158, 1] (the list of references is by no means complete, for a review see [134]).

In this chapter, the basic formalisms for the description of quantum degenerate gases in optical lattices will be presented. Starting from a review of the theory of optical lattices, I will discuss formalisms describing quantum degenerate gases in 3D optical lattices both in the weakly and the strongly interacting regime. I will conclude this chapter with a description of our optical lattice setup and a presentation of different diagnostic methods useful when working with optical lattices.

5.1 Optical lattices

Optical lattices are periodic potentials that are realized by means of various laser beam configurations suitable for the formation of standing wave configurations [159]. The simplest optical lattice is formed by using counterpropagating laser beams to form a simple standing wave. The resulting periodic potential can then be used to trap atoms via the optical dipole force (see section 3.1) in a periodic pattern thereby localizing them periodically in space.

5.1.1 Optical lattice potentials

A wealth of different geometries and periodic potentials for atoms can most easily be realized based on the optical dipole force [159, 117]. Below, I will discuss various geometries with different dimensionality starting from the most simple one-dimensional standing wave configuration and finally discussing higher dimensional potentials.

5.1.1.1 1D optical lattice

When retroreflecting a Gaussian laser beam of an optical dipole trap, the resulting standing wave interference between the incoming and the outgoing laser beam of equal linear polarization and wavelength gives rise to an optical dipole potential with a periodicity $\lambda/2$ given by the distance between the nodes and antinodes of the standing wave (see Fig. 5.1). Depending on the detuning of the lattice laser wavelength relative to the atomic

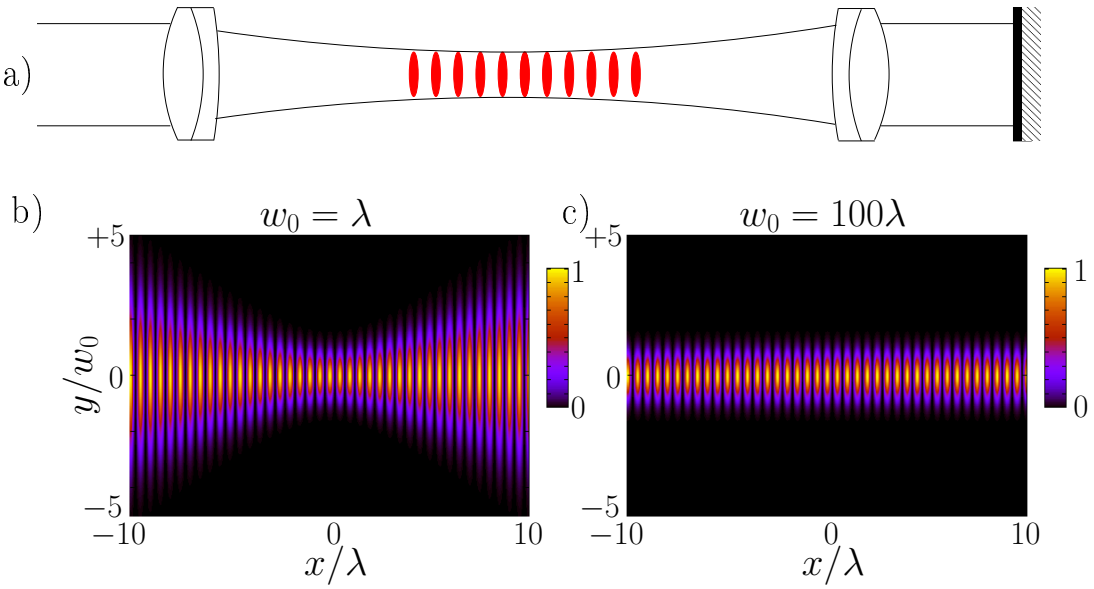

Figure 5.1: Periodic pancake-like potential formed by the interference pattern of a retroreflected Gaussian laser beam. a) Schematic sketch b) Dipole potential in false color representation in the $x = 0$ plane for the unrealistic case of $w_0 = \lambda$ (I have not accounted for the curvature of the wavefronts.). c) For the realistic case $w_0 = 100\lambda$. In our experiments, this corresponds to $w_0 \approx 100$ μm.

transitions, the atoms are either trapped in the nodes (red-detuning) or antinodes (blue-detuning)[1] of the standing wave interference pattern. The resulting optical potential is given by

$$V_{\text{Lattice}}^{\text{1D}}(r,z) = 4V(0)\cos^2(kz)\exp\left(-2\frac{r^2}{w(z)^2}\right) \tag{5.1}$$

and is composed of an array of 2D-like (pancake-like) structures in the z-direction with a Gaussian envelope in the radial direction. In equation 5.1, $k = 2\pi/\lambda$ denotes the wavevector of the lattice laser beam, $w(z)$ is the z-dependent waist (with $w(0) = w_0$) of the Gaussian laser beam and $V(0)$ is the potential depth of a single beam optical dipole trap. Note that the maximum dipole potential in the nodes of the standing wave pattern V_{Lattice} is four times the dipole potential of a single-beam dipole trap $V(0)$ due to constructive interference of the counterpropagating beams: $V_{\text{Lattice}} = 4V(0)$. In the center of the confining potential at $z = r = 0$, the 2d-like geometry of the individual wells can easily be described by two characteristic trapping frequencies: Expanding the potential of a single well quadratically around its minimum in the z and r-directions, one obtains a cylindrically symmetric harmonic potential characterized by two trapping frequencies. In the axial direction, the trapping frequency is characterized by

$$\omega_z = \frac{2E_r}{\hbar}\sqrt{\frac{V_{\text{Lattice}}}{E_r}} \tag{5.2}$$

whereas the trapping frequency in the radial direction is

$$\omega_r = \sqrt{\frac{4E_r}{mw_0^2}}\sqrt{\frac{V_{\text{Lattice}}}{E_r}} \tag{5.3}$$

With $E_r = \hbar^2k^2/(2m)$, a convenient unit for the depth of an optical lattice potential $V_{\text{Lattice}} = 4V(0) = sE_r$ has been introduced given by the atomic recoil energy.[2]

5.1.1.2 Higher-dimensional optical lattices

Different geometries can be realized by using higher dimensional optical lattices. These can be created by superimposing additional standing waves from different directions.

2D optical lattice configuration To form a two-dimensional lattice potential, two standing waves can be superimposed orthogonal to each other. In general, the dipole potential of two retroreflected laser beams with arbitrary polarization vectors $\vec{e}_1$ and $\vec{e}_2$ and phase ϕ, but propagating orthogonally one to each other ($\vec{k}_1 \perp k_2$), is given by

$$V(y,z) = V_{\text{Lattice}}(\cos^2(ky) + \cos^2(kz) + 2\vec{e}_1 \cdot \vec{e}_2 \cos\phi \cos(ky)\cos(kz)). \tag{5.4}$$

[1] In the case of a simple 1D optical lattice, a blue-detuned retroreflected Gaussian laser beam does not constitute a trap because atoms can escape from the antinodes of the potential.

[2] The trapping frequencies in a single lattice well vary slightly with position r and z due to the Gaussian shape of the laser beam (see section 5.1.1.2).

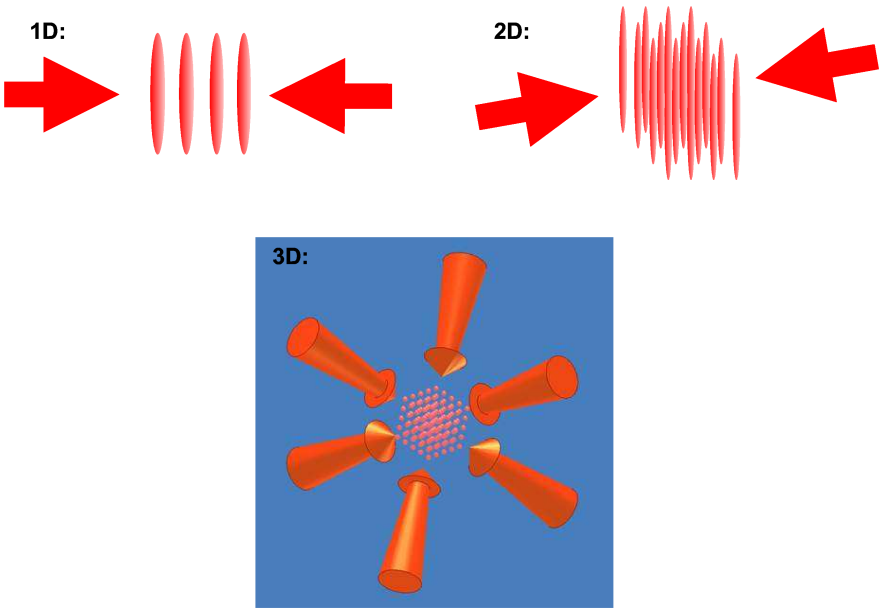

Figure 5.2: Optical lattice configurations in 1D, 2D and 3D: a) 1D-optical lattice is composed of an array of pancake-like structures b) 2D optical lattice consists of an array of quasi-one-dimensional tubes c) With three orthogonal retroreflected laser beams a simple cubic lattice structure is formed.

The above potential reduces to a simple square lattice if the polarizations of the two lattice beams are perfectly orthogonal $\vec{e}_1 \cdot \vec{e}_2 = 0$. The resulting potential is then simply given by the sum of two superimposed 1D lattices

$$V(y,z) = V_{\text{Lattice}}(\cos^2(ky) + \cos^2(kz)) \tag{5.5}$$

resulting in an array of 1D-like geometries as illustrated in Fig. 5.2 b). The geometry of a single tube can again be characterized by two characteristic trapping frequencies, the "radial" trapping frequencies of a single tube

$$\omega_z = \omega_y = \omega_r = \frac{2E_r}{\hbar}\sqrt{\frac{V_{\text{Lattice}}}{E_r}} \tag{5.6}$$

and the axial trapping frequency

$$\omega_x = \omega_{axial} = \sqrt{\frac{8E_r}{mw_0^2}}\sqrt{\frac{V_{\text{Lattice}}}{E_r}} \tag{5.7}$$

only determined by the waists of the two lattice laser beams.

In case that $\vec{e}_1 \cdot \vec{e}_2 \neq 0$, the additional cross-interference term in equation 5.4 plays a dominant role leading to a variation of the potential depth of neighboring lattice sites (see 5.3). Phase fluctuations may then lead to a time-dependent variation of the lattice geometry inducing heating and decoherence processes.

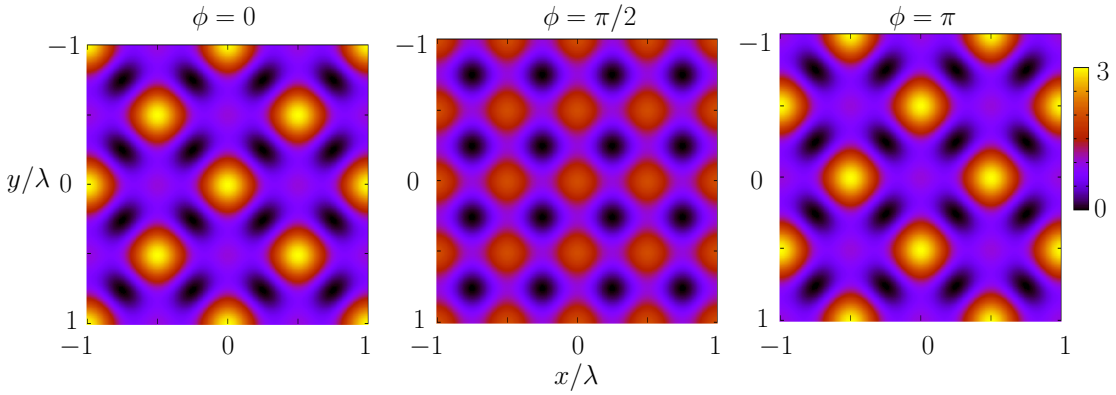

Figure 5.3: Variation of lattice geometry in the extreme case of $\vec{e}_1 \cdot \vec{e}_2 = 1$. a) $\phi = 0$ b) $\phi = \pi/2$ c) $\phi = \pi$. From a) to c), initially trapping lattice wells are transformed into non-trapping wells and vice versa

When a simple cubic square lattice is to be realized in the experiments, the polarizations of the two lattice laser beams are chosen orthogonal with respect to each other reducing cross-interference terms as much as possible. Residual interference due to not perfectly orthogonal polarizations are then further suppressed by choosing different laser frequencies for both lattice beams. For large frequency differences on the order of a few ten MHz, the residual interference averages out in the effective potential.

3D optical lattice configurations The 2D optical lattice can easily be upgraded to a 3D optical lattice by superimposing one additional retroreflected laser beam perpendicular to the 2D lattice laser beams. In our experiments on Fermi-Bose mixtures in 3D optical lattices (see chapter 6 and chapter 7), we have used a simple cubic 3D optical lattice (see Fig. 5.2). This has been realized by superimposing three mutually orthogonal standing waves (for a description of the setup, see section 5.4). Care has been taken to avoid additional cross interferences similar to the cross-interference term in equation 5.4 by choosing orthogonal polarizations and operating the different lattice beams at slightly different frequency to average out residual interferences. The resulting optical potential, including the "external" overlapping confinement due to the Gaussian shape of the lattice laser beams, is given by

$$\begin{aligned} V(x,y,z) &= V^x_{\text{Lattice}} \cos(kx)^2 \exp(-2(y^2+z^2)/w_x(x)^2) \\ &+ V^y_{\text{Lattice}} \cos(ky)^2 \exp(-2(x^2+z^2)/w_y(y)^2) \\ &+ V^z_{\text{Lattice}} \cos(kz)^2 \exp(-2(x^2+y^2)/w_z(z)^2) \end{aligned} \tag{5.8}$$

In practice, the resulting optical potential of equation 5.8 is often regarded as a homogeneous optical lattice superimposed with an external harmonic trapping potential. This is justified for typical experimental parameters and typical extensions of atomic clouds in the lattice. The trapping frequencies for the effective external harmonic confinement can be derived by expanding the potential of equation 5.8 in the case of $\lambda \ll x, y, z \ll w_x, w_y, w_z$.

The potential is then given by

$$\begin{aligned} V(x,y,z) &\approx V^x_{\text{Lattice}} \cos(kx)^2 \left(1 - 2\frac{(y^2+z^2)}{w_x^2}\right) \\ &+ V^y_{\text{Lattice}} \cos(ky)^2 \left(1 - 2\frac{(x^2+z^2)}{w_y^2}\right) \\ &+ V^z_{\text{Lattice}} \cos(kz)^2 \left(1 - 2\frac{(x^2+y^2)}{w_z^2}\right) \end{aligned} \tag{5.9}$$

which can be written as

$$\begin{aligned} V(x,y,z) &\approx V^x_{\text{Lattice}} \cos(kx)^2 + V^y_{\text{Lattice}} \cos(ky)^2 + V^z_{\text{Lattice}} \cos(kz)^2 \\ &+ \frac{1}{2} m(\omega_x^2 x^2 + \omega_y^2 y^2 + \omega_z^2 z^2) \end{aligned} \tag{5.10}$$

with the external trapping frequencies given by

$$\omega_x = \sqrt{\frac{4E_r}{m}\left(\frac{1}{w_y^2}\frac{V^y_{\text{Lattice}}}{E_r} + \frac{1}{w_z^2}\frac{V^z_{\text{Lattice}}}{E_r}\right)} \tag{5.11}$$

Similar equations hold for ω_y and ω_z and are obtained by a cyclic permutation of the indices.

In deep optical lattices, atoms are often regarded to be localized at individual lattice sites. For sufficiently deep optical lattices, the potential of a single optical lattice well can be approximated by a harmonic potential with the trapping frequency given by

$$\omega^{\text{lat}}_{x/y/z} = \frac{2E_r}{\hbar}\sqrt{\frac{V^{x/y/z}_{\text{Lattice}}}{E_r}} \tag{5.12}$$

In practice, the depths of the individual lattice wells and the associated trapping frequencies are of course position dependent due to the Gaussian shape of the lattice laser beams. The trapping frequencies at the individual lattice wells for deep optical lattices vary according to

$$\omega^{\text{lat}}_x = \omega^{\text{lat}}_x(0) \exp\left(-\frac{y^2+z^2}{w_x(x)^2}\right) \tag{5.13}$$

Whereas this effect is below the 10^{-5} level along the axis of propagation of the lattice beam (e.g. along the x-axis in the current example) for a waist of $w_x(0) \approx 100$ μm, it is much larger in radial direction. For typical extensions of bosonic and fermionic clouds on the order of $\frac{1}{4} \cdot w_x(0)$ the frequency of a single lattice well decreases from the center to the border of the cloud by 10%.

5.2 Energy spectrum of single particles confined in optical lattices

In the non-interacting or weakly interacting regime, the description of quantum degenerate gases in optical lattices can be reduced to a single-particle problem: Based on a calculation

of the energy spectrum of a single particle confined in a periodic potential, the many-body wavefunction of the quantum degenerate ensemble is constructed from single-particle eigenstates taking into account the statistics of the atoms. In the following section, an overview on the energy spectrum of particles moving in a periodic potential will be given. Starting from the energy spectrum in the case of an infinitely extended, homogeneous periodic potential, we will extend our studies to the more realistic case of a periodic potential superimposed with a harmonic trapping potential.

5.2.1 Homogeneous lattices - Bloch bands

The physics of particles moving in a periodic potential is a well-known quantum mechanical problem. It has first been considered rigorously in the context of solid state physics by Felix Bloch. In 1928, Bloch introduced the formalism to describe the conduction of electrons in crystalline solids [160]. The same formalism can be applied to atoms placed in a periodic potential which is in our case given by the dipole potential of the optical lattice. The wave functions of particles moving in a sinusoidal periodic potential $V(x) = V_0 \cos^2(kx)$ are given by Bloch wave functions which are the eigenfunctions of the corresponding Schrödinger equation given by

$$\left(-\frac{\hbar^2}{2m}\frac{\partial^2}{\partial x^2} + V_0 \cos^2(kx)\right)\Psi(x) = E\Psi(x), \tag{5.14}$$

where we have restricted ourselves to the one-dimensional case for convenience only.[3] According to Bloch's theorem, these Bloch functions can be written as product states of plane waves with quasimomentum q and envelope functions which have the same periodicity as the underlying potential. The wavefunctions are then given by

$$\Psi_{\vec{q},n}(\vec{r}) = \exp(i\vec{q}\cdot\vec{r})u_{n,\vec{q}}(\vec{r}). \tag{5.15}$$

with $u_{n,\vec{q}}(\vec{r})$ being the periodic envelope function. Due to the periodicity of the envelope functions, the wavefunctions of the confined particles are delocalized over the whole lattice. Note that in equation 5.15, an additional quantum number, the band index n, has been introduced. As the quasimomentum $\vec{q}$ is unique only up to a reciprocal lattice vector k, it is therefore convenient to restrict the quasimomenta to the first Brillouin zone, which means $-\hbar k < q_i < +\hbar k$. Due to this restriction, an infinite number of eigenfunctions and corresponding eigenstates exists for a given quasimomentum $\vec{q}$ which are labelled by the band index n. Characteristic for the energy spectrum of a particle confined in a periodic potential is the emergence of energy bands, which are separated by an energy gap depending on the strength of the periodic potential.

Fig. 5.4 shows the calculated energy spectrum of particles confined in optical lattices for various different lattice depths $V_0/E_r = s$. In the limit of vanishing optical lattice potential $s = 0$, the quasimomentum q is just the free particle momentum and the energy spectrum is given by the free particle energy parabola $E_q = \frac{q^2}{2m}$, mapped onto the first Brillouin zone. With increasing lattice depth, an energy gap appears between the different

[3] The generalization to the three-dimensional case with an assumed simple cubic periodic potential of the form $V(\vec{r}) = V_x \cos^2(kx) + V_y \cos^2(ky) + V_z \cos^2(kz)$ is straightforward, as the corresponding Hamiltonian is fully separable.

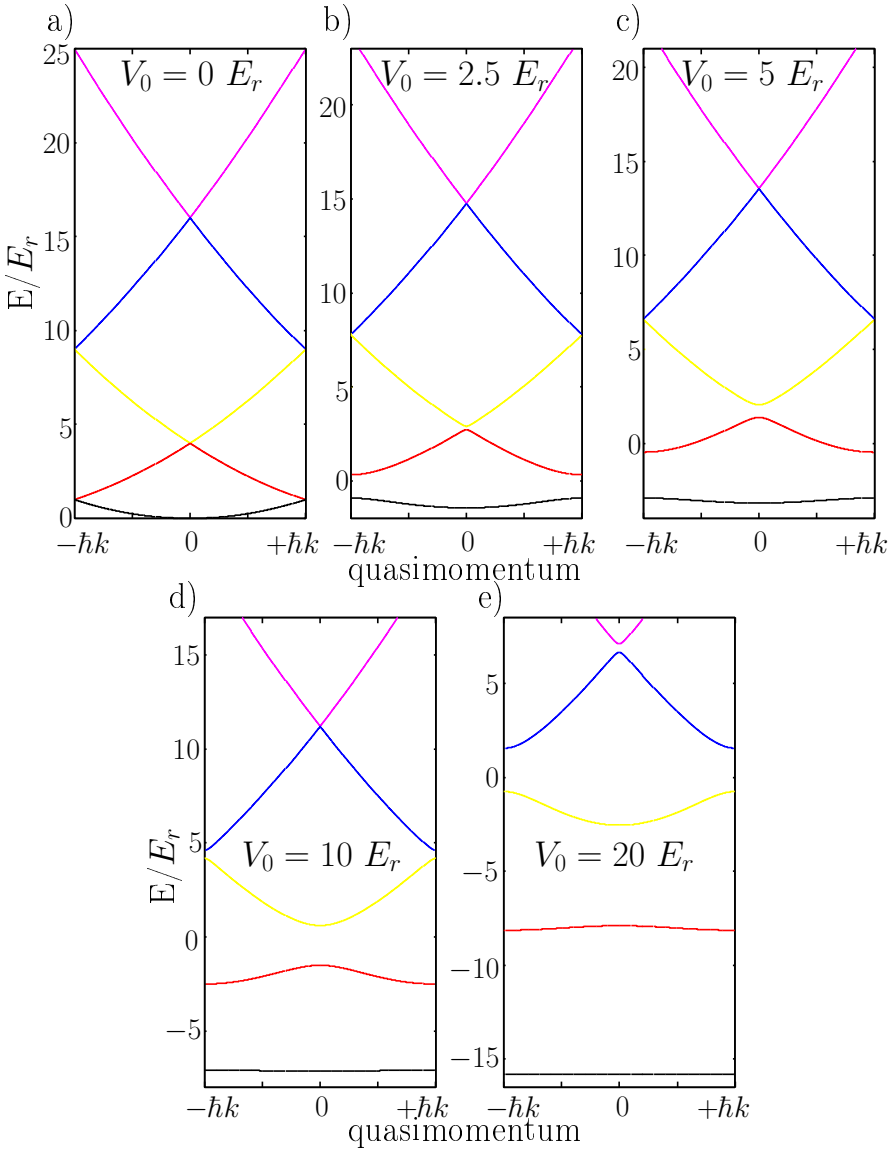

Figure 5.4: Energy spectrum of a single particle confined in a 1D periodic structure. The spectrum shows the typical band structure for different potential depths V_0. Higher bands have been mapped into the first Brillouin zone. In the case of an infinitely homogeneous optical lattice, states with energy above zero are untrapped. a) $V_0 = 0\ E_r$. The spectrum is given by the free particle energy parabola, mapped into the first Brillouin zone. b) $V_0 = 2.5\ E_r$. With increasing lattice depth the typical band structure develops and band gaps appear, starting with the lowest bands. c) $V_0 = 5\ E_r$. d) $V_0 = 10\ E_r$. e) $V_0 = 20\ E_r$. In the case of deep optical lattices, the bands correspond to the vibrational oscillator levels in a single lattice well.

bands whereas the width of each band becomes smaller. In the limit of infinitely deep optical lattices, the resulting bands correspond to the oscillator levels of a single lattice well which can be characterized by a harmonic trapping frequency (see equation 5.12).

5.2.2 Inhomogeneous optical lattices

In typical experiments dealing with ultracold atoms confined in optical lattices, the lattice potential is neither homogeneous nor infinitely extended. Usually, a harmonic confinement is superimposed with the optical lattice which has to be taken into account for a rigorous description of atoms confined in optical lattices (see Fig. 5.5). The harmonic confinement is often due to an additional optical or magnetic potential that is used to prepare quantum degenerate atomic ensemble prior to ramping up the optical lattice and is independent of the optical lattice potential itself. In addition, the optical lattice beams themselves produce an additional harmonic confinement which is particularly strong in the radial direction (see section 5.1.1.2). This additional harmonic confinement is given by equation 5.11 and is thus strongly dependent on the lattice depth and increases with increasing lattice depth. When independent tuning of lattice depth and external harmonic confinement is desirable, it is thus advisable to make the lattice potential as homogeneous as possible and to choose large beam waists for the retroreflected lattice beams in addition to an independent magnetic or optical external confinement. This configuration also ensures that the depth of a single lattice well is no longer dependent on the position of the lattice well (compare equation 5.13).

A 1D lattice potential of $V_{\text{Lattice}} = 5\ E_r$ with additional harmonic confinement of $\omega_{\text{Rb}} = 2\pi \cdot 100\text{Hz}$ is shown in Fig. 5.5. The assumed parameters correspond to a realistic experimental configuration. The inhomogeneity of the lattice has important influence on the band structure. The resulting spectrum can be assumed to become position dependent as illustrated in Fig. 5.6 for the same parameters.

However, a rigorous treatment of single particles confined in inhomogeneous optical lattices can only be obtained by a calculation of the corresponding one-particle energy spectrum: The energy spectrum of the periodic potential with superimposed harmonic confinement can be calculated by numerically solving the one-dimensional Schrödinger equation

$$\left(-\frac{\hbar^2}{2m}\Delta + V(x)\right)\Psi(x) = E\Psi(x) \tag{5.16}$$

with

$$V(x) = \frac{1}{2}m\omega_{\text{ho}}^2 x^2 + sE_r\cos(kx+\phi)^2 \tag{5.17}$$

and an arbitrarily chosen phase $\phi = 16.5°$ (see below). Fig. 5.7 shows the calculated spectrum as a function of the depth of the optical lattice. In the calculations, the atomic recoil energy $E_r = \hbar^2k^2/2m$, giving a typical energy scale for the band structure of a pure periodic potential, has been assumed to be 12.5 times the harmonic oscillator energy scale $\hbar\omega_{\text{ho}}$. This corresponds to the assumption $k^2\hat{a}^2 = 25$, where $\hat{a}$ is the harmonic oscillator length. Although this assumption is unrealistic in actual experiments where $E_r/\hbar\omega_{ext} \approx 50 - 100$, it does not affect the qualitative behavior of the harmonic oscillator eigenstates (for $s = 0$) transferring into eigenstates of the combined potential with increasing s. Apart from significantly reducing the dimensionality of the problem in terms of basis vectors that

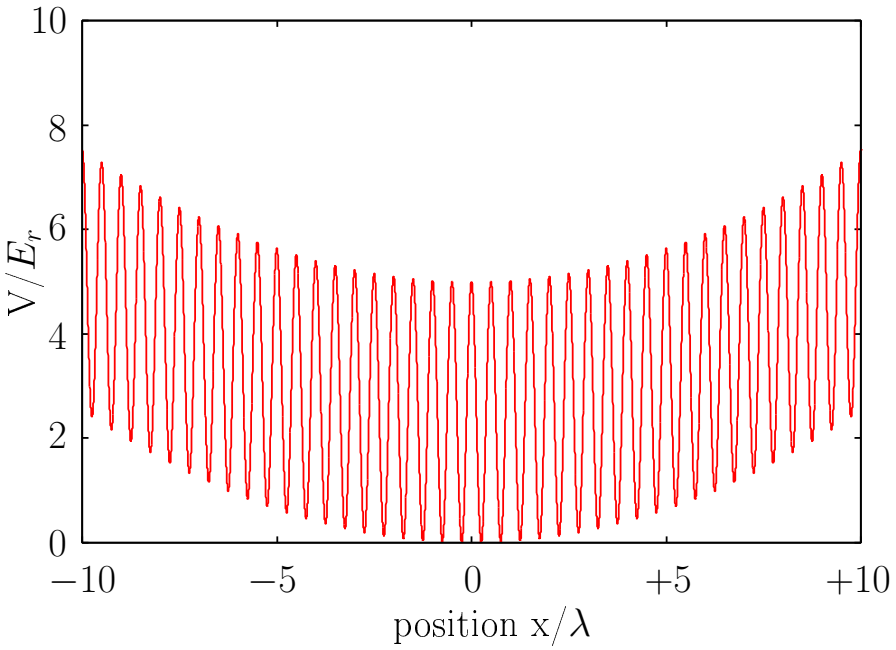

Figure 5.5: Potential of a 1D inhomogeneous optical lattice. The chosen parameters correspond to typical experimental parameters: $V_0 = 5\ E_r$, $a_{\mathrm{ho}} = \lambda$ which for ($\lambda = 1.03\mu$m) correspond to a harmonic trapping frequency for ^{87}Rb of $\omega = 2\pi \cdot 100$ Hz

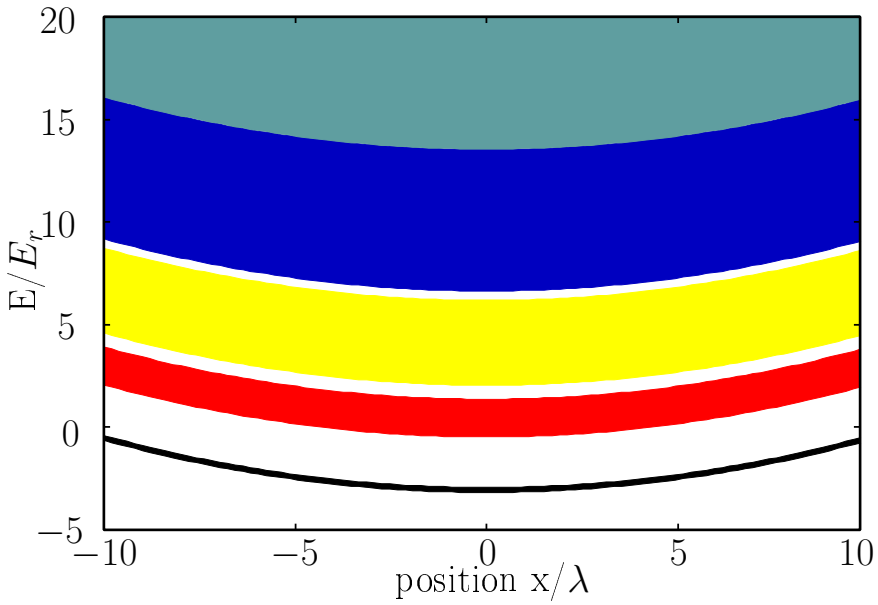

Figure 5.6: Sketch of the position dependence of the resulting band structure for an inhomogeneous optical lattice at $V_0 = 5\ E_r$ and additional harmonic confinement characterized by the harmonic oscillator length $a_{\mathrm{ho}} = \lambda$, corresponding to a harmonic oscillator frequency for ^{87}Rb of $\omega_{Rb} = 2\pi \cdot 100$ Hz.

have to be taken into account, the above assumption increases the clarity of the spectrum which hence does not consist a few $50 - 100$ energy levels in the first band.

Already from the spectrum, the eigenstates visually fall into two categories, the energy eigenstates with $E < E_r$ at $s = 0$ and the eigenstates with $E > E_r$ at $s = 0$. Whereas the energy of the eigenstates with $E < E_r$ for $s = 0$ decrease continuously relative to the lowest eigenenergy, the energy of eigenstates with $E > E_r$ at $s = 0$ partly decreases or increases and shows a series of avoided crossings.

Fig. 5.8 and 5.9 show the single-particle eigenstates and eigenfunctions in the combined potential for 4 different lattice depths. Starting from the harmonic oscillator eigenenergies and eigenstates in Fig. 5.8 a) at $V_{\mathrm{Lattice}} = 0$, with increasing lattice depth a pseudo band gap opens up in the center of the harmonic trap and the eigenfunctions become more and more localized. The localization process starts at the boundary of the potential (see Fig. 5.8 b)) and extends with increasing lattice depth down to the center of the trap (see Fig. 5.9 c) and Fig. 5.9 d), corresponding to 8 E_r and 40 E_r respectively). In the limit of deep optical lattices (see Fig. 5.9d)), the eigenstates are each localized on a different lattice well with site index i where i is the position of the lattice well in units of the lattice well separation given by $\lambda/2$ relative to $x = 0$. The eigenenergies of these localized states are given by

$$E_i^1 = \frac{1}{2}\hbar\omega_{\mathrm{Lattice}} + \frac{1}{2}m\omega^2\left(\lambda/2\right)^2 i^2 \tag{5.18}$$

in the first pseudoband and

$$E_i^n = (\frac{1}{2} + (n-1))\hbar\omega + \frac{1}{2}m\omega^2\left(\lambda/2\right)^2 i^2 \tag{5.19}$$

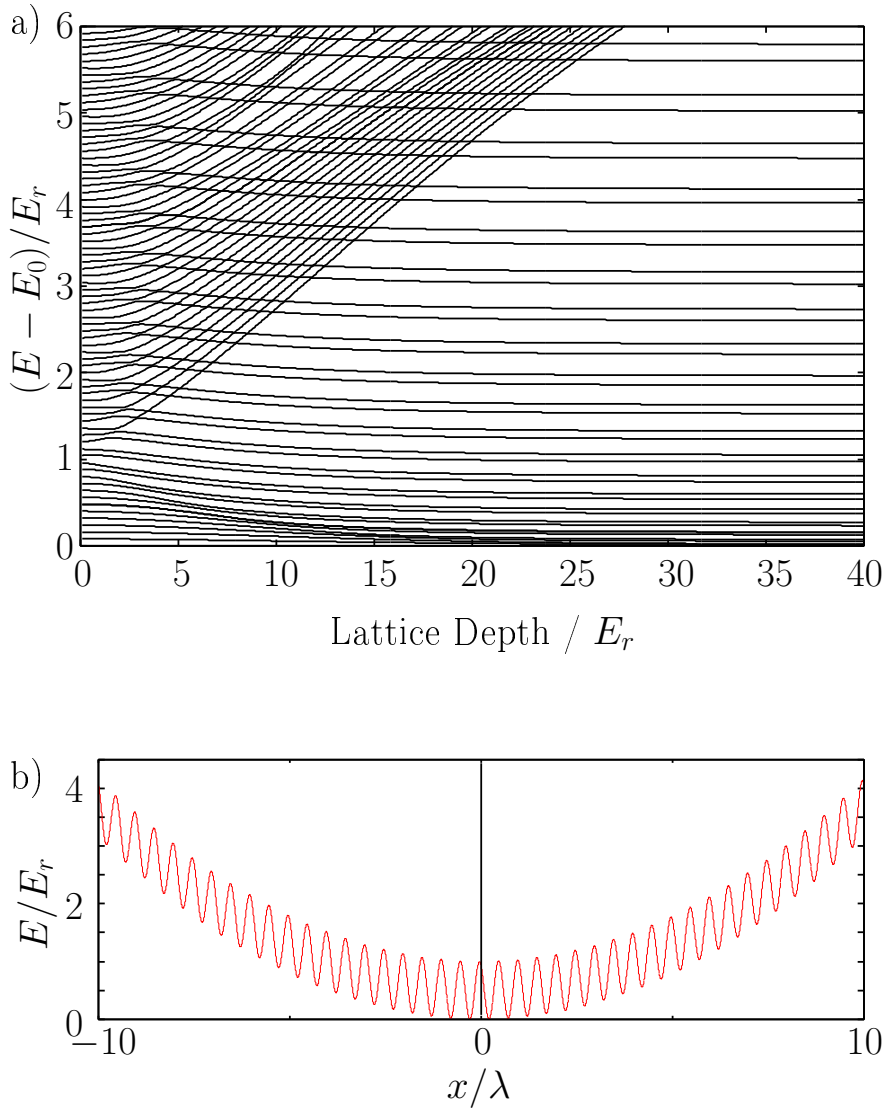

Figure 5.7: a) Eigenstates of a single particle confined in a periodic potential of the form $V_{\text{periodic}} = V_0 \cos(kx + \phi)^2$ which is overlapped with a harmonic potential $V_{\text{ho}}(x) = \frac{1}{2}m\omega^2 x^2$. We assume $12.5\hbar\omega = E_r$. This corresponds to $k^2\hat{a}^2 = 25$ where $\hat{a}$ is the harmonic oscillator length. We have introduced a symmetry breaking (see b)) into the problem by choosing an arbitrary phase $\phi = 16.5°$. The periodic potential is then no longer symmetric with respect to $x = 0$. This avoids degeneracy of single particle states in the deep optical lattice where the energy of the single particle eigenstates are given by $E_i = \frac{1}{2}m\omega^2 \left(\frac{\lambda}{2}\right)^2 i^2$ where i is the site position in units of $\lambda/2$ with respect to $x = 0$. b) Sketch of the periodic plus harmonic potential used for the calculations in a)

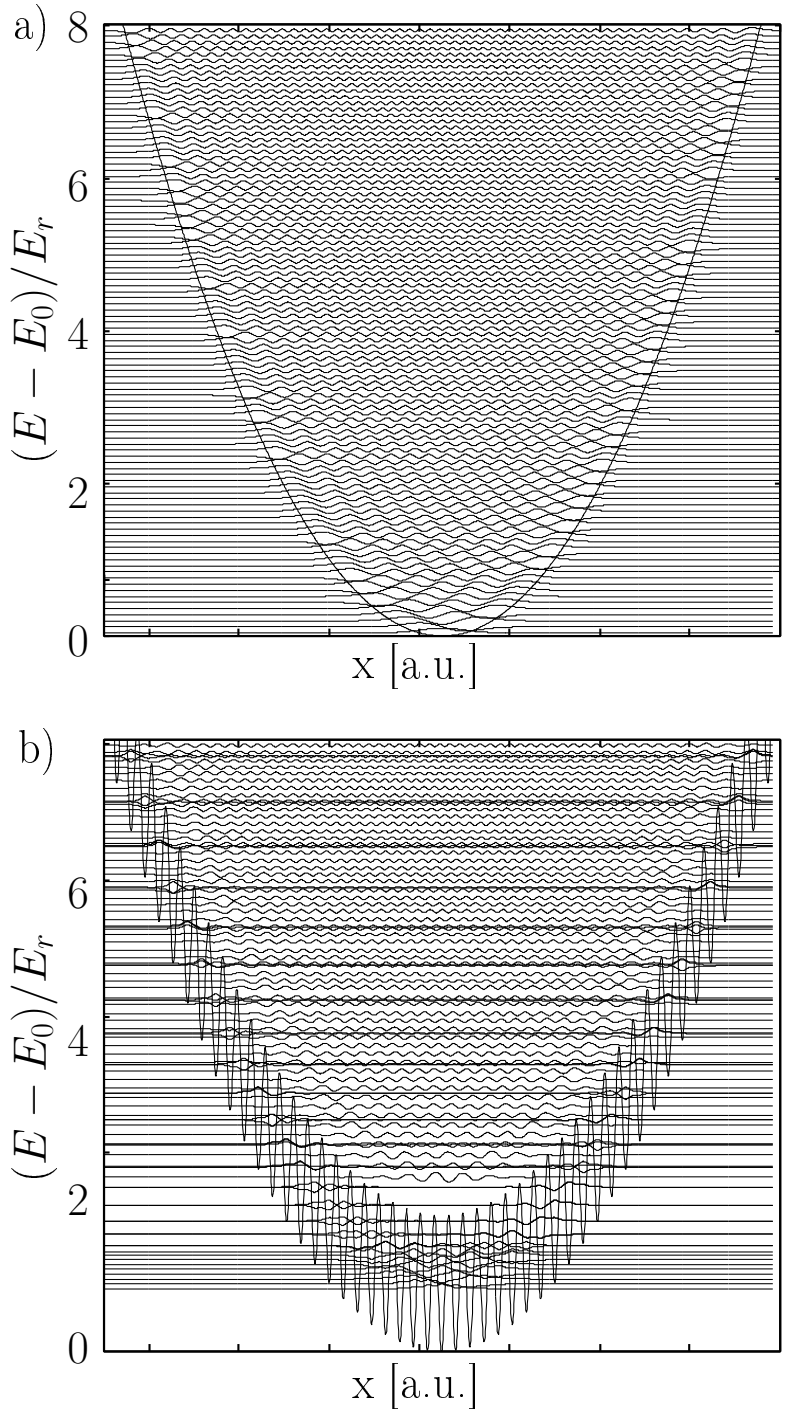

Figure 5.8: Single particle eigenenergies and eigenfunctions for a) $V_0 = 0$ b) $V_0 = 4E_r$. In all cases, we assume $E_r = 12.5\hbar\omega$. Plotted are the energy eigenvalues along with the eigenfunctions.

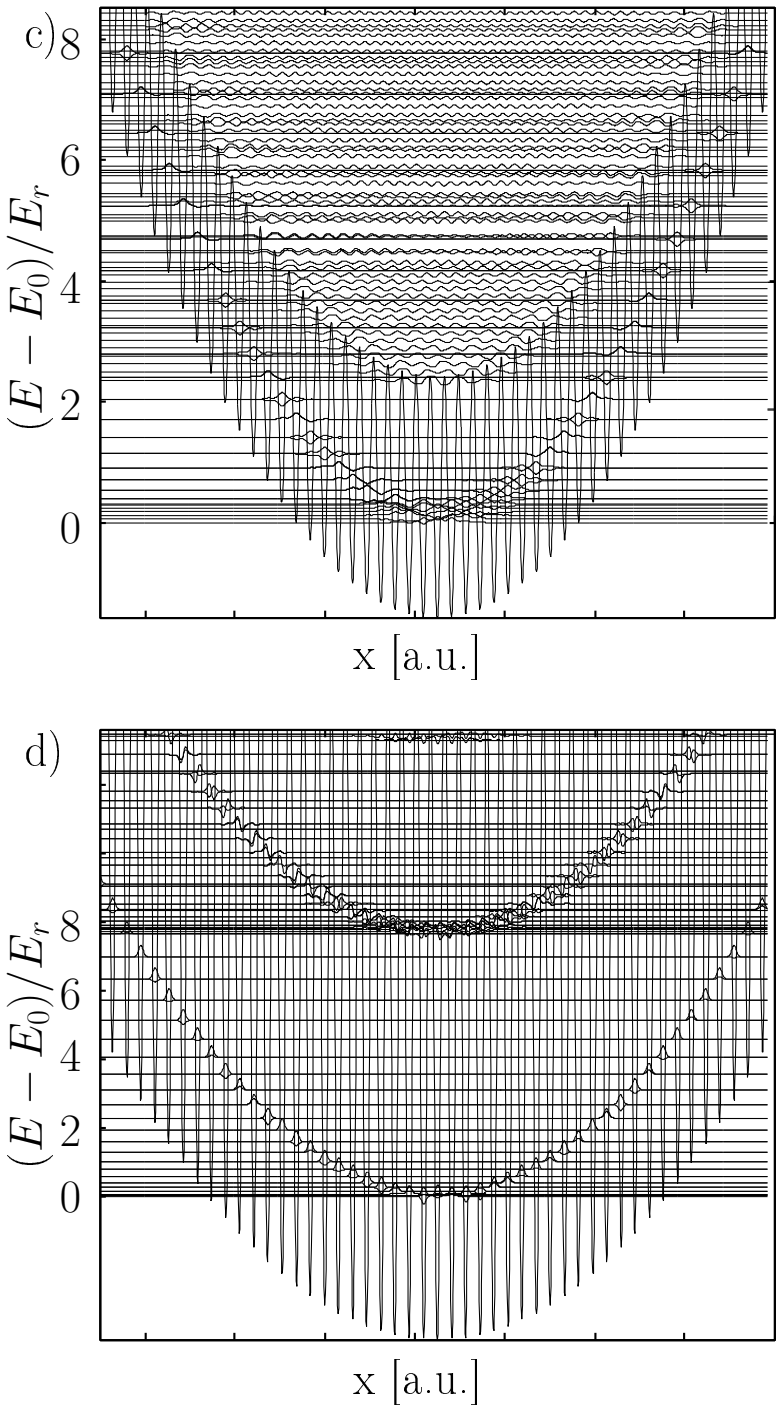

Figure 5.9: Single particle eigenenergies and eigenfunctions for c) $V_0 = 8E_r$ d) $V_0 = 40E_r$. In all cases, we assume $E_r = 12.5\hbar\omega$. In all cases, we assume $E_r = 12.5\hbar\omega$. Plotted are the energy eigenvalues along with the eigenfunctions.

in the nth pseudoband where ω_{Lattice} is the harmonic oscillator frequency on a single lattice well given by (see equation 5.12). Note that in the case of very steep harmonic confinement, states in the boundaries of the first pseudoband can become degenerate to or have even higher energy than states in the center of the second pseudoband. Tunnelling between the first and the second pseudoband is nevertheless suppressed as long as these states are localized at different positions in space. In the assumed example, we have introduced a symmetry breaking into the problem (see Fig. 5.7b)) by choosing an arbitrary phase $\phi = 16.5°$ in the periodic potential (see equation 5.17). The periodic potential is then no longer symmetric with respect to $x = 0$. This avoids degeneracy of single particle eigenstates which, in the limit of deep optical lattices, are localized on either side of $x = 0$.

It has been pointed out by Viverit and coworkers [161] that the structure of eigenstates in a combined periodic plus harmonic potential along with the Pauli exclusion principle for fermionic atoms is very favorable for the creation of a lattice with unit occupancy with very high efficiency [161]. The localization of eigenfunctions in deep optical lattices has been probed experimentally with fermions loaded into a one-dimensional optical lattice by selectively addressing these localized states with a radio-frequency field [162].

5.3 Many-particle approach

Although the single-particle approach of section 5.2 is very useful to describe an ensemble of non-interacting particles confined in an optical lattice, the single-particle approach is invalid when interactions between the particles cannot be neglected or even dominate the behavior of the system. In this case, a many-particle approach has to be followed. An appropriate model for the description of particles confined in a periodic potential is the Hubbard model [163, 164]. It has been introduced in solid state physics to describe the transition between conducting and insulating systems. In the following, we will derive the Hubbard Hamiltonian from the full many-particle Hamiltonian and introduce the main approximate assumptions of the model. We will then discuss the model in the context of fermionic and bosonic particles and finally extend the Hamiltonian to the Bose-Fermi Hubbard Hamiltonian for the description of interacting Bose-Fermi mixtures in an optical lattice.

5.3.1 The Hubbard model

Consider a single-component many-particle system of fermions or bosons confined in a periodic potential which is overlapped with an additional harmonic trapping potential similar to equation 5.10 and interacting via an arbitrary interaction potential $W(\vec{r}, \vec{r}')$. The full many-particle Hamiltonian is then given by

$$\begin{aligned} H_{B/F} &= \int d^3r \Psi^\dagger_{B/F}(\vec{r}) \left(\frac{\vec{p}}{2m_{B/F}} + V_{\text{Lattice}} + V_{\text{ho}} \right) \Psi_{B/F}(\vec{r}) \\ &+ \frac{1}{2} \int d^3r d^3r' \Psi^\dagger_{B/F}(\vec{r}) \Psi^\dagger_{B/F}(\vec{r}') W(\vec{r}, \vec{r}') \Psi_{B/F}(\vec{r}) \Psi_{B/F}(\vec{r}') \end{aligned} \tag{5.20}$$

where the first term accounts for kinetic and potential energy of the ensemble of particles and the second term is the interaction energy. $\Psi_{B/F}(\vec{r})$ are the bosonic and fermionic field operators satisfying the bosonic commutation and fermionic anticommutation relation.

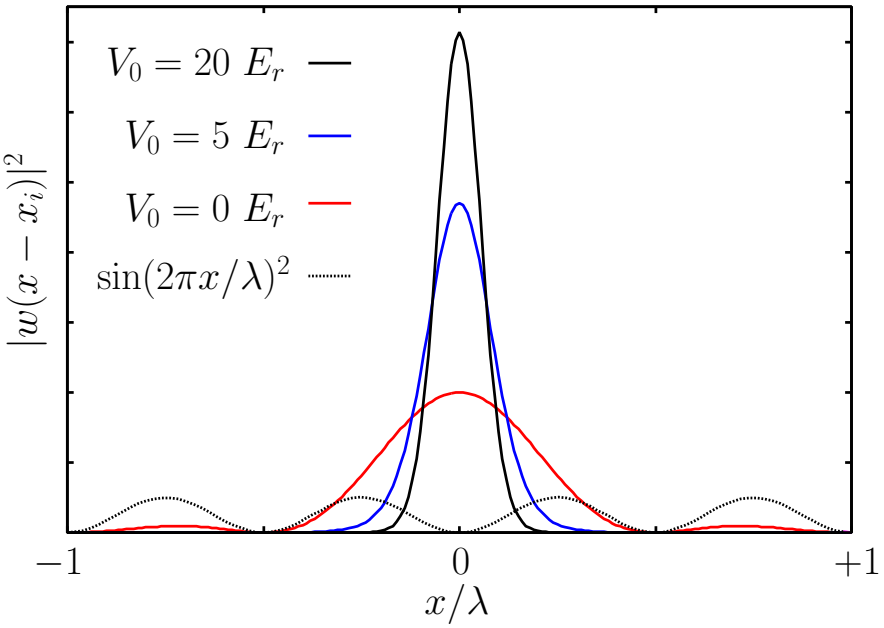

Figure 5.10: Probability density of the Wannier functions of the lowest Bloch band. I have plotted the probability density for $V_0 = 0\ E_r$, $V_0 = 5\ E_r$ and $V_0 = 20\ E_r$. With increasing lattice depth, the Wannier functions become more and more localized to a single lattice well. In addition, I have plotted the underlying $\sin(kx)^2$-potential.

For the expansion of the field operators, an appropriate basis of single-particle states is needed. As pointed out in section 5.2.1, the eigenstates of a particle confined in a periodic potential are given by the Bloch functions which are delocalized over the whole lattice. However, when the lattice is deep and tunnelling is strongly suppressed, atoms are localized on a certain lattice site. Hence, another approach seems more intuitive: A convenient complete set of orthonormal functions is given by the so-called Wannier functions [165]. The Wannier functions are the Fourier transform of the Bloch functions and defined as follows:

$$w_n(\vec{r} - \vec{r}_i) = \frac{1}{\mathcal{N}^{1/2}} \sum_{\vec{q}} \exp(-i\vec{q} \cdot \vec{r}_i) \Psi_{n,\vec{q}}(\vec{r}) \tag{5.21}$$

where $\mathcal{N}$ is a normalization constant and $\Psi_{n,\vec{q}}$ is the Bloch function of the band n with quasimomentum $\vec{q}$ and band index n. In contrast to the Bloch functions, the Wannier functions $w_n(\vec{r} - \vec{r}_i)$ are localized at a lattice site $\vec{r}_i$, as illustrated in Figure 5.10 for lattice depth of 0 E_r, 5 E_r and 20 E_r.

Based on the Wannier functions, the field operators can be expanded $\Psi_{B/F}(\vec{r}) = \sum_i w_n(\vec{r} - \vec{r}_i)\ a_i$ and the Hamiltonian in equation 5.20 reads

$$H = -\sum_{i,j} J_{ij} a_i^\dagger a_j + \frac{1}{2} \sum_{ijkl} U_{i,j,k,l} a_i^\dagger a_j^\dagger a_k a_l \tag{5.22}$$

with the tunnelling matrix elements

$$J_{ij} = \int d^3r w_1^*(\vec{r}-\vec{r}_i)\left(\frac{\vec{p}}{2m_{B/F}} + V_{\text{Lattice}} + V_{\text{ho}}\right) w_1(\vec{r}-\vec{r}_j) \tag{5.23}$$

and the interaction matrix elements

$$U_{ijkl} = \int d^3r w_1^*(\vec{r}-\vec{r}_i) w_1^*(\vec{r}-\vec{r}_j) W(\vec{r},\vec{r}') w_1(\vec{r}-\vec{r}_k) w_1(\vec{r}-\vec{r}_k). \tag{5.24}$$

In the above equation, $a_i^\dagger/a_i$ stands for the bosonic $b_i^\dagger/b_i$ and fermionic $f_i^\dagger/f_i$ creation and annihilation operator, and we have restricted ourselves to particles confined in a single Bloch band for ease of notation.

The Hubbard model introduces a number of stringent simplifications which are, however, well-justified for the case of dilute ultracold gases in optical lattices.

1. First, the Hubbard model restricts to the lowest Bloch band and is thus a good approximation for particles in a periodic potential at sufficiently low filling and temperatures.

2. Second, due to the localized nature of the Wannier functions, only nearest neighbor tunnelling matrix elements are considered (subsequently denoted by $\langle i,j\rangle$).

3. Third, the interaction potential $W(\vec{r},\vec{r}') = V(\vec{r}-\vec{r}')$ is assumed to be strongly peaked at $\vec{r}=\vec{r}'$ so that long-range interactions can be ignored. The numerical value for the off-site interaction matrix elements are neglected compared to the large onsite matrix elements $U_{i,i,i,i}$. In dilute atomic gases, interactions between particles can even be described by a single s-wave-scattering length a_s due to the suppression of nonzero angular momentum scattering at sufficiently low temperatures. The interaction potential is then often simply described by a contact potential of the form $V(\vec{r}-\vec{r}') = \frac{4\pi\hbar^2}{m}\delta(\vec{r}-\vec{r}')$.[4]

With these simplifying assumptions including the contact interaction potential, the Hubbard Hamiltonian reads:

$$H = -\sum_{\langle i,j\rangle} a_i^\dagger a_j + \frac{1}{2}U_0 \sum_i n_i(n_i-1) + \epsilon_i n_i \tag{5.25}$$

where $J_{i,j} = J$ for $\{i,j\} \in \langle i,j\rangle$, $U_0 = U_{i,i,i,i}$ and $n_i = a_i^\dagger a_i$. The term ϵ_i

$$\epsilon_i = \int d^3r w_1^*(\vec{r}-\vec{r}_i) V_{\text{ho}}(\vec{r}) w_1(\vec{r}-\vec{r}_i) \tag{5.26}$$

is due to the diagonal tunnelling elements J_{ii} and a site dependent energy offset due to the additional trapping potential V_{ho}.

The tunnelling and interaction matrix elements are given by the following integrals

$$J_{i,j} = \int d^3r w_1^*(\vec{r}-\vec{r}_i)\left(\frac{\vec{p}}{2m_{B/F}} + V_{\text{Lattice}} + V_{\text{ho}}\right) w_1(\vec{r}-\vec{r}_i) \tag{5.27}$$

[4]For single-component fermions, s-wave scattering is forbidden due to the Pauli exclusion principle, so that in the considered limit the fermions are non-interacting.

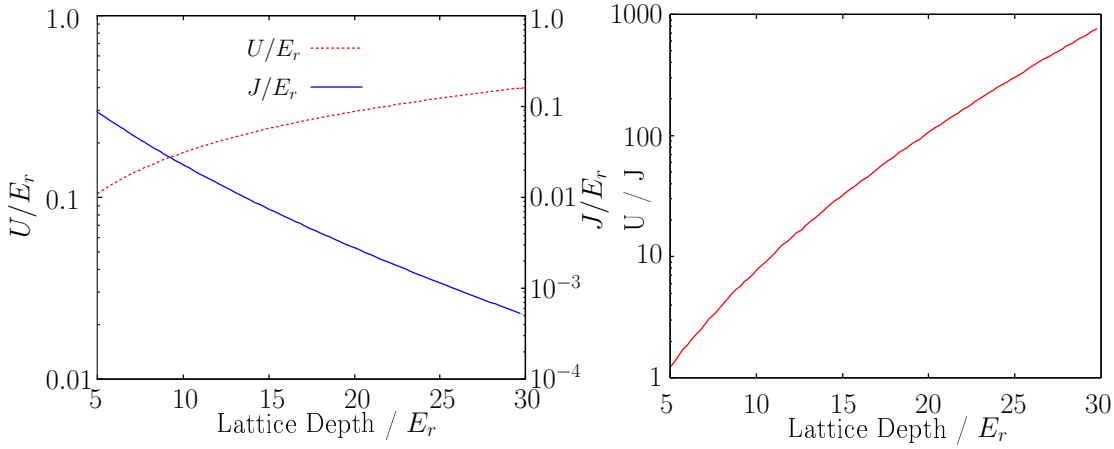

Figure 5.11: Interaction and tunnelling matrix element as a function of lattice depth a) Whereas the interaction matrix element U increases only moderately with lattice depth, the tunnelling matrix element is exponentially suppressed. b) Ratio of U/J as a function of lattice depth. The ratio can be tuned over several orders of magnitude within experimentally accessible lattice depths.

and

$$U_0 = \frac{4\pi\hbar^2 a_s}{m} \int d^3r \, |w_1(\vec{r})|^4 \tag{5.28}$$

which can be calculated analytically in the limit of deep optical lattices $V_0 \gg E_r$. In this case, the Wannier functions can be approximated by the Gaussian ground state of the harmonic oscillator with trapping frequency ω_{Lattice} given by equation 5.12. One then obtains the following expression for the on-site matrix element in the tight-binding limit [18, 166]:

$$U = 2\sqrt{\frac{2}{\pi}} k a_s E_r \left(V_{\text{Lattice}}/E_r\right)^{3/4} \tag{5.29}$$

The tunnelling matrix element is directly related to the bandwidth of the lowest Bloch band and can be obtained analytically in the limit $V_{\text{Lattice}} \gg E_r$ [166]:

$$J = \frac{4E_r}{\sqrt{\pi}} \left(\frac{V_0}{E_r}\right)^{3/4} \exp(-2\sqrt{V_0/E_r}). \tag{5.30}$$

In Fig. 5.11 a), both the interaction matrix elements and the tunnelling matrix elements are plotted as a function of lattice depth. For the calculation of the interaction matrix elements, we have assumed $a_s = 100a_0$ which corresponds to the $s-$wave scattering length between two ^{87}Rb atoms in the $|F = 2, m_F = 2>$ state. Whereas U increases only moderately with increasing lattice depth, the kinetic energy falls off exponentially.

From equations 5.30 and 5.29, it is obvious that the ratio of onsite interaction U to tunnelling J can be tuned over several orders of magnitude without changing the s-wave scattering length a_s (see Fig. 5.11b)). By changing the lattice depth, atoms confined in optical lattices give the opportunity to access the strongly interacting/correlated regime without making use of mechanisms to tune the scattering length such as Feshbach resonances.

5.3.2 Phase diagram of repulsively interacting bosons in 3D optical lattices

The phase transition of a superfluid to a Mott-Insulating state in repulsively interacting bosons has first been discussed in the context of liquid Helium [152]. In 1998, D. Jaksch and coworkers pointed out that the Bose-Hubbard Hamiltonian is suitable for the description of bosons confined in 3D optical lattices and discussed the phase transition in this new context [18]. In 2002, this phase transition has been observed experimentally in a seminal experiment by Markus Greiner and coworkers with ^{87}Rb prepared in a single Zeeman state loaded into a three dimensional optical lattice [19].

Let us consider the Hubbard Hamiltonian in the regime of weak interactions where onsite interaction is negligible against the kinetic energy ($U \ll J$). In this limit, the atoms are delocalized across the lattice. The atoms condense into the lowest Bloch state and form a macroscopic wave function. The many-body ground state is superfluid and can be written as

$$\Psi_{\text{Superfluid}} \propto \left(\sum_{i=1}^{N} a_i^\dagger \right)^N |0\rangle \tag{5.31}$$

where $|0\rangle$ is the vacuum state (empty lattice) and N the number of lattice sites. In the case of the macroscopic wavefunction, the probability distribution of the local occupation numbers n_i obeys a Poissonian distribution.

In the limit $U/J \gg 1$, however, atom number fluctuations are energetically too expensive and the ground state becomes a product of local Fock states:

$$\Psi_{\text{Mott}} \propto \prod_{i=1}^{N} \left(a_i^\dagger \right)^n |0\rangle \tag{5.32}$$

The quantum critical point for the phase transition for a superfluid to Mott-insulator state with n atoms per lattice site has been calculated in mean-field theory and is determined by [152, 167, 18, 168]

$$U = z(2n + 1 + 2\sqrt{n(n+1)})J \tag{5.33}$$

where z is the number of nearest neighbors in the lattice. In the case of the simple cubic lattice in our experiment, $z = 6$. In the case of the inhomogeneous system, when a weak harmonic trap is overlapped upon the optical lattice, the above criterion can nevertheless be used to estimate the quantum critical point of the system. The density is then nonuniform, increasing from the edges of the cloud towards the center. The lattice depth needed to observe the Mott-insulator transition is then different for shells with a local occupation of n. Shells with different occupation number n will undergo the phase transition at different optical lattice depths, starting from the edges of the cloud towards the center[169].

Similar to the seminal experiment by Markus Greiner and coworkers [19], we have been able to observe the phase transition of a superfluid to a Mott-insulator state in our experiment in a ^{87}Rb $|F = 2, m_F = 2\rangle$ cloud loaded into a three-dimensional optical lattice with $\lambda = 1030$ nm. By adiabatically ramping up the optical lattice we have been able to reversibly tune the system from the superfluid to the Mott-insulator ground state. In our experiment, we have estimated the peak occupation number n of the cloud to be < 6.

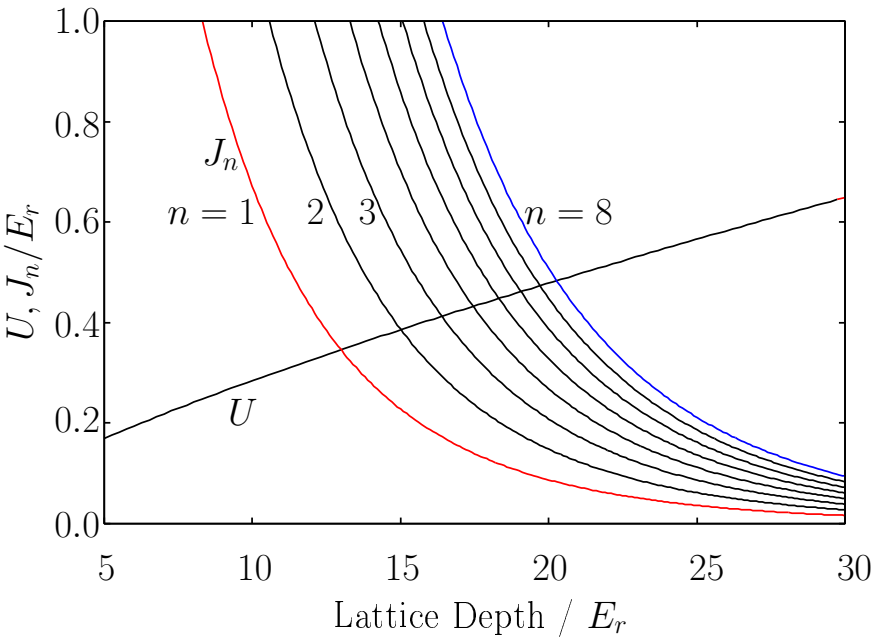

Figure 5.12: Quantum critical point for the superfluid to Mott insulator state for different lattice occupancies $n = 1, ...8$. The quantum phase transition for a lattice occupancy n occurs at the lattice depth where $U = z(2n + 1 + 2\sqrt{n(n+1)})J$ [168].

Based on a band structure calculation we then obtain quantum critical points of 13.0 E_r, 15.0 E_r, 16.4 E_r, 17.5 E_r and 18.4 E_r (see Fig. 5.12). The observation of the superfluid to Mott insulator transition is done by time-of flight imaging of the bosonic cloud. The time-of-flight images reveal the momentum distribution of the atoms. Fig. 5.13 shows series of images of the bosonic cloud after sudden switch off the lattice and 15 ms time-of-flight for different lattice depth. At low lattice depth, we observe a characteristic interference pattern with a series of peaks at momenta $n\hbar\vec{k}$ around the central $p = 0$ momentum peak. The interference pattern reflects the momentum components of the lowest Bloch state with quasimomentum $q = 0$ (see equation 5.31). Above a certain lattice depth (≈ 13 E_r), these interference fringes begin to decrease (b) and c)) and eventually vanish completely at lattice depth of ≈ 20 E_r (d). The disappearance of the interference pattern with increasing lattice depth indicates the loss of phase coherence associated with the transition from the superfluid state to the Mott insulator state. In the pure Mott state, the atomic cloud is a product of local Fock states with a Gaussian momentum distribution. The continuous decrease of the interference pattern instead of a sudden transition is due to the inhomogeneity of the system with various phase transition points for different occupation numbers. Ramping down the lattice again, the interference pattern can be restored proving that the system remains in the ground state during the ramp-up and down process.[5]

Strictly speaking, the disappearance of phase coherence is a necessary but not a sufficient sign of the phase transition from the superfluid to Mott insulator state and addi-

[5]For a quantitative analysis of the time-of-flight images, see chapter 6.

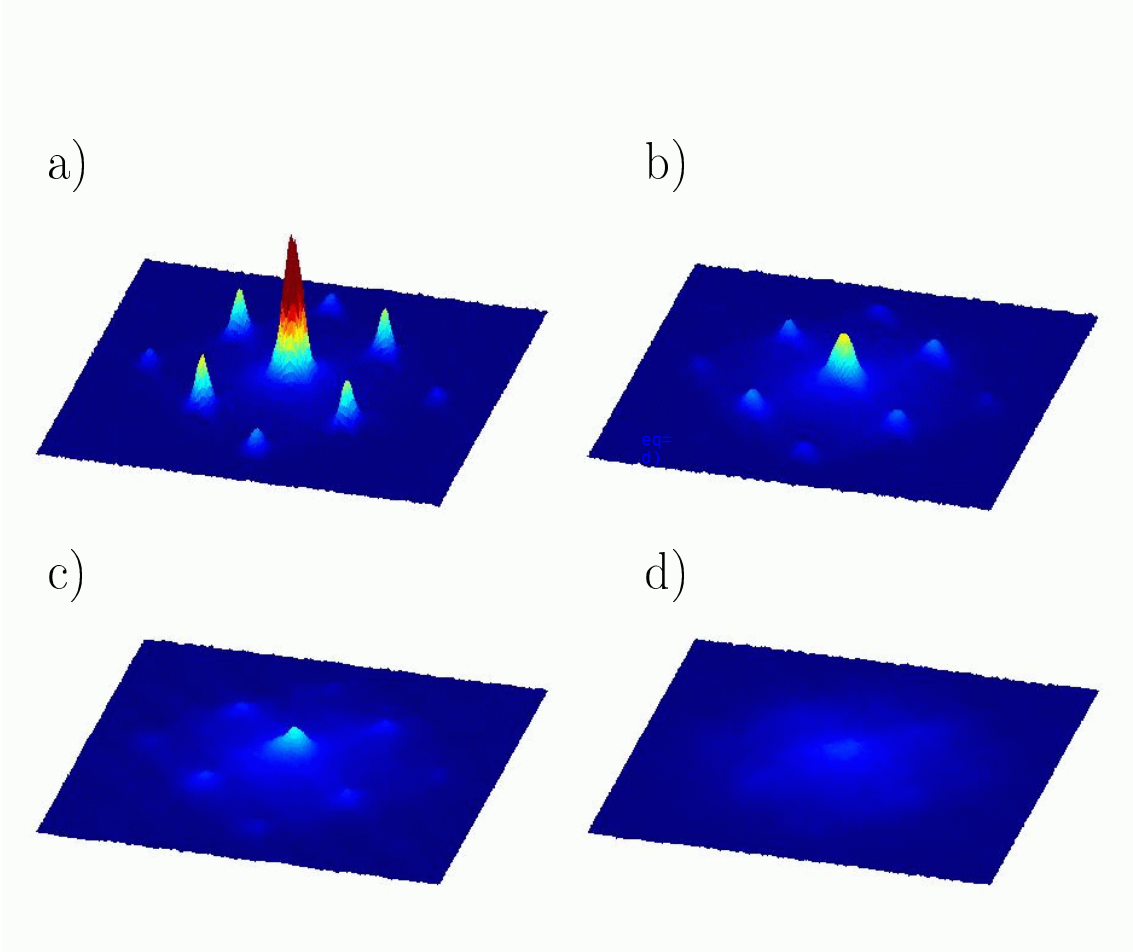

Figure 5.13: Superfluid to Mott-insulator transition for a bosonic cloud loaded into an optical lattice. At lattice depth of $V_{\text{Lattice}} = 10E_r$ the typical matter wave interference pattern is observed. With increasing lattice depth (b) and (c)) the interference pattern decreases and vanishes in the limit of deep optical lattices (d) ($> 20\ E_r$).

tional evidence is required. Further evidence for the Mott-Insulator state can be obtained by probing the excitation spectrum of the system similar to the experiment by Markus Greiner and coworkers [19]. Deep in the Mott insulator state, a finite excitation gap with energy U is observed corresponding to the system's increase in energy when an atom tunnels to a lattice well which is already occupied by one atom. The shell structure of the Mott-insulator state has been probed using spatially selective microwave transitions and spin-changing collisions [169]. By using density-dependent transition frequency shifts on the clock transition in ^{87}Rb, Campbell and coworkers have been able to spectroscopically identify sites with different occupation numbers [170].

5.3.3 Fermions confined in optical lattices

At ultralow temperatures, single-component Fermi gases can be regarded as non-interacting ideal gases. $s-$wave scattering is forbidden due to the Pauli exclusion principle and the cross-section of the next higher order process ($p-$wave scattering) decreases with temperature according to $\sigma_p \propto T^2$. The Fermi Hubbard Hamiltonian then reduces to

$$H = -J \sum_{<i,j>} f_i^\dagger f_j + \epsilon_i m_i. \tag{5.34}$$

with $\epsilon_i = 0$ in the homogeneous case. Although the Hamiltonian is simple, it exhibits a crossover from an insulating state with $\langle m_i \rangle = 1$ (band insulator) to a conducting state with $\langle m_i \rangle < 1$ (see [171]; experimentally, the band insulator has been observed in pioneering experiments with fermions loaded into optical lattices by Köhl and coworkers [156]).

In this case, it is more intuitive to go back to the single particle picture of section 5.2.2. At $T = 0$, N fermions occupy the N energetically lowest eigenstates of the system. The energy of the last occupied quantum state is referred to as the Fermi energy of the system E_F. For $T > 0$, N fermions distribute over the available energy eigenstates according to Fermi Dirac statistics

$$f(E) = \frac{1}{\exp((E-\mu)/kT) + 1} \tag{5.35}$$

where μ is the chemical potential which is determined via the condition

$$N = \int dE g(E) f(E) \tag{5.36}$$

where $g(E)$ is the density of states.

When ramping up the optical lattice, the system transforms from a pure 3D harmonic potential with eigenstates and eigenenergies given by

$$E_{n_x,n_y,n_z} = (n_x + n_y + n_z + \frac{3}{2})\hbar\omega_{\text{ho}} \tag{5.37}$$

into a tight optical lattice. Whereas the structure of eigenstates of the inhomogeneous system is complicated in the intermediate regime where tunnelling between different lattice sites is still allowed (for the 1D eigenstates of the periodic plus harmonic potential, see section 5.2.2), it becomes very simple in the limit of deep optical lattices. For convenience, we restrict ourselves to the first pseudoband and the eigenenergies are then given by

$$E^{\text{Lattice}}_{i_x,i_y,i_z} = \frac{1}{2} m\omega_{ho}^2 \left(\frac{\lambda}{2}\right)^2 (i_x^2 + i_y^2 + i_z^2) + \frac{3}{2}\hbar\omega_{\text{Lattice}} \tag{5.38}$$

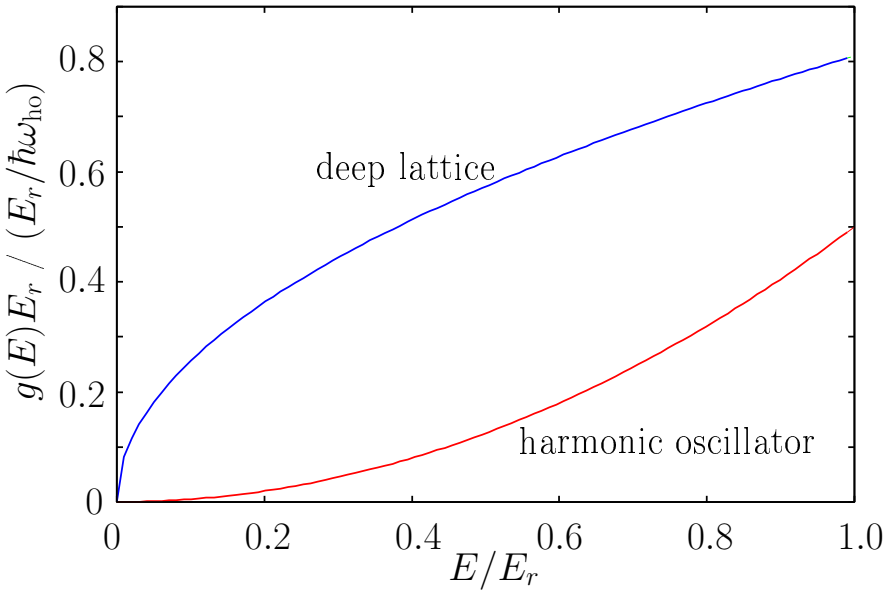

Figure 5.14: Density of states for a pure harmonic oscillator in comparison to a deep optical lattice restricted to the first pseudoband. The description is only valid in case of $\hbar\omega_{\rm ho} \ll E_r$

where $i_{x/y/z}$ are the lattice site indices relative to the center $x = y = z = 0$ in units of $\lambda/2$; $\omega_{\rm Lattice}$ is the harmonic oscillator frequency of a single lattice site.

Note that the structure of eigenenergies is completely different in the two limiting cases of a vanishing lattice and a very tight lattice. In the limit of a vanishing lattice, the density of states $g(E)$ is the well-known density of states of a three-dimensional harmonic oscillator[6]

$$g_{\rm ho}(E) = \frac{E^2}{2\hbar^3\omega_{\rm ho}^3}. \tag{5.39}$$

In the limit of tight optical lattices, the structure of energy eigenstates (see equation 5.38) is similar to that of a free Fermi gas in a "box" of side lengths L where the energy eigenstates are given by

$$E^{\rm free}_{i_x,i_y,i_z} = \frac{p_{i_x}^2 + p_{i_y}^2 + p_{i_z}^2}{2m} = \frac{\hbar^2}{2m}\left(\frac{2\pi}{L}\right)^2 (i_x^2 + i_y^2 + i_z^2) \tag{5.40}$$

with the density of states in three-dimensions

$$g_{\rm free}(E) = \left(\frac{mL^2}{2\pi\hbar^2}\right)^{3/2} \frac{E^{1/2}}{\Gamma(3/2)} \tag{5.41}$$

By comparing equation 5.38 to equation 5.40, we obtain by simple rescaling for the Fermi

[6] We restrict ourselves to the spherically symmetric case. When going to an arbitrary three-dimensional harmonic oscillator, $\omega_{ho}^3 = \omega_1\omega_2\omega_3$

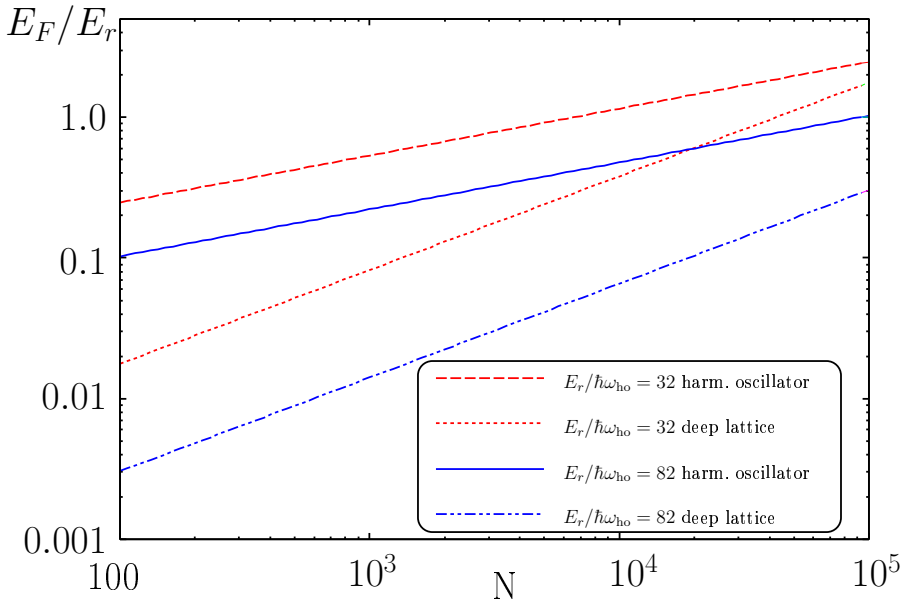

Figure 5.15: Fermi energy E_F for a pure harmonic oscillator potential in comparison to a deep optical lattice overlapped by the same harmonic oscillator potential. We assume typical experimental parameters $E_r/\hbar\omega_{\rm ho} = 32$ and $E_r/\hbar\omega_{\rm ho} = 82$ for the case of the combined magnetic and optical potential and the magic trap respectively.

gas in the tight lattice

$$g_{\rm Lattice}(E) = \left(\frac{\pi}{\frac{m\omega_{\rm ho}^2}{2}\left(\frac{\lambda}{2}\right)^2} \right)^{3/2} \frac{E^{1/2}}{\Gamma(3/2)} \tag{5.42}$$

Fig. 5.14 shows a comparison of the density of states in the case of a pure 3D harmonic oscillator and a deep 3D optical lattice restricted to the first pseudoband. The characteristic plots are only valid in the limit $\hbar\omega_{\rm ho} \ll E_r$ when the discrete nature of the energy eigenstates is no longer important.

Due to the different density of states, the Fermi energy of a purely harmonically trapped Fermi gas is for our experimental parameters ($E_r \approx 30 - 80\ \hbar\omega_{\rm ho}$ and $N_F < 10^5$) much larger than the Fermi energy of a Fermi gas in a deep optical lattice overlapped with the same harmonic confinement. Whereas the Fermi energy of a purely harmonically trapped gas is given by

$$E_F^{\rm ho} = (6N)^{1/3}\hbar\omega_{\rm ho} \tag{5.43}$$

the Fermi energy of N atoms in a deep optical lattice $E_F^{\rm Lattice}$ is

$$E_F^{\rm Lattice} = \left(\frac{3N}{4\pi}\right)^{2/3} \frac{m\omega_{\rm ho}}{2}\left(\frac{\lambda}{2}\right)^2. \tag{5.44}$$

Fig. 5.15 shows the Fermi energy as a function of atom number for a pure harmonic oscillator and a deep optical lattice in the cases relevant for our experiments, namely

$\omega_{\rm ho}^{\rm K} = 2\pi \cdot 140$ Hz[7] and $\omega_{\rm ho}^{\rm K} = 2\pi \cdot 56$ Hz[8] corresponding to $E_r^{\rm K}/\hbar\omega_{\rm ho}^{\rm K} \approx 32$ and $E_r^{\rm K}/\hbar\omega_{\rm ho}^{\rm K} \approx 82$. When $E_F(N) > E_r$ at $s = 0$ (for vanishing optical lattices), strict adiabaticity with respect to the energy splitting of the avoided crossings is required when ramping up the lattice to avoid transfer of atoms initially in energy states eigenstates with $E > E_r$ at $s = 0$ into energy states in the boundaries of the first pseudoband or even into higher bands (see Fig. 5.7). For a discussion of adiabatic heating/cooling issues see section 6.6.2.

5.3.4 Fermi-Bose mixtures in 3D optical lattices

The Fermi Bose mixtures confined in a 3D optical lattice is theoretically described by the Hubbard Hamiltonian. It has first been introduced by A. Albus and coworkers [172]. It can be derived similarly to the Hubbard Hamiltonian of equation 5.25 describing a one-component system of fermions or bosons.

The Fermi-Bose Hubbard Hamiltonian consists of the Hamiltonian for the one-component Fermi system H_F, the one-component Bose system H_B and an interaction term accounting for interactions between fermions and bosons. Due to the low temperatures, the scattering between fermions and bosons can be assumed to be purely $s-$wave, modelled by a contact interaction potential

$$V_{FB}(\vec{r},\vec{r}') = \frac{2\pi\hbar^2}{m_{\rm reduced}} a_{FB}\delta(\vec{r}-\vec{r}') \tag{5.45}$$

where $m_{\rm reduced} = \frac{m_B \cdot m_F}{m_B + m_F}$ is the reduced mass and a_{FB} the Fermi Bose $s-$wave scattering length. The Hamiltonian then reads:

$$H = H_B + H_F + V_{BF} \tag{5.46}$$

where H_B is the Bose Hubbard Hamiltonian

$$H_B = -J_B \sum_{<i,j>} b_i^\dagger b_j + \frac{1}{2} U_{BB} \sum_i n_i(n_i - 1) + \epsilon_i^B n_i \quad . \tag{5.47}$$

H_F is the Fermi-Hubbard Hamiltonian

$$H_F = -J_F \sum_{<i,j>} f_i^\dagger f_j + \epsilon_i^F m_i \quad , \tag{5.48}$$

and V_{FB} accounts for interactions between Fermions and Bosons.

$$V_{FB} \;=\; \int d^3r d^3r' \Psi_B^\dagger(\vec{r}) \Psi_F^\dagger(\vec{r}') V_{BF}(\vec{r}-\vec{r}') \Psi_F(\vec{r}') \Psi_B(\vec{r}) \tag{5.49}$$

Inserting the contact interaction of equation 5.45 in equation 5.49, one obtains

$$\begin{aligned} V_{FB} &= \frac{2\pi\hbar^2}{m_{\rm reduced}} a_{FB} \int d^3r \Psi_B^\dagger(\vec{r}) \Psi_F^\dagger(\vec{r}') \Psi_F(\vec{r}) \Psi_B(\vec{r}) \qquad (5.50)\\ &= \frac{2\pi\hbar^2}{m_{\rm reduced}} a_{FB} \sum_{i,j,k,l} b_i^\dagger f_j^\dagger f_k b_l \int d^3r w^B(\vec{r}-\vec{r}_i)^* w^F(\vec{r}-\vec{r}_j)^* w^F(\vec{r}-\vec{r}_k) w^B(\vec{r}-\vec{r}_l) \\ &\approx U_{FB} \sum_i \hat{n}_i \hat{m}_i \end{aligned}$$

[7] The parameters correspond to the parameters of the combined optical and magnetic potential (see section 6.1).

[8] The parameters correspond to the parameters of the magic trap (see section 3).

where we have accounted only for onsite interaction and U_{FB} is given by the following expression:

$$U_{BF} = \int d^3r \left|w_1^F(\vec{r})\right|^2 \left|w_1^B(\vec{r})\right|^2. \tag{5.51}$$

The full Fermi-Bose Hubbard Hamiltonian then reads:

$$\begin{aligned} H_{BF} &= -J_B \sum_{<i,j>} b_i^\dagger b_j + \frac{1}{2}U_{BB}\sum_i n_i(n_i-1) + \epsilon_i^B n_i && (5.52)\\ &- J_F \sum_{<i,j>} f_i^\dagger f_j + \epsilon_i^F m_i && (5.53)\\ &+ U_{BF}\sum n_i^B m_i && (5.54) \end{aligned}$$

Similar to the case of a purely bosonic system, the interaction matrix element can again be calculated analytically in the tight-binding limit and is given by

$$U_{BF} = \sqrt{\frac{8}{\pi}} k a_{\mathrm{BF}} E_r \sqrt{\frac{V_0}{E_r}} \frac{1 + m_{\mathrm{B}}/m_{\mathrm{F}}}{1+\sqrt{m_{\mathrm{B}}/m_{\mathrm{F}}}} \tag{5.55}$$

where a_{FB} is the Fermi-Bose s-wave scattering length and E_r is the bosonic recoil energy. In the case of a mixture of fermionic ^{40}K and bosonic ^{87}Rb with $a_{\mathrm{FB}}^{\mathrm{triplet}} = -205(10)a_0$ [137] in the corresponding spin states $|9/2, 9/2>$ and $|2, 2>$,

$$U_{\mathrm{FB}} = -2.6 U_{\mathrm{BB}}. \tag{5.56}$$

The properties of the Fermi-Bose Hubbard Hamiltonian have been studied in a number of theoretical publications. The ground state properties of the mixed system has first been studied by Albus and coworkers [172] who pointed out that the Fermi-Bose Hubbard Hamiltonian exhibits a rich phase diagram depending on the strength and sign of a_{BB} and a_{FB} and the depth of the optical lattice. Apart from the superfluid to Mott-insulator transition in the bosonic cloud, Albus and coworkers observed a "simultaneous transition to demixing in the boson fermion sector" and a "transition to a multiply degenerate phase" in the limit of deep optical lattices. Lewenstein and coworkers studied theoretically the limit of zero tunnelling ($J = 0$) and predicted an extraordinary rich phase diagram with novel quantum phases as for example pairing of fermions with one or more bosons or bosonic holes [26]. The effects of inhomogeneity on the ground state and the Mott and superfluid regions emerging in systems of fermions and bosons confined in optical lattices has been studied by Marcus Cramer and coworkers [133]. Apart from these three works, there are a number of theoretical studies on Fermi-Bose mixtures confined in optical lattices of different dimensions or geometry and in disordered potentials [173, 174, 30, 175, 29, 176, 177]. Boson induced fermionic superfluidity has been discussed in [28, 29, 178].

However, there have been no experimental studies on a Fermi-Bose mixed system in 3D optical lattices until recently. The first realization of this intriguing new many-body system has been reported almost simultaneously by the Zurich group and ourselves in 2006. In these experiments, the bosonic coherence properties have been studied, affected by the admixture of a varying fermionic impurity fraction [179, 5]. An in depth discussion of these experiments can be found in chapter 6.

5.4 Experimental realization of a 3D optical lattice

In this section, we will discuss practical aspects necessary for the realization of quantum degenerate Fermi-Bose mixtures in 3D optical lattices. Starting with an overview of the setup, I will discuss lattice alignment and lattice depth calibration issues and conclude with a few aspects on lattice loading.

5.4.1 Lattice setup

An overview of the lattice setup in our experiment is given in Fig. 5.16. The optical lattice is operated at 1030 nm by a commercial 20 W Yb:YAG laser and is formed by three orthogonal retroreflected laser beams. The three laser beams intersect at the position of the atomic clouds and form a simple cubic three-dimensional lattice potential of the form $V(\vec{r}) = V^x_{\text{Lattice}} \cos(kx)^2 + V^y_{\text{Lattice}} \cos(ky)^2 + V^z_{\text{Lattice}} \cos(kz)^2$. In order to avoid heating of the atomic cloud in the optical lattice by spatial shaking of the lattice interference pattern due to frequency fluctuations of the laser, the lattice laser has been frequency stabilized by a Pound-Drever-Hall frequency stabilization on an optical cavity with a Finesse of > 500. The short-term linewidth of the laser has thereby been reduced from < 5 MHz to < 20 kHz. Residual slow drifts of the cavity due to thermal drifts of the cavity length do not affect our experiments performed on a time scale of a few ten milliseconds (for details on the frequency stabilization, see the thesis of Christian Ospelkaus [35] and the diploma thesis of Oliver Wille [180]). In order to avoid cross interferences between the different lattice laser beams giving rise to a fluctuating depth of neighboring lattice wells, the three orthogonal lattice laser beams are operated with mutually orthogonal polarizations and are each operated at a slightly different frequency. The frequency offsets are on the order of a few ten MHz and are realized by Acousto-Optical modulators shifting the frequencies of the lattice laser beams compared to the "initial" lattice laser beams by 115 MHz, 125 MHz and 135 MHz. The lattice laser light is transported to the experiment by single-mode optical fibers spatially filtering the mode of the beams to achieve a pure Gaussian TEM00 mode for each of the lattice beams. The intensities of each of the three laser beams are actively stabilized using photodiodes behind the fiber and a feedback-loop to the radio-frequency power operating the Acousto-Optic Modulators. Behind the optical fiber, the lattice laser beams are collimated using aspheric telescopes and finally focused onto the atomic ensembles by high-quality achromatic lenses. Circular $1/e^2$ radii of the beams are 82 μm, 92 μm and 55/100 μm[9] respectively. The incoming laser beams are then recollimated again using achromatic lenses and finally retroreflected. The use of high-quality optics is crucial to get rid of residual interference fringes in the Gaussian beam profile giving rise to distorting overlapping potential gradients. To avoid the build-up of an additional resonator between the retroreflecting mirror and the fiber, we use fibers polished with an angle of 8° on both the incoupling and the outcoupling side of the fiber.[10]

[9] The lattice laser beam focus has been changed from initially 55 μm to 100 μm during the experiments described in chapter 6.

[10] For more details on the experimental setup of the lattice see the diploma thesis of Oliver Wille [180].

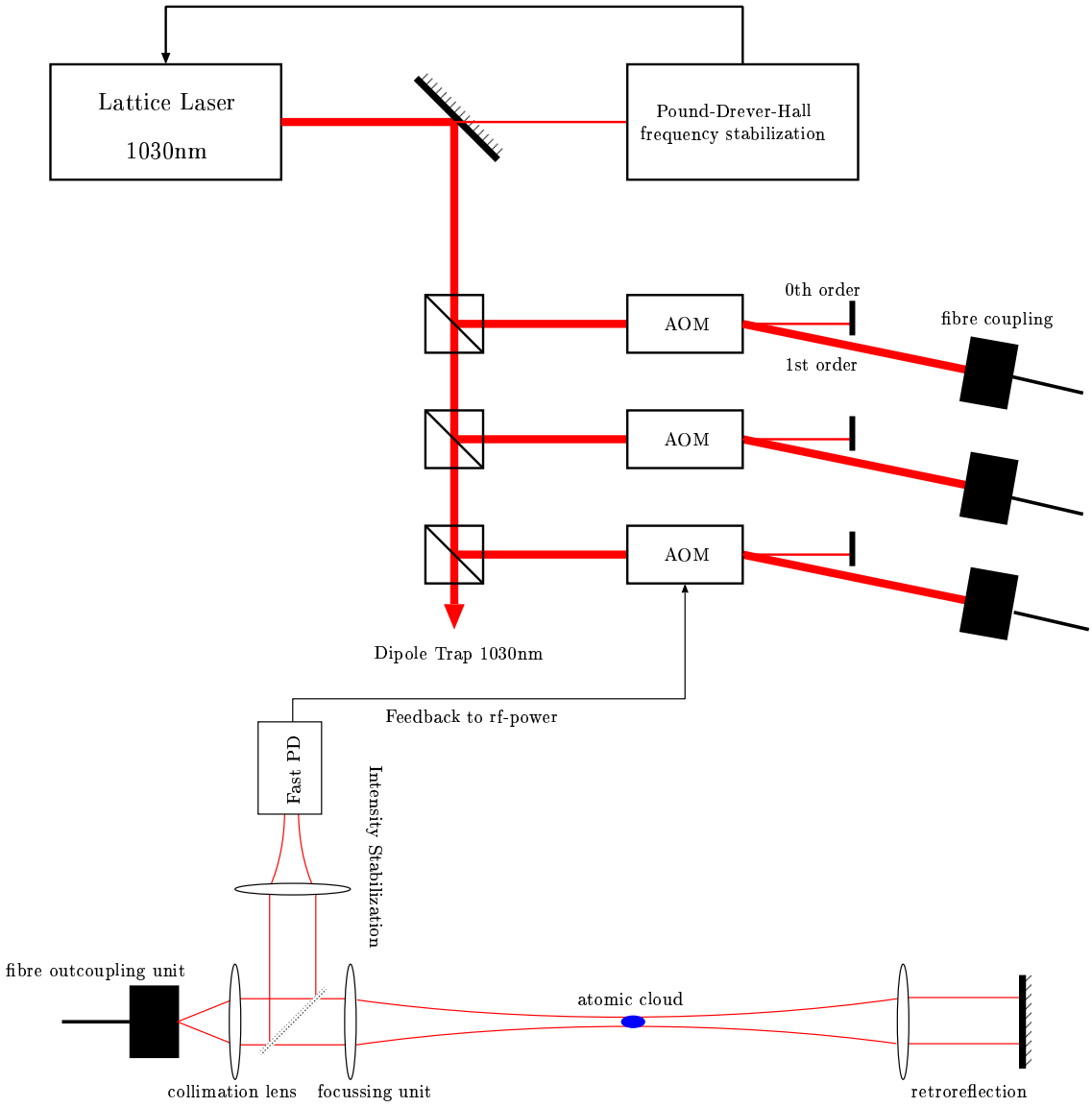

Figure 5.16: Schematic sketch of the lattice setup. The frequency stabilized lattice laser is operated at 1030 nm. Three lattice laser beams are prepared and frequency shifted using acousto-optical modulators. The acousto-optical modulators are operated at slightly different frequencies to assure frequency offsets between the different lattice laser beams of ≈ 10 MHz, thereby avoiding cross-interferences between the different lattice beams. The lattice laser light is fiber-coupled and transported to the vacuum chamber. Behind the fiber, all three lattice beams are actively intensity stabilized and then irradiated onto the atomic cloud. To form a simple cubic lattice, three orthogonal laser beams with mutual orthogonal polarization are used. For convenience, only a single lattice laser beam setup is shown.

5.4.2 Lattice alignment

Accurate alignment of the optical lattice is crucial for any lattice experiments. We have therefore integrated three additional imaging systems in our experiment. The additional detection systems allow for imaging of the atomic clouds along the lattice axes. It is therefore possible to simultaneously image atomic clouds and the lattice laser beam onto a single CCD camera. The imaging is performed either using one of the MOT beams on the corresponding axis or using additional separate beams such as the state preparation beam. A detailed sketch of the optical setup of a typical lattice axis including MOT and detection optics is shown in Figure 5.17. The lattice laser beam of one axis is coupled out of

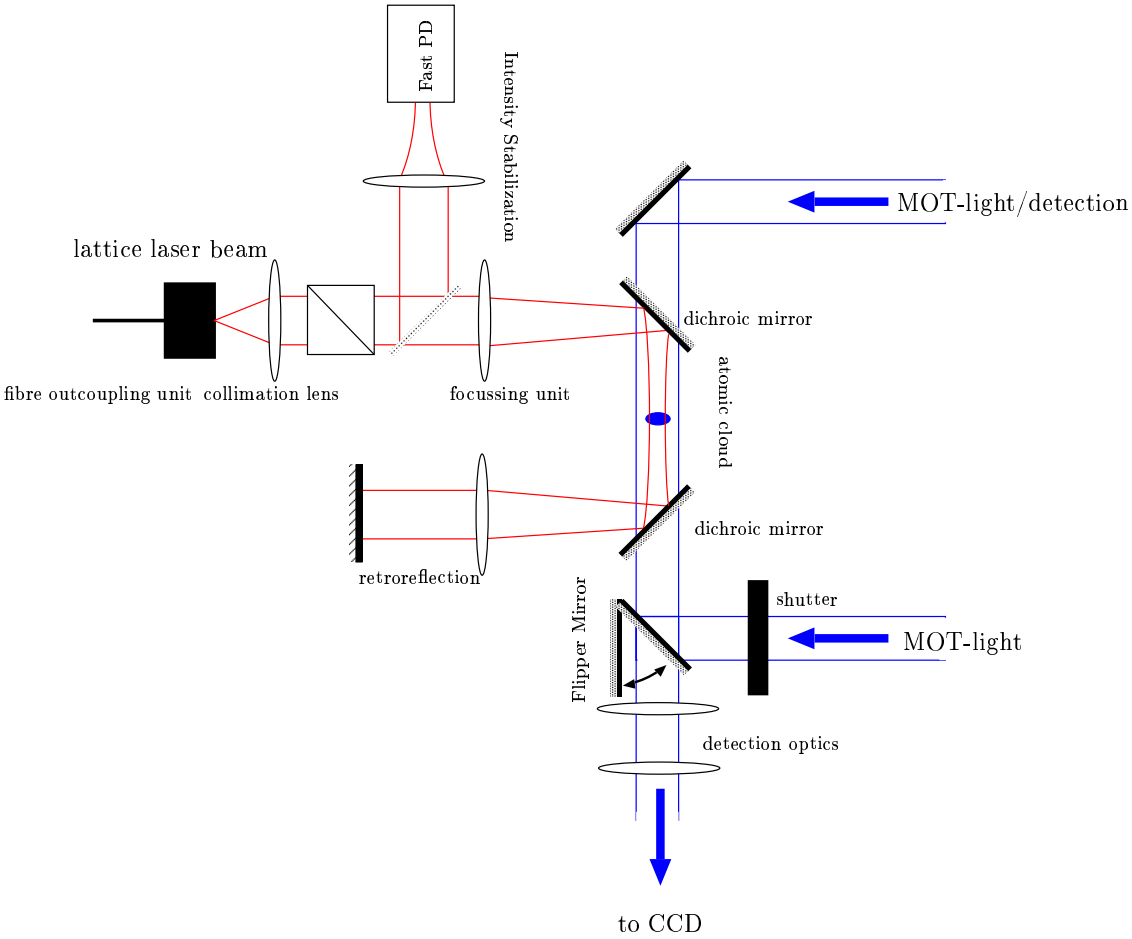

Figure 5.17: Schematic sketch of the lattice beam preparation including the overlapping scheme for the detection and MOT beams. The MOT beams are overlapped with the lattice laser beams using dichroic mirrors which are HR coated at 1030 nm and AR coated at 767 nm and 780 nm. Using a flipper mirror, one of the MOT beams can be redirected through detection optics onto a scientific CCD camera. During detection, the counter-propagating MOT beam is blocked by a large-area shutter.

the fiber, collimated, appropriately polarized, intensity stabilized and then focussed onto the atomic cloud. The lattice beam is directed onto the atomic ensemble using a dichroic

mirror which is high-reflection coated at 1030 nm and anti-reflection coated at 767 nm and 780 nm corresponding to the wavelength of the D_2-line of ^{40}K and ^{87}Rb. The same dichroic mirror is also integrated into the retroreflection unit of the lattice laser beam. The AR-coating of these mirrors allows overlapping the MOT beams for ^{40}K and ^{87}Rb with the lattice laser beam so that both the lattice and the MOT can in principle be operated simultaneously. The detection setup is additionally integrated into the experiment by a flipper mirror which allows to redirect one of the MOT beams through detection optics onto a scientific CCD camera. During detection, the counter-propagating MOT beam is blocked by a large-area shutter.

Accurate alignment of the lattice laser beams onto the atomic cloud is achieved as follows: In a first step, we simultaneously detect the lattice laser beam and the degenerate atoms on the same CCD camera. Simultaneous detection of the laser beam and the atomic cloud is possible due to some residual transmission of the 1030 nm light through the dichroic mirror. The lattice laser beams are adjusted to the same position. In a next step, we block the retroreflected beam and align the incoming lattice laser beam to excite only shape oscillations of the atomic cloud. Finally, the retroreflected beam is fine-adjusted using the same procedure.

5.4.3 Lattice depth calibration

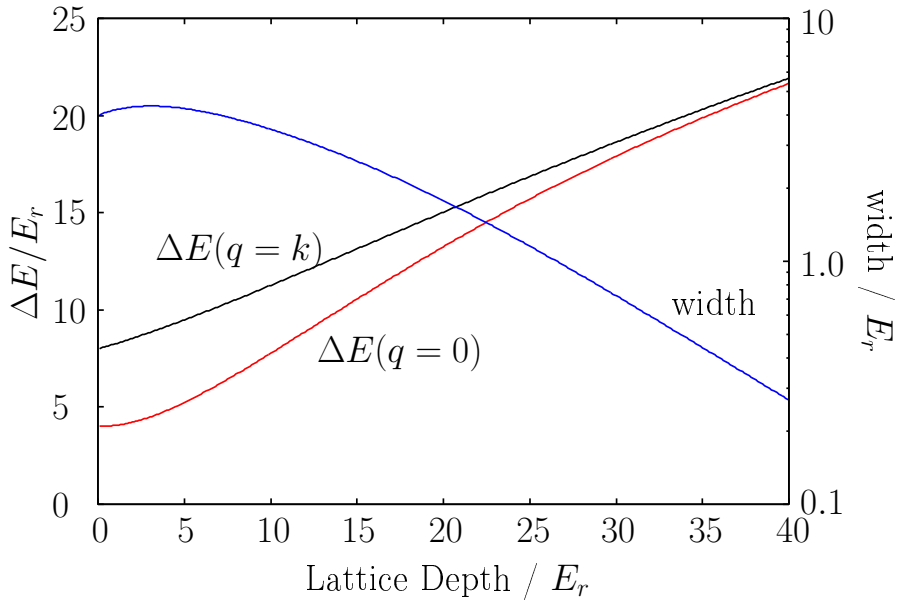

Figure 5.18: Energy difference between the first and the third Bloch band as a function of lattice depth. The energy difference is plotted in two limits: for $q = 0$ (center of the Brillouin zone, red line) and $q = k$ (at the edge of the Brillouin zone, black line). Due to the finite widths of the involved Bloch bands, the energy of the transition from the first to the third band depends on the quasimomentum q. The width of the transition can be estimated based on the energy difference between the transitions at the edge and at the center of the Brillouin zone (blue line).

The lattice depth is calibrated by studying the energy difference between the first and the third band in a one-dimensional optical lattice. This is performed by periodically modulating the lattice depth [181] which results in heating and loss of atoms on resonance. Due to the finite width of the involved bands, the calibration either has to be performed with an atomic cloud occupying essentially only the lowest energy states in the lattice ($q = 0$) or in the limit of a deep optical lattice where the width of the involved bands tend to zero. Fig. 5.18 illustrates the energy difference between the first and the third band as a function of lattice depth in the center of ($q = 0$) and at the edge ($q = k$) of the Brillouin zone. In the same diagram, I have plotted the width of the transition which is estimated based on the energy difference between the transitions at the edge and at the center of the Brillouin zone $\Delta E(q = k) - \Delta E(q = 0)$. At a lattice depth of 40 E_r, the energy difference between the first and the third band is > 20 E_r with a width of < 0.3 E_r corresponding to a relative uncertainty of < 0.015.

The calibration of each of the optical lattice beams has typically been performed at a lattice depth $> 40E_r$ with a cloud of ^{87}Rb atoms confined in the lowest Bloch band, but not necessarily in the lowest quasimomentum state. The width of the observed loss feature at ≈ 50 kHz is on the order of 5 kHz which is much larger than estimated based on the width of the involved bands.

The essential broadening mechanism, probably dominating the width, is related to the radial inhomogeneity of the optical lattice. Due to the Gaussian shape of the lattice beams with a typical beam waist of 100 μm, the lattice depth varies easily across the extension of typical thermal atomic clouds by 20%. Due to $\omega_{\mathrm{Lattice}} \propto \sqrt{V_{\mathrm{Lattice}}/E_r}$, this results in a variation of the vibrational frequency of $\approx 10\%$, being on the order of the observed broadening of the transition.

5.5 Probing atomic states in the optical lattice

5.5.1 Probing the momentum distribution

The momentum distribution of the atoms loaded into a three-dimensional optical lattice with a lattice vector characterized by the reciprocal lattice vector $\vec{k}$ can be probed by time of flight imaging. When the optical lattice is switched off fast against the band separation so that the atomic states cannot follow the change in the energy states, the atomic states are directly projected onto free atomic states. Initial Bloch states characterized by the quasimomentum q are projected onto the basis of free atomic states with "real" momentum p. Due to the periodicity of the Bloch envelope function, a Bloch state Ψ_q is composed of free atomic states with momenta $\vec{p} = \vec{q}$ and $\vec{q} + n2\hbar\vec{k}$. The momentum components of the lowest Bloch state with $q = 0$ can be revealed in the experiment by probing the momentum distribution of a Bose-Einstein condensate loaded into a shallow optical lattice where the system is still superfluid. In a shallow optical lattice, a Bose-Einstein condensate macroscopically occupies the lowest Bloch state with quasimomentum $q = 0$. Projecting the macroscopic wavefunction onto free atomic state, we obtain the characteristic interference pattern with the free atomic momenta $p = 0$, $p = \pm 2\hbar k$,.... This interference pattern is shown in Fig. 5.19 imaged along two different imaging axes of our experiment, along the z-axis and the x-axis.

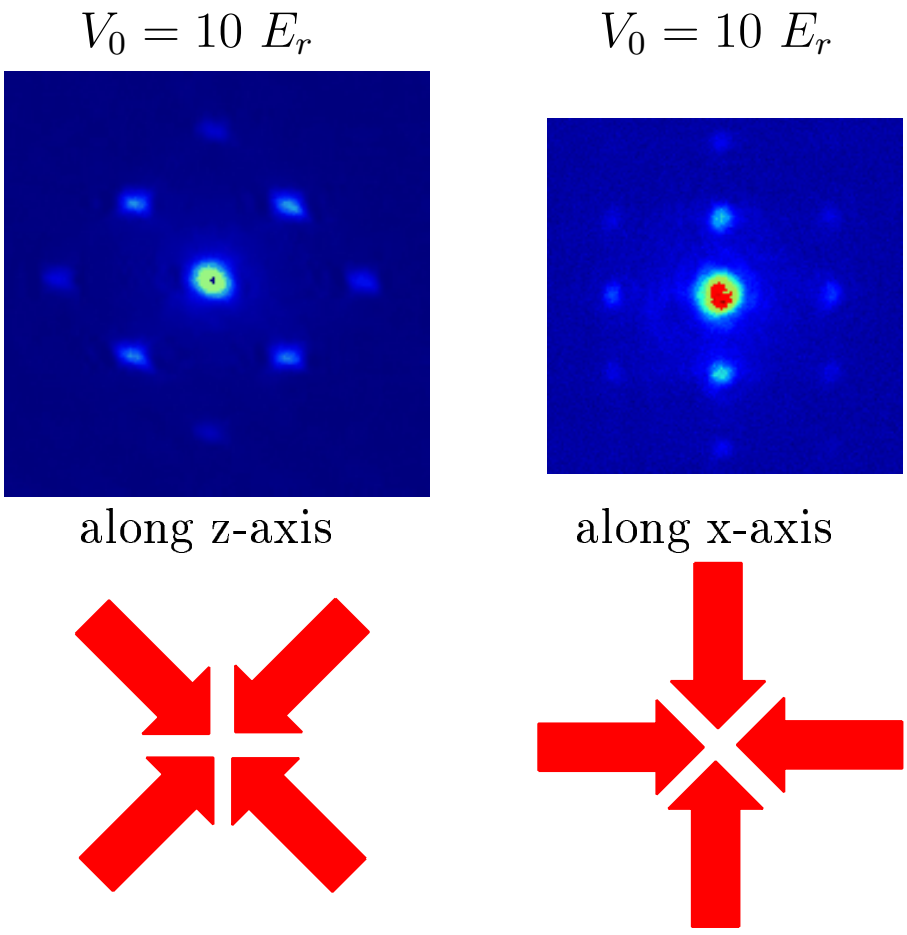

Figure 5.19: Momentum distribution of a Bose-Einstein condensate in a 3D optical lattice of $V_0 = 10\ E_r$. Apart from the $p = 0$ component, integer multiples of $\vec{p} = \hbar\vec{k}$ are observed. a) Momentum distribution imaged along the z-axis of our experiment. b) Momentum distribution imaged along the $x-$axis. Note that the peaks in vertical direction are actually $\frac{1}{\sqrt{2}}\hbar k$ peaks which stem from the projection of the diagonal $\hbar k$ peaks from a) onto the imaging plane of b).

The interference pattern can also be understood in a less formal picture. The interference stems from the coherent interference of wave packets released from different lattice sites. Essential for the observation of the interference pattern is phase coherence across the lattice. In the case of Bose-Einstein condensate, the many-body wavefunction is a macroscopic wave function with well-defined phase across the lattice and a sharp interference pattern is therefore observed. In the Mott-insulating state, however, the macroscopic phase coherence across the system is lost, instead, the many-body wave function is a product of Fock states and the coherence length of the system is smaller than the separation between two lattice sites. This is reflected in the vanishing of the macroscopic interference pattern.

5.5.2 Probing the quasimomentum distribution

The quasimomentum distribution of the atoms confined in the optical lattice can also be probed by time of flight images. In this case, the quasimomentum distribution has to be converted into real free atomic momentum prior to time of flight. The lattice potential is therefore ramped down adiabatically with respect to the band separation (i.e. slow compared to the vibrational frequency of the atoms in a single lattice well) thereby converting Bloch states with quasimomentum q into free atom states with atomic momentum $p = q$. To get an unaltered picture of the quasimomentum distribution, the ramp down process has to be fast compared to collisional processes redistributing atoms among the different quasimomentum states [182].

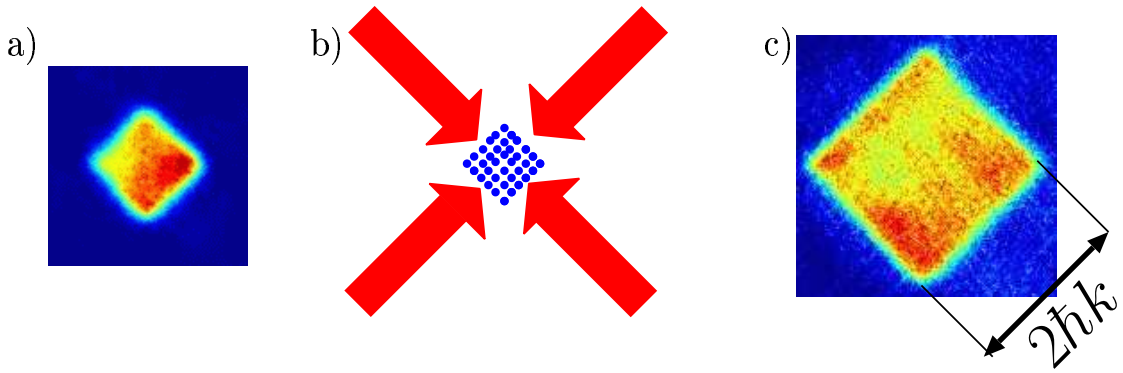

Figure 5.20: Quasimomentum distribution of fermionic atoms c) and bosonic atoms a) in a 3D optical lattice. b) illustrates the geometry of our lattice setup with two lattice beams irradiated onto the atoms under 45°. For the measurement, the lattice has been ramped up to $30E_r^{^{87}\mathrm{Rb}}$. After a hold time of 5 ms, the lattice is ramped down adiabatically with respect to band separation to convert the quasimomentum distribution into real atomic momentum.

Fig. 5.20 shows images of the quasimomentum distribution of bosonic and fermionic atoms loaded into a 3D optical lattice. The lattice has been ramped up to 30 E_r^{Rb} for ^{87}Rb atoms (corresponding to a lattice depth of ≈ 15 E_r^{K} for ^{40}K.[11]. After a hold time of

[11] Note that the dipole potentials for both species are approximately equal whereas $E_r^{^{40}\mathrm{K}} = \frac{87}{40} E_r^{^{87}\mathrm{Rb}}$

20 ms in the deep optical lattice, any confining potentials have been ramped down within 1 ms, thereby converting quasimomentum into free momentum. The two clouds are then subjected to 10 ms of ballistic expansion and finally imaged onto a CCD camera by a resonant light pulse.

Both images show the quasimomentum distribution of an almost homogeneously occupied first Brillouin zone. In the case of fermionic atoms, the homogeneous population can be achieved most naturally due to the Pauli exclusion principle by choosing an appropriate number of atoms to fill the first band. A Bose-Einstein condensate, however, loaded into an optical lattice forms a macroscopic wavefunction occupying only the lowest quasimomentum state $q = 0$ with a small quasimomentum spread due to interactions[12]. To achieve a homogeneous population of the first band, it is therefore necessary to heat the cloud in the optical lattice by small amplitude modulations prior to ramping down the lattice. The atoms are thereby redistributed over the first Brillouin zone. The different size of the first Brillouin zone after time-of-flight is due to the smaller mass of fermionic potassium compared to rubidium resulting in a velocity that is approximately two times larger for the potassium atoms compared to the rubidium atoms.

[12]This picture is of course only valid for sufficiently shallow optical lattices (see section 5.3.2)

Chapter 6

Fermi-Bose mixtures in optical lattices

Since the realization of strongly correlated systems with pure bosonic [19] and pure fermionic gases [25] in 3D optical lattices, there has been increasing theoretical interest in mixtures composed of fermionic and bosonic quantum gases. The different quantum statistical behavior of the two components gives rise to fundamentally novel quantum many-body phases. In the extreme case of pairing of fermions with one or more bosons, a whole zoo of new quantum phases of these "composite fermions" has been predicted [26]. Fermi-Bose mixtures in 3D optical lattices may exhibit fermionic pairing mediated by the presence of bosonic atoms in full analogy to solid state superconductivity, and there are interesting connections to high-T_C superconductivity [27, 28, 29]. Even before such "atom pairs" form, Fermi-Bose correlations are predicted to become manifest in polaron-related physics of fermions dressed by a bosonic cloud [30] and quantum percolation [31]. These phenomena are connected to disorder induced localization scenarios. In reduced dimensionality, phenomena such as charge-density waves [30, 29] and supersolids [32] are predicted to occur.

From the experimental point of view, studies on mixtures confined in optical lattices have been extremely rare. By the end of 2005, the only experiment with Fermi-Bose mixtures in optical lattices has been reported by Ott and coworkers at LENS [33]. In these experiments, the "insulating" behavior of a trapped ideal Fermi gas in a 1D lattice has been compared to collisionally induced transport of fermionic atoms in the presence of a bosonic cloud.

In this chapter, we report on the first realization of a Fermi-Bose quantum many-body system confined in a 3D optical lattice. In these studies, we investigate the coherence properties of bosonic atoms when interacting with a varying fraction of fermionic impurities. When ramping up the optical lattice, we observe the phase coherence properties of the bosonic cloud to be strongly affected by a very small fraction ($N_F/N_B \approx 3\%$) of fermionic atoms and find a fermion concentration dependent shift of the coherence properties with respect to the properties of a pure bosonic ensemble. A very small admixture of fermionic impurities induces a significant loss of coherence at much lower lattice depths as compared to the pure bosonic case. While the coherence properties of the pure bosonic system (loss of coherence with increasing lattice depth) can be explained in terms of the

superfluid to Mott-insulator transition and the associated many-body wavefunctions in the superfluid and the Mott-insulating regime (see section 5.3.2), the nature of the observed shift of the coherence properties towards lower optical lattice depth in the mixture is still a point of intensive discussions in the community. Possible scenarios include thermodynamic effects like adiabatic heating when ramping up the optical lattice[1], disorder induced localization scenarios or a shift of the quantum critical point of the bosonic superfluid to Mott-insulator transition due to attractive interactions with the fermionic atoms ($a_{\mathrm{FB}} = -215(10)a_0$ [137]).

This chapter is organized as follows: First, I will describe how we prepare quantum degenerate Fermi-Bose mixtures in 3D lattices. I will then discuss qualitatively the fermion induced effects on the bosonic coherence properties when ramping up the optical lattice. Based on two different quantitative methods for the analysis of the bosonic coherence properties, we analyze the fermion induced effects on the bosonic cloud as a function of lattice depth and fermionic impurity concentration. Finally, we discuss possible scenario which might cause these phenomena. In parallel to this work, similar studies and results have been reported at ETH Zürich [179].

6.1 Experimental Procedure

Preparation of quantum degenerate mixtures prior to ramping up the optical lattice For studying mixtures of fermionic and bosonic atoms in 3D optical lattices, we create the mixture similarly to the procedure described in chapter 2. In brief, we create Fermi-Bose mixtures by first collecting and precooling bosonic ^{87}Rb and fermionic ^{40}K atoms using the combined 2D-3D MOT laser cooling system. After transfer to the Ioffe-Pritchard type magnetic trapping potential, we perform forced rf evaporative cooling of the rubidium component in the $|2,2\rangle$ state (which in turn sympathetically cools the potassium atoms in the $|9/2,9/2\rangle$ state) until the mixture is close to quantum degeneracy.

In order to load the mixture into a 3D optical lattice, the cigar-shaped strongly elongated geometry of the magnetic trap with an aspect ratio of ≈ 20 is unfavorable and at the time where most of these experiments were performed, the magic dipole trap had not yet been implemented. We therefore increase the confinement in the axial direction of the magnetic trap to $\omega_{ax} = 2\pi \cdot 50$ Hz (this and all the subsequent trapping frequencies correspond to the trapping frequency for the ^{87}Rb component). To this end, we add an additional optical dipole trap at $\lambda = 1030$ nm perpendicular to the long axis (x-axis) of the magnetic trap. At the same time, we reduce the radial trapping frequency of the magnetic trap from $\omega_{\mathrm{rad}} = 2\pi \cdot 250$ Hz to $\omega_{\mathrm{rad}} = 2\pi \cdot 150$ Hz, thereby achieving an aspect ratio of 1:3.

For the study of degenerate gases in optical lattices, it is favorable to work with low-density clouds to avoid lattice site occupations $\gg 1$ which result in enhanced atom loss in the tight lattice wells. In experiments with a single species bosonic quantum gas, the particle number was therefore restricted to a few times 10^5 atoms in the condensate. These condensates were confined in a very shallow almost spherically symmetric magnetic trap with a mean trapping frequency of $\hat{\omega} \approx 2\pi \cdot 20$ Hz [19], corresponding to central

[1] Note that the latter is a reversible thermodynamics effect happening at constant entropy and quite different from irreversible heating processes due to noise or loss processes.

condensate densities $n(0) \approx 10^{14}/\mathrm{cm}^3$. In the case of our experiment, a further lowering of the radial trapping frequency would be desirable. However, in the experiments reported here, the trapping frequency in the radial direction was chosen as a compromise between the realization of clouds with as low density as possible without running into trouble due to a possibly large differential gravitational sag reducing the overlap of the two atomic clouds. At $\omega_{\mathrm{rad}} = 2\pi \cdot 150$ Hz, the differential gravitational sag between the condensate and the Fermi gas becomes comparable to the size of the Thomas Fermi radius of a condensate of 10^5 atoms which is on the order of 10 μm. For even lower trapping frequencies, the differential gravitational sag increases $\propto 1/\omega_{\mathrm{rad}}^2$ whereas the size of the cylindrically shaped condensate increases only with $\propto 1/\omega_{\mathrm{rad}}^{\alpha}$ where $\alpha \approx 1/2$.

Quantum degeneracy is achieved in the combined optical and magnetic potential by forced rf-induced evaporative cooling. In order to keep the density as low as possible, we restrict particle numbers in the condensate to $< 10^5$, thereby typically realizing condensates with a peak density of $n(0) \leq 5 \cdot 10^{14}/\mathrm{cm}^3$ prior to ramping up the lattice. The ^{87}Rb condensates have no discernible thermal cloud and coexist with a variable 0-20% fermionic ^{40}K atom impurity component.

With the realization of the "magic" dipole trap (which I have presented in detail in chapter 3) we have later been able to produce low-density two-species mixtures without being limited by the differential gravitational sag. Some of the data presented in this chapter was recorded with the mixture confined in the "magic trap". This trap is characterized by an almost spherically symmetric trapping potential with a mean trapping frequency of $\omega_{\mathrm{magic}} = 2\pi \cdot 50$ Hz. In this case, typical peak condensate densities are $n(0) \leq 2 \cdot 10^{14}/\mathrm{cm}^3$

Loading of the mixture into the optical lattice To load the mixture into the optical lattice, we have overlapped the lattice either with the combined magnetic and optical trapping potential or with the purely optical potential of the "magic" trap. The optical lattice potential is created by three orthogonal and retroreflected laser beams at 1030 nm with waists of 82/92 μm in the radial directions and 55 μm in the axial direction with respect to the original trap (c.f. 5.4). The 55 μm focus has later been exchanged against a 100 μm focus for the lattice experiments starting with mixtures prepared in the magic trap. The optical lattice is ramped up with a linear ramp of $0.5 - 1$ E_r^{Rb}/ms to various lattice depths between 0 E_r^{Rb} and 25 E_r^{Rb}. After a sudden switch off of the lattice potential and typically 15 ms time-of-flight, we probe the momentum distribution of the bosonic cloud. Throughout the measurements, we have checked that the atoms occupy only the lowest Bloch band by adiabatically ramping down the lattice with respect to band separation and probing the quasimomentum distribution (see section 5.5.2). We could not detect any discernible fraction of atoms in higher Bloch bands.

Due to the additional harmonic confinement by the magnetic trap and the Gaussian lattice laser profiles, the mixture occupies a few ten thousand lattice sites with an occupation rising from 0 in the outer regions to 1 fermion and >5 bosons per site at the center.

6.2 Influence of fermions on bosonic coherence - A qualitative study

In this section, we will present the first studies on a mixed Fermi-Bose many-body system loaded into a three-dimensional optical lattice.[2] In these experiments, we have studied the influence of fermionic impurities on the bosonic coherence properties and observed a significant reduction of the bosonic coherence due to the admixture of fermions. As already briefly mentioned in section 5.5.1, the coherence properties of a bosonic cloud can be revealed by a study of the bosonic interference pattern after a sudden switch off of the lattice and time-of-flight expansion. Whereas the observation of sharp interference peaks is a striking signature of long-range phase coherence of the bosonic cloud, decreasing interference peaks and the appearance of an incoherent background indicates the reduction of the coherence length. In a pure bosonic component, the loss of phase coherence with increasing lattice depth accompanies the transition from a superfluid to a Mott-insulating state (see section 5.3.2).

In a first experiment, we have qualitatively studied the influence of a small admixture of fermionic atoms on the bosonic cloud. In these experiments, we have prepared $2 \cdot 10^4$ fermionic ^{40}K atoms, coexisting with a pure Bose-Einstein condensate of 10^5 ^{87}Rb atoms with no discernible thermal cloud in the above described (see section 6.1) combined magnetic and optical potential with trapping frequencies of $\omega = 2\pi \cdot (50, 150, 150)$ Hz. Finally, the lattice is ramped up to various lattice depths between 2.5 E_r^{Rb} and 25 E_r^{Rb}.

Fig. 6.1 shows three sample images of the interference pattern of the pure bosonic cloud (top row) in comparison to the interference pattern of the bosonic cloud interacting with $2 \cdot 10^4$ fermionic impurities (bottom row). The images have been taken after 15 ms time-of-flight. To ensure that experimental conditions are really comparable in the two cases, we have prepared the pure bosonic component with the same experimental sequence as the mixture prior to ramping up the optical lattice: In both cases, we have prepared a deeply degenerate mixture of fermionic and bosonic atoms in the combined magnetic and optical potential. The pure bosonic cloud is then realized immediately before ramping up the optical lattice by a removal of the fermionic atoms from the trap with a short resonant light pulse, leaving back a pure Bose Einstein condensate. The three sample images of Fig. 6.1 have been taken at lattice depths of 12.5 E_r^{Rb}, 20 E_r^{Rb} and 25 E_r^{Rb}, respectively. The lattice depths are given in units of the recoil energy for the ^{87}Rb component $E_r^{\mathrm{Rb}} = (\hbar^2 k^2)/(2m_{\mathrm{Rb}}) \approx h \cdot 2.14\,\mathrm{kHz}$ where $k = 2\pi/\lambda$.

In both cases, starting with a pure condensate or with a mixture of bosonic and fermionic atoms, we clearly observe a loss of interference contrast with increasing lattice depth marking the breakdown of long range phase coherence. As already mentioned, in case of the pure bosonic gas, the loss of coherence accompanies the well-known superfluid to Mott-insulator phase transition [18, 19, 117] which occurs as a result of competition between the minimization of kinetic energy, parameterized by the tunnelling matrix element J which tends to delocalize the atomic wavefunction over the crystal and the minimization of interaction energy U (Fig. 6.1a). As can be clearly seen from Fig. 6.1b, the presence of fermionic impurities induces a loss of coherence at much lower lattice depths than for

[2] Related experiments have been reported simultaneously by the group of T. Esslinger at ETH Zürich [179].

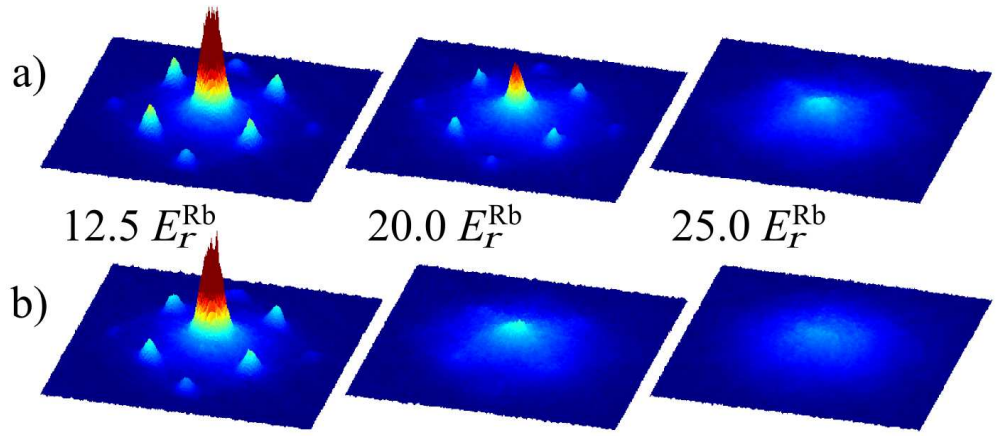

Figure 6.1: Time of flight absorption images of the bosonic component 15 ms after switching off the lattice and trap potentials. (The colors and pseudo-3d representation encode the particle column density integrated along the imaging direction). **a**. Pure bosonic ensemble of 10^5 atoms at three different lattice depths. **b**. Bosonic ensemble interacting with a fermionic impurity fraction of 20% for the same lattice depths as in a). We observe a striking loss of interference contrast in the images of the bosonic cloud interacting with fermions compared to the pure bosonic cloud.

a pure BEC. At 12.5 E_r^{Rb}, we observe sharp interference peaks in the pure bosonic cloud and the mixture. At 20 E_r^{Rb}, however, the interference pattern vanishes almost completely in case of the mixed system, whereas significant interference is still visible in the case of pure ^{87}Rb.

6.3 Characterizing the phase coherence properties of the bosonic cloud

For a quantitative analysis of the observed phenomena, we adopt two different approaches appropriate for the characterization of the coherence properties of the bosonic cloud. These approaches have both been developed in the context of studies on the superfluid to Mott-insulator transition in an ensemble of repulsively interacting bosons.

1. First, we characterize the interference pattern using the visibility of the interference fringes [183, 184]. The definition of visibility, in this context, is motivated by the definition of the interference contrast in optics. The visibility can be related to the correlation properties of the many-body wavefunction of the atomic cloud [183, 184].

2. Second, we analyze the width of the central $p = 0$ peak which is directly related to the inverse coherence length of the ensemble apart from some deviations due to the repulsive interactions between the bosonic atoms [185].

In the following, I will first introduce the two different techniques taking data of a pure bosonic ensemble as an example. I will then apply the techniques to the analysis of mixed systems and introduce a quantitative measure of the observed reduction in bosonic coherence.

6.3.1 Visibility

Fig. 6.2 (left) shows a typical interference pattern of a bosonic ensemble after time of flight released from a shallow optical lattice where a macroscopic fraction of the system occupies the lowest Bloch state and phase coherence is present across the lattice. An intuitive definition of the contrast of the interference pattern is given by [183, 184]

$$\mathcal{V} = \frac{n_{\max} - n_{\min}}{n_{\max} + n_{\min}} \tag{6.1}$$

where $n_{\max}$ is the total atom number in the first order interference fringes reflecting the $p = 2\hbar k$ momentum component and $n_{\min}$ is the sum of number of atoms in equivalent areas at intermediate positions between the maxima.

At first sight, the relation of the visibility to the bosonic many-body wavefunction is not clear. However, it can be derived from the density distribution of the atoms after time of flight which is given by [186, 187, 166, 184]

$$n(\vec{r}) \propto \left| \hat{w}\left(\vec{k} = \frac{m\vec{r}}{\hbar t}\right) \right|^2 \mathcal{S}\left(\vec{k} = \frac{m\vec{r}}{\hbar t}\right) \tag{6.2}$$

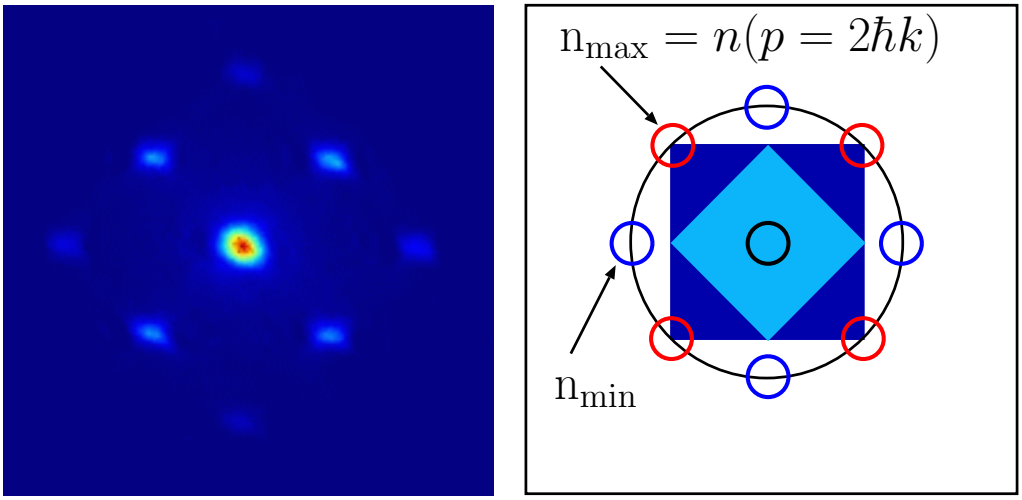

$$\mathcal{V} = \frac{n_{max} - n_{min}}{n_{max} + n_{min}}$$

Figure 6.2: Definition of the visibility of the bosonic interference pattern $\mathcal{V}$ [183, 184]. The visibility is calculated from the atom numbers in the first order interference fringes in comparison to the atom numbers in equivalent areas at intermediate positions between these maxima. The definition is illustrated by a typical interference pattern for shallow optical lattices (a) and with a schematic sketch (b). Apart from the interference fringes, the schematic sketch illustrates the first (light blue) and second Brillouin zone (dark blue).

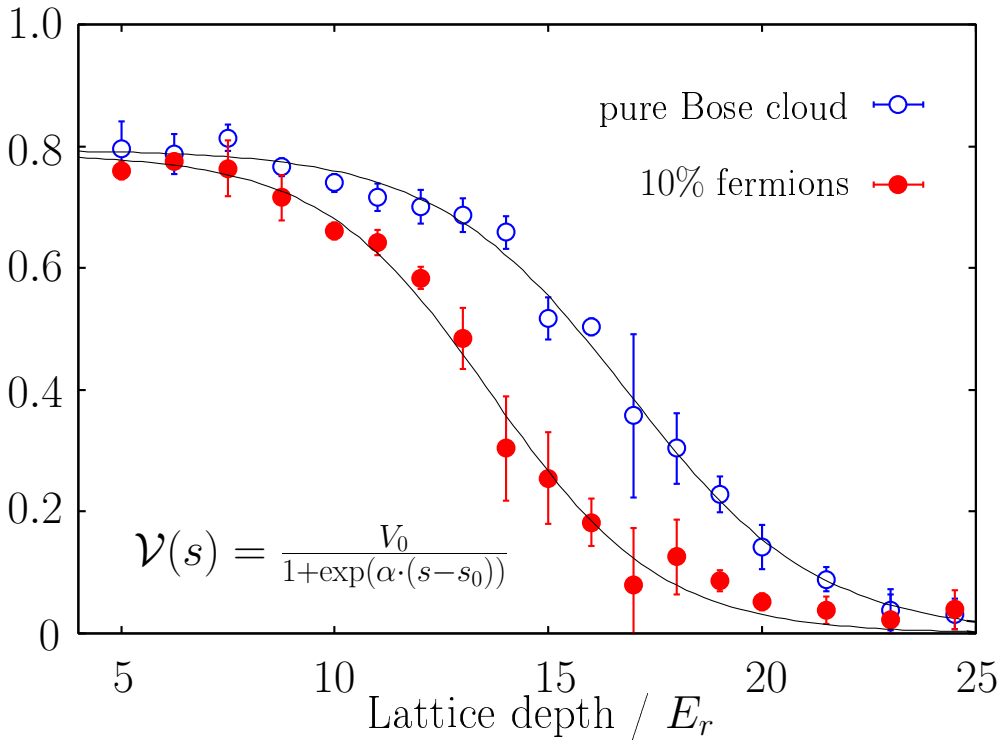

Figure 6.3: Visibility data for both a pure bosonic and a mixed system with an impurity fraction of 10%. We have fitted a phenomenological fit function to the data given by $\mathcal{V}(s) = \mathcal{V}_0/(1+\exp(\alpha\cdot(s-s_0))$.

where $\hat{w}$ is the Fourier transformation of the Wannier function $w(\vec{r})$ and

$$\mathcal{S}(\vec{k}) = \sum_{i,j} \exp(i\vec{k}\cdot(\vec{r}_i - \vec{r}_j)) \left\langle b_i^\dagger b_j \right\rangle \tag{6.3}$$

is the quasimomentum distribution when we restrict ourselves to the lowest Bloch band. As $\mathcal{S}$ is the Fourier transformation of the correlation function $\left\langle b_i^\dagger b_j \right\rangle$, sharp interference fringes are only possible when the correlation function varies slowly across the lattice. As outlined in [183], this is the case of long-range phase coherence. $\left\langle b_i^\dagger b_j \right\rangle$ extends only over a few lattice sites in the case of short range coherence, resulting in a reduction of contrast and visibility. Note that based on the definition of equation 6.1, the Wannier envelope $|\hat{w}|^2$ cancels out and the visibility $\mathcal{V}$ is directly related to the Fourier transform of the correlation function.

Fig. 6.3 shows the visibility of a bosonic cloud of 10^5 atoms loaded into an optical lattice as a function of lattice depth. The data have been obtained starting from a pure condensate in the magic trap with trapping frequencies of $\omega = 2\pi \cdot 50$ Hz in the axial and radial direction. The optical lattice is ramped up with a linear ramp of 0.5 E_r^{Rb}/ms to various final lattice depths. $n_{\max}$ and $n_{\min}$ as defined in Fig. 6.2 are extracted from the time-of-flight images using a circle with a radius of 4 pixels around the center of the first order interference peaks and the displaced intermediate region, respectively. In the

same figure, I have plotted the visibility of the bosonic cloud in a mixed system with 10% impurity fraction.

Let us first study the visibility of the pure bosonic cloud. Starting from lattice depth of 10 E_r^{Rb}, we observe a continuous decrease in the visibility of the bosonic interference pattern which becomes particularly steep above 15 E_r^{Rb}. Note that in our system, the quantum critical points for the onset of the superfluid to Mott-insulator transition in a pure bosonic system are lattice depths of 13.5 E_r^{Rb}, 15.5 E_r^{Rb}, 16.9 E_r^{Rb}, 18.0 E_r^{Rb} and 18.8 E_r^{Rb} for $n = 1$,.....$n = 5$ respectively (see section 5.3.2). The observed loss of interference contrast is ascribed to the increasing fraction of atoms which enters the Mott-insulating phase. The quasi-continuous decrease in visibility, instead of a sharp one above just one lattice depth corresponding to the quantum critical point of the transition, can be explained by the inhomogeneity of the system (see section 5.3.2) where atoms in different shells enter the Mott-insulating state with n atoms per site at different lattice depths.

Phenomenological fit function For the analysis of the visibility data, we use a phenomenological fit function defined by

$$\mathcal{V}(s) = \frac{\mathcal{V}_0}{1 + \exp\left(\alpha \cdot (s - s_0)\right)} \tag{6.4}$$

where $\mathcal{V}_0$ is the initial visibility in the limit $s \to 0$, s_0 is a measure for the "critical" lattice depth and α is an additional fit parameter accounting for the steepness of the loss of contrast.[3] As can be seen in Fig. 6.3, the phenomenological function describes the experimental data quite well. Especially, the fit function accounts for the limiting cases of the superfluid state with a theoretical visibility of $\mathcal{V} = 1$ and the pure Mott-state with a visibility of $\mathcal{V} = 0$.

Comparison of pure bosonic to mixed systems Based on the phenomenological fit function of equation 6.4, we can now compare the decrease in visibility for a pure bosonic cloud to the decrease in case of a mixed system. The corresponding data is plotted in Fig. 6.3. Every data point corresponds to 5 to 10 averaged measurements. The errorbars denote the standard deviation of the 5-10 measurements. To both the visibility data of the bosonic and the visibility data of the mixed system with 10% impurity fraction, we have fitted the phenomenological fit function of equation 6.4. The obtained fit parameters are summarized in table 6.1. Whereas $\mathcal{V}_0$ and the fit parameter α are equal in the two cases

System	s_0/E_r^{Rb}	α	$\mathcal{V}_0$
pure Bose cloud	16.8 ± 0.2	0.45 ± 0.03	0.8 ± 0.02
10% impurities	13.7 ± 0.3	0.5 ± 0.05	0.8 ± 0.02

Table 6.1: Comparison of the parameters of the phenomenological function for a fit to two data sets, one for a pure bosonic system and one for a system with 10% impurity fraction. The errors correspond to the fit errors only. Note that e.g. the lattice depth calibration is estimated to be accurate within 5%, resulting in an error bar on s_0 of ≈ 1 E_r^{Rb}.

within the fit errors, we obtain a significantly lower "critical" lattice depth in the case of

[3] For typical fit results with $\alpha \approx 0.4$ and $s_0 \approx 15$, we obtain $\exp(-\alpha s_0) \approx 0$ and therefore $\mathcal{V}(s \to 0) \approx \mathcal{V}_0$

the mixed system than in the pure bosonic case. We observe a shift in the characteristic parameter s_0 of $\Delta s = s_0^{\mathrm{pure}} - s_0^{\mathrm{mixed}} \approx -3E_r^{\mathrm{Rb}}$ towards lower lattice depth when comparing the mixed to the pure system. We have checked that we do not observe a significant variation in s_0^{mixed} for the mixed system when fixing α and $\mathcal{V}_0$ to the values of the pure bosonic system.

Comparison of the "phenomenological" analysis to the analysis of [184] To estimate the reliability of the analysis based on the phenomenological fit function, we have analyzed the visibility data a second time, this time based on an analytically known dependence of the visibility in the limit of deep optical lattices. Based on perturbation theory in the limit of very weak tunnelling, the ground state of the system can be approximated by

$$|\Psi\rangle \approx |\Psi\rangle_{\mathrm{MI}} + \frac{J}{U} \sum_{<i,j>} b_i^\dagger b_j \, |\Psi\rangle_{\mathrm{MI}} \tag{6.5}$$

where $|\Psi\rangle_{\mathrm{MI}}$ is the Mott-insulating state. The analytical expression for the "column" integrated visibility is then given by [184]

$$\mathcal{V} \propto \frac{zJ}{U} \tag{6.6}$$

which is valid in the limit of deep optical lattices where tunnelling is strongly suppressed.

To compare our analysis of the visibility data based on the phenomenological fit function to an analysis based on the known dependence of the visibility in the limit of deep optical lattices, we have analyzed the visibility both for the pure bosonic cloud and the mixture in the limit of deep optical lattices. Fig. 6.4 shows the visibility data from the previous paragraph, this time plotted as a function of (U/zJ) which is directly related to the lattice depth in the tight-binding limit via

$$\frac{U}{zJ} = \frac{k a_{\mathrm{BB}}}{\sqrt{2}z} \exp(2\sqrt{s}), \tag{6.7}$$

where z is the number of nearest neighbor lattice sites ($z = 6$ in case of a simple cubic 3D lattice). To extract a shift from the data, we have fitted a function $C\left(\frac{U}{zJ}\right)^{\nu}$ in the limit of deep optical lattices ($U/zJ > 10$) and a constant in the limit of shallow optical lattices. From these fits, we can again extract critical lattice depths for both, the pure bosonic cloud and the mixture where the critical depth is defined as the intersection point between the two fits. We observe a critical $(U/zJ)_c \approx 9.9$ in the case of the pure bosonic cloud which corresponds to a lattice depth of 15.6 E_r^{Rb} and a critical depth of $(U/zJ) \approx 3.3$ corresponding to $V_0 \approx 11.6\ E_r^{\mathrm{Rb}}$ in the case of the mixture. The exponent ν is comparable to each other in both cases. We observe $\nu = -1.3(1)$ for the pure bosonic cloud and $\nu = -1.2(2)$ in case of the mixture. From the analysis, we extract a shift of $\approx -4\ E_r^{\mathrm{Rb}}$ which is comparable to the shift extracted from the phenomenological fit function. However, the extracted shift depends critically on the chosen fit interval for the deep lattice limit and varies easily by $\pm 1\ E_r^{\mathrm{Rb}}$, whereas the analysis based on the phenomenological fit function is independent of the fit interval.

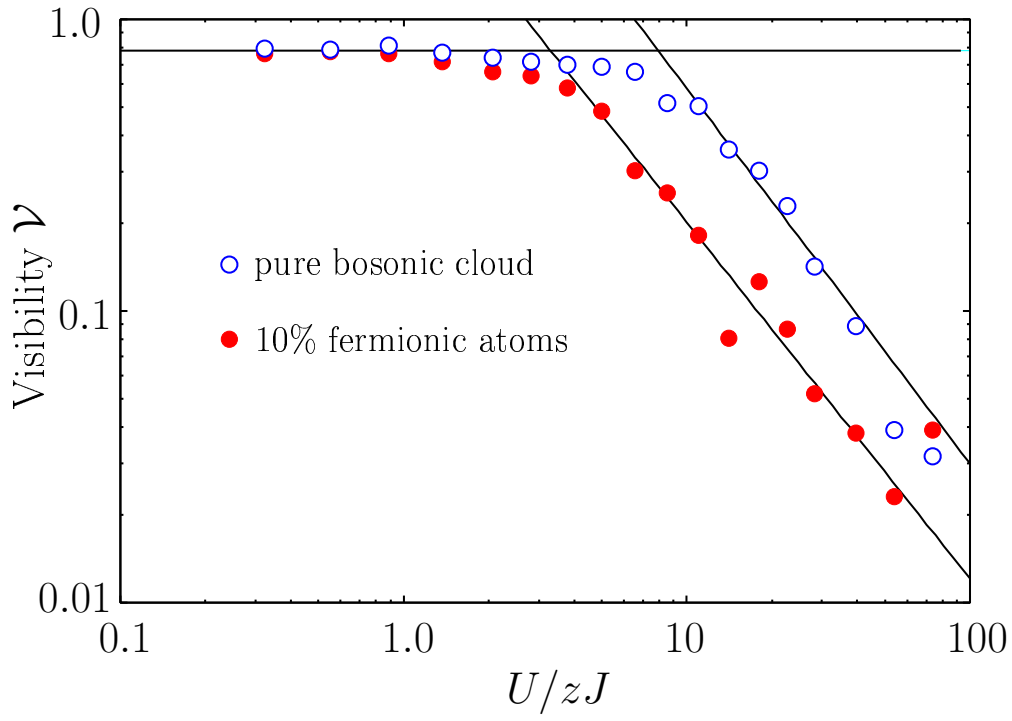

Figure 6.4: Visibility data both for a pure bosonic and a mixed system with an impurity fraction of 10%. This time, we have plotted the visibility against U/zJ where $U/J = \frac{ka_{BB}}{\sqrt{2}} \exp(2\sqrt{s})$ with $s = V_0/E_r^{Rb}$.

6.3.2 Width of the central interference fringe

The phase coherence properties of the bosonic cloud loaded into the optical lattice can also be characterized by the width of the central interference fringe w which is directly related to the correlation length ζ of the system via $\zeta \propto w^{-1}$. The analysis is again motivated by fundamental properties of the superfluid to Mott-insulator transition of a pure bosonic system. Whereas, in the superfluid phase, the correlation length diverges, ζ becomes finite in the Mott-insulating state and is on the order of the inverse energy gap of the system $\zeta \propto U^{-1}$ [185].

Fig. 6.5 shows the half-width of the central interference fringe as a function of lattice depth for the pure bosonic and the mixed system for the data of section 6.3.1. In both cases, the width stays constant for some time or even slightly decreases for shallow optical lattices. At a certain lattice depth, the width suddenly turns off and increases rapidly. The characteristic lattice depth for the sudden increase is extracted from the data by fitting two linear fits to the descending and ascending branches of the data. The characteristic lattice depth is then defined by the intersection point of the two linear curves.

Table 6.2 summarizes the characteristic lattice depths for the two cases. The error bars are again based on the fit errors. Whereas the critical lattice depth of the pure bosonic cloud is given by 16.5(1.6) E_r^{Rb}, in the mixed system, we observe a critical depth of 12.5(1.5) E_r^{Rb}. The critical depth is thus shifted by -4.0(2.0) E_r^{Rb} towards shallower

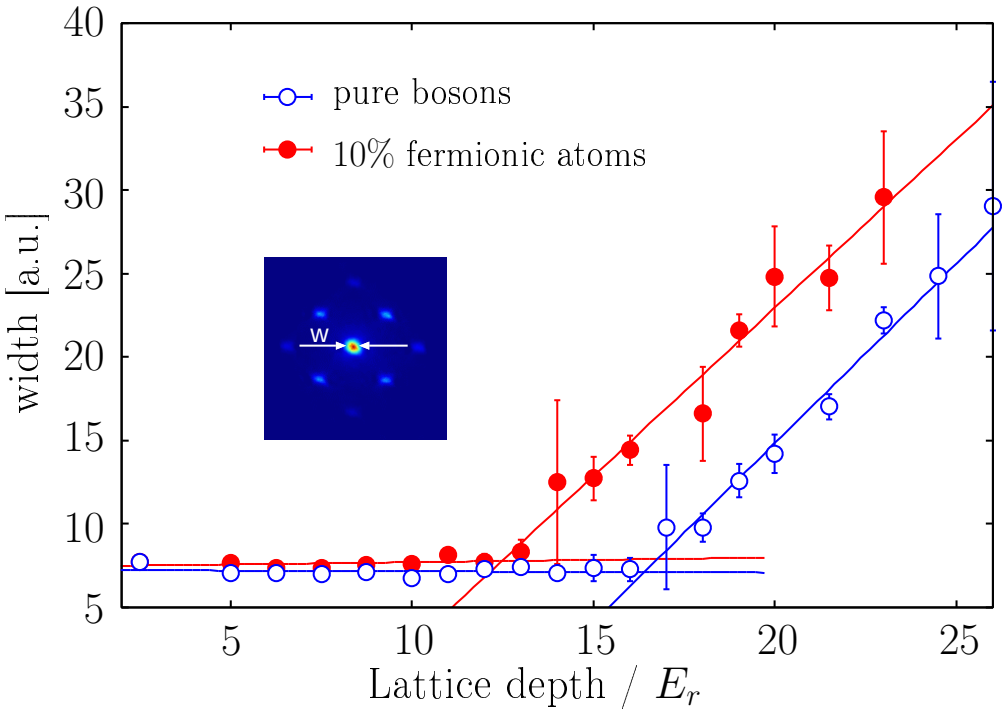

Figure 6.5: Width of the central interference fringe of the bosonic cloud both for a pure bosonic cloud and a mixed system with 10% impurity fraction. The width data shows a sudden increase above a certain lattice depth. The associated characteristic depth can be extracted from the data as the crossing point of two straight lines fitted to the data at low lattice depth and at high lattice depth.

optical lattices. The result is comparable to the respective results extracted from the visibility data.

6.4 Particle number dependence

Based on the techniques of section 6.3, we have studied the change of coherence properties in the bosonic cloud as a function of particle number of the fermionic impurities. We have therefore prepared mixtures of $\approx 10^5$ bosons with a variable fraction of admixed fermionic atoms in the optical lattice. In the experiments, we have prepared mixtures with 3%, 7%, 10% and 20% fermionic atoms corresponding to $3 \cdot 10^3$, $7 \cdot 10^3$, $1 \cdot 10^4$ and $2 \cdot 10^4$ fermions,

System	s_0/E_r^{Rb}
pure Bose cloud	16.5 ± 1.6
10% impurities	12.5 ± 1.5

Table 6.2: Comparison of the "critical depth" of a pure bosonic cloud to a mixed system with 10% impurity fraction as extracted from the width data.

respectively, in the combined magnetic and optical potential with trapping frequencies of $\vec{\omega} = 2\pi \cdot (50, 150, 150)$ Hz or in the magic trap with trapping frequencies of $\omega = 2\pi \cdot 50$ Hz. When choosing the above fractions of fermionic impurities, care has been taken to realize mixtures where the extension of the fermionic atoms is mostly still within the extension of the bosonic cloud in the optical lattice. The extensions of both fermionic and bosonic atoms are estimated for a pure harmonic confinement prior to ramp-up of the optical lattice and for a deep optical lattice: The extension of $2 \cdot 10^4$ fermions at $T = 0$ in a harmonic trap with trapping frequencies of $\omega = 2\pi \cdot (50, 150, 150)$ Hz is given by

$$R_i = \sqrt{\frac{2E_F}{m\omega_i^2}} \quad \text{with} \quad E_F = (6N)^{1/3}\hbar(\omega_{\text{rad}}^2\omega_{\text{ax}})^{1/3} \tag{6.8}$$

and is $R_{\text{rad}} \approx 8$ μm and $R_{\text{ax}} \approx 24$ μm for the above parameters with a central density of $n(0) = \frac{1}{6\pi^2}\left(\frac{2m}{\hbar^2}E_F\right)^{3/2} \approx 8 \cdot 10^{12}/\text{cm}^3$, thereby just reaching a density corresponding to the lattice site density $\approx 7.5 \cdot 10^{12}/\text{cm}^3$. In a deep optical lattice, the corresponding radius under the assumption of unity filling, can be derived from the condition that the extension of the fermionic cloud in the different directions is determined by the condition

$$\frac{1}{2}m\omega_{\text{rad}}^2 x_{\text{rad}}^2 = \frac{1}{2}m\omega_{\text{ax}}^2 x_{\text{ax}}^2 \tag{6.9}$$

where $x_{\text{rad/ax}} = i_{\text{rad/ax}} \cdot \lambda/2$ corresponds to the coordinate of the last occupied lattice site in radial/axial direction and $N = \frac{4}{3}\pi i_{\text{rad}}^2 \cdot i_{\text{ax}}$. The radial/axial extension of the cloud is then given by

$$\begin{aligned} x_{\text{rad}} &= i_{\text{rad}}\lambda/2 = \left(\frac{3N}{4\pi}\frac{\omega_{\text{ax}}}{\omega_{\text{rad}}}\right)^{1/3} \cdot \lambda/2 \approx 6\ \mu\text{m} \\ x_{\text{ax}} &= i_{\text{ax}}\lambda/2 = \left(\frac{3N}{4\pi}\frac{\omega_{\text{rad}}^2}{\omega_{\text{ax}}^2}\right)^{1/3} \cdot \lambda/2 \approx 18\ \mu\text{m} \end{aligned} \tag{6.10}$$

These numbers have to be compared to the extension of a pure BEC of $\approx 10^5$ atoms, whose radial/axial radius is $\approx 6\,\mu$m/$\approx 18\,\mu$m in the pure harmonic trap and for 25 E_r^{Rb} lattice depth 7.5 μm/20.5 μm. The extensions of the cloud in the deep optical lattice have been estimated based on a chemical potential of the cloud in the deep optical lattice of

$$\mu^{\text{deep lattice}} = \left(\frac{15}{16}\frac{(\lambda/2)^3 m^{3/2} N U_{\text{BB}}(s = 25\ E_r^{\text{Rb}})\omega_{\text{ax}}\omega_{\text{rad}}^2}{\sqrt{2}\pi}\right)^{2/5} \text{[188]}. \tag{6.11}$$

Fig. 6.6 shows sample data comparing the coherence properties of the bosonic cloud with an impurity concentration of 3% and 7% to the properties of a pure bosonic ensemble. The data has been analyzed as outlined in section 6.3. The loss of interference contrast and a decrease of correlation length in comparison to a pure bosonic cloud is clearly visible in the visibility curve (see Fig. 6.6a)) as well as in the width data (see Fig. 6.6b)). The loss of coherence in the bosonic clouds shifts towards shallower optical lattices with increasing impurity fraction. Already for 3% impurity concentration, the visibility data shows a significant shift of approximately -2 E_r^{Rb}. The corresponding width data, however, essentially exhibits a steeper slope with no pronounced shift compared to the pure

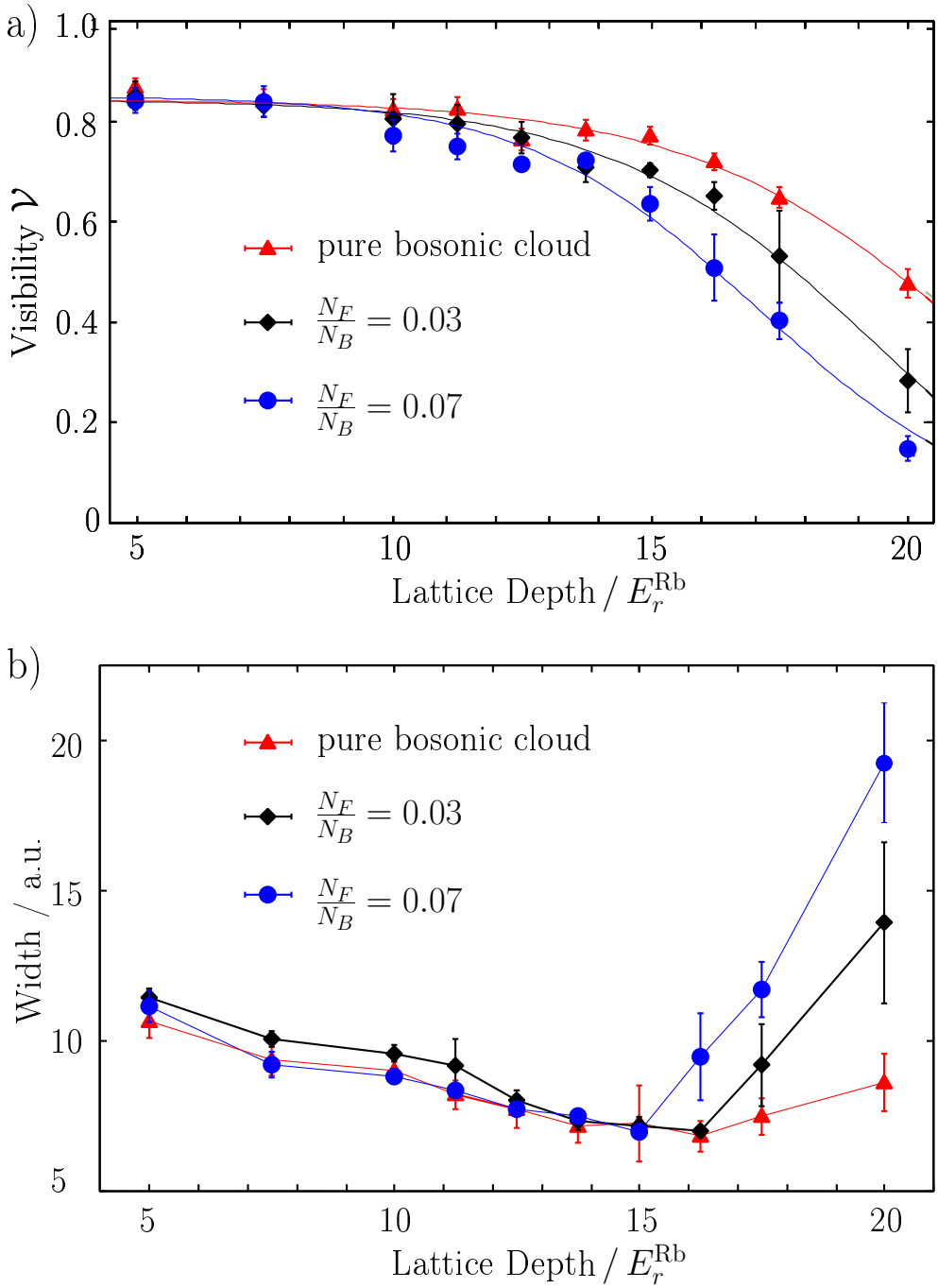

Figure 6.6: Visibility $\mathcal{V}$ (a) and central peak width (b) of the bosonic interference pattern for different fermionic impurity concentrations.

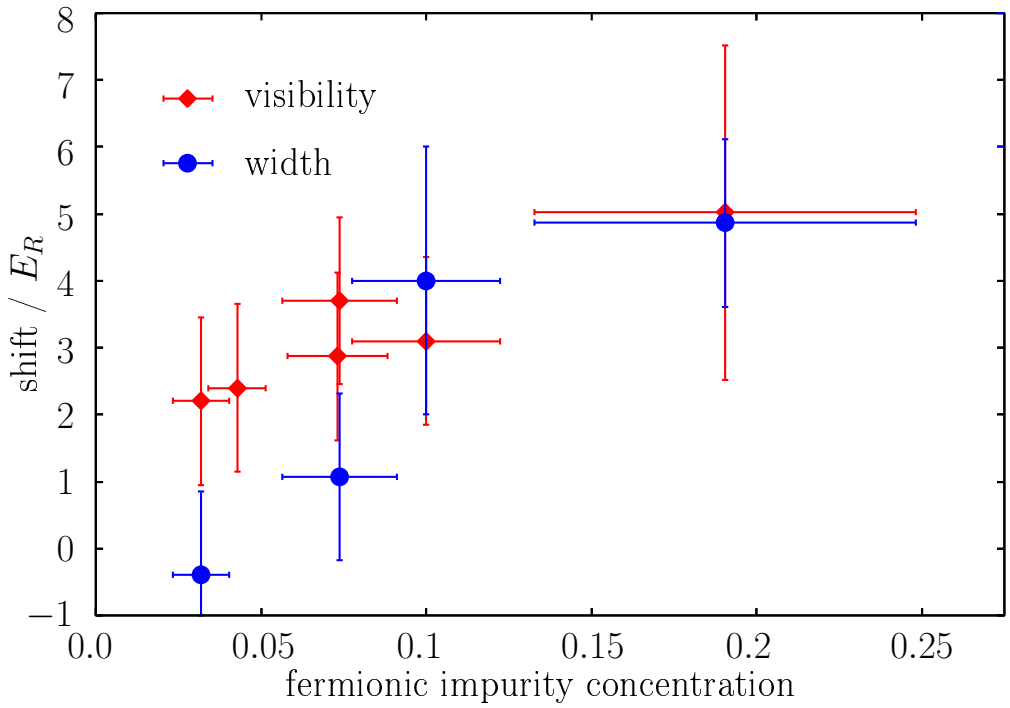

Figure 6.7: Observed shift of the "critical" lattice depth characterizing the loss of coherence in the bosonic cloud as a function of fermionic impurity concentration.

bosonic system. When increasing the impurity fraction to 7%, the shift in both the visibility and the width data becomes significantly larger. We observe shifts of $-3\ E_r^{\mathrm{Rb}}$ from the visibility data and $\approx -1\ E_r^{\mathrm{Rb}}$ from the width data.

Fig. 6.7 summarizes our findings on the particle number dependence. We have analyzed samples with 10^5 bosons with varying impurity concentration between 3% and 20%. In case of the visibility data, the error bars in the diagram correspond to the "sample" rate of the underlying data. A sample rate of $1 - 1.25\ E_r^{\mathrm{Rb}}$ has been translated into an assumed maximum error of the same size; this error is larger than the error based on the fit errors. In case of the width data, we have calculated the error bars based on the underlying fit errors of the involved parameters. As can be seen from 6.7, an increasing impurity concentration leads to a considerable shift of the bosonic coherence properties towards shallower optical lattices. The shift increases with impurity concentration and reaches $-5\ E_r^{\mathrm{Rb}}$ for an impurity concentration of 20%. Note that the different data points correspond to ensembles that have been prepared on different days and under various conditions. Whereas most of the measurements have been done with an external harmonic confinement given by a combined magnetic and optical potential with an aspect ratio of 1 : 3 (see above), some of the data points have been recorded with an almost spherically symmetric confinement of $\omega = 2\pi \cdot 50$ Hz determined by the magic trap (see chapter 3). In all these cases, we observe qualitatively and quantitatively the same characteristic behavior.

6.5 Studies on systematic effects

To exclude trivial irreversible heating effects as a source of the observed systematic shift in the coherence properties of the bosonic cloud, we have studied the reversibility of the observed coherence loss. To this end, we have ramped up the optical lattice to final lattice depths between 15 E_r^{Rb} and 20 E_r^{Rb}, where the coherence of the bosonic cloud is either completely lost or at least significantly distorted, and have subsequently ramped down the lattice with the same ramp speed to varying lattice depths between 5 E_r^{Rb} and 7.5 E_r^{Rb}. Apart from some signs of non-adiabaticity visible in a slight asymmetry of the obtained visibility data with respect to the reversal point at deep optical lattices, we have been able to restore the initial visibility of the bosonic cloud almost completely. The maximum observed irreversible loss of visibility is on the order of 10%. In case that the overall ramp sequence has not been fully reversible, allowing for an additional equilibration time of $5 - 10$ ms after ramp-down has resulted in a near complete recovery of visibility.

6.6 Discussion

As already outlined in the introduction to this chapter, there is currently an intense discussion on the nature of the observed shift of the coherence properties of the bosonic cloud due to a small admixture of fermionic atoms. Possible scenarios include a shift of the superfluid to Mott insulator transition of the bosonic cloud due to interactions with the fermionic impurities, thermodynamic effects such as adiabatic heating and effects of disorder induced localization scenarios. In the following section, I will briefly review the current status of the discussion and provide the interested reader with some simple estimates.

6.6.1 Shift of the superfluid to Mott-insulator transition

One of the possible scenarios is a shift of the superfluid to Mott insulator transition of the bosonic cloud due to the admixture of attractively interacting fermions. I will discuss the effects of fermions on the quantum critical point of the bosonic phase transition based on two different models, the Fermi-Bose Hubbard approximation and a simple mean-field estimate.

6.6.1.1 Fermi-Bose Hubbard approximation

Homogeneous System in Bose-Fermi-Hubbard approximation The change of the quantum critical point of the bosonic superfluid to Mott-insulator transition in a homogeneous system due to the presence of fermionic atoms has been discussed in a very recent work by Pollet and coworkers [189]. Based on the Fermi-Bose-Hubbard Hamiltonian, Pollet *et al.* have discussed in zero and first order perturbation theory the change in $(U/zJ)_c$ due to interactions with the fermionic cloud. We summarize here the main results:

Let us consider the Bose-Fermi Hubbard Hamiltonian of a homogeneous system

$$H_{BF} = -J_B \sum_{<i,j>} b_i^\dagger b_j + \frac{1}{2} U_{BB} \sum_i n_i(n_i - 1) \tag{6.12}$$

$$
\begin{aligned}
- \quad & J_F \sum_{<i,j>} f_i^\dagger f_j \\
+ \quad & U_{BF} \sum_i n_i^B m_i
\end{aligned}
\tag{6.13}
$$

which can directly be derived from the more general inhomogeneous case of section 5.3.4 by setting $\epsilon_i^{F/B} = 0$.

Let us consider the influence of the fermions as a perturbation of the pure bosonic Hubbard Hamiltonian. The lowest order effect that the fermions have on the bosons can be derived when replacing the fermionic particle number operators m_i by their expectation values. In this case, the perturbation to the pure bosonic Hubbard Hamiltonian is: $U_{\mathrm{FB}} \sum n_i^B \langle m_i \rangle$. To lowest order perturbation theory, the fermionic expectation values $\langle m_i \rangle$ are calculated by solving the pure fermionic Hubbard Hamiltonian (neglecting the effects of the bosons on the fermionic cloud). In the homogeneous system considered here, $\langle m_i \rangle$ is independent of the lattice site $\langle m_i \rangle = \langle m_j \rangle = \langle m \rangle$. To lowest order perturbation theory, the fermions thus induce an overall shift of the system's energy and do not change the phase diagram of the bosonic cloud at all.

The next order effect can be derived when adopting the results of linear response theory. In this case, one assumes the unknown bosonic density $n_B(\vec{q})$ to induce a fermionic density $\langle n_F(\vec{q}) \rangle = U_{FB} \Xi(T, \vec{q}) n_B(\vec{q})$ where $\Xi(T, \vec{q})$ is the Lindhard response function known from the theory of screening when calculating electronic charge distributions in condensed matter physics [160, 173, 189]. The induced fermionic density distribution results in a back-action on the bosons and thus in an effective interaction for the pure bosonic cloud given by $\hat{U}_{\mathrm{BB}}^{\mathrm{eff}} = U_{\mathrm{BB}} + U_{\mathrm{FB}}^2 \Xi(T, \vec{q})$. As the Lindhard function is always negative, the interaction matrix elements between two initially repulsively interacting bosons is effectively reduced by an amount $U_{\mathrm{FB}}^2 \Xi(T, \vec{q})$ independent of the sign of U_{FB}. This induced attractive interaction is in analogy to phonon induced attraction between electrons in conventional superconductors and is at the heart of recent proposals on boson-induced Cooper pairing of fermions in optical lattices [28]. Based on these considerations, the superfluid to Mott-Insulator transition is shifted towards deeper optical lattices independent of the sign of Bose-Fermi interaction U_{FB}.

Inhomogeneous system in BFH approximation The situation becomes more complicated when considering an inhomogeneous situation where the atoms experience both an optical lattice and an external harmonic trapping potential. In this case, the equilibrium densities of both components bosons and fermions will be enhanced in the center of the confining potential (see section 4.3) due to the attractive interactions. However, enhanced density results in an increased mean bosonic occupation number on a single lattice site, thereby shifting the transition from a superfluid to a Mott insulating state towards deeper optical lattices (see equation 5.33).

6.6.1.2 Mean-field approach - Induced effective potential

Let us now come back to the scenario of a homogeneous optical lattice without additional overlapped harmonic potential. Let us consider the fermionic density distribution in the lattice as an additional mean-field potential $U_{MF}^F(\vec{r})$ which enters into the

bosonic many-particle Hamiltonian via the confining external potential $V_{\text{effective}}(\vec{r}) = V_{\text{periodic}}(\vec{r}) + U_{MF}^{F}(\vec{r})$. To lowest order perturbation theory, the additional fermionic mean-field potential is determined by the unperturbed fermionic density distribution given by $n_F(\vec{r}-\vec{r}_i) = \langle m \rangle \sum_i |w^{\mathrm{F}}(\vec{r}-\vec{r}_i)|$, resulting in

$$U_{MF}^{F} = n_F(\vec{r}) U_{BF} = \langle m \rangle \, U_{BF} \sum_i |w^F(\vec{r}-\vec{r}_i)|^2, \tag{6.14}$$

where w^F is the fermionic Wannier function for the case of a pure sinusoidal external lattice potential of depth V_{Lattice}. Taking into account this additional potential, the bosonic many-particle Hamiltonian reads:

$$\begin{aligned} H_B &= \int d^3r \Psi_B^\dagger(\vec{r}) \left(\frac{p^2}{2m} + V_{\text{periodic}}(\vec{r}) + n_F(\vec{r}) U_{\mathrm{BF}} \right) \Psi_{\mathrm{B}}(\vec{r}) \\ &+ \frac{1}{2} U_{\mathrm{BB}} \int d^3r \Psi_{\mathrm{B}}^\dagger(\vec{r}) \Psi_{\mathrm{B}}^\dagger(\vec{r}) \Psi_{\mathrm{B}}(\vec{r}) \Psi_{\mathrm{B}}(\vec{r}) \end{aligned} \tag{6.15}$$

The fermions thus alter the properties of the pure external periodic potential and change both the depth and geometry of a single lattice well (see also Fig. 6.12e). From the effective many-body Hamiltonian of equation 6.15, we can derive an effective Bose-Hubbard Hamiltonian. The presence of the fermionic mean-field potential then changes both onsite interaction and tunnelling matrix elements of the bosonic atoms.

A rough estimate on the shift of the superfluid to Mott-insulator due to the additional mean-field potential of the fermionic cloud can be obtained as follows:

Estimating the change of the bosonic tunnelling matrix element J We first estimate the change of the bosonic tunnelling matrix element due to the presence of exactly one fermionic atom on each lattice site ($\langle m \rangle = 1$). In the tight-binding limit, the fermionic Wannier function can be approximated by a Gaussian wavefunction of the form

$$\phi^F(\vec{r}) = \left(\frac{m\omega_{\text{Lattice}}^{\mathrm{K}}}{\pi\hbar} \right)^{3/4} \exp\left(-\frac{1}{2} \frac{m\omega_{\text{Lattice}}^{\mathrm{K}}}{\hbar} \vec{r}^2 \right) \tag{6.16}$$

where $\omega_{\text{Lattice}}^{\mathrm{K}} = \omega_{\text{Lattice}}^{\mathrm{K}}(s)$ is the oscillator frequency of a ^{40}K atom confined on a single lattice well of depth $s = V_{\text{Lattice}}/E_r^{\mathrm{Rb}}$. To lowest order, fermionic atoms, which interact attractively with the bosonic atoms, induce an effectively deeper optical lattice where the new depth is given by

$$V_{\text{Lattice}}^{\text{effective}}(s) \approx V_{\text{Lattice}} + U_{\mathrm{BF}} n_{\mathrm{F}}(\vec{r}=0) \langle m \rangle \approx s \cdot E_r^{\mathrm{Rb}} + \left(\frac{m\omega_{\text{Lattice}}^{\mathrm{K}}(s)}{\pi\hbar} \right)^{3/2} U_{\mathrm{BF}}. \tag{6.17}$$

From a band structure calculation based on the effective lattice depth, we obtain a new tunnelling matrix element $J^{+\mathrm{F}}$ for the bosonic cloud changed by the presence of fermionic atoms. In this picture, the effective bosonic tunnelling matrix element is significantly reduced in case of attractive interactions between bosons and fermions (see Fig. 6.8). Note that this is only a very rough estimate for several reasons. First, the fermions alter significantly the geometry of a single confining lattice well which is totally neglected in

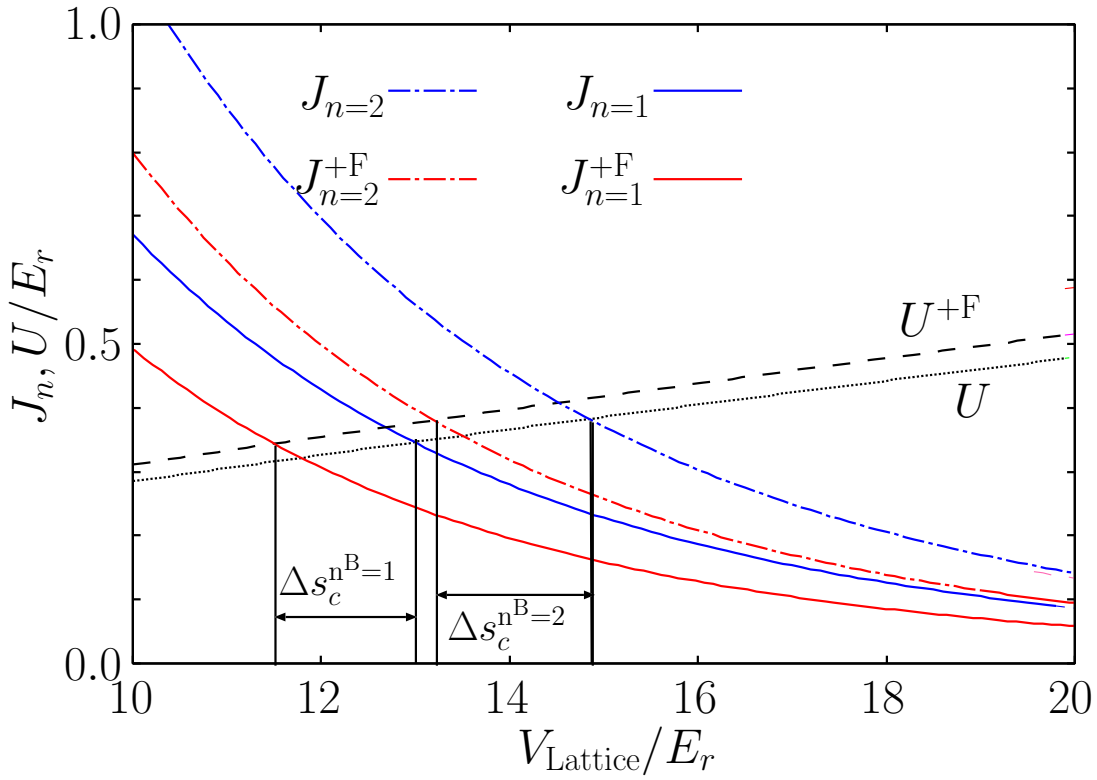

Figure 6.8: Rough estimate on the shift of Mott-insulator transition based on a fermionic mean-field potential (see text). Plotted in this diagram are the onsite interaction matrix elements for bosons in a pure bosonic cloud U, for bosons interacting with the mean-field potential generated by the fermionic cloud $U^{+\mathrm{F}}$ and the tunnelling matrix elements for both cases $J_n = (2n + 1 + 2\sqrt{n(n+1)})J$ and $J_n^{+F} = (2n + 1 + 2\sqrt{n(n+1)})J^{+F}$. A rough estimate on the shift of the quantum critical points Δs_c can be extracted from the diagram.

the above approach. Second, the fermionic densities have been assumed to be completely undisturbed by the bosonic cloud. Third, due to the lighter mass of the fermions compared to the bosonic atoms, the fermions are only localized on a single lattice well at much deeper optical lattices than the bosons and are still mobile at typical lattice depths of 20 E_r^{Rb} corresponding to $V_{\mathrm{Lattice}} \approx 10\ E_r^{\mathrm{K}}$.

Estimating the change in onsite interaction U An estimate for the change of the bosonic onsite interaction matrix element in the tight binding limit can be obtained similarly. The change of geometry of a single confining lattice well due to the fermionic density distribution is neglected and an effective lattice depth derived as in equation 6.17. The new onsite interaction matrix element can then be obtained from equation 5.29.

Estimating the effect on the quantum critical point Fig. 6.8 summarizes the results of the approach outlined above. Plotted in this diagram are the onsite interac-

tion matrix element U for bosons in a pure bosonic cloud (black dotted line), the onsite interaction matrix element for bosons interacting with fermions on a single lattice well (dashed black line) and tunnelling matrix elements for the pure bosonic cloud J_{n} (blue) and the cloud interacting with a fermionic mean-field potential $J_{\mathrm{n}}^{+\mathrm{F}}$ (red) where $J_n = (2n + 1 + 2\sqrt{n(n+1)}J$ and n is the bosonic occupation number of a single lattice site (see equation 5.33). Following the mean-field approach and the outlined rough estimate, the onsite interaction matrix element for the bosons is significantly enhanced due to interactions with the fermionic mean-field, whereas the tunnelling matrix elements are significantly reduced. Both contribute to a significant shift of the Mott-insulator transition towards shallower optical lattices. Based on the criterion of equation 5.33, we obtain a shift $\Delta s_c \approx 1.5\ E_r^{\mathrm{Rb}}$ for $n = 1, 2$ (see Fig. 6.8) which is still much smaller than the observed shift of $5\ E_r^{\mathrm{Rb}}$ of the coherence properties of the bosonic cloud interacting with $2 \cdot 10^4$ fermionic atoms.

Note that for a rigorous estimate, the change of geometry of the periodic potential due to the presence of the fermionic cloud has to be taken into account as well as the inhomogeneity of the periodic potential which is in actual experiments overlapped by a harmonic potential. Whereas the sign of the correction due to the geometry change can only be obtained by a numerical calculation, the effect of inhomogeneity of the optical lattice is similar to the effect described in section 6.6.1.1. In brief, due to attractive interactions between fermions and bosons, the bosonic occupation number in the center of the trap will be enhanced which results in a shift of the quantum critical points towards deeper optical lattices. Numerical calculations are currently performed by M. Cramer.

6.6.2 Adiabatic heating or cooling

When adiabatically loading either bosonic or fermionic quantum gases into an optical lattice, the density of states for the components changes markedly (as we have seen for the case of non-interacting atoms in section 5.2.2), thereby e. g. changing the characteristic temperatures for degeneracy in bosonic and fermionic quantum gases, T_c and T_F. Adiabatic loading of atoms occurs at constant entropy S, not at constant temperature, and the absolute temperature may change. The change in degeneracy characterised by T/T_c and T/T_F depends on the starting conditions such as temperature and atom number as well as the trap geometry and the interactions present in the system. Note that the temperature change is reversible as it occurs at constant entropy and is a purely thermodynamic effect. However, increasing T/T_c with increasing lattice depth may lead to a decreasing condensate fraction which might result in loss of coherence of the bosonic cloud.

Adiabatic temperature change at constant entropy due to adiabatic loading of atoms into an optical lattice has been discussed in the literature for a homogeneous non-interacting Fermi gas [190] and for homogeneous and inhomogeneous interacting and non-interacting bosonic clouds [191, 192].

To illustrate how this adiabatic temperature change occurs, we consider here the example of non-interacting fermions in an inhomogeneous optical lattice composed of the periodic potential and a superimposed harmonic oscillator potential: When loading single-component non-interacting fermions into a 3D optical lattice, the density of states changes from the density of states of a pure harmonic oscillator to the density of states in the limit of a deep optical lattice (see section 5.3.3). Based on the density of states, we can calculate

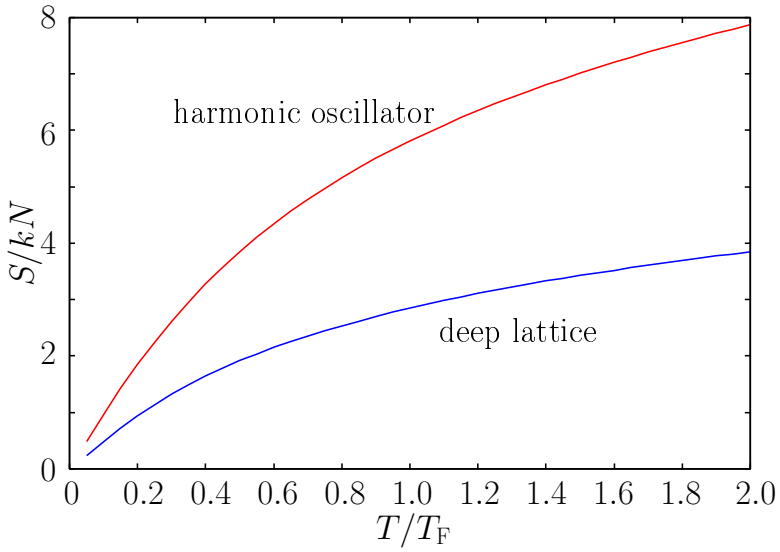

Figure 6.9: Entropy per particle in the two limiting cases: $V_{\text{Lattice}} = 0$ corresponding to pure harmonic oscillator (red) and deep optical lattice (blue).

the entropy of non-interacting fermions in the two limiting cases: Assuming $\hbar\omega \ll E_F$, we obtain

$$S^{\text{ho}}/kN = 4\frac{f_4(z)}{f_3(z)} - \ln(z) \tag{6.18}$$

$$S^{\text{deep lattice}}/kN = \frac{5}{2}\frac{f_{5/2}(z)}{f_{3/2}(z)} - \ln(z) \tag{6.19}$$

where $z = \exp(-\frac{\mu}{kT})$ is the fugacity. The entropy per particle of a single-component fermionic gas in the two limiting cases is plotted in Fig. 6.9. As can be seen from the figure, the entropy per particle is much lower in the case of a deep optical lattice than in the case of the "initial" pure harmonic oscillator. Adiabatic lattice loading occurs at constant entropy which results in rapid heating of the fermionic cloud in terms of T/T_{F} when changing the external confining potential from that of a pure harmonic oscillator to a deep optical lattice plus harmonic oscillator. The change in the degeneracy parameter T/T_{F} is illustrated in Fig. 6.10. In this figure we have plotted the final $(T/T_{\text{F}})^{\text{deep lattice}}$ versus the initial $(T/T_{\text{F}})^{\text{ho}}$. However, the absolute temperature change depends on the ratio of Fermi temperatures $T_{\text{F}}^{\text{deep lattice}}/T_{\text{F}}^{\text{ho}}$ (which is in most experimentally relevant cases < 1, c.f. section 5.3.3) and the initial temperature T_{initial} of the cloud in the harmonic oscillator potential. The regimes of adiabatic cooling/heating are illustrated in Fig. 6.11. For typical experimental parameters of our experiment ($N = 10^4$, $E_r^{\text{K}}/\hbar\omega^{\text{K}} = 82$), the critical temperature separating adiabatic cooling from adiabatic heating regions is then given by $kT_{\text{initial}}/E_r^{\text{K}} \approx 0.45$. At lower temperatures, the absolute temperature T_{final} becomes smaller than the initial temperature T_{initial} whereas adiabatic heating occurs above the critical temperature.

While this very simple example is useful for an understanding of adiabatic heating and cooling phenomena, it does not provide estimates for the interacting Fermi-Bose mixture.

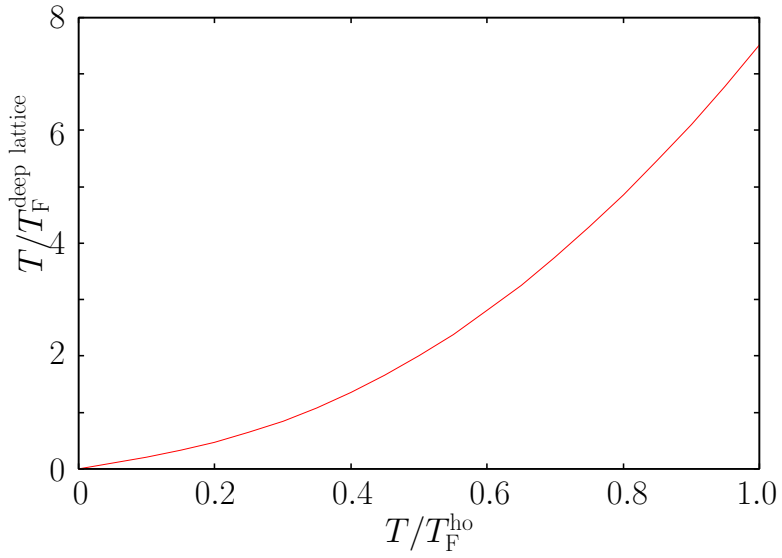

Figure 6.10: Change in T/T_{F} when adiabatically transforming a pure harmonic oscillator potential into a deep optical lattice plus harmonic confinement: $(T/T_{\mathrm{F}})^{\mathrm{deep\ lattice}}$ as a function of $(T/T_{\mathrm{F}})^{\mathrm{ho}}$. Adiabatic loading of atoms into an optical lattice occurs at constant entropy which results in rapid heating of the fermionic cloud in terms of the degeneracy parameter T/T_{F}.

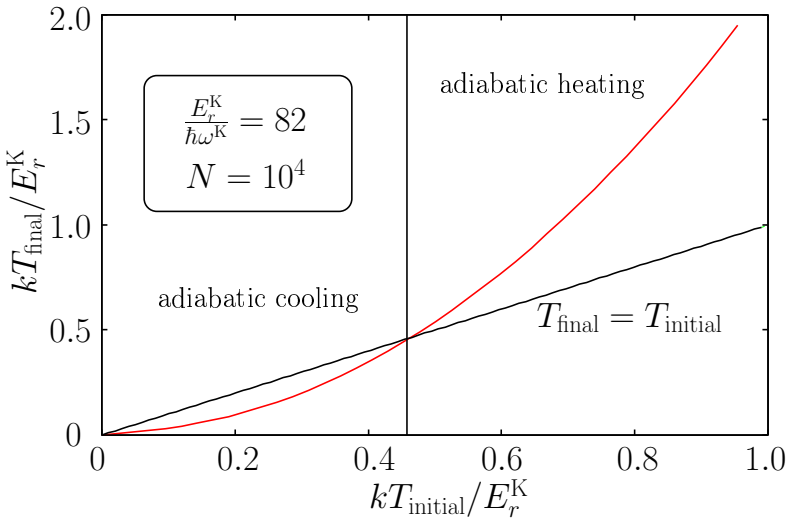

Figure 6.11: T_{final} in the deep optical lattice as a function of T_{initial} in the harmonic oscillator potential. We assume typical experimental parameters from our experiments: $N = 10^4$, $E_r^{\mathrm{K}}/\hbar\omega^{\mathrm{K}} = 82$. For comparison, we have plotted the line $T_{\mathrm{final}} = \mathrm{T}_{\mathrm{initial}}$ in the same diagram.

It has been pointed out by Rey *et al.* [192] that even in the case of a single-component pure bosonic cloud, adiabatic cooling/heating critically depends on a wide parameter space like

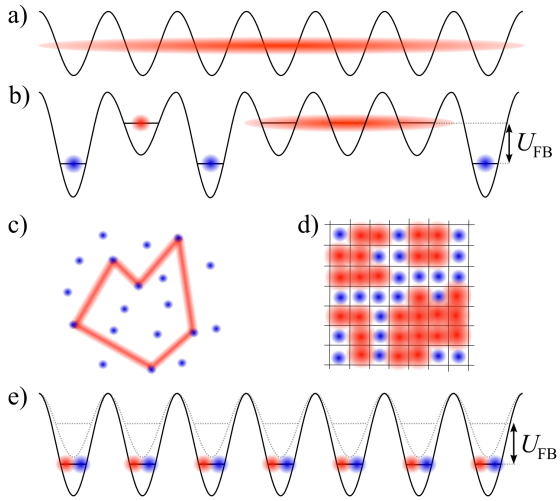

Figure 6.12: Schematic localization scenarios. **a**. Pure bosonic superfluid in an optical lattice. **b**. Shift of the effective potential depth due to fermionic impurities. **c**. Localization by interfering paths of the bosonic wavefunction scattered by randomly distributed fermionic impurities. **d**. Localization due to percolation. A random fermion distribution hampers the establishment of a coherent connection and causes the localization of bosonic ensembles in superfluid "islands". **e**. Mott insulator transition induced by a uniform distribution of attractive fermionic impurities, resulting in an effectively deeper lattice potential for the bosons.

initial temperatures, interactions and harmonic confinement.

Estimates for the mixture can in principle be obtained by an extension of the above approach to non-interacting Fermi-Bose mixtures based on the available literature on single-component systems and eventually including the effects of Fermi-Bose interactions. These steps are currently underway.

6.6.3 Disorder-enhanced localization scenarios

Let us finally review intuitively possible disorder-related localization scenarios which have been discussed in the literature and which might be observable in Fermi-Bose mixtures and would possibly also lead to reduced coherence in the bosonic cloud. For illustration purposes, let us start with a pure bosonic superfluid (Fig. 6.12 a). Adding fermionic impurities and considering the attractive ^{40}K — ^{87}Rb Fermi-Bose interaction energy as an additional potential for the bosons, the "defects" caused by the fermionic impurities can be described by a local change of the effective optical lattice depth for the bosons due to the interparticle interaction (Fig. 6.12 b). If the energy level shift caused by the interaction energy is large enough, the superfluid bosonic wavefunction will not extend into this defect region, but will be scattered by the impurity. If scattering becomes frequent, interference effects along a closed scattering path are predicted to suppress transport and lead to a localization scenario similar to Anderson localization (Fig. 6.12 c). A further increase in the impurity density will lead to the formation of "forbidden walls". Once the

walls in this quantum percolation scenario lead to a sufficiently complicated labyrinth like structure for the bosonic wavefunction, a single coherent superfluid phase can no longer be sustained and several separated domains will be formed (Fig. 6.12 d).

6.7 Conclusions

In this chapter, I have presented experiments which have for the first time combined Fermi-Bose mixtures with crystals made of light. We have investigated the coherence properties of the bosonic cloud when admixing a small fermionic impurity fraction and observe a significant shift of the loss of coherence in the bosonic cloud. The nature of the observed effect is still a point of controversial discussion and we have discussed possible starting points which might contribute to the explanation of the observed effect.

Definitely, further experiments are required to shine more light on the observed phenomena. A possible shift of the Mott-insulating transition can be probed by a spectroscopic investigation of the excitation spectrum of the mixture similar to probing of the excitation gap of the pure bosonic Mott insulator in [19, 154]. Lattice site occupation can be probed by rf spectroscopic techniques [170]. The correlation properties of the fermionic and bosonic components can be revealed by noise correlation techniques [193, 194, 195]. With the availability of heteronuclear Feshbach resonances (see chapter 4 and 7), it is straightforward to extend our studies to almost arbitrary interaction strength between the fermionic and bosonic constituents. In any case, further studies will have to concentrate on isolation and identification of underlying phases and associated phase transitions in this rich system.

Chapter 7

Heteronuclear Molecules

There has been a long quest for production of ultracold molecules in recent years. In particular, heteronuclear molecules would open up intriguing perspectives both in view of their internal properties and their interactions. The electric dipole moment of heteronuclear molecules in their internal ground states makes them one of the best candidates for tests of fundamental physics like the search for a permanent electric dipole moment of the electron and parity violation [196] as well as for studies on the drifts of fundamental constants. In addition, polar molecules are a key for novel promising quantum computation schemes [38]. Furthermore, their large anisotropic interactions give rise to quantum magnetism [197], new types of superfluid pairing [198] and a variety of quantum phases [199]. Currently, two main routes to the production of ultracold ground-state molecules are being pursued. One approach aims at cooling thermal ensembles of molecules, e. g. using buffer gas cooling [200], Stark deceleration [201] or velocity filtering [202]. The other approach starts with ultracold atomic ensembles and assembles them into molecules by means of photoassociation [203] or Feshbach resonances [120, 121, 122, 123]. In the latter case, ultracold molecules in a highly excited rovibrational state are created which can subsequently be transferred into their internal ground state by appropriate Raman-like transitions [204]. One major issue has been the stability of these highly excited molecules. While molecules created in bosonic quantum gases have a very short collisional lifetime, bosonic molecules from two fermionic atoms are relatively stable due to the Pauli principle [124, 125, 117, 118, 127]. In other cases, as recently demonstrated for bosonic samples [24, 158] and also expected for heteronuclear mixtures, it is favorable to produce the molecules in separated wells of optical lattices to suppress collisional inelastic losses. So far, molecules produced at Feshbach resonances have been limited to homonuclear systems.

In this chapter, I report on the first creation of ultracold heteronuclear molecules in a 3D optical lattice at a Feshbach resonance. This approach produces ultracold molecules in the ground state of individual lattice sites. This method offers several advantages: long lifetimes allow for further manipulation towards the internal molecular ground state. Moreover, the inherent order within the lattice enables studies of new quantum phases of dipole-dipole interacting systems.

In particular, we perform rf association of fermionic ^{40}K and bosonic ^{87}Rb atoms close to a heteronuclear Feshbach resonance. Molecules form both on the repulsive and on the attractive side of the resonance, which is a consequence of two-body physics in the

presence of strong external confinement. We measure the binding energy as a function of the magnetic field by rf spectroscopy [205, 206] and study the lifetime and production efficiency of the bound pairs.

This chapter follows closely PRL 97, 120402 (2006) [1]. An in-depth discussion can be found in the thesis of Christian Ospelkaus [35]

7.1 Feshbach molecules in a 3D optical lattice

Quite generally, a Feshbach resonance occurs when the total energy of two colliding atoms is equal to the energy of a bound molecular state. In free space, the Feshbach molecular state describes a stable molecule on the side of the resonance with positive scattering lengths. Molecule formation, that means a transition from a two-atom state of two colliding atoms to a bound molecular state, is thus possible in the vicinity of a Feshbach resonance and has been demonstrated in a number of experiments. One common technique is molecule formation by an adiabatic magnetic field ramp from the attractive side of the resonance (bound state of closed channel above the free-atom threshold) to the repulsive side (bound state below free atom threshold), thereby adiabatically transforming the two-atom state into a bound molecular state. The bound molecular state, however, ceases to exist at the position of the resonance and beyond on the attractive side. In free space, molecules close to a Feshbach resonance only exist for $a > 0$.

This picture is modified in the presence of an optical lattice potential [207] where the two atoms forming the molecule reside in the tightly confining potential of a single lattice well. In this case, bound states for $a < 0$ also exist (so-called confinement-induced molecules [23]). These exhibit a smooth transition into "real" molecules bound even in the absence of the external confinement on the $a > 0$ side of the Feshbach resonance. As the scattering length becomes smaller and smaller again on the repulsive side of the resonance, molecules become more and more deeply bound.

We investigate molecule formation in a heteronuclear Fermi-Bose mixture of ^{40}K and ^{87}Rb confined in a 3D optical lattice in the vicinity of the 546.8 G heteronuclear Feshbach resonance (for a sketch of the expected variation of a_{FB} across the resonance see Fig. 4.6).

7.2 Experimental sequence

We create quantum degenerate mixtures of ^{87}Rb in the $|F = 2, m_F = 2\rangle$ state and ^{40}K in the $|F = 9/2, m_F = 9/2\rangle$ state in a crossed optical dipole trap (mean ^{87}Rb trapping frequency 50 Hz). In order to get a maximum of lattice sites occupied by one boson and one fermion, we have found it beneficial to limit the particle number at this stage to a few ten thousand. We then prepare the mixture in the $^{87}\mathrm{Rb} \otimes {}^{40}\mathrm{K}\ |1,1\rangle \otimes |9/2,-7/2\rangle$ state at a magnetic field close to the Feshbach resonance at 546.8(1) G (see [37, 136, 148, 2] and chapter 4) for the $|1,1\rangle \otimes |9/2,-9/2\rangle$ state using the following procedure: First, ^{87}Rb atoms are transferred from $|2,2\rangle$ to $|1,1\rangle$ by a microwave sweep at 20 G and any remaining atoms in the upper hyperfine $|2,X\rangle$ states are removed by a resonant light pulse. ^{40}K atoms are transferred into the $|9/2,-7/2\rangle$ state by performing an rf sweep at the same magnetic field with almost 100% efficiency. We then increase the magnetic field to a value close to the resonance and ramp up a 3-dimensional optical lattice at a wavelength of 1030nm, where

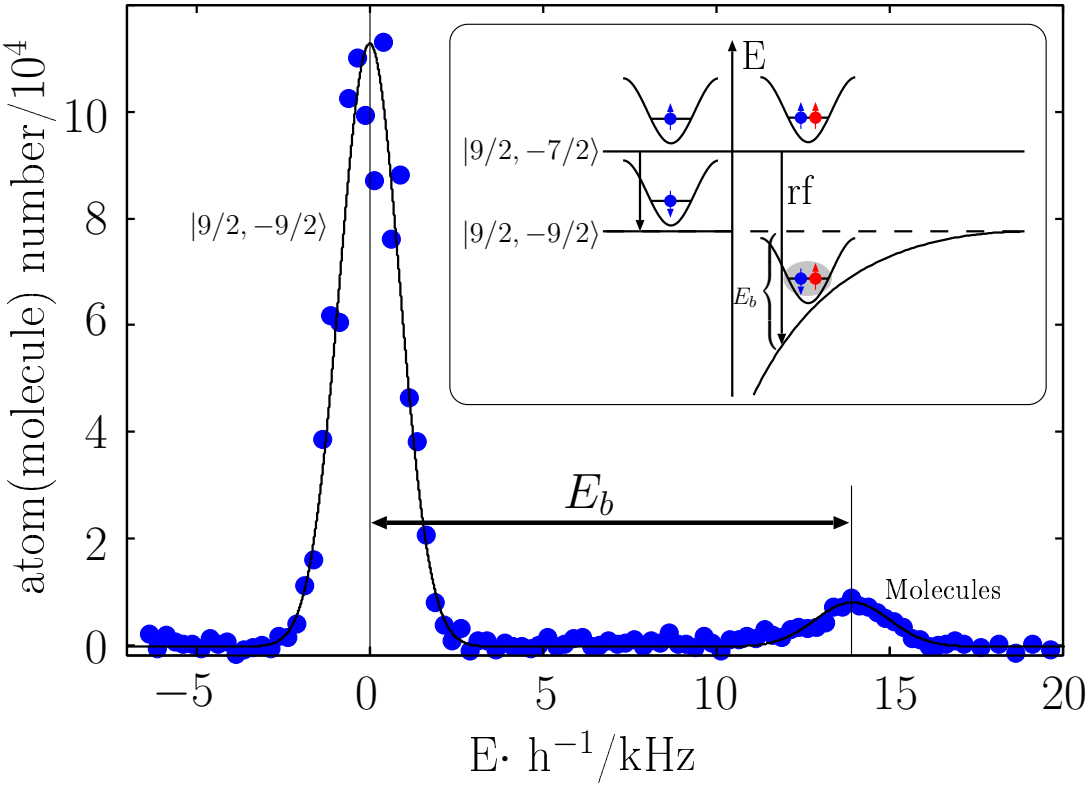

Figure 7.1: rf spectroscopy of ^{40}K - ^{87}Rb in a 3D optical lattice on the $|9/2,-7/2\rangle \rightarrow |9/2,-9/2\rangle$ transition (see inset) at a lattice depth of $U_{\rm lat} = 27.5E_r$ and a magnetic field of 547.13 G, where the interaction is attractive. $E_r = \hbar^2k^2/2m_{\rm Rb}$ is the ^{87}Rb recoil energy. The spectrum is plotted as a function of detuning from the undisturbed atomic resonance frequency and clearly shows the large atomic peak at zero detuning. The peak at 13.9kHz is due to association of $|1,1\rangle \otimes |9/2,-7/2\rangle$ atom pairs into a bound state.

the trapping potential for both species is approximately equal. The optical lattice light is derived from a frequency stabilized 20W Yb:YAG disc laser with a 50 ms linewidth of 20 kHz. The lattice is formed by three retroreflected laser beams with orthogonal polarizations and a minimum detuning of 10 MHz between individual beams.

7.3 Rf-association of molecules and rf-spectroscopy

In the optical lattice, we create molecules by rf association (see inset of Fig. 7.1) of pairs of one ^{87}Rb and one ^{40}K atom at a single lattice site[1] (see Fig. 7.1). The binding energy is measured as a frequency shift between the molecular and atomic feature. In the following, we discuss the measurement procedure in detail. The $|1,1\rangle \otimes |9/2,-7/2\rangle$ state

[1]We have also created Feshbach molecules by sweeping the magnetic field across the resonance and probed them via rf dissociation. However – due to limitations in the magnetic field settling time – for an accurate measurement of the binding energy it is more favorable in our setup to apply the rf association method.

that we prepare in the optical lattice has scattering properties which are to a good approximation independent of the magnetic field in the region where we probe the system. The corresponding energy thus serves as reference level for the following measurements. In order to measure interaction shifts and determine molecular binding energies of the Feshbach-resonant $|1,1\rangle \otimes |9/2,-9/2\rangle$ mixture, we perform rf spectroscopy on the ^{40}K $|9/2,-7/2\rangle \rightarrow |9/2,-9/2\rangle$ transition in the optical lattice (see inset in Fig. 7.1). At magnetic field values close to the Feshbach resonance, this transition occurs at about 80 MHz and has a magnetic field sensitivity of 67 kHz/G. We detect left-over atoms in the $|9/2,-7/2\rangle$ state at high magnetic field by detuning the imaging laser by -834 MHz with respect to the low-field $|9/2,9/2\rangle \rightarrow |11/2,11/2\rangle$ cycling transition. Atoms in the $|9/2,-9/2\rangle$ state and molecules are probed at a detuning of -765 MHz. Using high field imaging and separate CCD cameras, we can thus state-selectively detect both atoms and weakly bound molecules in a single experimental run. The rf spectroscopy is performed by shining in an rf pulse with a Gaussian amplitude envelope with a $1/e^2$ full width of 400 μs and a total pulse length of 800 μs, resulting in an rf $1/e^2$ half linewidth of 1.7 kHz. The pulse power is chosen to achieve full transfer on the single atom transition.

Fig. 7.1 shows a typical rf spectrum with atomic and molecular resonance peaks. The peak at zero frequency with respect to the unperturbed atomic transition frequency between the two Zeeman substates is the single atom peak from lattice sites occupied by only one fermion. On the high energy side of the spectrum at a detuning of 13.9 kHz with respect to the atomic transition, we observe a distinct feature which is due to rf association of atoms into molecules. The spectrum in Fig. 7.1 was recorded at 547.02 G on the high field side of the resonance, where the interaction between bosons and fermions is attractive and stable molecules do not exist in free space. The presence of the optical lattice nevertheless admits a bound state at $a_{\mathrm{FB}} < 0$ [23, 207]. From the rf spectrum, we can determine the separation between the single atom and the molecular peak with high precision and thus extract the binding energy up to a constant offset due to non-zero background scattering lengths. At the same time, the atomic peak provides us with a precise magnetic field calibration across the whole resonance. We find that the magnetic field deviates by no more than 9 mG from the calibration over one week, which corresponds to a maximum frequency shift of about 500 Hz.

7.4 Binding Energy of the molecules across the resonance

Fig. 7.2 as the main result of this chapter shows our results for the binding energy as a function of magnetic field across the resonance for two different lattice depths of $40E_R$ and $27.5E_r$, respectively, where $E_r = \hbar^2k^2/2m_{\mathrm{Rb}}$ is the ^{87}Rb recoil energy. [2] Above the resonance, we observe the association of confinement-induced molecules which do not exist in free-space. Depending on the magnetic field value in the vicinity of the Feshbach resonance and thus the scattering length, the binding energy varies between 5 and 20 kHz in a 40 E_r deep optical lattice. Across the resonance, we observe a smooth transition into "real" molecules bound even in the absence of the external confinement on the $a > 0$ side of the Feshbach resonance. This is clearly visible in the bottom branch of the spectrum in

[2] The lattice depth has been calibrated by observing the response of a ^{87}Rb cloud to modulation of the lattice potential.

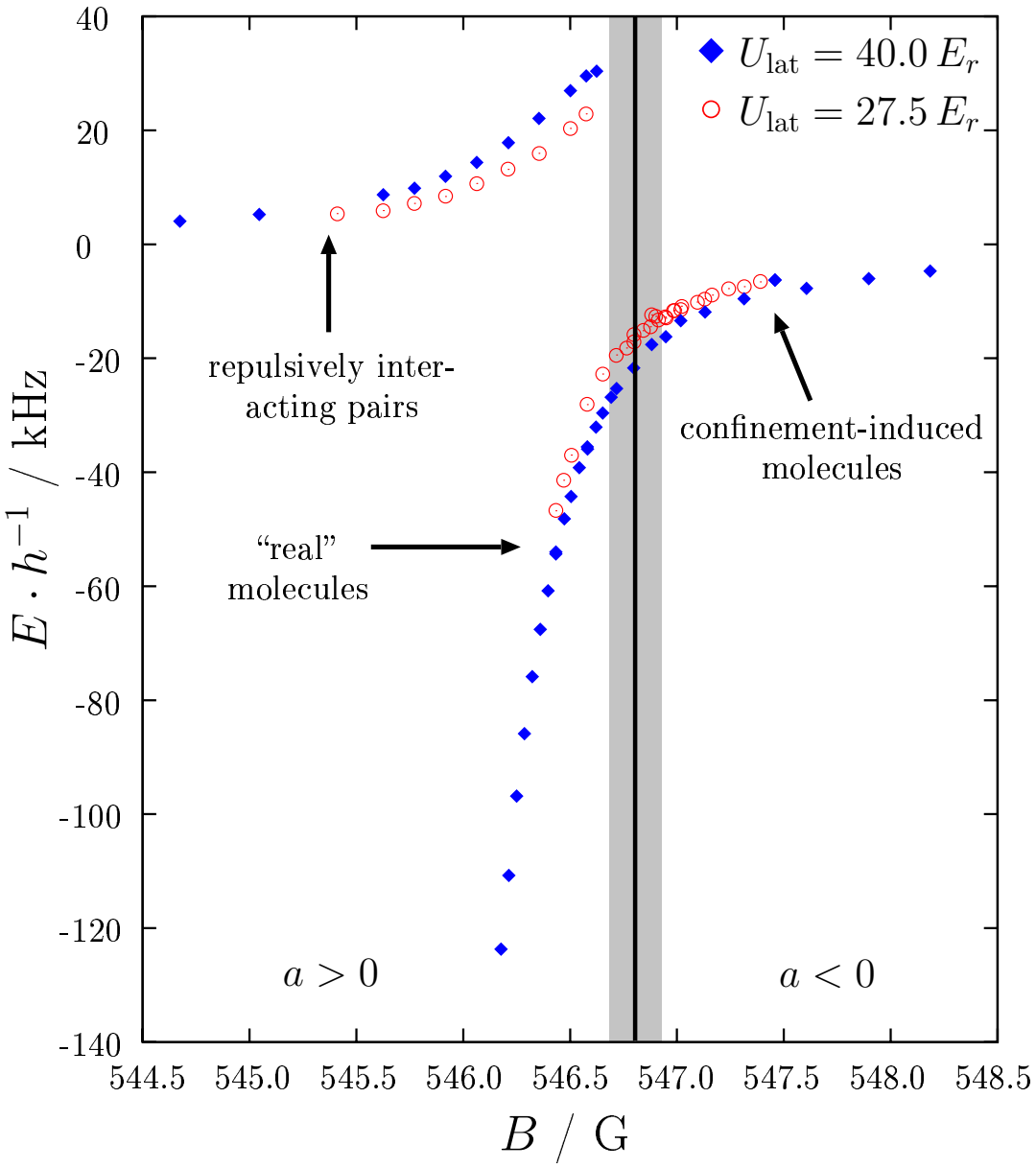

Figure 7.2: Binding energy of heteronuclear ^{40}K - ^{87}Rb molecules in an optical lattice for two different lattice depths U_{lat} in units of the ^{87}Rb recoil energy $E_r = \hbar^2 k^2 / 2m_{\mathrm{Rb}}$. The center of the Feshbach resonance is located at 546.8(1) G. We observe attractively bound molecules which are confinement-induced at a positive detuning with respect to the resonance center and "real" molecules which are stable in free space below the center of the resonance. In addition, we observe repulsively interacting pairs with a positive"binding energy" below the resonance.

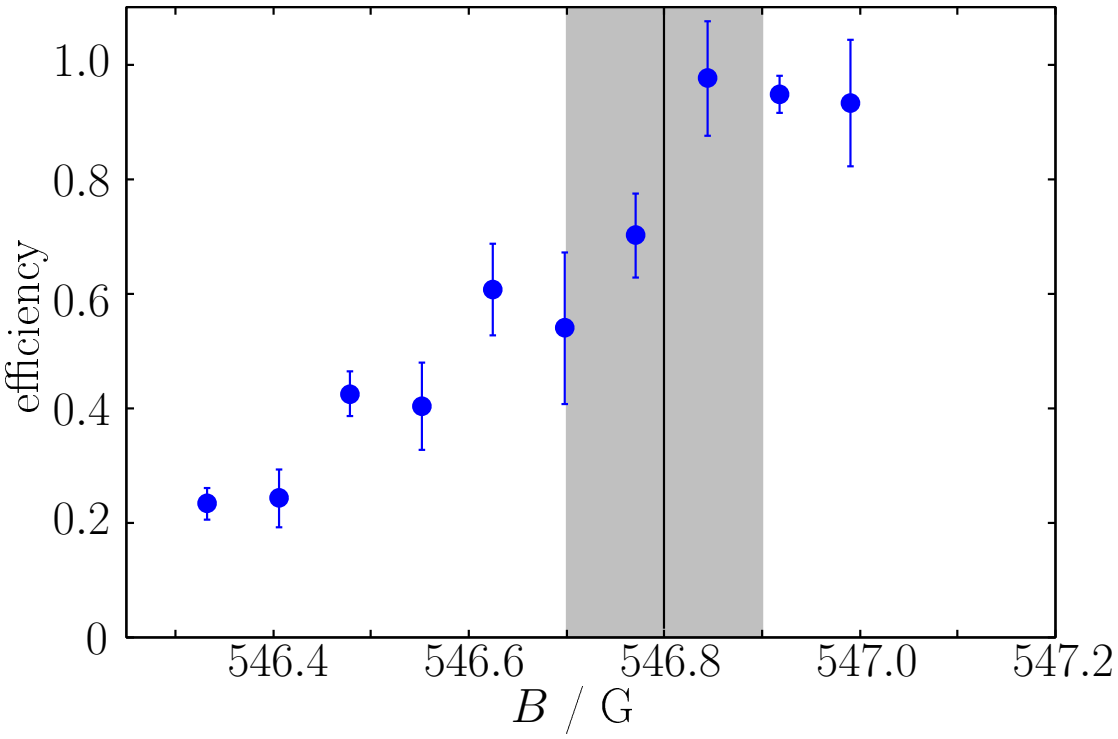

Figure 7.3: Transfer efficiency of the rf association process as a function of magnetic field. The transfer efficiency is normalized to its peak value on the attractive side of the Feshbach resonance, where we have observed the highest efficiency within the plotted magnetic field range.

Fig. 7.2. As the scattering length becomes smaller and smaller again on the repulsive side of the resonance, molecules become more and more deeply bound. We observe binding energies > 120 kHz. On this side of the resonance, we can observe an additional energy branch with positive "binding" energy. This branch is due to repulsively interacting atom pairs in a single lattice well. In this case, the repulsive interaction between Bosons and Fermions ($a > 0$) shifts the two-particle ground state towards a higher energy [207]. As expected, Fig. 7.2 shows that increasing lattice depth tends to increase both the "positive binding energy" of the repulsive pairs and the binding energy of the molecular branch away from the noninteracting case. A qualitative and quantitative analysis of the binding energy across the resonance and the "positive" binding energy of the repulsively interacting pairs is contained in the thesis of Christian Ospelkaus [35].

7.5 Association efficiency

As a further point, we have analyzed the transfer efficiency of the rf association (Fig. 7.3). We detect the molecule number as a function of the magnetic field across the Feshbach resonance and normalize it to the high-field side of the resonance, where the overlap between the initial attractively interacting state and the bound state wave function is highest in the magnetic field range covered by our experiments. The transfer efficiency

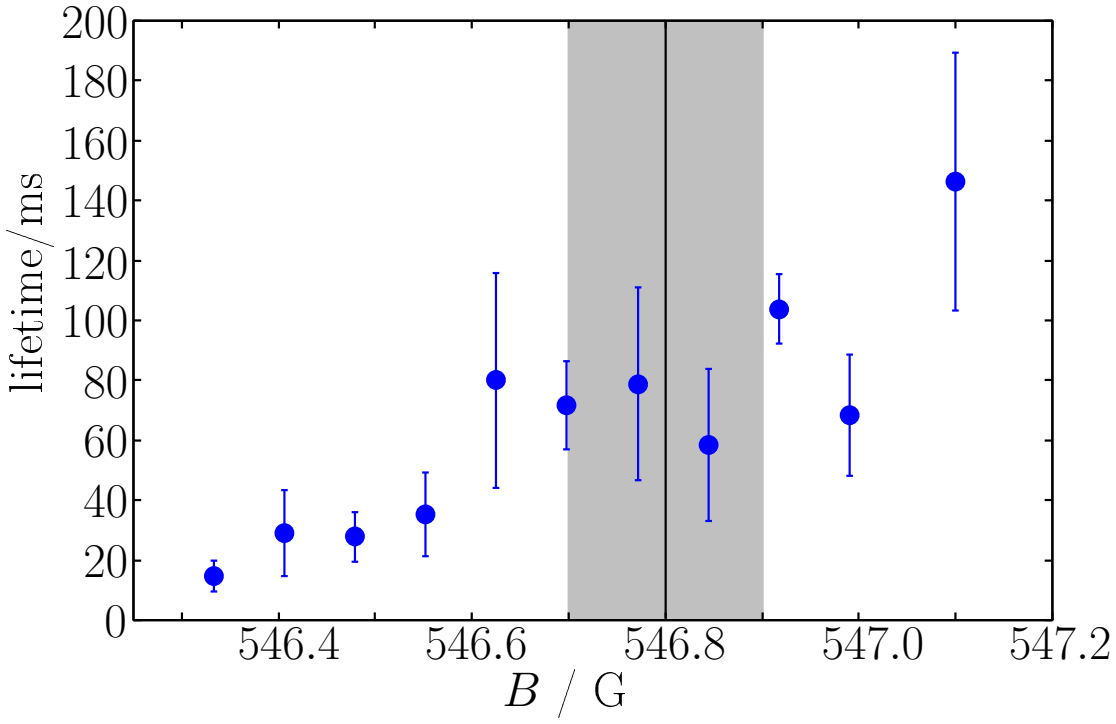

Figure 7.4: Lifetime of heteronuclear molecules in the optical lattice as a function of magnetic field. On the repulsive side of the resonance below 546.8(1) G the lifetime tends to decrease.

is observed to be almost constant for attractive interactions and then decreases on the repulsive side of the resonance. As expected from the decreasing overlap of atomic and molecular wave functions for more deeply bound molecules, the transfer efficiency drops to about 20% on the low-field side of the resonance. On the attractive side of the resonance, we achieve a total efficiency for the transfer of ^{40}K $|9/2, -7/2\rangle$ into molecular ^{87}Rb-^{40}K states of about 10%, producing approximately 10^4 molecules. This corresponds roughly to the estimated fraction of lattice sites with one fermion and one boson as compared to the total fermion number. Purification schemes for the bosonic component and adjustment of the relative population are possible routes to increase the efficiency.

7.6 Lifetime of the molecules

One of the main concerns in ultracold Feshbach chemistry is the lifetime of the molecules. In general, these molecules are very fragile objects due to their highly excited internal state. Initial experiments with molecules created from bosonic atoms [120, 121, 122, 123] accordingly showed a very short lifetime, which has recently been overcome in the presence of a deep 3D optical lattice [24, 158]. Molecules created from two fermionic atoms have shown a long lifetime close to Feshbach resonances due to Pauli-forbidden inelastic decay [116]. For heteronuclear molecules composed of a bosonic and a fermionic atom, the situation is somewhat more complicated; suppression of collisions due to their fermionic

character is expected for more deeply bound molecules [36]. However, in this case, remaining free atoms are expected to strongly limit the lifetime of the molecules. We therefore produce the heteronuclear molecules within 3D optical lattices where the large tunnelling time strongly reduces inelastic collisional losses. Fig. 7.4 shows a measurement of the lifetime of the heteronuclear molecular sample in an optical lattice with a depth of 40.0 E_r as a function of magnetic field. We find a lifetime of about 120 ms for weakly bound confinement-induced molecules. In the vicinity of the resonance, the lifetime is about 80 ms, and drops to 20 to 40 ms for more deeply bound molecules. The measurement is performed by rf associating atoms in the $|1,1\rangle \otimes |9/2,-7/2\rangle$ state into molecules and transferring any remaining $|9/2,-7/2\rangle$ atoms into the $|9/2,-5/2\rangle$ state using an rf sweep at 85 MHz. A resonant light pulse on the $|9/2,-7/2\rangle$ detection frequency ensures that no atoms in this state are left. Since high-field imaging detects both atoms and weakly bound molecules, it is of potential concern that molecules may fall apart and form unpaired $|9/2,-9/2\rangle$ atoms. We therefore drive a π pulse on the atomic $|9/2,-7/2\rangle \rightarrow |9/2,-9/2\rangle$ transition prior to imaging in order to detect any free $|9/2,-9/2\rangle$ atoms on the $|9/2,-7/2\rangle$ detection transition, but have found no atomic signal. This proves that our lifetime measurement really measures the lifetime of the molecular sample. The lifetime may be currently limited due to remaining fermionic ^{40}K atoms which, for this measurement, are in the $|9/2,-5/2\rangle$ state.[3]. For these atoms, the optical lattice potential is only 20 E_r^{K} deep ($E_r^{\mathrm{K}} = \hbar^2k^2/(2m_{\mathrm{K}})$), which corresponds to a tunnelling time on the order of 10 ms. The observed dependency of the lifetime on the binding energy is still an open question.

Evidence for short-lived ^{40}K-^{87}Rb molecule formation in an optical dipole trap was recently reported by the group of D. S. Jin at JILA [208] and in a mixture of ^{85}Rb-^{87}Rb in the group of C. Wieman [209].

[3]We performed other measurements on the system where ^{40}K remained in the $|9/2,-7/2\rangle$ state and found comparable lifetimes.

Chapter 8

Conclusions and outlook

Within this thesis, an experimental apparatus for the preparation of quantum degenerate Fermi-Bose mixtures in 3D optical lattices has been realized. Important milestones towards a mixed statistics many-body system with tunable interactions in 3D optical lattices as a versatile model system for the simulation of quantum many-body Hamiltonians and the exploration of fundamentally novel quantum phases have been presented.

Starting from the realization of the so far largest particle numbers in a magnetically trapped degenerate ^{40}K–^{87}Rb system, we have investigated interaction effects due to the large and attractive background interaction between the components. As an essential prerequisite for the realization of tunable interactions in the mixture via magnetic fields in the vicinity of a Feshbach resonance, I have presented a crossed dipole trap operating at a special "magic" wavelength to compensate for the differential gravitational sag between the two species and to ensure optimal overlap of the constituents.

Tuning of heteronuclear interactions in the vicinity of a Feshbach resonance has been demonstrated for the first time within this thesis and has allowed studies of arbitrary interactions between bosons and fermions. The complete phase diagram of harmonically trapped mixtures has been accessed. Starting with experiments on stable density distributions for attractively and repulsively interacting mixtures, for strong repulsive interactions, phase separation has been observed and a Feshbach-induced collapse for strong attractive interactions. In the presence of gravity, phase separation occurs as a stacking effect in the vertical direction. A heteronuclear p-wave resonance has been identified, confirming a theoretical assignment of Feshbach resonances in the ^{40}K–^{87}Rb system and opening intriguing perspectives for tuning of the anisotropy of the interaction. These studies on heteronuclear Feshbach resonances pave the way for studies with strongly interacting Fermi-Bose mixtures.

The availability of tunable interactions may also lead to the observation of bright soliton-like structures in Fermi-Bose mixtures [210]. These structures are expected to occur for experimental situations close to 1D geometries, such as an elongated optical dipole trap or a 2D optical lattice. In such an almost one-dimensional configuration, a small window in the phase diagram is expected to open up between stable attractively interacting mixtures and the mean field collapse. In this window, fully self-trapped soliton-like states are predicted to become stable. The availability of tunable interactions may give access to this regime similar to experiments on bright solitons in attractively interacting

Bose-Einstein condensates [105, 104].

From the very beginning, the experimental setup described here has been designed for studies in 3D optical lattices. Within this thesis, Fermi-Bose mixtures have been loaded into a three-dimensional optical lattice for the first time, demonstrating a large fermion-induced loss of coherence of the bosonic sample. The results are currently the subject of intense theoretical analysis, and explanations ranging from disorder-related localization phenomena over adiabatic thermodynamic effects and a mean-field induced shift of the superfluid to Mott-insulator transition are being discussed.

Further insight into these observations may be gained by implementing additional diagnostics. This may include Bragg spectroscopy, excitation spectroscopy to probe possible excitation gaps in deep optical lattices, probing of lattice occupation through rf or microwave spectroscopy and noise correlation analysis. The studies may also be extended to mixtures with varying heteronuclear interaction strength.

In 1D or 2D optical lattices one or several spatial degrees of freedom can experimentally be frozen out, resulting in the preparation of low-dimensional systems. Depending on interaction strength and lattice occupation, charge-density wave or pairing phases may be observable. Low dimensional systems are of particular interest for direct comparison of experimental results to theory. For 1-dimensional situations (2D optical lattice) exactly solvable models exist and direct comparison to quasi-exact DMRG calculations is possible.

The combination of tunable interactions with 3-dimensional optical lattices has resulted in the demonstration of ultracold heteronuclear Feshbach molecule formation. Long-lived heteronuclear Feshbach molecules have been created in a controlled fashion through rf association of atoms to molecules. This has allowed a precise determination of the binding energy of the molecular sample as a function of the magnetic field. Lifetimes between 20 ms and 100 ms have been experimentally observed, and the efficiency of the rf association process has been analyzed.

Molecule formation may be the starting point for studies of pairing phases in the optical lattice, including studies of 3-body bound states. After molecule association and removal of the left-over atomic fraction, the lattice potential may be ramped down. The molecule formed from a bosonic ^{87}Rb and a fermionic ^{40}K atom is again a fermion, and the observation of a molecular Fermi sea may be demonstrated.

In the optical lattice, Feshbach molecules are created in their absolute external ground state, but in a highly excited rovibrational state. Pulsed two-color photoassociation may be used to transfer these molecules into their internal ground state. The resulting molecule would exhibit a permanent electric dipole moment (polar molecule). The dipole moment gives rise to a long-range, anisotropic interaction. In the optical lattice, this long-range interaction may be used to implement scalable quantum computation schemes. In the many-body limit, these polar molecules give access to novel quantum gases with long-range anisotropic interactions.

Appendix A

^{87}Rb laser system

The ^{87}Rb laser system has been based on the concept developed at the neighbouring BEC experiment by Holger Schmaljohann and Michael Erhard [39, 40]. A detailed characterisation of the ^{87}Rb laser setup in our experiment can be found in the diploma thesis of Juergen Fuchs [44]. The laser system is entirely built with semiconductor laser diodes. Two external cavity diode lasers (M1 and M2) are stabilised to the saturated absorption crossover resonances ^{87}Rb $F = 2 \leftrightarrow F' = 2, 3$ and ^{87}Rb $F = 1 \leftrightarrow F' = 1, 2$ of the D_2-line at $\lambda \approx 780$nm respectively using FM-spectroscopy (see the locking scheme of Fig. A.1). These two laser frequencies serve as a starting point for the generation of light in the vicinity of the cooling transition ^{87}Rb $5^2S_{1/2}F = 2 \leftrightarrow 5^2P_{3/2}F' = 3$ and the repumping line ^{87}Rb $5^2S_{1/2}F = 1 \leftrightarrow 5^2P_{3/2}F' = 2$.

The cooling master M1 runs approximately 160 MHz blue-detuned with respect to the $F = 2 \rightarrow F' = 3$ cycling transition. A probe beam is shifted by -267 MHz to the red (using a 120MHz AOM in double pass configuration) allowing the laser frequency to be locked to the $F = 2 \rightarrow F' = 2, 3$ crossover resonance. The output power of M1 is then amplified by injection seeding of a slave diode laser S1. An acousto-optical modulator operated at 80 MHz in double pass configuration shifts a part of the laser light from S1 by 160 MHz to the red thereby providing near-resonant light on the cooling transition ^{87}Rb $5^2S_{1/2}F = 2 \leftrightarrow 5^2P_{3/2}F' = 3$ for detection, state preparation and the pushing beam. Two further beams originating from the S1 laser are also frequency shifted by ≈ 160 MHz to the red each of them injecting a slave laser (S1 and S2). The laser light from these slaves is amplified in a final stage by two tapered amplifier semiconductor chips providing largely enough cooling power for the 2D and 3D MOT. While fast switching of detection, state preparation and pushing light is assured by acousto-optical modulators, fast switching of the cooling light for the 3D-MOT is done using an Electro-Optic Modulator.

Repumping light is prepared starting from the repumper master M2. This external cavity diode laser is locked to the $F = 1 \rightarrow F' = 1, 2$ crossover resonance. Its output power is again amplified by injection locking the slave laser S2. Light from slave S2 is frequency shifted 80 MHz to the blue using an AOM in single pass thereby producing resonant light on the $F = 1 \rightarrow F' = 2$ repumping transition. The repumping light is split up into two beams and coupled into the same optical fibres as the 2D MOT and 3D MOT using orthogonal polarisations.

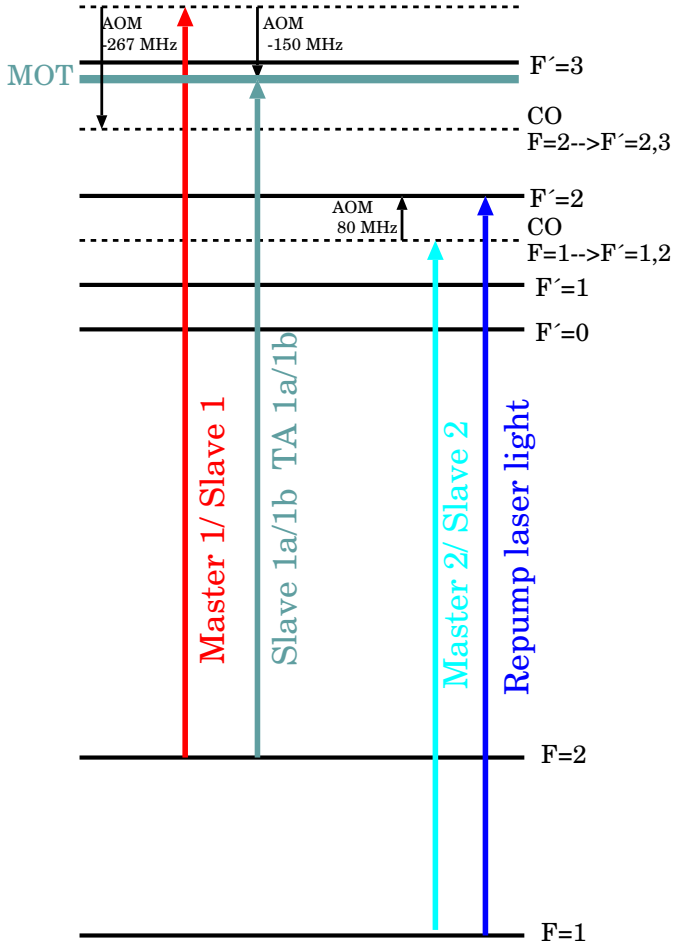

Figure A.1: Locking scheme of the ^{87}Rb laser system. For a detailed description see text.

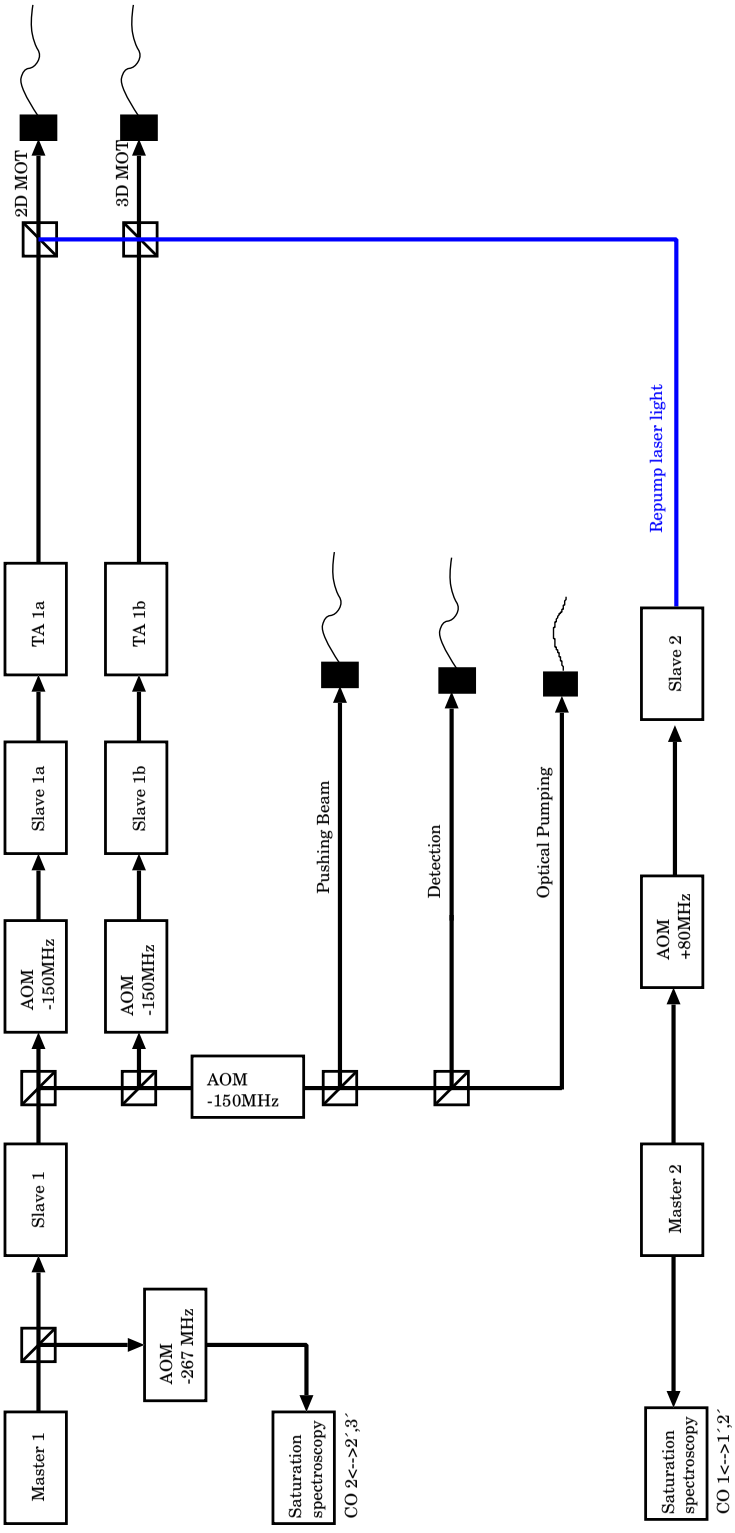

Figure A.2: Sketch of the ^{87}Rb laser system. Description see text.

Appendix B

^{40}K laser system

The laser light for manipulation of ^{40}K atoms on the D_2-transition at $\lambda \approx 767$nm is delivered by two independent sources: a 2W Ti:Sa laser providing the necessary frequencies for cooling, trapping, manipulation and detection of ^{40}K on the $4^2S_{1/2}F = 9/2 \rightarrow 4^2P_{3/2}F = 11/2$ transition and a commercial MOPA-system from Toptica Photonics with a power of up to 400 mW to allow for sufficient repump power for both the 2D and the 3D magneto-optical trap on the ^{40}K $4^2S_{1/2}F = 7/2 \rightarrow 4^2P_{3/2}F = 9/2$ transition.

Both the cooling laser and the repumping laser are locked on saturated absorption lines of ^{39}K. The cooling laser is locked 420 MHz to the blue of the $4^2S_{1/2}F = 2, 1 \rightarrow 4^2P_{3/2}$ cross-over line.[1] Light from the Ti:Sa is then split up into three beams. Each of the laser beams is frequency shifted by ≈ 160 MHz to the blue to provide near-resonant light on the cooling transition of ^{40}K ($F = 9/2 \rightarrow F = 11/2$). Two of the beams provide cooling light for the 2D and 3D MOT, respectively, and are directly fibre-coupled. The third beam is split up into three after frequency shifting providing light for detection, state preparation and pushing respectively.

For repumping, we rely on a tapered amplifier system from Toptica Photonics. The system consists of an extended cavity diode laser injecting a Tapered amplifier with a specified output power of 500 mW. Slightly red-detuned laser light with respect to the ^{40}K $F = 7/2 \rightarrow F'9/2$ transition is realized by frequency shifting the laser light for the saturated absorption spectroscopy by 420 MHz with an acousto-optical modulator and then locking the laser onto the $4^2S_{1/2}F = 2 \rightarrow 4^2P_{3/2}$ line of ^{39}K. The tapered amplifier provides laser light for repumping in the 2D-MOT, the bright 3D-MOT and the dark SPOT. Whereas cooling and bright repumping light for the 2D and 3D-MOT is fibre coupled each into a single optical fibre, the light for the dark repumper is transported separately to the experiment.

Rapid switching of the light for the cooling light of the MOT, detection, state preparation and pushing beam is ensured by the acousto-optical modulators, the repumping light is switched on and off by an electro-optical modulator.

For a sketch of both the locking scheme and the laser setup, see Fig. B.1 and B.2.

[1] The hyperfine structure of the ^{39}K $4^2P_{3/2}$ manifold is too small to be resolved in saturated absorption spectroscopy.

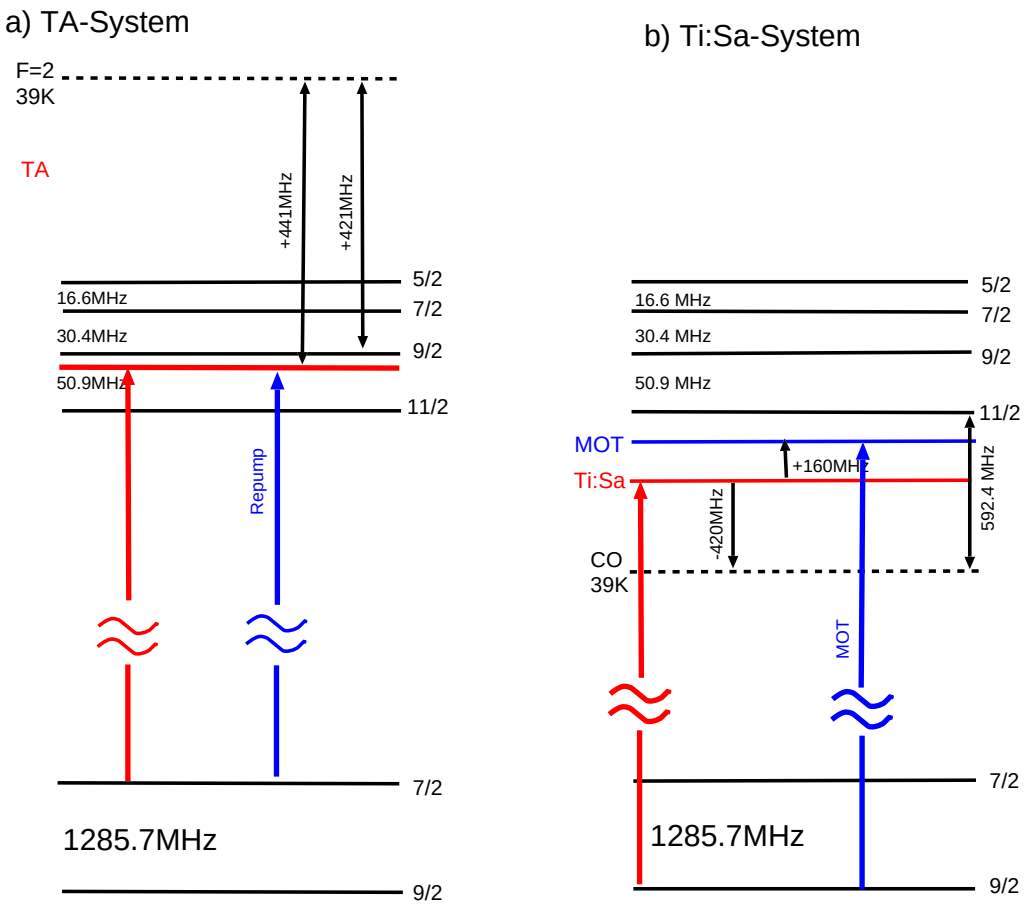

Figure B.1: Locking scheme of the potassium laser system. For a detailed description see text.

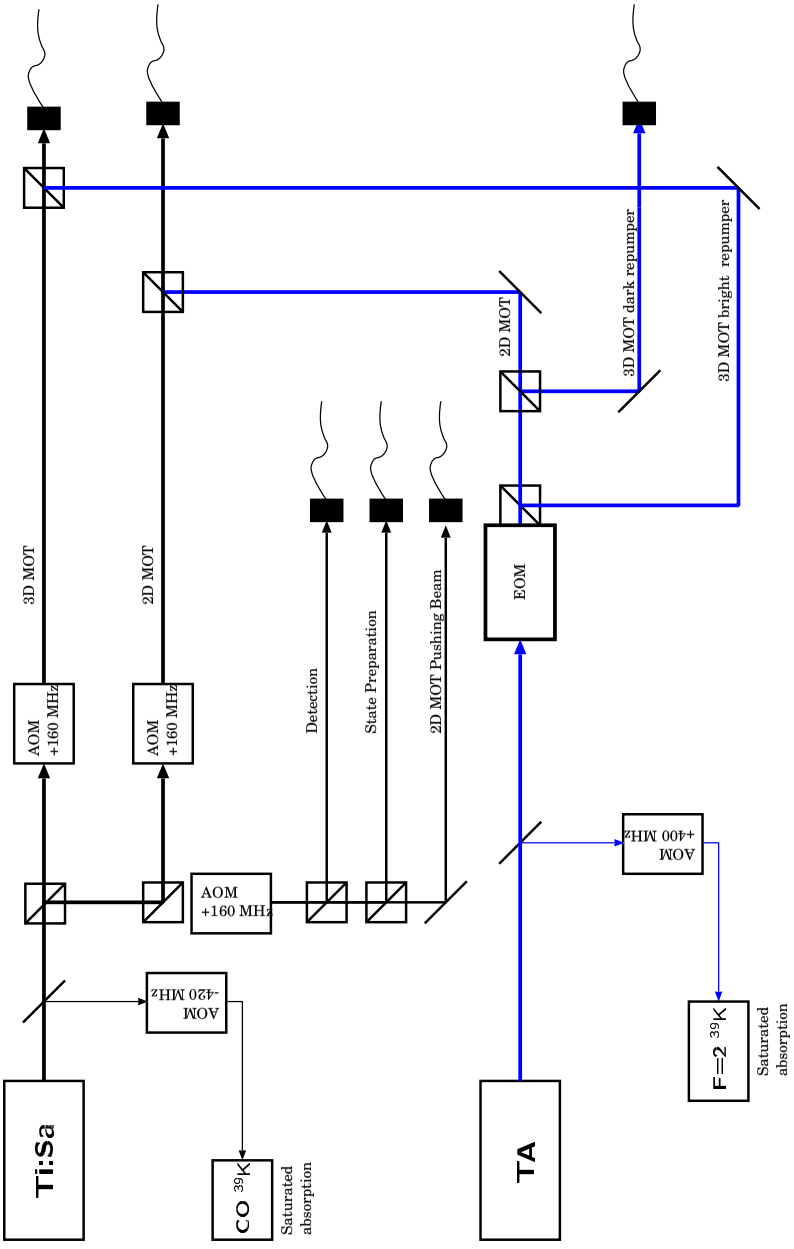

Figure B.2: Sketch of the ^{40}K laser system. For a detailed description see text.

Bibliography

[1] C. Ospelkaus, S. Ospelkaus, L. Humbert, P. Ernst, K. Sengstock and K. Bongs: *Ultracold Heteronuclear Molecules in a 3D Optical Lattice*. Phys. Rev. Lett. **97**, 120402 (2006). doi:10.1103/PhysRevLett.97.120402.

[2] S. Ospelkaus, C. Ospelkaus, L. Humbert, K. Sengstock and K. Bongs: *Tuning of Heteronuclear Interactions in a Degenerate Fermi-Bose Mixture*. Phys. Rev. Lett. **97**, 120403 (2006). doi:10.1103/PhysRevLett.97.120403.

[3] S. Ospelkaus, C. Ospelkaus, O. Wille, M. Succo, P. Ernst, K. Sengstock and K. Bongs: *Localization of Bosonic Atoms by Fermionic Impurities in a Three-Dimensional Optical Lattice*. Phys. Rev. Lett. **96**, 180403 (2006). doi:10.1103/PhysRevLett.96.180403.

[4] C. Ospelkaus, S. Ospelkaus, K. Sengstock and K. Bongs: *Interaction-Driven Dynamics of ^{40}K $-^{87}$ Rb Fermion-Boson Gas Mixtures in the Large-Particle-Number Limit*. Phys. Rev. Lett. **96**, 020401 (2006). doi:10.1103/PhysRevLett.96.020401.

[5] S. Ospelkaus, C. Ospelkaus, R. Dinter, J. Fuchs, M. Nakat, K. Sengstock and K. Bongs: *Degenerate K-Rb Fermi-Bose gas mixtures with large particle numbers*. Journal of Modern Optics (2006). doi:10.1080/09500340600777763.

[6] M. H. Anderson, J. R. Ensher, M. R. Matthews, C. E. Wieman and E. A. Cornell: *Observation of Bose-Einstein Condensation in a Dilute Atomic Vapor*. Science **269**, 198 (1995). doi:10.1126/science.269.5221.198.

[7] K. B. Davis, M. O. Mewes, M. R. Andrews, N. J. van Druten, D. S. Durfee, D. M. Kurn and W. Ketterle: *Bose-Einstein Condensation in a Gas of Sodium Atoms*. Phys. Rev. Lett. **75**, 3969–3973 (1995). doi:10.1103/PhysRevLett.75.3969.

[8] C. C. Bradley, C. A. Sackett, J. J. Tollett and R. G. Hulet: *Evidence of Bose-Einstein Condensation in an Atomic Gas with Attractive Interactions*. Phys. Rev. Lett. **75**, 1687–1690 (1995). doi:10.1103/PhysRevLett.75.1687.

[9] B. DeMarco and D. S. Jin: *Onset of Fermi Degeneracy in a Trapped Atomic Gas*. Science **285**, 1703–1706 (1999). doi:10.1126/science.285.5434.1703.

[10] Ph. Courteille, R. S. Freeland, D. J. Heinzen, F. A. van Abeelen and B. J. Verhaar: *Observation of a Feshbach Resonance in Cold Atom Scattering*. Phys. Rev. Lett. **81**, 69–72 (1998). doi:10.1103/PhysRevLett.81.69.

[11] S. Inouye, M. R. Andrews, H.-J. Stenger, J. amd Miesner, D. M. Stamper-Kurn and W. Ketterle: *Observation of a Feshbach resonance in a Bose-Einstein condensate.* Nature **392**, 151–154 (1998). doi:10.1038/32354.

[12] C. A. Regal, M. Greiner and D. S. Jin: *Observation of Resonance Condensation of Fermionic Atom Pairs.* Phys. Rev. Lett. **92**, 040403 (2004). doi: 10.1103/PhysRevLett.92.040403.

[13] M. Bartenstein, A. Altmeyer, S. Riedl, S. Jochim, C. Chin, J. Hecker Denschlag and R. Grimm: *Crossover from a Molecular Bose-Einstein Condensate to a Degenerate Fermi Gas.* Phys. Rev. Lett. **92**, 120401 (2004). doi:10.1103/PhysRevLett.92.120401.

[14] M. W. Zwierlein, C. A. Stan, C. H. Schunck, S. M. F. Raupach, A. J. Kerman and W. Ketterle: *Condensation of Pairs of Fermionic Atoms near a Feshbach Resonance.* Phys. Rev. Lett. **92**, 120403 (2004). doi:10.1103/PhysRevLett.92.120403.

[15] T. Bourdel, L. Khaykovich, J. Cubizolles, J. Zhang, F. Chevy, M. Teichmann, L. Tarruell, S. J. J. M. F. Kokkelmans and C. Salomon: *Experimental Study of the BEC-BCS Crossover Region in Lithium 6.* Phys. Rev. Lett. **93**, 050401 (2004). doi:10.1103/PhysRevLett.93.050401.

[16] J. Kinast, S. L. Hemmer, M. E. Gehm, A. Turlapov and J. E. Thomas: *Evidence for Superfluidity in a Resonantly Interacting Fermi Gas.* Phys. Rev. Lett. **92**, 150402 (2004). doi:10.1103/PhysRevLett.92.150402.

[17] M. W. Zwierlein, J. R. Abo-Shaeer, A. Schirotzek, C. H. Schunck and W. Ketterle: *Vortices and superfluidity in a strongly interacting Fermi gas.* Nature **435**, 1047–1051 (2005). doi:10.1038/nature03858.

[18] D. Jaksch, C. Bruder, J. I. Cirac, C. W. Gardiner and P. Zoller: *Cold Bosonic Atoms in Optical Lattices.* Phys. Rev. Lett. **81**, 3108–3111 (1998). doi: 10.1103/PhysRevLett.81.3108.

[19] Markus Greiner, Olaf Mandel, Tilman Esslinger, Theodor W. Hänsch and Immanuel Bloch: *Quantum phase transition from a superfluid to a Mott insulator in a gas of ultracold atoms.* Nature **415**, 39–44 (2002). doi:10.1038/415039a.

[20] Belen Paredes, Artur Widera, Valentin Murg, Olaf Mandel, Simon Fölling, Ignacio Cirac, Gora V. Shlyapnikov, Theodor W. Hänsch and Immanuel Bloch: *Tonks Girardeau gas of ultracold atoms in an optical lattice.* Nature **429**, 277 (2004). doi: 10.1038/nature02530.

[21] Toshiya Kinoshita, Trevor Wenger and David S. Weiss: *Observation of a One-Dimensional Tonks-Girardeau Gas.* Science **305**, 1125–1128 (2004). doi: 10.1126/science.1100700.

[22] Zoran Hadzibabic, Peter Krüger, Marc Cheneau, Baptiste Battelier and Jean Dalibard: *Berezinskii-Kosterlitz-Thouless crossover in a trapped atomic gas.* Nature **441**, 1118–1121 (2006). doi:10.1038/nature04851.

[23] Thilo Stöferle, Henning Moritz, Kenneth Günter, Michael Köhl and Tilman Esslinger: *Molecules of Fermionic Atoms in an Optical Lattice*. Phys. Rev. Lett. **96**, 030401 (2006). doi:10.1103/PhysRevLett.96.030401.

[24] G. Thalhammer, K. Winkler, F. Lang, S. Schmid, R. Grimm and J. Hecker Denschlag: *Long-Lived Feshbach Molecules in a Three-Dimensional Optical Lattice*. Phys. Rev. Lett. **96**, 050402 (2006). doi:10.1103/PhysRevLett.96.050402.

[25] J. K. Chin, D. E. Miller, Y. Liu, C. Stan, W. Setiawan, C. Sanner, K. Xu and W. Ketterle: *Evidence for superfluidity of ultracold fermions in an optical lattice*. Nature **443**, 961 (2006). doi:10.1038/nature05224.

[26] M. Lewenstein, L. Santos, M. A. Baranov and H. Fehrmann: *Atomic Bose-Fermi Mixtures in an Optical Lattice*. Phys. Rev. Lett. **92**, 050401 (2004). doi:10.1103/PhysRevLett.92.050401.

[27] H. Heiselberg, C. J. Pethick, H. Smith and L. Viverit: *Influence of Induced Interactions on the Superfluid Transition in Dilute Fermi Gases*. Phys. Rev. Lett. **85**, 2418–2421 (2000). doi:10.1103/PhysRevLett.85.2418.

[28] Fabrizio Illuminati and Alexander Albus: *High-Temperature Atomic Superfluidity in Lattice Bose-Fermi Mixtures*. Phys. Rev. Lett. **93**, 090406 (2004). doi:10.1103/PhysRevLett.93.090406.

[29] D.-W. Wang, M. D. Lukin and E. Demler: *Engineering superfluidity in Bose-Fermi mixtures of ultracold atoms*. Phys. Rev. A **72**, 051604 (2005). doi:10.1103/PhysRevA.72.051604.

[30] L. Mathey, D.-W. Wang, W. Hofstetter, M. D. Lukin and Eugene Demler: *Luttinger Liquid of Polarons in One-Dimensional Boson-Fermion Mixtures*. Phys. Rev. Lett. **93**, 120404 (2004). doi:10.1103/PhysRevLett.93.120404.

[31] A. Sanpera, A. Kantian, L. Sanchez-Palencia, J. Zakrzewski and M. Lewenstein: *Atomic Fermi-Bose Mixtures in Inhomogeneous and Random Lattices: From Fermi Glass to Quantum Spin Glass and Quantum Percolation*. Phys. Rev. Lett. **93**, 040401 (2004). doi:10.1103/PhysRevLett.93.040401.

[32] H. P. Büchler and G. Blatter: *Supersolid versus Phase Separation in Atomic Bose-Fermi Mixtures*. Phys. Rev. Lett. **91**, 130404 (2003). doi:10.1103/PhysRevLett.91.130404.

[33] H. Ott, E. de Mirandes, F. Ferlaino, G. Roati, G. Modugno and M. Inguscio: *Collisionally Induced Transport in Periodic Potentials*. Phys. Rev. Lett. **92**, 160601 (2004). doi:10.1103/PhysRevLett.92.160601.

[34] E. A. Hinds: *Testing time reversal symmetry using molecules*. Phys. Scripta **34**, T70 (1997).

[35] Christian Ospelkaus: *Fermi-Bose mixtures - From mean-field interaction to ultracold chemistry*. Dissertation, Universität Hamburg (2006).

[36] C. A. Stan, M. W. Zwierlein, C. H. Schunck, S. M. F. Raupach and W. Ketterle: *Observation of Feshbach Resonances between Two Different Atomic Species*. Phys. Rev. Lett. **93**, 143001 (2004). doi:10.1103/PhysRevLett.93.143001.

[37] S. Inouye, J. Goldwin, M. L. Olsen, C. Ticknor, J. L. Bohn and D. S. Jin: *Observation of Heteronuclear Feshbach Resonances in a Mixture of Bosons and Fermions*. Phys. Rev. Lett. **93**, 183201 (2004). doi:10.1103/PhysRevLett.93.183201.

[38] D. DeMille: *Quantum Computation with Trapped Polar Molecules*. Phys. Rev. Lett. **88**, 067901 (2002). doi:10.1103/PhysRevLett.88.067901.

[39] Holger Schmaljohann: *Spindynamik in Bose-Einstein Kondensaten*. Dissertation, Universität Hamburg (2004).

[40] Michael Erhard: *Experimente mit mehrkomponentigen Bose-Einstein-Kondensaten*. Dissertation, Universität Hamburg (2004).

[41] K. Dieckmann, R. J. C. Spreeuw, M. Weidemüller and J. T. M. Walraven: *Two-dimensional magneto-optical trap as a source of slow atoms*. Phys. Rev. A **58**, 3891–3895 (1998). doi:10.1103/PhysRevA.58.3891.

[42] E. L. Raab, M. Prentiss, Alex Cable, Steven Chu and D. E. Pritchard: *Trapping of Neutral Sodium Atoms with Radiation Pressure*. Phys. Rev. Lett. **59**, 2631–2634 (1987). doi:10.1103/PhysRevLett.59.2631.

[43] B. DeMarco, H. Rohner and D. S. Jin: *An enriched* ^{40}K *source for fermionic atom studies*. Review of Scientific Instruments **70**, 1967 (1999). doi:10.1063/1.1149695.

[44] Jürgen Fuchs: *Aufbau und Charakterisierung einer 2D und 3D magnetooptischen Fallenkombination für* ^{87}*Rb*. Diploma thesis, Universität Hamburg (2004).

[45] Wolfgang Ketterle, Kendall B. Davis, Michael A. Joffe, Alex Martin and David E. Pritchard: *High densities of cold atoms in a dark spontaneous-force optical trap*. Phys. Rev. Lett. **70**, 2253–2256 (1993). doi:10.1103/PhysRevLett.70.2253.

[46] Erling Riis, David S. Weiss, Kathryn A. Moler and Steven Chu: *Atom funnel for the production of a slow, high-density atomic beam*. Phys. Rev. Lett. **64**, 1658–1661 (1990). doi:10.1103/PhysRevLett.64.1658.

[47] J. Nellessen, J. Werner and W. Ertmer: *Magneto-optical compression of a monoenergetic sodium atomic beam*. Optics Communications **78**, 300–308 (1990). doi:10.1016/0030-4018(90)90365-Z.

[48] A. Scholz, M. Christ, D. Doll, J. Ludwig and W. Ertmer: *Magneto-optical preparation of a slow, cold and bright Ne* atomic beam*. Optics Communications **111**, 155–162 (1994). doi:10.1016/0030-4018(94)90155-4.

[49] P. Berthoud, A. Joyet, G. Dudle, N. Sagna and P. Thomann: *A continuous beam of slow, cold cesium atoms magnetically extracted from a 2D magneto-optical trap*. Europhysics Letters **41**, 141–146 (1998).

[50] H. Chen and E. Riis: *Cold atomic beam from a rubidium funnel.* Applied Physics B **70**, 665–670 (2000). doi:10.1007/s003400050878.

[51] J. Schoser, A. Batär, R. Löw, V. Schweikhard, A. Grabowski, Yu. B. Ovchinnikov and T. Pfau: *Intense source of cold Rb atoms from a pure two-dimensional magneto-optical trap.* Phys. Rev. A **66**, 023410 (2002). doi:10.1103/PhysRevA.66.023410.

[52] J. Catani, P. Maioli, L. De Sarlo, F. Minardi and M. Inguscio: *Intense slow beams of bosonic potassium isotopes.* Phys. Rev. A **73**, 033415 (2006). doi:10.1103/PhysRevA.73.033415.

[53] R. S. III Williamson, P. A. Voytas, R. T. Newell and T. Walker: *A magneto-optical trap loaded from a pyramidal funnel.* Optics Express **3**, 111–117 (1998).

[54] F. S. Cataliotti, E. A. Cornell, C. Fort, M. Inguscio, F. Marin, M. Prevedelli, L. Ricci and G. M. Tino: *Magneto-optical trapping of Fermionic potassium atoms.* Phys. Rev. A **57**, 1136–1138 (1998). doi:10.1103/PhysRevA.57.1136.

[55] R. S. III Williamson and T. Walker: *Magneto-optical trapping and ultracold collisions of potassium atoms.* Journal of the Optical Society of America B **12**, 1393–1397 (1995).

[56] H. Wang, P. L. Gould and W. C. Stwalley: *Photoassociative spectroscopy of ultracold ^{39}K atoms in a high-density vapor-cell magneto-optical trap.* Phys. Rev. A **53**, R1216–R1219 (1996). doi:10.1103/PhysRevA.53.R1216.

[57] M. Prevedelli, F. S. Cataliotti, E. A. Cornell, J. R. Ensher, C. Fort, L. Ricci, G. M. Tino and M. Inguscio: *Trapping and cooling of potassium isotopes in a double-magneto-optical-trap apparatus.* Phys. Rev. A **59**, 886–888 (1999). doi:10.1103/PhysRevA.59.886.

[58] Marlon Nakat: *Kohärente Grundzustandsmanipulation von fermionischem Kalium hoher Teilchenzahl.* Diploma thesis, Universität Hamburg (2004).

[59] J. Goldwin, S. B. Papp, B. DeMarco and D. S. Jin: *Two-species magneto-optical trap with ^{40}K and ^{87}Rb.* Phys. Rev. A **65**, 021402 (2002). doi:10.1103/PhysRevA.65.021402.

[60] Paul D. Lett, Richard N. Watts, Christoph I. Westbrook, William D. Phillips, Phillip L. Gould and Harold J. Metcalf: *Observation of Atoms Laser Cooled below the Doppler Limit.* Phys. Rev. Lett. **61**, 169–172 (1988). doi:10.1103/PhysRevLett.61.169.

[61] J. Dalibard and C. Cohen-Tannoudji: *Laser cooling below the Doppler limit by polarization gradients: simple theoretical models.* Journal of the Optical Society of America B **6**, 2023 (1989).

[62] G. Modugno, C. Benkő, P. Hannaford, G. Roati and M. Inguscio: *Sub-Doppler laser cooling of fermionic ^{40}K atoms.* Phys. Rev. A **60**, R3373–R3376 (1999). doi:10.1103/PhysRevA.60.R3373.

[63] C.V. Heer: *Feasibility of Containment of quantum magnetic dipoles.* Review of Scientific Instruments (1963), 34(5), 532-7 **34**, 532 (1963).

[64] Alan L. Migdall, John V. Prodan, William D. Phillips, Thomas H. Bergeman and Harold J. Metcalf: *First Observation of Magnetically Trapped Neutral Atoms.* Phys. Rev. Lett. **54**, 2596–2599 (1985). doi:10.1103/PhysRevLett.54.2596.

[65] Harald F. Hess, Greg P. Kochanski, John M. Doyle, Naoto Masuhara, Daniel Kleppner and Thomas J. Greytak: *Magnetic trapping of spin-polarized atomic hydrogen.* Phys. Rev. Lett. **59**, 672–675 (1987). doi:10.1103/PhysRevLett.59.672.

[66] R. van Roijen, J. J. Berkhout, S. Jaakkola and J. T. M. Walraven: *Experiments with Atomic Hydrogen in a Magnetic Trapping Field.* Phys. Rev. Lett. **61**, 931–934 (1988). doi:10.1103/PhysRevLett.61.931.

[67] Naoto Masuhara, John M. Doyle, Jon C. Sandberg, Daniel Kleppner, Thomas J. Greytak, Harald F. Hess and Greg P. Kochanski: *Evaporative Cooling of Spin-Polarized Atomic Hydrogen.* Phys. Rev. Lett. **61**, 935–938 (1988). doi:10.1103/PhysRevLett.61.935.

[68] W.H. Wing: *On neutral particle trapping in quasistatic electromagnetic fields.* Progress in Quantum Electronics **8**, 181–199 (1984).

[69] Ralf Dinter: *Aufbau und Charakterisierung einer Magnetfalle zur simultanen Speicherung von ^{40}K und ^{87}Rb.* Diploma thesis, Universität Hamburg (2004).

[70] Wolfgang Petrich, Michael H. Anderson, Jason R. Ensher and Eric A. Cornell: *Stable, Tightly Confining Magnetic Trap for Evaporative Cooling of Neutral Atoms.* Phys. Rev. Lett. **74**, 3352–3355 (1995). doi:10.1103/PhysRevLett.74.3352.

[71] David E. Pritchard: *Cooling Neutral Atoms in a Magnetic Trap for Precision Spectroscopy.* Phys. Rev. Lett. **51**, 1336–1339 (1983). doi:10.1103/PhysRevLett.51.1336.

[72] M.-O. Mewes, M. R. Andrews, N. J. van Druten, D. M. Kurn, D. S. Durfee and W. Ketterle: *Bose-Einstein Condensation in a Tightly Confining dc Magnetic Trap.* Phys. Rev. Lett. **77**, 416–419 (1996). doi:10.1103/PhysRevLett.77.416.

[73] Lene Vestergaard Hau, B. D. Busch, Chien Liu, Zachary Dutton, Michael M. Burns and J. A. Golovchenko: *Near-resonant spatial images of confined Bose-Einstein condensates in a 4-Dee magnetic bottle.* Phys. Rev. A **58**, R54–R57 (1998). doi:10.1103/PhysRevA.58.R54.

[74] B. DeMarco, J. L. Bohn, J. P. Burke, M. Holland and D. S. Jin: *Measurement of p-Wave Threshold Law Using Evaporatively Cooled Fermionic Atoms.* Phys. Rev. Lett. **82**, 4208–4211 (1999). doi:10.1103/PhysRevLett.82.4208.

[75] G. Roati, F. Riboli, G. Modugno and M. Inguscio: *Fermi-Bose Quantum Degenerate $^{40}K-^{87}Rb$ Mixture with Attractive Interaction.* Phys. Rev. Lett. **89**, 150403 (2002). doi:10.1103/PhysRevLett.89.150403.

[76] Jinha Kim, Bretislav Friedrich, Daniel P. Katz, David Patterson, Jonathan D. Weinstein, Robert DeCarvalho and John M. Doyle: *Buffer-Gas Loading and Magnetic Trapping of Atomic Europium.* Phys. Rev. Lett. **78**, 3665–3668 (1997). doi: 10.1103/PhysRevLett.78.3665.

[77] C. J. Myatt, E. A. Burt, R. W. Ghrist, E. A. Cornell and C. E. Wieman: *Production of Two Overlapping Bose-Einstein Condensates by Sympathetic Cooling.* Phys. Rev. Lett. **78**, 586–589 (1997). doi:10.1103/PhysRevLett.78.586.

[78] F. Schreck, G. Ferrari, K. L. Corwin, J. Cubizolles, L. Khaykovich, M.-O. Mewes and C. Salomon: *Sympathetic cooling of bosonic and fermionic lithium gases towards quantum degeneracy.* Phys. Rev. A **64**, 011402 (2001). doi: 10.1103/PhysRevA.64.011402.

[79] F. Schreck, L. Khaykovich, K. L. Corwin, G. Ferrari, T. Bourdel, J. Cubizolles and C. Salomon: *Quasipure Bose-Einstein Condensate Immersed in a Fermi Sea.* Phys. Rev. Lett. **87**, 080403 (2001). doi:10.1103/PhysRevLett.87.080403.

[80] Francesca Ferlaino, Chiara D'Errico, Giacomo Roati, Matteo Zaccanti, Massimo Inguscio, Giovanni Modugno and Andrea Simoni: *Erratum: Feshbach spectroscopy of a $K - Rb$ atomic mixture [Phys. Rev. A 73, 040702 (2006)].* Phys. Rev. A **74**, 039903 (2006). doi:10.1103/PhysRevA.74.039903.

[81] Giovanni Modugno, Giacomo Roati, Francesco Riboli, Francesca Ferlaino and Massimo Brecha, Robert J. amd Inguscio: *Collapse of a Degenerate Fermi Gas.* Science **297**, 2240–2243 (2002). doi:10.1126/science.1077386.

[82] Klaus Mølmer: *Bose Condensates and Fermi Gases at Zero Temperature.* Phys. Rev. Lett. **80**, 1804–1807 (1998). doi:10.1103/PhysRevLett.80.1804.

[83] S. T. Chui, V. N. Ryzhov and E. E. Tareyeva: *Stability of the Bose system in Bose-Fermi mixture with attraction between bosons and fermions.* JETP Letters **80**, 274–279 (2004). doi:10.1134/1.1813686.

[84] M. Modugno, F. Ferlaino, F. Riboli, G. Roati, G. Modugno and M. Inguscio: *Mean-field analysis of the stability of a K-Rb Fermi-Bose mixture.* Phys. Rev. A **68**, 043626 (2003). doi:10.1103/PhysRevA.68.043626.

[85] J. Goldwin, S. Inouye, M. L. Olsen, B. Newman, B. D. DePaola and D. S. Jin: *Measurement of the interaction strength in a Bose-Fermi mixture with ^{87}Rb and ^{40}K.* Phys. Rev. A **70**, 021601 (2004). doi:10.1103/PhysRevA.70.021601.

[86] Sadhan K. Adhikari: *Mean-field description of a dynamical collapse of a fermionic condensate in a trapped boson-fermion mixture.* Phys. Rev. A **70**, 043617 (2004). doi:10.1103/PhysRevA.70.043617.

[87] F. Ferlaino, E. de Mirandes, G. Roati, G. Modugno and M. Inguscio: *Expansion of a Fermi Gas Interacting with a Bose-Einstein Condensate.* Phys. Rev. Lett. **92**, 140405 (2004). doi:10.1103/PhysRevLett.92.140405.

[88] V.S. Letokhov: *Narrowing of the Doppler width in a standing light wave.* JETP Letters **7**, 272 (1968).

[89] A. Ashkin: *Acceleration and Trapping of Particles by Radiation Pressure.* Phys. Rev. Lett. **24**, 156–159 (1970). doi:10.1103/PhysRevLett.24.156.

[90] Steven Chu, J. E. Bjorkholm, A. Ashkin and A. Cable: *Experimental Observation of Optically Trapped Atoms.* Phys. Rev. Lett. **57**, 314–317 (1986). doi:10.1103/PhysRevLett.57.314.

[91] D. M. Stamper-Kurn, M. R. Andrews, A. P. Chikkatur, S. Inouye, H.-J. Miesner, J. Stenger and W. Ketterle: *Optical Confinement of a Bose-Einstein Condensate.* Phys. Rev. Lett. **80**, 2027–2030 (1998). doi:10.1103/PhysRevLett.80.2027.

[92] R. Grimm, M. Weidemüller and Yu. B. Ovchinnikov: *Optical dipole traps for neutral atoms.* Advances in Atomic, Molecular and Optical Physics **42**, 40–170 (2000).

[93] J. Dalibard and C. Cohen-Tannoudji: *Dressed-atom approach to atomic motion in laser light: The dipole force revisited.* Journal of the Optical Society of America B **2**, 1707 (1985).

[94] H. Feshbach: *A unified theory of nuclear reactions.* Ann. Phys. **19**, 287 (1962).

[95] E. Tiesinga, A. J. Moerdijk, B. J. Verhaar and H. T. C. Stoof: *Conditions for Bose-Einstein condensation in magnetically trapped atomic cesium.* Phys. Rev. A **46**, R1167–R1170 (1992). doi:10.1103/PhysRevA.46.R1167.

[96] E. Tiesinga, B. J. Verhaar and H. T. C. Stoof: *Threshold and resonance phenomena in ultracold ground-state collisions.* Phys. Rev. A **47**, 4114–4122 (1993). doi:10.1103/PhysRevA.47.4114.

[97] M. Marinescu and L. You: *Controlling Atom-Atom Interaction at Ultralow Temperatures by dc Electric Fields.* Phys. Rev. Lett. **81**, 4596–4599 (1998). doi:10.1103/PhysRevLett.81.4596.

[98] A. J. Moerdijk, B. J. Verhaar and T. M. Nagtegaal: *Collisions of dressed ground-state atoms.* Phys. Rev. A **53**, 4343–4351 (1996). doi:10.1103/PhysRevA.53.4343.

[99] P. O. Fedichev, Yu. Kagan, G. V. Shlyapnikov and J. T. M. Walraven: *Influence of Nearly Resonant Light on the Scattering Length in Low-Temperature Atomic Gases.* Phys. Rev. Lett. **77**, 2913–2916 (1996). doi:10.1103/PhysRevLett.77.2913.

[100] John L. Bohn and P. S. Julienne: *Prospects for influencing scattering lengths with far-off-resonant light.* Phys. Rev. A **56**, 1486–1491 (1997). doi:10.1103/PhysRevA.56.1486.

[101] A. J. Moerdijk, B. J. Verhaar and A. Axelsson: *Resonances in ultracold collisions of ^6Li, ^7Li, and ^{23}Na.* Phys. Rev. A **51**, 4852–4861 (1995). doi:10.1103/PhysRevA.51.4852.

[102] H. M. J. M. Boesten, J. M. Vogels, J. G. C. Tempelaars and B. J. Verhaar: *Properties of cold collisions of ^{39}K atoms and of ^{41}K atoms in relation to Bose-Einstein condensation.* Phys. Rev. A **54**, R3726–R3729 (1996). doi:10.1103/PhysRevA.54.R3726.

[103] K. Dieckmann, C. A. Stan, S. Gupta, Z. Hadzibabic, C. H. Schunck and W. Ketterle: *Decay of an Ultracold Fermionic Lithium Gas near a Feshbach Resonance.* Phys. Rev. Lett. **89**, 203201 (2002). doi:10.1103/PhysRevLett.89.203201.

[104] L. Khaykovich, G. Schreck, F. G. Ferrari, T. T. Bourdel, J. J. Cubizolles, L. D. Carr and C. Castin, Y. Salomon: *Formation of matter-wave bright soliton.* Science **296**, 2390–2393 (2002). doi:10.1126/science.1071021.

[105] Kevin E. Strecker, Guthrie B. Partridge, Andrew G. Truscott and Randall G. Hulet: *Formation and propagation of matter-wave soliton trains.* Nature **417**, 150–153 (2002). doi:10.1038/nature747.

[106] T. Loftus, C. A. Regal, C. Ticknor, J. L. Bohn and D. S. Jin: *Resonant Control of Elastic Collisions in an Optically Trapped Fermi Gas of Atoms.* Phys. Rev. Lett. **88**, 173201 (2002). doi:10.1103/PhysRevLett.88.173201.

[107] J. L. Roberts, N. R. Claussen, James P. Burke, Chris H. Greene, E. A. Cornell and C. E. Wieman: *Resonant Magnetic Field Control of Elastic Scattering in Cold ^{85}Rb.* Phys. Rev. Lett. **81**, 5109–5112 (1998). doi:10.1103/PhysRevLett.81.5109.

[108] A. Marte, T. Volz, J. Schuster, S. Dürr, G. Rempe, E. G. M. van Kempen and B. J. Verhaar: *Feshbach Resonances in Rubidium 87: Precision Measurement and Analysis.* Phys. Rev. Lett. **89**, 283202 (2002). doi:10.1103/PhysRevLett.89.283202.

[109] Vladan Vuletić, Andrew J. Kerman, Cheng Chin and Steven Chu: *Observation of Low-Field Feshbach Resonances in Collisions of Cesium Atoms.* Phys. Rev. Lett. **82**, 1406–1409 (1999). doi:10.1103/PhysRevLett.82.1406.

[110] F. K. Fatemi, K. M. Jones and P. D. Lett: *Observation of Optically Induced Feshbach Resonances in Collisions of Cold Atoms.* Phys. Rev. Lett. **85**, 4462–4465 (2000). doi:10.1103/PhysRevLett.85.4462.

[111] M. Theis, G. Thalhammer, K. Winkler, M. Hellwig, G. Ruff, R. Grimm and J. Hecker Denschlag: *Tuning the Scattering Length with an Optically Induced Feshbach Resonance.* Phys. Rev. Lett. **93**, 123001 (2004). doi:10.1103/PhysRevLett.93.123001.

[112] S. L. Cornish, N. R. Claussen, J. L. Roberts, E. A. Cornell and C. E. Wieman: *Stable ^{85}Rb Bose-Einstein Condensates with Widely Tunable Interactions.* Phys. Rev. Lett. **85**, 1795–1798 (2000). doi:10.1103/PhysRevLett.85.1795.

[113] Jens Weber, Tino Jens Herbig, Michael Mark, Hanns-Christoph Nägerle and Rudolf Grimm: *Bose-Einstein Condensation of Cesium.* Science **299**, 232 (2003). doi: 10.1126/science.1079699.

[114] Jordan M. Gerton, Dmitry Strekalov, Ionut Prodan and Randall G. Hulet: *Direct observation of growth and collapse of a Bose-Einstein condensate with attractive interactions.* Nature **408**, 692–695 (2000). doi:10.1038/35047030.

[115] L. D. Carr, G. V. Shlyapnikov and Y. Castin: *Achieving a BCS Transition in an Atomic Fermi Gas.* Phys. Rev. Lett. **92**, 150404 (2004). doi: 10.1103/PhysRevLett.92.150404.

[116] D. S. Petrov, C. Salomon and G. V. Shlyapnikov: *Weakly Bound Dimers of Fermionic Atoms.* Phys. Rev. Lett. **93**, 090404 (2004). doi: 10.1103/PhysRevLett.93.090404.

[117] Markus Greiner, Cindy A. Regal and Deborah S. Jin: *Emergence of a molecular Bose-Einstein condensate from a Fermi gas.* Nature **426**, 537 (2003). doi: 10.1038/nature02199.

[118] S. Jochim, M. Bartenstein, A. Altmeyer, G. Hendl, S. Riedl, C. Chin, J. Hecker Denschlag and R. Grimm: *Bose-Einstein Condensation of Molecules.* Science **302**, 2101–2103 (2003). doi:10.1126/science.1093280.

[119] J. L. Roberts, N. R. Claussen, S. L. Cornish, E. A. Donley, E. A. Cornell and C. E. Wieman: *Controlled Collapse of a Bose-Einstein Condensate.* Phys. Rev. Lett. **86**, 4211–4214 (2001). doi:10.1103/PhysRevLett.86.4211.

[120] Elizabeth A. Donley, Neil R. Claussen, Sarah T. Thompson and Carl E. Wieman: *Atom molecule coherence in a Bose Einstein condensate.* Nature **417**, 529–532 (2002). doi:10.1038/417529a.

[121] Jens Herbig, Tobias Kraemer, Michael Mark, Tino Weber, Cheng Chin, Hanns-Christoph Nagerl and Rudolf Grimm: *Preparation of a Pure Molecular Quantum Gas.* Science **301**, 1510–1513 (2003). doi:10.1126/science.1088876.

[122] K. Xu, T. Mukaiyama, J. R. Abo-Shaeer, J. K. Chin, D. E. Miller and W. Ketterle: *Formation of Quantum-Degenerate Sodium Molecules.* Phys. Rev. Lett. **91**, 210402 (2003). doi:10.1103/PhysRevLett.91.210402.

[123] Stephan Dürr, Thomas Volz, Andreas Marte and Gerhard Rempe: *Observation of Molecules Produced from a Bose-Einstein Condensate.* Phys. Rev. Lett. **92**, 020406 (2004). doi:10.1103/PhysRevLett.92.020406.

[124] Cindy A. Regal, Christopher Ticknor, John L. Bohn and Deborah S. Jin: *Creation of ultracold molecules from a Fermi gas of atoms.* Nature **424**, 47–50 (2003). doi: 10.1038/nature01738.

[125] Kevin E. Strecker, Guthrie B. Partridge and Randall G. Hulet: *Conversion of an Atomic Fermi Gas to a Long-Lived Molecular Bose Gas.* Phys. Rev. Lett. **91**, 080406 (2003). doi:10.1103/PhysRevLett.91.080406.

[126] J. Cubizolles, T. Bourdel, S. J. J. M. F. Kokkelmans, G. V. Shlyapnikov and C. Salomon: *Production of Long-Lived Ultracold Li_2 Molecules from a Fermi Gas.* Phys. Rev. Lett. **91**, 240401 (2003). doi:10.1103/PhysRevLett.91.240401.

[127] M. W. Zwierlein, C. A. Stan, C. H. Schunck, S. M. F. Raupach, S. Gupta, Z. Hadzibabic and W. Ketterle: *Observation of Bose-Einstein Condensation of Molecules.* Phys. Rev. Lett. **91**, 250401 (2003). doi:10.1103/PhysRevLett.91.250401.

[128] M. Iskin and C. A. R. Sá de Melo: *Two-Species Fermion Mixtures with Population Imbalance*. Phys. Rev. Lett. **97**, 100404 (2006). doi:10.1103/PhysRevLett.97.100404.

[129] S. T. Wu, C.H. Pao and S. K. Yip: *Resonant pairing between Fermions with unequal masses*. arXiv:cond-mat/0604572 (2006).

[130] M. J. Bijlsma, B. A. Heringa and H. T. C. Stoof: *Phonon exchange in dilute Fermi-Bose mixtures: Tailoring the Fermi-Fermi interaction*. Phys. Rev. A **61**, 053601 (2000). doi:10.1103/PhysRevA.61.053601.

[131] L. Viverit: *Boson-induced s-wave pairing in dilute boson-fermion mixtures*. Phys. Rev. A **66**, 023605 (2002). doi:10.1103/PhysRevA.66.023605.

[132] D. V. Efremov and L. Viverit: *p-wave Cooper pairing of fermions in mixtures of dilute Fermi and Bose gases*. Phys. Rev. B **65**, 134519 (2002). doi:10.1103/PhysRevB.65.134519.

[133] M. Cramer, J. Eisert and F. Illuminati: *Inhomogeneous Atomic Bose-Fermi Mixtures in Cubic Lattices*. Phys. Rev. Lett. **93**, 190405 (2004). doi:10.1103/PhysRevLett.93.190405.

[134] Maciej Lewenstein, Anna Sanpera, Veronica Ahufinger, Bogdan Damski, Aditi Sen De and Ujjwal Sen: *Ultracold atomic gases in optical lattices: Mimicking condensed matter physics and beyond*. arXiv:cond-mat/0606771 (2006).

[135] G. Ferrari, M. Inguscio, W. Jastrzebski, G. Modugno, G. Roati and A. Simoni: *Collisional Properties of Ultracold K-Rb Mixtures*. Phys. Rev. Lett. **89**, 053202 (2002). doi:10.1103/PhysRevLett.89.053202.

[136] Francesca Ferlaino, Chiara D'Errico, Giacomo Roati, Matteo Zaccanti, Massimo Inguscio, Giovanni Modugno and Andrea Simoni: *Feshbach spectroscopy of a $K-Rb$ atomic mixture*. Phys. Rev. A **73**, 040702 (2006). doi:10.1103/PhysRevA.73.040702.

[137] Francesca Ferlaino, Chiara D'Errico, Giacomo Roati, Matteo Zaccanti, Massimo Inguscio, Giovanni Modugno and Andrea Simoni: *Erratum: Feshbach spectroscopy of a $K-Rb$ atomic mixture [Phys. Rev. A 73, 040702 (2006)]*. Phys. Rev. A **74**, 039903 (2006). doi:10.1103/PhysRevA.74.039903.

[138] Jonathan Michael Goldwin: *Quantum degeneracy and interactions in the ^{87}Rb - ^{40}K Bose Fermi mixture*. Phd-thesis, Graduate School of the University of Colorado (2005).

[139] M.-O. Mewes, M. R. Andrews, D. M. Kurn, D. S. Durfee, C. G. Townsend and W. Ketterle: *Output Coupler for Bose-Einstein Condensed Atoms*. Phys. Rev. Lett. **78**, 582–585 (1997). doi:10.1103/PhysRevLett.78.582.

[140] N. V. Vitanov, T. Halfmann, B. W. Shore and K. Bergmann: *Laser-induced population trasnfer by adiabatic passage techniques*. Annu. Rev. Phys. Chem. **52**, 763 (2001).

[141] Manuel Succo: *Degenerate Quantum Gases in Optical Lattice Potentials.* Diploma thesis, Universität Hamburg (2006).

[142] Leif Humbert: *Untersuchung und Manipulation von Quantengasmischungen aus ^{40}K und ^{87}Rb.* Diploma thesis, Universität Hamburg (2006).

[143] C. A. Regal, C. Ticknor, J. L. Bohn and D. S. Jin: *Tuning p-Wave Interactions in an Ultracold Fermi Gas of Atoms.* Phys. Rev. Lett. **90**, 053201 (2003). doi: 10.1103/PhysRevLett.90.053201.

[144] J. Zhang, E. G. M. van Kempen, T. Bourdel, L. Khaykovich, J. Cubizolles, F. Chevy, M. Teichmann, L. Tarruell, S. J. J. M. F. Kokkelmans and C. Salomon: *P-wave Feshbach resonances of ultracold ^6Li.* Phys. Rev. A **70**, 030702 (2004). doi: 10.1103/PhysRevA.70.030702.

[145] C. H. Schunck, M. W. Zwierlein, C. A. Stan, S. M. F. Raupach, W. Ketterle, A. Simoni, E. Tiesinga, C. J. Williams and P. S. Julienne: *Feshbach resonances in fermionic ^6Li.* Phys. Rev. A **71**, 045601 (2005). doi:10.1103/PhysRevA.71.045601.

[146] Kenneth Günter, Thilo Stöferle, Henning Moritz, Michael Köhl and Tilman Esslinger: *p-Wave Interactions in Low-Dimensional Fermionic Gases.* Phys. Rev. Lett. **95**, 230401 (2005). doi:10.1103/PhysRevLett.95.230401.

[147] C. Ticknor, C. A. Regal, D. S. Jin and J. L. Bohn: *Multiplet structure of Feshbach resonances in nonzero partial waves.* Phys. Rev. A **69**, 042712 (2004). doi: 10.1103/PhysRevA.69.042712.

[148] M. Zaccanti, C. D'Errico, F. Ferlaino, G. Roati, M. Inguscio and G. Modugno: *Control of the interaction in a Fermi-Bose mixture.* Phys. Rev. A **74**, 041605(R) (2006). doi:10.1103/PhysRevA.74.041605.

[149] Yu. Kagan, E. L. Surkov and G. V. Shlyapnikov: *Evolution and Global Collapse of Trapped Bose Condensates under Variations of the Scattering Length.* Phys. Rev. Lett. **79**, 2604–2607 (1997). doi:10.1103/PhysRevLett.79.2604.

[150] E. G. M. van Kempen, S. J. J. M. F. Kokkelmans, D. J. Heinzen and B. J. Verhaar: *Interisotope Determination of Ultracold Rubidium Interactions from Three High-Precision Experiments.* Phys. Rev. Lett. **88**, 093201 (2002). doi: 10.1103/PhysRevLett.88.093201.

[151] R. Roth and H. Feldmeier: *Mean-field instability of trapped dilute boson-fermion mixtures.* Phys. Rev. A **65**, 021603 (2002). doi:10.1103/PhysRevA.65.021603.

[152] Matthew P. A. Fisher, Peter B. Weichman, G. Grinstein and Daniel S. Fisher: *Boson localization and the superfluid-insulator transition.* Phys. Rev. B **40**, 546–570 (1989). doi:10.1103/PhysRevB.40.546.

[153] Olaf Mandel, Markus Greiner, Artur Widera, Tim Rom, Theodor W. Hänsch and Immanuel Bloch: *Coherent Transport of Neutral Atoms in Spin-Dependent Optical Lattice Potentials.* Phys. Rev. Lett. **91**, 010407 (2003). doi: 10.1103/PhysRevLett.91.010407.

[154] Thilo Stöferle, Henning Moritz, Christian Schori, Michael Köhl and Tilman Esslinger: *Transition from a Strongly Interacting 1D Superfluid to a Mott Insulator.* Phys. Rev. Lett. **92**, 130403 (2004). doi:10.1103/PhysRevLett.92.130403.

[155] Tim Rom, Thorsten Best, Olaf Mandel, Artur Widera, Markus Greiner, Theodor W. Hänsch and Immanuel Bloch: *State Selective Production of Molecules in Optical Lattices.* Phys. Rev. Lett. **93**, 073002 (2004). doi:10.1103/PhysRevLett.93.073002.

[156] Michael Köhl, Henning Moritz, Thilo Stöferle, Kenneth Günter and Tilman Esslinger: *Fermionic Atoms in a Three Dimensional Optical Lattice: Observing Fermi Surfaces, Dynamics, and Interactions.* Phys. Rev. Lett. **94**, 080403 (2005). doi:10.1103/PhysRevLett.94.080403.

[157] Thilo Stöferle, Henning Moritz, Kenneth Günter, Michael Köhl and Tilman Esslinger: *Molecules of Fermionic Atoms in an Optical Lattice.* Phys. Rev. Lett. **96**, 030401 (2006). doi:10.1103/PhysRevLett.96.030401.

[158] T. Volz, N. Syassen, D. M. Bauer, E. Hansis, S. Dürr and G. Rempe: *Preparation of a quantum state with one molecule at each site of an optical lattice.* Nature Physics **2**, 692 (2006).

[159] P. S. Jessen and I. H. Deutsch: *Optical lattices.* Advances in Atomic, Molecular and Optical Physics **37**, 36 (1996).

[160] Neil W. Ashcroft and Mermin David N.: *Solid State Physics.* Saunders College Publishing (1976).

[161] L. Viverit, C. Menotti, T. Calarco and A. Smerzi: *Efficient and Robust Initialization of a Qubit Register with Fermionic Atoms.* Phys. Rev. Lett. **93**, 110401 (2004). doi:10.1103/PhysRevLett.93.110401.

[162] H. Ott, E. de Mirandes, F. Ferlaino, G. Roati, V. Türck, G. Modugno and M. Inguscio: *Radio Frequency Selective Addressing of Localized Atoms in a Periodic Potential.* Phys. Rev. Lett. **93**, 120407 (2004). doi:10.1103/PhysRevLett.93.120407.

[163] Martin C. Gutzwiller: *Effect of Correlation on the Ferromagnetism of Transition Metals.* Phys. Rev. Lett. **10**, 159–162 (1963). doi:10.1103/PhysRevLett.10.159.

[164] J. Hubbard: *Electron Correlations in Narrow Energy Bands.* Proceedings of the Royal Society of London. Series A, Mathematical and Physical Sciences **276**, 238–257 (1963).

[165] Gregory H. Wannier: *The Structure of Electronic Excitation Levels in Insulating Crystals.* Phys. Rev. **52**, 191–197 (1937). doi:10.1103/PhysRev.52.191.

[166] W. Zwerger: *Mott-Hubbard transition of cold atoms in optical lattices.* Journal of Optics B **5**, S9–S16 (2003). doi:10.1088/1464-4266/5/2/352.

[167] Werner Krauth, Michel Caffarel and Jean-Philippe Bouchaud: *Gutzwiller wave function for a model of strongly interacting bosons.* Phys. Rev. B **45**, 3137–3140 (1992). doi:10.1103/PhysRevB.45.3137.

[168] K. Xu, Y. Liu, J. R. Abo-Shaeer, T. Mukaiyama, J. K. Chin, D. E. Miller, W. Ketterle, Kevin M. Jones and Eite Tiesinga: *Sodium Bose-Einstein condensates in an optical lattice*. Phys. Rev. A **72**, 043604 (2005). doi:10.1103/PhysRevA.72.043604.

[169] Simon Fölling, Artur Widera, Torben Müller, Fabrice Gerbier and Immanuel Bloch: *Formation of Spatial Shell Structure in the Superfluid to Mott Insulator Transition*. Phys. Rev. Lett. **97**, 060403 (2006). doi:10.1103/PhysRevLett.97.060403.

[170] Gretchen K. Campbell, Jongchul Mun, Micah Boyd, Patrick Medley, Aaron E. Leanhardt, Luis G. Marcassa, David E. Pritchard and Wolfgang Ketterle: *Imaging the Mott Insulator Shells by Using Atomic Clock Shifts*. Science **313**, 649–652 (2006). doi:10.1126/science.1130365.

[171] Subir Sachdev: *Quantum Phase Transitions*. Cambridge University Press (2000).

[172] Alexander Albus, Fabrizio Illuminati and Jens Eisert: *Mixtures of bosonic and fermionic atoms in optical lattices*. Phys. Rev. A **68**, 023606 (2003). doi:10.1103/PhysRevA.68.023606.

[173] H. P. Büchler and G. Blatter: *Phase separation of atomic Bose-Fermi mixtures in an optical lattice*. Phys. Rev. A **69**, 063603 (2004). doi:10.1103/PhysRevA.69.063603.

[174] Robert Roth and Keith Burnett: *Quantum phases of atomic boson-fermion mixtures in optical lattices*. Phys. Rev. A **69**, 021601 (2004). doi:10.1103/PhysRevA.69.021601.

[175] V. Ahufinger, L. Sanchez-Palencia, A. Kantian, A. Sanpera and M. Lewenstein: *Disordered ultracold atomic gases in optical lattices: A case study of Fermi-Bose mixtures*. Phys. Rev. A **72**, 063616 (2005). doi:10.1103/PhysRevA.72.063616.

[176] Lode Pollet, Matthias Troyer, Kris Van Houcke and Stefan M. A. Rombouts: *Phase Diagram of Bose-Fermi Mixtures in One-Dimensional Optical Lattices*. Phys. Rev. Lett. **96**, 190402 (2006). doi:10.1103/PhysRevLett.96.190402.

[177] L. Mathey, S.-W. Tsai and A. H. Castro Neto: *Competing Types of Order in Two-Dimensional Bose-Fermi Mixtures*. Phys. Rev. Lett. **97**, 030601 (2006). doi:10.1103/PhysRevLett.97.030601.

[178] Daw-Wei Wang: *Strong-Coupling Theory for the Superfluidity of Bose-Fermi Mixtures*. Phys. Rev. Lett. **96**, 140404 (2006). doi:10.1103/PhysRevLett.96.140404.

[179] Kenneth Günter, Thilo Stöferle, Henning Moritz, Michael Köhl and Tilman Esslinger: *Bose-Fermi Mixtures in a Three-Dimensional Optical Lattice*. Phys. Rev. Lett. **96**, 180402 (2006). doi:10.1103/PhysRevLett.96.180402.

[180] Oliver Wille: *Aufbau eines 3D-optischen Gitters für quantenentartete Fermi-Bose-Mischungen aus ^{40}K und ^{87}Rb*. Diploma thesis, Universität Hamburg (2005).

[181] R. Jáuregui, N. Poli, G. Roati and G. Modugno: *Anharmonic parametric excitation in optical lattices*. Phys. Rev. A **64**, 033403 (2001). doi:10.1103/PhysRevA.64.033403.

[182] Markus Greiner, Immanuel Bloch, Olaf Mandel, Theodor W. Hänsch and Tilman Esslinger: *Exploring Phase Coherence in a 2D Lattice of Bose-Einstein Condensates*. Phys. Rev. Lett. **87**, 160405 (2001). doi:10.1103/PhysRevLett.87.160405.

[183] Fabrice Gerbier, Artur Widera, Simon Fölling, Olaf Mandel, Tatjana Gericke and Immanuel Bloch: *Phase Coherence of an Atomic Mott Insulator*. Phys. Rev. Lett. **95**, 050404 (2005). doi:10.1103/PhysRevLett.95.050404.

[184] Fabrice Gerbier, Artur Widera, Simon Fölling, Olaf Mandel, Tatjana Gericke and Immanuel Bloch: *Interference pattern and visibility of a Mott insulator*. Phys. Rev. A **72**, 053606 (2005). doi:10.1103/PhysRevA.72.053606.

[185] C. Kollath, U. Schollwöck, J. von Delft and W. Zwerger: *Spatial correlations of trapped one-dimensional bosons in an optical lattice*. Phys. Rev. A **69**, 031601 (2004). doi:10.1103/PhysRevA.69.031601.

[186] P. Pedri, L. Pitaevskii, S. Stringari, C. Fort, S. Burger, F. S. Cataliotti, P. Maddaloni, F. Minardi and M. Inguscio: *Expansion of a Coherent Array of Bose-Einstein Condensates*. Phys. Rev. Lett. **87**, 220401 (2001). doi:10.1103/PhysRevLett.87.220401.

[187] V. A. Kashurnikov, N. V. Prokof'ev and B. V. Svistunov: *Revealing the superfluid–Mott-insulator transition in an optical lattice*. Phys. Rev. A **66**, 031601 (2002). doi:10.1103/PhysRevA.66.031601.

[188] Markus Greiner: *Ultracold Quantum gases in three–dimensional optical lattice potentials*. Phd thesis, Ludwigs-Maximilians-Universität München (2003).

[189] Lode Pollet, Corinna Kollath, Ulrich Schollwoeck and Matthias Troyer: *Mixture of bosonic and spin-polarized fermionic atoms in an optical lattice*. arXiv:cond-mat/0609604.

[190] P. B. Blakie and A. Bezett: *Adiabatic cooling of fermions in an optical lattice*. Phys. Rev. A **71**, 033616 (2005). doi:10.1103/PhysRevA.71.033616.

[191] P. B. Blakie and J. V. Porto: *Adiabatic loading of bosons into optical lattices*. Phys. Rev. A **69**, 013603 (2004). doi:10.1103/PhysRevA.69.013603.

[192] Ana Maria Rey, Guido Pupillo and J. V. Porto: *The role of interactions, tunneling, and harmonic confinement on the adiabatic loading of bosons in an optical lattice*. Phys. Rev. A **73**, 023608 (2006). doi:10.1103/PhysRevA.73.023608.

[193] M. Greiner, C. A. Regal, J. T. Stewart and D. S. Jin: *Probing Pair-Correlated Fermionic Atoms through Correlations in Atom Shot Noise*. Phys. Rev. Lett. **94**, 110401 (2005). doi:10.1103/PhysRevLett.94.110401.

[194] Simon Fölling, Fabrice Gerbier, Artur Widera, Olaf Mandel, Tatjana Gericke and Immanuel Bloch: *Spatial quantum noise interferometry in expanding ultracold atom clouds*. Nature **434**, 481 (2005). doi:10.1038/nature03500.

[195] T. Rom, Th. Best, D. van Oosten, U. Schneider, S. Foelling, B. Paredes and I. Bloch: *Spatial quantum noise interferometry in expanding ultracold atom clouds.* Nature **444**, 733 (2006).

[196] M. G. Kozlov and L. N. Labzowsky: *Parity violation effects in diatomics.* Journal of Physics B: Atomic, Molecular and Optical Physics **28**, 1933–1961 (1995).

[197] Ryan Barnett, Dmitry Petrov, Mikhail Lukin and Eugene Demler: *Quantum Magnetism with Multicomponent Dipolar Molecules in an Optical Lattice.* Phys. Rev. Lett. **96**, 190401 (2006). doi:10.1103/PhysRevLett.96.190401.

[198] M. A. Baranov, M. S. Mar'enko, Val. S. Rychkov and G. V. Shlyapnikov: *Superfluid pairing in a polarized dipolar Fermi gas.* Phys. Rev. A **66**, 013606 (2002). doi:10.1103/PhysRevA.66.013606.

[199] K. Góral, L. Santos and M. Lewenstein: *Quantum Phases of Dipolar Bosons in Optical Lattices.* Phys. Rev. Lett. **88**, 170406 (2002). doi:10.1103/PhysRevLett.88.170406.

[200] Jonathan D. Weinstein, Robert deCarvalho, Bretislav Friedrich and John M. Doyle: *Magnetic trapping of calcium monohydride molecules at millikelvin temperatures.* Nature **395**, 148–150 (1998). doi:10.1038/25949.

[201] Hendrick L. Bethlem, Giel Berden and Gerard Meijer: *Decelerating Neutral Dipolar Molecules.* Phys. Rev. Lett. **83**, 1558–1561 (1999). doi:10.1103/PhysRevLett.83.1558.

[202] S. A. Rangwala, T. Junglen, T. Rieger, P. W. H. Pinkse and G. Rempe: *Continuous source of translationally cold dipolar molecules.* Phys. Rev. A **67**, 043406 (2003). doi:10.1103/PhysRevA.67.043406.

[203] F. Masnou-Seeuws and P. Pillet: *Formation of ultracold molecules via photoassociation in a gas of laser cooled atoms.* Advances in Atomic, Molecular and Optical Physics **47**, 53–127 (2001).

[204] Jeremy M. Sage, Sunil Sainis, Thomas Bergeman and David DeMille: *Optical Production of Ultracold Polar Molecules.* Phys. Rev. Lett. **94**, 203001 (2005). doi:10.1103/PhysRevLett.94.203001.

[205] C. A. Regal and D. S. Jin: *Measurement of Positive and Negative Scattering Lengths in a Fermi Gas of Atoms.* Phys. Rev. Lett. **90**, 230404 (2003). doi:10.1103/PhysRevLett.90.230404.

[206] S. Gupta, Z. Hadzibabic, M. W. Zwierlein, C. A. Stan, K. Dieckmann, C. H. Schunck, E. G. M. van Kempen, B. J. Verhaar and W. Ketterle: *Radio-Frequency Spectroscopy of Ultracold Fermions.* Science **300**, 1723–1726 (2003). doi:10.1126/science.1085335.

[207] Thomas Busch, Berthold-Georg Englert, Kazimierz Rzazewski and Martin Wilkens: *Two Cold Atoms in a Harmonic Trap.* Foundations of Physics **28**, 549–559 (1998). doi:10.1023/A:1018705520999.

[208] D. S. Jin: Poster at ICAP 2006, Innsbruck (2006).

[209] S. B. Papp and C. E. Wieman: *Observation of Heteronuclear Feshbach Molecules from a ^{85}Rb $-^{87}$ Rb Gas.* Phys. Rev. Lett. **97**, 180404 (2006). doi: 10.1103/PhysRevLett.97.180404.

[210] T. Karpiuk, M. Brewczyk, S. Ospelkaus-Schwarzer, K. Bongs, M. Gajda and K. Rzążewski: *Soliton Trains in Bose-Fermi Mixtures.* Phys. Rev. Lett. **93**, 100401 (2004). doi:10.1103/PhysRevLett.93.100401.

List of publications

1. C. Ospelkaus, S. Ospelkaus, L. Humbert, P. Ernst, K. Sengstock, and K. Bongs: *Ultracold Heteronuclear Molecules in a 3D Optical Lattice*. Phys. Rev. Lett. **97**, 120402 (2006).

2. S. Ospelkaus, C. Ospelkaus, L. Humbert, K. Sengstock, and K. Bongs: *Tuning of Heteronuclear Interactions in a Degenerate Fermi-Bose Mixture*. Phys. Rev. Lett. **97**, 120403 (2006).

3. S. Ospelkaus, C. Ospelkaus, R. Dinter, J. Fuchs, M. Nakat, K. Sengstock and K. Bongs: *Degenerate K-Rb Fermi-Bose gas mixtures with large particle numbers*. Journal of Modern Optics, advanced online publication (2006).

4. S. Ospelkaus, C. Ospelkaus, O. Wille, M. Succo, P. Ernst, K. Sengstock, and K. Bongs: *Localization of Bosonic Atoms by Fermionic Impurities in a Three-Dimensional Optical Lattice*. Phys. Rev. Lett. **96**, 180403 (2006).

5. C. Ospelkaus, S. Ospelkaus, K. Sengstock, and K. Bongs: *Interaction-Driven Dynamics of ^{40}K–^{87}Rb Fermion-Boson Gas Mixtures in the Large-Particle-Number Limit*. Phys. Rev. Lett. **96**, 020401 (2006).

6. T. Karpiuk, M. Brewczyk, S. Ospelkaus-Schwarzer, K. Bongs, M. Gajda, and K. Rzążewski: *Soliton Trains in Bose-Fermi Mixtures*. Phys. Rev. Lett. **93**, 100401 (2004).